IntechOpen

Biophysics

Edited by A.N. Misra

BIOPHYSICS

Edited by **A.N. Misra**

Biophysics
http://dx.doi.org/10.5772/1877
Edited by A.N. Misra

Contributors

Vladimir Nikitin, Sayed Nour, Donald Jacobs, Amarendra Narayan Misra, Anatoly Skalny, Mikhail Karganov, A.Kh Tambiev, João Paulo Prates Ramalho, Luís Loura, Alfredo Palace Carvalho

Notice

Statements and opinions expressed in the chapters are these of the individual contributors and not necessarily those of the editors or publisher. No responsibility is accepted for the accuracy of information contained in the published chapters. The publisher assumes no responsibility for any damage or injury to persons or property arising out of the use of any materials, instructions, methods or ideas contained in the book.

First published in Croatia, 2012 by INTECH d.o.o.
eBook (PDF) Published by IN TECH d.o.o.
Place and year of publication of eBook (PDF): Rijeka, 2019.
IntechOpen is the global imprint of IN TECH d.o.o.
Printed in Croatia

Legal deposit, Croatia: National and University Library in Zagreb

Additional hard and PDF copies can be obtained from orders@intechopen.com

Biophysics
Edited by A.N. Misra
p. cm.
ISBN 978-953-51-0376-9
eBook (PDF) ISBN 978-953-51-5253-8

Meet the editor

Prof Dr Amarendra Narayan Misra has 35 years of research experience and 30 years of Post-Graduate teaching experience in Plant Biology, Molecular Biology & Biotechnology. He served as Professor of Plant Molecular Biology & Biotechnology, University of Pune; Guest Researcher, University of Tokyo; Professor of Plant Physiology & Biochemistry, Utkal University; founding Professor of Department of Biosciences & Biotechnology at Fakir Mohan University. He is currently founding Professor of Centre for Life Sciences, School of Natural Sciences, Central University of Jharkhand (CUJ), Ranchi, India. Prof. Misra served universities in various other capacities of University management/academic councils/administration for innovating and improving teaching and research. He guided more than 9 Ph.D. and 43 M.Sc., M.Tech. and M.Phil. students and published more than 135 papers in the field of Plant Biology, Biotechnology & Bioinformatics. His research interests cover the structure and function of photosynthetic membranes, luminescence, biosensors, tissue culture and mechanism of stress adaptation of tropical crop plants. Received fellowships/awards from CEC, FEBS, DBT, DST, CSIR, INSA, UGC, JSPS. Prof. Misra studied and collaborated during his research with scientists from more than 10 countries across the globe including Argentina, Brazil, Bulgaria, Japan, Poland, Switzerland, Ukrain, UK, USA.

Contents

Dedicated to my parents Dr. Sachidananda Misra and Mrs. Sailabala Misra.

Preface

Biophysics is a vast cross-disciplinary subject encompassing the fields of biology, physics and computational biology etc in microbes, plants, animals and human being. Wide array of subjects from molecular, physiological and structural are covered in this book. Most of these chapters are oriented toward new techniques or the application of techniques in the novel fields. The contributions from scientists and experts from different continents and countries focuss on major aspects of biophysics. The book covers a wide range of topics reflecting the complexity of the biological systems.

Although the field of biophysics is ever emerging and innovative, the recent topics covered in this book are contemporary and application-oriented in the field of biology, agriculture, and medicine. This book contains mainly reviews of photobiology, molecular motors, medical biophysics such as micotools and hoemodynamic theory.

Topics on Photobiology deal with Electromagnetic radiation and life: bioelementological point of view; Laser correlation spectroscopy approach to bioelementology problems: nutritional, ecological and toxic aspects; Chlorophyll fluorescence in plant biology, Thermoluminescence in chloroplast thylakoid. Topics on biotechnology and medical biophysics deal with molecular motors, micotools and application of hoemodynamic theory in mechanical cardiac assist devices.

Sun is the main source of electromagnetic radiation on earth that sustains life that has practical application in various fields: medicine, biology, agriculture and biotechnology.

The organization and structure/function relationships of biomembranes area represent substantial number of biochemical and biophysics probes. Fluorescence techniques are frequently used as a tools to characterize the structure and dynamics of biomembranes. However, a novel computer simulation method for the study of molecular dynamics (MD) of membranes for atomic-scale information using fluorescent membrane probes is described. The chapters on chlorophyll fluorescence

in plant biology and thermoluminescence in chloroplast thylakoid deal with the aspects of theory, technique and applications in biomembranes.

Bioelements are building blocks of life and physical-chemical principles regulate all the elemental behavior for the life processes to continue in the living system. Interesting introductory chapter describes how this phenomenon ios regulated by light and explains the method of laser correlation spectroscopy that measures this phenomenon in a living system.

Polyhydroxyalkanoates (PHAs) is biopolymer produced by various microbes. In this book the authors have projected luminous bacteria as a novel potential PHA producer. That can be greatly used in biotechnology.

Energetics of biomolecular machines or molecular motors, is calculated in the chapter for Molecular Motors by calculating flux and free energy. This is used for predicting the conformational transitions and the extent to which the power stroke and the thermal ratchet mechanisms that take part in the molecular motor motion.

Nowdays microtools are used in microsurgery of single cells and microscopic things such as cells or organelles. Microsurgery of a single cell, replacing its elements, the introduction of foreign genetic material makes this area of medicine, agriculture, basic and experimental biology especially relevant. Appearance in the hands of microsurgeon of a single cell of the new microtools that have the ability of active interference in functioning of the cell without causing a significant damage to it have changed the experimental biology.

Cardiovascular diseases (CVD) still cause the highest mortality in developed countries. Recently, congestive heart failure (CHF) was defined by the NIH as the new epidemic in USA with 5 millions new cases per year. Mechanical cardiac assist devices (CAD) are currently indicated for CHF patients. “Flow and Rate”: Concept and clinical applications of a new hemodynamic theory deals with transplantation problems and how to overcome them.

I would like to express my sincere thanks to the authors around the world for their excellent contributions to the book. I hope that the book will enhance the knowledge and give an insight into the present problems in biophysics. I express my appreciation to all the authors of this book.

Last but not the least, I express sincere thanks to my daughter Eva, son Rishi, son-in-law Divya and my granddaughter Diksha for their love, affection, encouragements and assistance during the preparation of this book which gave me immense inspiration for devoting my time and energy to this work. My parents, brothers and sisters and their family members have been a constant source of encouragement for my work and endeavours. I am indebted to them. There is none but my teachers at all levels who contributed to my knowledge and have been a

perpetual source of aspiration for all constructive academic work, that I have ever done in any sphere of my life. I owe them this piece of work and dedicate this book to them.

The assistance of InTech team is admirable and is willfully acknowledged.

Prof. Dr. A.N. Misra
Post-Graduate Department of Biosciences & Biotechnology
Fakir Mohan University, Balasore &
Centre for Life Sciences, School of Natural Sciences
Central University of Jharkhand, Ratu-Lohardaga Road, Brambe, Ranchi
India

1

Laser Correlation Spectroscopy: Nutritional, Ecological and Toxic Aspects

M. Karganov[1], I. Alchinova[1], E. Arkhipova[1] and A.V. Skalny[2]
[1]*Lab. of Polysystemic Investigations,*
Institute of General Pathology and Pathophysiology,
Russian Academy of Medical Sciences, Moscow,
[2]*Institute of Bioelementology, Orenburg State University, Orenburg,*
Russia

1. Introduction

Changes in physiological status of the organism under the effect of environmental factors modulate metabolic processes, which in turn, affects the composition of biological fluids and possibly of bioelements – substances, important for building and maintenance of the living matter. Bioelements are the elemental functioning units of living matter, which are biologically active complexes of chemical elements as atoms, ions and nanoparticles with organic compounds of exogenous (primary) or biogenous (secondary) origin (Skalny, 2009, 2011). Evaluation of subfraction composition of samples provides information on percentage of biosubstrate constituents and yields integral characteristics reflecting the function of systems and their readiness to adequate protection of the body. This initially biophysical method, named laser correlation spectroscopy (LCS) is used for screening of large groups of conventionally healthy individuals for diagnosis of body functional strain and detection of risk groups (Karganov et al., 2009). Optimized software takes into account individual peculiarities in internal sanogenetic systems of the organism when determining consequences for health in persons exposed to low doses of potentially harmful factors (Kryzhanovsky, 2004). LCS allows measuring particle size in native biological fluids. It is successfully used in clinical practice for evaluation of the disease severity and treatment efficiency in patients with asthma, diabetes mellitus, myasthenia, some haematological diseases, and other pathologies (Kovalev et al., 2002; Piruzyan et al., 2004; Karganov et al., 2006).

2. Principles of laser correlation spectroscopy

Laser correlation spectroscopy (LCS) (analogs: spectroscopy of quasi-elastic light scatter, optical mixing spectroscopy, photon-correlation spectroscopy) consists in measurement of spectral characteristics of light scattered in quasi-elastic mode from the spectrum of intensity fluctuations of the recorded light (Gulari et al., 1979; Hautz et al., 1981; Horn, Dalgleish, 1985; Hwand, Cummins, 1982; Chu, 1974). Two schemes of measurements can be used: homodyne (selective recording of the light scattered by the system) and heterodyne

(recording of beats between the scattered light and reference fixed high-intensity light). The spectrum of light intensity fluctuations is a Fourier-transform of a correlation function of intensity fluctuations of the recorded field. In the device used by us, a heterodyne scheme (Fig. 1) is applied (Lebedev et al., 1997). Helium-neon laser serves as a source of light (2).

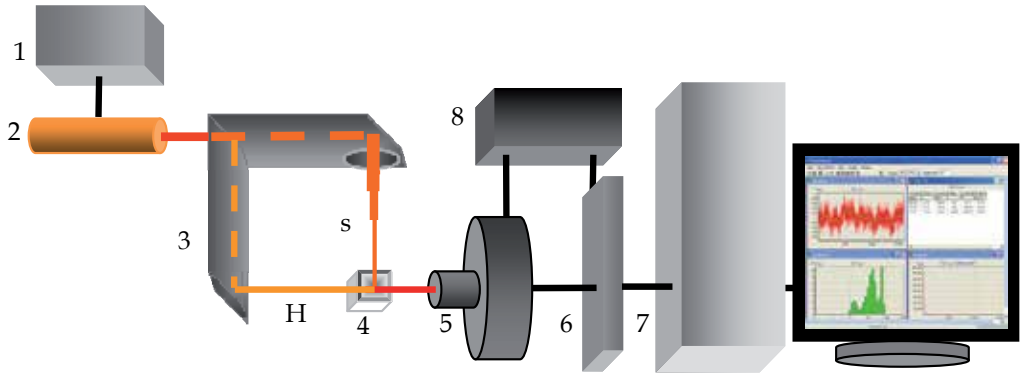

Fig. 1. Scheme of laser correlation spectroscope.

Laser beam is divided by a plate (3) and about 0.1% light beam (S) is separated from the main beam, is transmitted to a photorecorder (5), and is mixed with the scattered portion. Not the spectrum of light scattered by the studied system, but the spectrum of photoelectric fluctuations at the photorecorder (5) output is directly recorded in LCS. This spectrum represents a result of mutual beats of electromagnetic filed harmonics and is located in a low-frequency band.

The fluctuation spectrum of photoinduced current I(ω) at uniform size of scattering particles is described by Lorenz curve:

$$I(\omega)=\mathrm{A}\ \frac{\Gamma}{\Gamma^2+\omega}, \tag{1}$$

where $\Gamma = D_\tau q^2$ is width at half peak of the spectrum and q is a transmitted wave vector of the light scattered by the sample,

$$q = \frac{4\pi n}{\lambda}\sin\frac{\theta}{2},$$

where n is medium refraction coefficient,
λ is wavelength,
θ is scattering angle,
and D_T is a coefficient of translation diffusion of scattering particles.

The size of scattering particles can be determined from D_T. The relationship between diffusion coefficient D_T and hydrodynamic radius of particles R_h is described by Einstein-Stokes formula:

$$R_h = \frac{kT}{6\pi\eta D_T},$$

where T is absolute temperature,
k is Boltzmann constant,
and η is medium viscosity.

Correlation spectroscopy analyzes not the determinate, but the stochastic signal. Therefore, the measured parameter of the spectrum has a statistical error related to stochastic nature of light scattering. For improving the accuracy, measurements should be performed in many independent realizations and the results should be averaged.

The size of particles can be evaluated by measuring the peak width in current fluctuation spectrum. However, biological fluids are as a rule not monodisperse and contain particles of different sizes. The spectrum of light scattered by monodisperse particles is approximated by a Lorentz curve (1), whereas for polydisperse system it is a sum, or, for continuous distributions, is an integral of Lorentzians with different widths.

In this case, the spectrum I (ω) is described by the formula:

$$I(\omega)=\mathrm{A}\int\frac{A(\Gamma)\Gamma}{\Gamma^2+\omega}d\Gamma\ , \qquad (2)$$

where $A(\Gamma)$ is a function describing the distribution of particles by diffusion coefficient ($\Gamma = D_T q^2$, see above), and, hence, by their size. Assessment of particle size distribution consists in solution of the integral equation (2) with Lorentz kernel. This type of tasks is characterized by significant instability of the solution relative to variation of the experimental data. Generally, this is solution of Fredholm integral equation of the first kind. Using regularization method we can find approximate solutions for incorrectly posed inverse problems. This substantially extends the possibilities of experimental data interpretation.

Model experiments showed that for obtaining precise distribution characteristics the noise level σ of the experimental spectrum should not exceed ~0.1-0.3%. At the same time, actual spectra at 10 min accumulation time have noise level of 1% (2000 Hz band) or even 3% (200 Hz). Preprocessing of the experimental data improves analysis of these spectra due to intensive smoothening without loosing information on the true distribution. The smoothening procedure can be repeated, this will reduce the scatter of experimental points.

Parameters of the reconstructed distribution appreciably approximate to actual values. The required information on the distribution shape can be obtained from experimental curves with noise level of 0.5-1%.

In the given algorithm, the regularization parameter is determined on the basis of known error of experimental data. For the analysis of recorded spectra, the noise level of spectral curve should be determined with an accuracy of 15-20%. Overestimated error increases the bias caused by regularization procedure, while underestimated errors can lead to the appearance of additional false components (Braginskaya et al., 1983). Thus, the developed protocol of mathematical processing (regularization procedure) of spectrum $I(\omega)$ yields function $A(\Gamma)$ describing particle distribution by scattering characteristics. Setting a certain model of scattering particles allows evaluation of the weight distribution of these particles by their size.

It is known that the major contribution into light scattering is made by proteins and their complexes that have spherical shape. The hydrodynamic radius of a spherical scattering particle somewhat surpasses the geometrical radius of a dry particle due to the formation of a shell consisting of solvent molecules. For globular proteins, the hydrodynamic size is close to the diameter of the macromolecule. For non-spherical particles, the contribution of orientation dynamics (and conformation dynamics for deformable particles) is significant. Therefore, the hydrodynamic size of non-spherical protein molecules is a rather rough parameter. At the same time, the coefficient of translation diffusion is an objective physical characteristic of the protein particle reflecting structural changes in macromolecules: aggregation, conformational transitions, enzyme-substrate interactions *etc.*

It should be noted that light scattering capacity of high-molecular-weight particles is higher than that of low-molecular-weight particles. Therefore, the method is more sensitive to large objects. In case of relatively high concentration, they can shield the low-molecular-weight fractions in LC spectrum.

A histogram of typical size distribution is presented in Fig.2. The size scale is discrete and consists of 32 points.

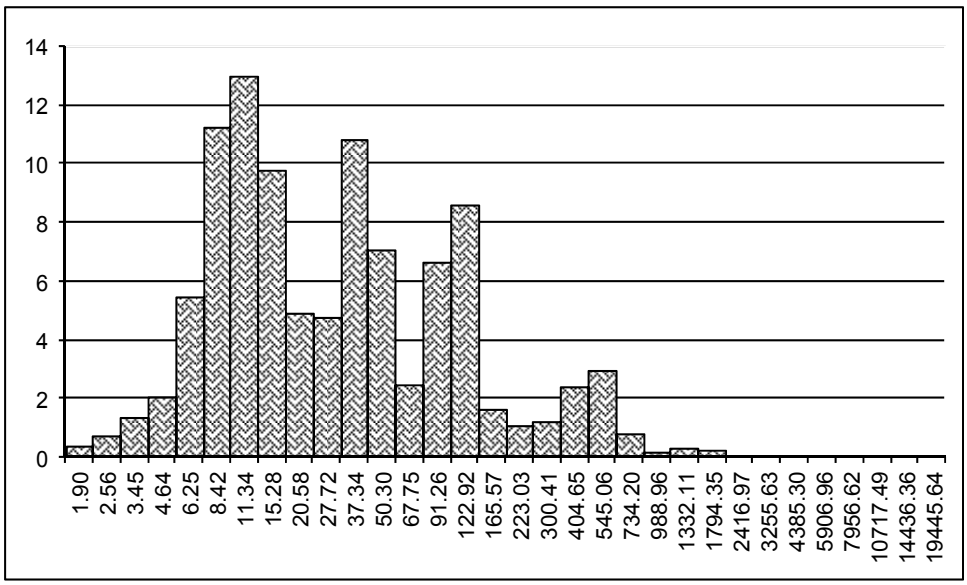

Fig. 2. Histogram of size distribution of particles in blood serum. Ordinate – contribution of particles of the corresponding zone into light scattering (%). Abscissa – particle size (nm).

The distribution histograms in the serum provide qualitative information on the mean particle sizes and their relative content. Strict correspondence of certain fragments of the spectrum to biological nature of serum components can be determined after additional studies.

Visual analysis of histograms is low-effective for screening studies; special classification programs are required to enable analysis of data bulk over a short time. The algorithm of classification analysis is based on methods of the theory of groups. For each serum n from group ν the histogram is described by a vector $A_i^{n(\nu)}$ and represent a point in a 32-space (i =

1,…..32; n = 1,..…N, where N is the number of patients in the group). For a group of patients with certain pathology, the points will be located in certain region of the space. After examination of a representative group of patients, a region corresponding to $A_i^{n(V)}$ values can be determined, which will allow qualitative attribution of a particular case to this group. The regions corresponding to normal health or different diseases can overlap, which means that the diagnosis cannot be made from LCS data only. Examination of a group of patients allows outlining a specific LCS data region in the 32-space. However, this comprehensive information requires a huge sample (if N cases is sufficient for one parameter, 32 parameters require N^{32} cases). It should be noted that A_i are obviously not independent values: mathematical analysis shows that the histogram contains information on 4-5 independent parameters. Moreover, not all parameters are of diagnostic value. The next approximation implied consideration of mean particle size in fractions 0-20 nm, 20-120 nm, and >120 nm and the relative number of particles in these fractions. Preliminary analysis showed that these parameters most adequately reflect relevant (from medical viewpoint) information contained in $\{A_i\}$ set. From mathematical point of view, this corresponds to projection of the 32-space to a 5-space. This reduction means certain information loss. On the other hand, this modification makes the entire procedure more resistant to stochastic measurement errors and reduces the necessary size of referent groups to acceptable values.

3. Basis for semiotic classifier

In case of blood plasma or serum, the total spectrum range is divided into 5 discrete intervals (by the size of scattering particles): I - 0-10 nm; II - 11-30 nm; III - 31-70 nm; IV - 71-150 nm; V - >150 nm. The first interval primarily includes low-molecular-weight monomer albumins and free glycolipid complexes; the second interval comprises globular proteins and low-molecular-weight lipoprotein complexes; the third interval contains larger lipoprotein complexes, RNP and DNP particles, and immune complexes with the lowest molecular weight; the fourth interval includes constitutive medium-molecular-weight immune complexes; the fifth interval is filled in case of immunopoiesis activation with the formation of high-molecular-weight immune complexes (usually associated with allergisation or autoimmune sensitization).

The same method is applied for the analysis of urine samples and oropharyngeal washout fluid (OPWF), but in these cases other informative intervals are used. For OPWF the spectrum is divided into 4 intervals: I - 0-50 nm; II - 51-400 nm; III - 400-2000 nm; IV - >2000 nm; for urine: I - <75 nm; II - 76-220 nm; III - 221-1500 nm; IV - >1500 nm. According to data obtained during studying of various pathological states, these intervals contain molecular components of cells: from polypeptide fragments to high-molecular weight protein complexes. It is assumed that increased areas in low- and medium-molecular-weight intervals of LC spectra reflect predominance of biosubstrate degradation processes, while increased areas in high- and very-high-molecular-weight intervals indicate predominance of biosubstrate polymerization processes.

Basing on the increase (or decrease) in the percent contribution of particles of a certain fraction into light scattering, a semiotic classification of LCS spectra was proposed including identification of 8 types of shifts in homeostasis and humoral immunity.

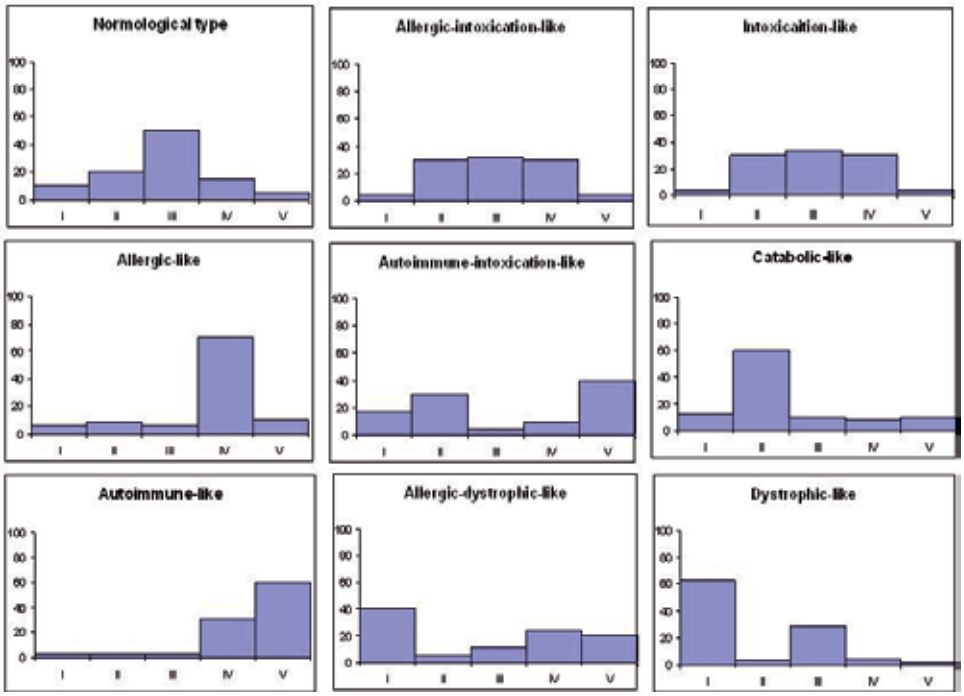

Fig. 3. Scheme of metabolic shifts, used in semiotic classifier. Ordinate – contribution of particles of the corresponding zone into light scattering (%).

Several gradations reflecting the degree of the above-listed spectral shifts correspond to each symptom-complex: initial, moderate, and pronounced.

4. Sample preparation and storage

For laser correlation spectroscopy, any biological fluid (blood serum/plasma, urine, oropharyngeal washout fluid, lachrymal fluid) can be used.

The oropharyngeal washout fluid is a multicomponent medium containing saliva and cell elements (epithelial cells and leukocytes). Some of the cells are partially or completely destroyed. The saliva is characterized by high proteolytic activity and its structural components (glyco- and lipoprotein complexes, immunoglobulins, etc.) are in a degraded state. Rapid and considerable dilution of this highly enzymatically active fluid sharply inhibits proteolytic activity. Simultaneously, structural components of the saliva are diluted to low concentrations making very difficult their detection by routine biochemical and physicochemical methods.

For preparing urine samples, medium portion of morning urine is used. The material (not less than 1 ml) is centrifuged for 30 min at 5000 rpm. The supernatant is collected in 1.5 ml disposable plastic tubes.

Blood is taken routinely: 200 µl of whole blood is transferred to plastic tubes with 800 µl physiological saline. The samples should be left at room temperature for 0.5-2 h and then centrifuged at 5000 rpm for 15 min. The supernatant is collected in new plastic tubes.

The samples can be frozen immediately after preparation and stored until analysis. Freezing is indispensable for transportation and long-term storage of the obtained biological material. Freezing and storage of samples at -25°C and below is an optimal regimen. Rapid freezing to -10°C/-15°C in the freezing compartment of domestic refrigerator is acceptable, but the samples should not be stored at this temperature for more than 3 months. Even single defrosting of the biological samples during storage is inadmissible.

Express LCS analysis of oropharyngeal washout fluids allowed us to perform screening of students of general and special schools in different regions of Russia influenced by various factors.

5. Ecological factors

For evaluation of the effect of recreation activities on functional state of children, we examined schoolchildren in a summer camp (Al'met'evsk, Tatarstan). This stationary country camp is located in ecologically benign region (pine forest) and meets recommendations for children recreation and nutrition in accordance with physiological and age-specific requirements. During examination, the peculiarities of homeostasis and humoral immunity were analyzed by laser correlation spectroscopy of oropharyngeal washout fluid.

The results of the first and second tests were compared in pairs. Shifts in the magnitude of the revealed changes along the axis "pronounced—moderate—initial" or transition from a shifted state to normal metabolism were taken as positive dynamics. Opposite shifts by degree of changes or transition from normal metabolism to predominance of catabolic or anabolic processes were taken as negative dynamics. Unchanged degree of metabolic shifts was regarded as the absence of dynamics.

A total of 62 schoolchildren (age 13±2 years) were examined. At the beginning of the session, schoolchildren with intoxication-like and dystrophy-like homeostatic shifts predominated (38 and 30%, respectively); pronounced shifts constituted 49%, initial and moderate shifts constituted 51%. On the whole, catabolic shifts predominated (79%) over anabolic (10%) and normological (11%) (Fig.4).

At the end of the session, we observed a decrease in the incidence of intoxication-like (from 38 to 22%) and dystrophy-like (from 30% to 14%) homeostatic shifts in tissues of the upper airways of the examined schoolchildren; the contribution of allergy-like shifts increased from 3 to 35, while the contribution of normological shifts remained unchanged.

By the end of the session, the metabolic shifts were classified as initial and moderate. The ratio of catabolic to anabolic shifts was 44% to 39%. Normological spectra constituted 17%.

Thus, using the LCS method we revealed differences in the direction of metabolic shifts in children at the beginning and after 1-month stay in the recreation camp. After this period, positive changes in metabolic status were observed in almost a half of children; in 22% examinees no changes were revealed and 31% children demonstrated negative dynamics.

By their magnitude (irrespective of the direction), 45.5% shifts at the beginning of the session were classified as pronounced and 54.5% as initial and moderate. At the end of the session, initial and moderate shifts (74%) predominated over pronounced ones (26%).

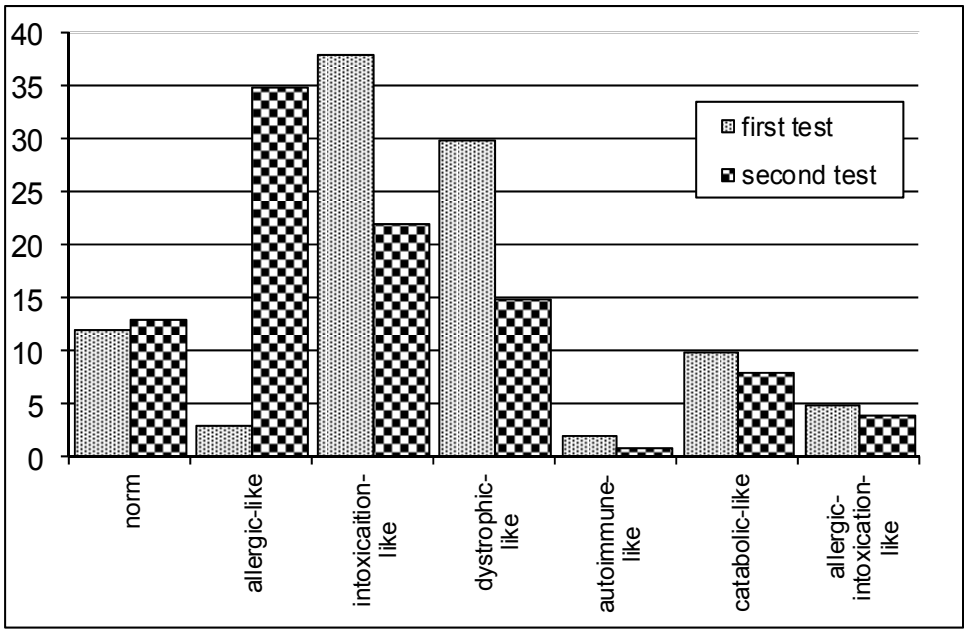

Fig. 4. Prevailing types of metabolic shifts in children in a summer camp. Ordinate - % of children with corresponding metabolic shift.

6. Nutrition factors (drinking regimen)

Various environmental factors act on human organism; for evaluation of the effect of a single factor, e.g. drinking water, on population health, copy-pair studies should be carried out.

Within the program for drinking regimen arrangement in Moscow schools (North-western and North-eastern districts) 240 pupils were examined.

Experimental groups consisted of preschool and primary school children attending schools with special water supply regimen. The control groups included children living in the same districts and attending schools with usual water supply conditions. Children in experimental schools of the North-western district drank "Moskoviya" mineral water over a period from September to May; the same water was used for cooking. In the North-eastern district, children drank "Troitsa" mineral water containing iodine, calcium, fluorine, magnesium, and sodium, and consumed "Zolotoi shar" vitaminized drink (30% of the dose recommended by the manufacturer). "Zolotoi shar" vitaminized drink contains vitamins C, A, E, D, B1, B2, B6, PP, biotin, folic acid, and pectin. The children received vitamins in dosage constituting 10-15% of daily physiological requirement. "Troitsa" and "Moskoviya" light-mineralization hydrocarbonate-calcium-magnesium waters (high-quality mineral waters according to Sanitary Regulations and Norms 2.1.4.1116-02) are intended for children's and dietetic nutrition. The children drank 300-400 ml per day.

Analysis of LC spectra showed that the initial distribution of predominant metabolic shifts (groups of catabolic and anabolic LC spectra) in children differed insignificantly in the two districts. Repeated examination was performed 6 months after the start of drinking bottled water.

Results of the change in drinking regimen were evaluated by individual dynamics of metabolic shifts. It was found that incidence of negative dynamics was significantly lower in children drinking specially prepared water (irrespective of its type). The percent of children with stable parameters of metabolism and with positive shifts increased under these conditions.

It was interesting to compare the effects of special drinking regimens. To this end we analyzed individual dynamics of metabolic shifts in children drinking "Moskoviya" water (North-western district) and "Troitsa" water with "Zolotoi shar" additive (North-eastern district).

It was found that special drinking regimen increased the percent of children with normological character of metabolism in both districts. However, the incidence of allergy-like metabolic shifts significantly increased in children of Northeastern district compared to the control. In children of the Northwestern district receiving water without additives, the incidence of anabolic (allergy-like) shifts was lower than in the control group. (Fig. 5).

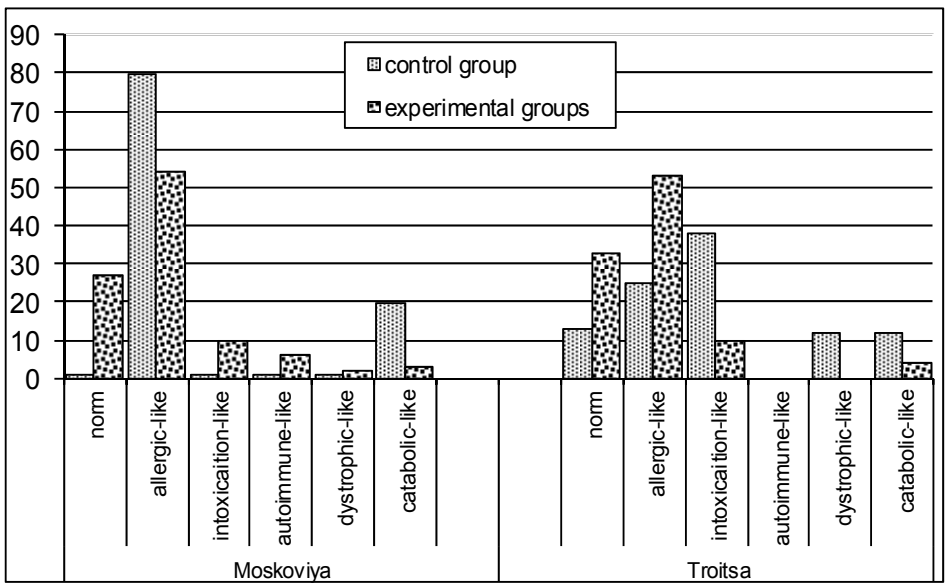

Fig. 5. Prevailing types of metabolic shifts in children with different drinking regimen. Ordinate - % of children with corresponding metabolic shift.

Moreover, drinking "Troitsa" water with "Zolotoi shar" additive led to an increase in the incidence of negative dynamics and a decrease in the incidence of neutral and positive dynamics. Taking into account the time of examination, this result can be explained as follows. The second examination was performed in May when the children are sensitized by natural allergens, and therefore we probably observed a combined effect of these factors and some components of "Zolotoi shar" additive.

Thus, complex examination of children consumed water with improved trace element composition and supplemented with vitamins over 6 months revealed a considerable decrease in the incidence of negative dynamics of metabolic processes in tissues of upper airways and gastrointestinal tract and an increase in the percent of children with normological type of metabolism.

7. Intoxication factors

Laboratory diagnostics allow not only obtaining specific results for each individual, but also combining basically different methods for more precise evaluation of the functional state of various body systems. This approach implies evaluation of combination and reciprocal influence of various parameters, their relationships with clinical symptoms and correlations with other indexes, rather than simple accumulation of laboratory data.

We present data obtained during combined use of standard trace element assay protocol in individuals with different content of some chemical elements (Hg, As, Mn, etc.) and laser correlation spectroscopy of blood serum, urine and OPWF. We analyzed biological samples obtained from 18 individuals conceivably exposed to toxicants: Hg and As.

Examination of biomaterials obtained from individuals exposed to mercury and arsenic showed that the incidence of some shifts significantly correlated with the content of these elements.

Biological samples for the analysis of trace elements were obtained twice with a 3-day interval; samples for LCS were taken once (during the second examination).

The content of chemical elements in biosubstrates was measured by inductively coupled plasma mass spectrometry (ICP-MS). The method of ICP-MS is characterized by high sensitivity and allows detection of a complex of trace and ultra-trace elements (Li, Be, B, V, Co, As, Se, Rb, Cd, Sn, Cs, Hg, Tl, Cr, Mn, Ni, Cu, Sr, Ba, Pb etc.) in samples.

ICP-MS measurements showed that the percent of individuals with normal mercury content considerably increased by the second measurement, which attests to toxicant elimination from the body. Similar tendency was observed during the analysis of arsenic content in the urine (Fig. 6).

The LCS analysis of serum revealed predominance of spectra, where small particles make the major contribution into light scatter. Intoxication-like and catabolic shifts prevailed, while dystrophic shifts were infrequent, which was a result of predominance of hydrolysis and catabolism.

LC-histograms of the urine and oropharyngeal washout fluids reflect the processes of epithelium destruction. In this sample, primarily normological and anabolic shifts were observed in the gastrointestinal system and upper airways, whereas in the excretory system normological, catabolic, and anabolic shifts were detected. Although we cannot prove the fact of intoxication or determine its degree, we revealed significant correlations between the results of LCS study and standard toxicological examination (Fig.7).

Analysis also revealed a negative correlation between the shifts in OPWF and arsenic concentration in the urine: the higher was the urinary concentration of metals, the greater was the contribution of small particles into light scatter.

The lower was the arsenic concentration in urine, the higher was the contribution of large particles into light scattering in OPWF ($r=-0.75$, $p<0.05$). We revealed two tendencies related to mercury concentration: in the urine ($r=0.06$, $p<0.05$) and in hair samples ($r=0.074$, $p<0.05$), which indicated that in samples with low metal concentrations the contribution of large particles into light scattering was higher.

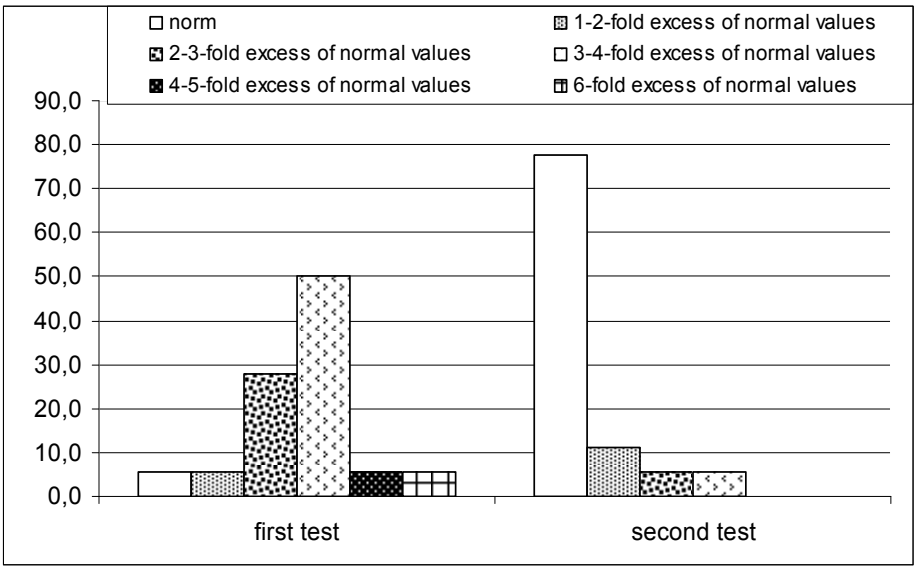

Fig. 6. Percent of individuals with normal and enhanced arsenic content.

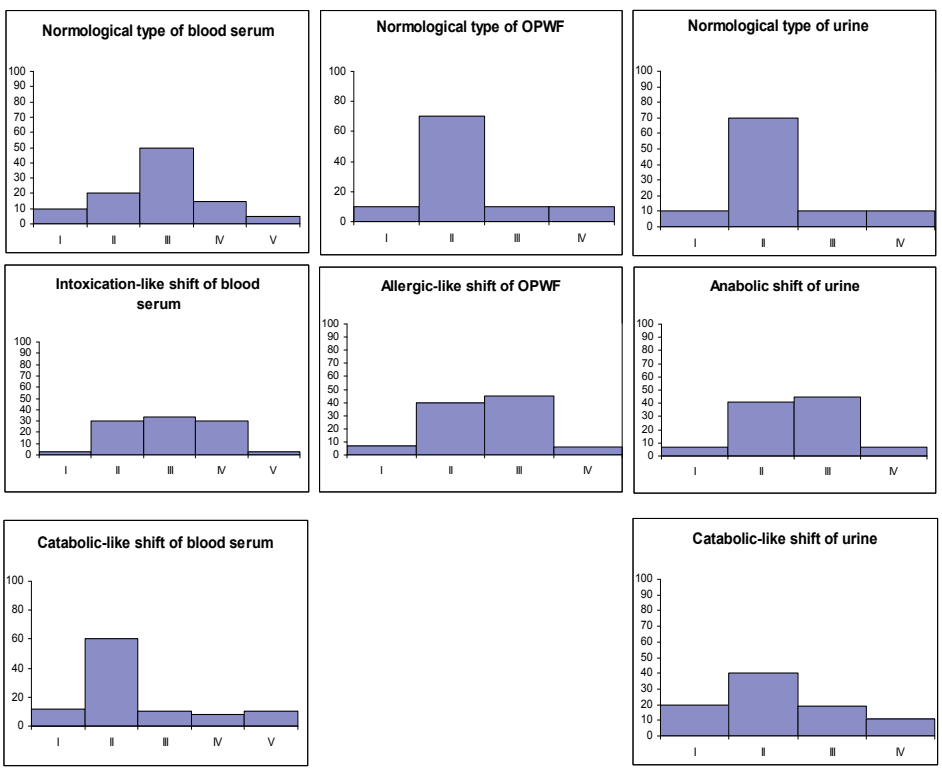

Fig. 7. Histograms of size distribution of particles in different biological fluids corresponding to different types of metabolic processes. Abscissa - informative zones of the spectrum, ordinate – contribution of particles of the corresponding zone into light scattering (%).

Significant correlations between shifts in the blood serum and metal concentration in the urine were found for samples taken during the second examination: mercury ($r=0.50$, $p<0.05$) and arsenic ($r=0.82$, $p<0.05$)

Analysis of the relationship between metal concentration and the contribution of certain particles into light scattering revealed a correlation between the presence of arsenic in urine and accumulation of the first-zone particles (0-10 nm) ($r=0.53$, $p<0.05$) in blood serum. An increase in arsenic content in the urine correlated with an increase in the contribution of second-zone particles (51-400 nm) ($r=0.76$, $p<0.05$) and a decrease in the contribution of the third-zone particles (401-2000 nm) ($r=-0.79$, $p<0.05$) in OPWF samples; the increase in arsenic content in hair samples correlated ($r=0,58$, $p<0,05$) with an increase in the contribution of first-zone particles (0-50 nm).

Thus, LCS analysis of biological fluids from individuals with elevated metal content revealed increased contribution of small particles into light scatter.

All these changes in the content of toxic elements did not exceed the biologically permissible levels and should not induce pathology development. It is known that elevated content of toxic elements by itself does not indicate the development of pathology. Moreover, individual peculiarities of sanogenetic systems of the organism determine various consequences for health in individuals exposed to equal low doses of potentially harmful factors (Kryzhanovsky, 2004). Nevertheless, their correlation with the contributions of particles of a certain size in biological fluids to light scatter suggests that changes in trace element composition are related to metabolic shifts.

It is known that mercury in low concentrations activates lipid peroxidation (LPO) and initially increases, but then decreases activity of antioxidant enzymes. In this case, accumulation of LPO products (malonic dialdehyde and β-microglobulin, protein in the urine) can be expected. Indeed, positive correlations were revealed between the content of toxic elements and relative content of small particles in the examined fluids. Moreover, the contribution of the fraction containing immunoglobulins into light scatter in the serum tended to decrease with increasing arsenic concentration in the urine. Previous studies showed that the intensity of light scatter by this fraction correlates with immunoglobulin content determined by routine laboratory methods.

The maximum number of correlations was found for shifts in the urine and oropharyngeal fluid. This is most likely related to initial stages of renal dysfunction and presumably peroral intoxication route.

The observed changes in the direction of metabolic shifts are stochastic and reflect either adaptive or disadaptive responses of the organism to low doses of toxic compounds. More numerous sample and broader range of effective concentrations are required for deciphering of the real significance of the detected relationships (Karganov et al., 2011).

Metabolic deviations, measured by LCS, are due to different external influences including effects of such typical ecopollutants as mercury and arsenic. Thus we can suppose the LCS can be an integrative method, useful for experimental and clinical bioelementological research, what was demonstrated in the experimental study described below.

8. Rat spleen genome DNA stability in experimental model of folate-induced hyperhomocysteinemia

Hyperhomocysteinemia is a result of disturbed methionine/cysteine metabolism and vitamin deficiency (B_6, B_{12}, folate). Homocysteine (HC), a product of natural degradation of the essential amino acid methionine, exhibits some toxic properties. High plasma content of HC is an independent risk factor for atherosclerosis, venous thrombosis, and other cardiovascular diseases (Thompson, Kim, 2004), as well as neurodegenerative disorders accompanying Alzheimer's (Miller, 1999) and Parkinson's diseases (Duan, 2002).

We have studied the influence of homocysteine level in blood plasma (control – 10.4±2.3, experiment – 33.2+6.3 μmol/l) on the structure of genomic DNA from the spleen of six-month rats under conditions of experimental folate-induced hyperhomocysteinemia. The specimens of DNA were kindly granted by Prof. Renat Zhdanov.

Particle size was different in the control and experimental samples (Fig. 8). In the control samples, particles with a diameter of 300-400 nm and 60-12 nm predominated (57 and 37%, respectively); in the experimental samples the percentage of 300-400-nm particles was the same (56%), while the content of 90-120-nm particles decreased to 26%. The experimental samples contained also medium-sized particles (165-220 nm, 11%) and large particles (545 nm), which were absent in the control (Fig. 8).

Measurements were performed also for DNA samples treated with DNaseI for 30 and 120 min (Fig. 8). The first distribution (30 min) showed that the content of 300-400-nm particles in the control samples decreased by 15%, but new particles with a diameter of 165 and 220 nm appeared (10 and 13%, respectively). In the control samples, particles with a diameter of 90-120 nm predominated (40% of all particles, Fig. 8).

In the experimental samples, large particles (300, 405, and 545 nm) practically completely disappeared (only 4.6% particles with a diameter of 300 nm were present). The amount of medium-sized (165 and 220 nm) and small (90, 120 nm) particles increased by more than 15% and by 10%, respectively. Thus, particles of all sizes, from 90 to 220 nm, were present in the experimental samples in equal amounts (about 23, 5%).

Repeated measurements were performed 120 min after DNaseI treatment. In the control, the proportion between the numbers of particles remained practically unchanged (changes did not exceed 2.5%, Fig. 8). At the same time, in the experimental samples the content of medium-sized and small particles differed considerably from the results of previous measurement. The content of medium-sized particles (165 and 220 nm) increased to 31 and 42%, (vs. 20 and 27%, respectively). The content of small particles (90 and 120 nm) decreased from 21 to 6% and from 24 to 13%, respectively. Particles with a diameter of 220 nm predominated (42% of total number of particles, vs. 5-7% in the control).

So, the presented data are good illustrations of the necessity of complex biophysical and biochemical investigation in life sciences, because biosphere is an assembly of bioelements and living organisms, existing under permanent regulatory influence of physic-chemical factors (Skalny, 2011).

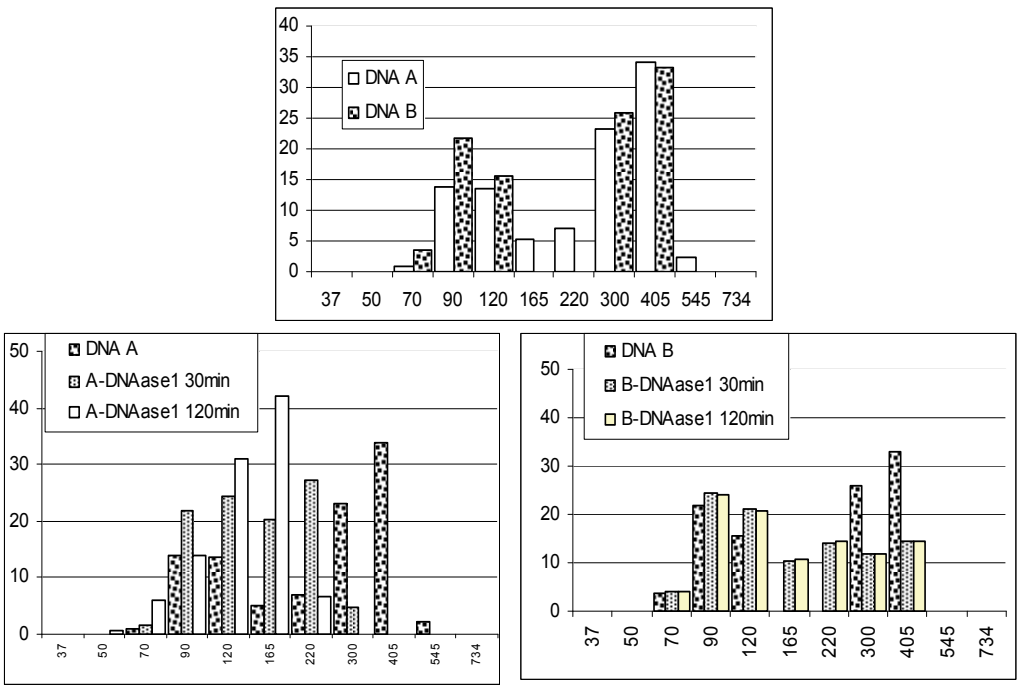

Fig. 8. Stability of rat spleen genome DNA in experimental model of folate-induced hyperhomocysteinemia. Abscissa – particle size (nm). Ordinate – contribution of particles of the corresponding zone into light scattering (%).

9. References

Braginskaya T.G., Dobichin P.D., Ivanova M.A. (1983) Analysis of the polydispersity by photon correlation spectroscopy. *Physical Scripts*, Vol.26, No.3, pp.309-315

Chu D. (1974) *Laser light scattering*. N.Y.: Acad. Press. 317 p

Lipin A.I., Tytovsky V.I., Yeligulashvili R.K. et al. (1988) Correlative laser spectroscopy for the determination of hepatitis B virus structures. *Hepatol. Lett*. No 6. pp. XXI-XXIII

Duan W., Ladenheim B., Culter R.G., Kruman I.I., Cadet J.L., Mattson V.P. (2002) Dietary folate deficience and elevated homocysteine levels endanger dopaminenergic neurons in models of Parkinson's disease. *J. Neurochem*. Vol.80. pp. 101-110

Gulari E., Tsunashima Y., Chu B. (1979) Photon correlation spectroscopy of particle distributions. *J. Chem. Phys*. Vol. 70, No 8. pp. 3965-3972

Hautz E., Cao A., Taillandier E. (1981) Conformational change of core particles studied by quasi-elastic light scattering. *Biochem*. Vol. 63, No 11-12. pp. 891-894

Horn D.S., Dalgleish D.G. (1985) A photon correlation spectroscopy study of size distributions of casein micelle suspensions. *Eur. Biophys*. Vol. 11, No 4. pp. 249-258.

Hwand I.S., Cummins H.Z. (1982) Dynamic light scattering of collagen. *J. Chem. Phys.* Vol. 77, No 2. pp. 616-627.

Karganov M., Skalny A., Alchinova I., Khlebnikova N., Grabeklis A., Lakarova E., Eisazadeh S. (2011) Combined use of laser correlation spectroscopy and ICP-AES, ICP-MS determination of macro- and trace elements in human biosubstrates for intoxication risk assessment. *Trace elements and electrolytes*, Vol.28, No.2. pp.124-127

Karganov M.Y., Kozhevnikova M.I., Aleschenko A.V., Khlebnikova N.N., Dmitrieva O.S., Alchinova I.B., Dmitrieva G.P., Pelevina I.I., Noskin L.A. (2006) Correlation between cytogenic abnormalities in cells and metabolic shifts during spinal deformities in children. *Studies in Health Technology and Informatics*, Vol.123, pp. 9-13

Kaznacheev V.P., Spirin E.A. (1991) *Cosmoplanetary phenomenon of the human: problems of a comprehensive study*. Novosibirsk: Nauka [in Russian].

Kovalev I.E., Karganov M.Y., Rumyantseva E.I., Kovaleva O.I. (2002) Laser correlation spectroscopy as an effective method of detection of DNA-containing and other macromolecular complexes in blood serum of patients with diabetes mellitus. *Doklady Biochemistry and Biophysics*, Vol. 386. No 1-6. pp. 281-283.

Kryzhanovsky G.N. (2004) Some categories of general pathology and biology: health, disease, homeostasis, sanogenesis, adaptation, immunity. New approaches and notions. *Pathophysiology*, Vol.11 No.2. pp.135-138

Lebedev A.D., Ivanova M.A., Lomakin A.V., Noskin V.A. (1997) Heterodyne quasi-elastic light scattering instrument for biomedical diagnostics. *Applied Optics*. Vol. 36, No 30. pp. 7518 – 7522

M.Karganov, I.Alchinova, E.Arkhipova, R.Dubovoi (2009) Non-invasive polysystemic analysis of ecological and anthropogenic factors influence on children. *J.Trends of Biomedicine*, Vol.24, No.1, pp.26-27

Miller J.W. (1999) Homocysteine and Alzheimer's disease. *Nutr. Rev*. Vol. 57. pp.126-129

Piruzyan L.A., Kovalev I.E., Rumyantseva E.I., Kovaleva V.L., Tyumentseva E.S., Balabolkin I.I., Karganov M.Yu., Kovaleva O.I. (2004) Laser correlation spectroscopy of macromolecular complexes in blood serum as an effective method of monitoring the progress of bronchial asthma in children. *Doklady Biochemistry and Biophysics*, Vol. 395. No 1-6. pp. 114-117.

Skalny A.V. (2009) Development of the concept of bioelements and the prospects of bioelementology. *Trace Elements in Medicine (Moscow),* Vol.10, No.3-4, pp.1-6. [in Russian]

Skalny A.V. (2011) Bioelementology as an interdisciplinary integrative approach in life sciences: terminology, classification, perspectives. *Journal of Trace Elements in Medicine and Biology*, Vol.25S. P.S3-S10.

Thompson M.P., Kim D. (2004) Links between fatty acids and expression of UCP2 and UCP3 mRNAs. *FEBS Letters*. Vol.568, No.1. P.4-9.

2

"Flow and Rate": Concept and Clinical Applications of a New Hemodynamic Theory

Sayed Nour
Therapeutic Innovations University of Paris XI, France

". . . From the heart arise the vessels which go to the whole body . . . if the physician lay the hands or his fingers to the head, to the back of the head, to the hands, to the place of the stomach, to the arms or to the feet, then he examines the heart, because all his limbs possess its vessels, that is: the heart speaks out of the vessels of every limb . . . If the heart trembles, has little power and sinks, the disease is advancing."
The Papyrus Ebers, c. 1534 BC (Stern,1875).

1. Introduction

Cardiovascular disease (CVD) is the first cause of mortality in developed countries, responsible for one death every 34 seconds and the estimated global annual cost is $ 403.1 billion according to recent statistics from the United States (Thom et al., 2006).

Furthermore, congestive heart failure (CHF) has been defined by the NIH, as the new epidemic in the USA, affecting more than 5 million new cases per year with a 5-year survival rate of less than 50% (Zickmund, et al. 2006).

Current therapies for CHF patients include medicinal provision of drugs such as cardiac glycosides, diuretics, AC inhibitors, anticoagulant (Couzens, 2009). However, medicinal therapies are usually insufficient necessitating complementary supports e.g., mechanically with cardiac assist devices (CAD) and/ or biologically with surgical procedures up till orthotopic heart transplants as an ultimate procedure.

Meanwhile, orthotopic heart transplant is still restricted due to the shortage of donors, plus operative morbidity and mortality (Schmauss & Weis, 2008).

Mechanical cardiac assist device (CAD) is usually used temporarily until the patient's hemodynamics improve, may offer an intermediate solution for the lake of donors as a bridge to a heart transplant (Park, et al., 2003), but in the heavy price of several disadvantages.

Permanent replacement of the heart with an artificial heart option is still a work in progress (Carpentier, 2011), with current technology having a short life expectancy. Thus, the artificial heart is primarily used as a bridge to transplant for patients wit biventricular failure. Furthermore the large size of an artificial heart limits its applications in specific categories, regarding body surface area (1.9±0.22 m^2), sex (95% men) and age (practically 0% children) (Roussel, et al., 2009).

Unfortunately, those aforementioned therapies still represent cost-effectiveness dilemma for health care systems in modern societies due to high cost, morbidity and mortality.

As a potential solution we are proposing a new therapeutic approach based on a fundamental revision of the entire circulatory system in correspondence to the physiopathology and physics laws applications with new generation of CAD.

The aim is directed to support and restore organ function, rather than to be replaced. Thus, it seeks to remedy the drawbacks of the state of present therapies and includes the innovation of new devices for providing cardiopulmonary and circulatory assistance.

This proposed therapy is based on a main concept (Think endothelial) and on a new hemodynamic theory entitled (Flow and Rate) that seeks to improve hemodynamics, organs microcirculations, restore and preserve the endothelial function by maintaining shear stress-mediated endothelial function with circulatory dynamics forces e.g., pressurized flow and shear rate (Nour, 2006).

1.1 Concept

Conceptually, the cardiovascular system is a closed pressurized hydraulic circuit (Figure 1), which is lined internally with endothelial cells (Samet & Lelkes, 1999; Furchgott, 1981).

Endothelium is constantly exposed to blood components and pulse pressure known as the tangential forces of shear stress (Hoeks et al., 1995).

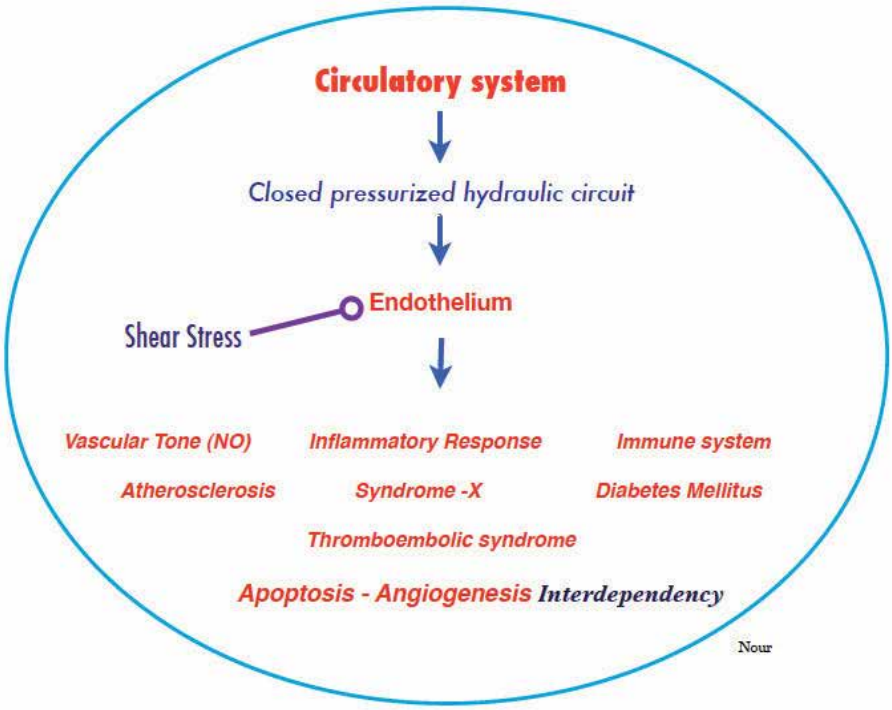

Fig. 1. Circulatory system's shear stress-mediated endothelial function

Shear stress controls and maintains endothelial function, which comprises the vascular tone by the synthesis of nitric oxide (NOS), blood coagulation, the inflammatory response, atherosclerosis, angiogenesis and apoptosis (Petrovic, et al., 2000; Limaye & Vadas, 2007; Lam et al., 2006).

In other terms, shear stress-mediated endothelial function controls embryogenesis, morphogenesis, organogenesis and maintenance of a healthy organism (Adamo, 2009).

In general, fluid movement in hydraulic circuits, which means momentum transfers with frictional losses, depends on driving forces, resistances, viscosity and conduits geometries (Kessler & Greenkorn, 1999).

The heart and peristaltic arteries represent the main circulatory driving forces that usually affect the left heart side.

Otherwise, accessory forces such as the respiratory pump, muscle pump, gravity, atmospheric pressure, oncotic pressure, skin baroreceptors, venous valves, pericardium, etc., are necessary to move up the steady blood flow at the right heart side (Nour, et al., 2009).

Endothelium controls vasoconstriction (e.g. catecholamine), vasodilatation with mediators like nitric oxide (NO) and vascular conditions with several processes like atherosclerosis and angiogenesis-apoptosis interdependency. This simply means that vascular resistances depend on vascular tone and vessels elasticity that are controlled mainly by shear stress-mediated endothelial function.

2. Fluid mechanics and cardiovascular pathophysiology

The clinical application of endothelial shear stress (ESS) should be realized in correspondence to cardiovascular biophysics, pathophysiological conditions as well as laws of fluid mechanics. This means a CAD should adapt the different criteria of each circuit of the right and left heart side (Figure 2), as follows:

1. The left heart circuit: it is characterized anatomically, by two high remodeling zones that represent the main circulatory pumps: the left ventricle (LV) and the aorta with the Valsalva as been shown on (Table1) and (Figure 2). Flow dynamics inside the Valsalva sinuses determines coronary ostia morphogenesis (Hutchins, 1988) and may contribute to a severe hemodynamic deterioration (Palmieri, 2001). So a shear stress-mediated endothelial function must be induced at the left heart side according to the Newton's principles by maintaining a physiological arterial pulse pressure (Feynman, et al., 2005). The LV almost, triples its myocardial mass during the first postnatal month with an important arterial angiogenesis. (Kozák-Bárány, 2001). According to Laplace's law, this LV remodeling could be enhanced by the posterior location of the LV (behind the RV), less limited by the pericardium and sternum, which increases the gravity effect, particularly in the neonatal supine position. The LV remodeling will be continued and maintained later on, influenced by ESS, the spherical shape of the LV (Yacoub, 1995), the elevated vascular resistances and the gravity effect at the aortic root. Disturbed flow dynamics at the left heart side induce atherosclerotic lesion (Samady, et al. 2011)), which is uncommon at the right heart side pulmonary arterial walls, most probably due to the constant delivery of ESS by the respiratory pump.

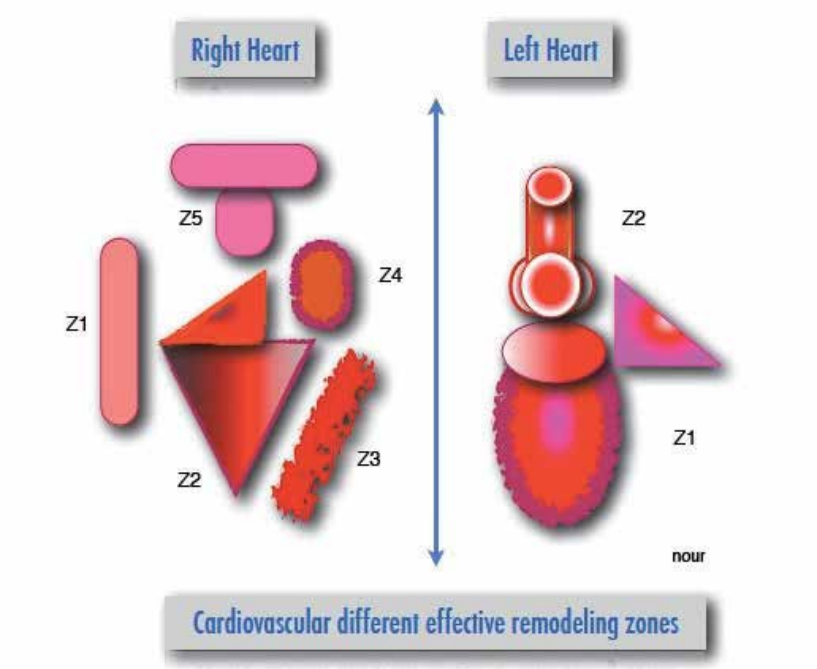

Fig. 2. Left and right heart circuits different remodeling zones

Zones	Sites	Remodeling	Main Factors
Z1	LV	High	↑ Laplace → posterior to RV less restricted by the pericardium; ↑ Newton → spherical shape (Tumkosit M 2007); ↑ resistances.
Z2	Aorta + Valsalva	High	↑ Shear stress (Newton): peristaltic pump + ↑gravity effect at the Valsalva; ↑ Laplace (less restricted external sheath at the arch), ↑ resistances.

Table 1. Left heart postnatal remodeling zones LV= left ventricle.

2. The right heart circuit: contrarily to the left, the right heart could adjust blood volume and shear rates at 5 different anatomical zones according to its physiological demands. In antenatal period, the right heart receives and pumps in equal rates more volume than the left, but keeps low remodeling due to pressure release through physiological shunts (Clark, 1987). After birth and shunts closure, both right and left ventricles share equal volume and rate inducing equal pulmonary and systemic cardiac output (CO), but remodeling remains inferior at the right heart side most probably due to venous steady flow and ventricular wall trabeculae. As shown in (Table 2) and (Figure 2), it could be identified by five different remodeling zones (Nour, 2009). Normally, the respiratory pump increases shear rates at the pulmonary endothelium externally creating an indirect or reversed pulse pressure shear stress (Newton). But with zones of steady flow and others with low pulse pressure the situation becomes more complex with physics

laws applications. In fact, both Bernoulli (Calvert, 2000), and Newton in addition to the gravity effect of Pascal's law as well (Humbert, 1947), must be considered to deliver a shear stress-mediated endothelial function.

Most importantly, the delivery of ESS with a CAD should be induced without disturbing the physiological remodeling of the right heart circuit (Buckberg, 2006). Direct induction of shear stress according to Newton's law like with an intravenous or intrapulmonary pulsatile perfusion must be avoided as it could induce serious hemodynamic conditions such as an irreversible pulmonary remodeling such us the Eisenmenger syndrome (D'Alto M, et al., 2007) or coronary bypass venous grafts disease. Also, the RV is preload dependant, that could not tolerate to be unloaded (Nour, 2009). This may explain failure of current pulsatile CAD in case of RV failure.

Zones	Anatomical site	Remodeling	Main Factors
Z1	SVC, IVC	Low	Absence of shear rates → Steady flow
Z2	A-V cavity	Mild	Trabeculae
Z3	Septum	Normal	Receiving interseptal left & right coronary supply
Z4	Infundibulum	High	↑ Coronary flow
Z5	PA tributary	Low	↓Pressure, Pulmonary Valve + Infudibulum

Table 2. Right heart postnatal remodeling zones (Nour et al 2009): SVC, IVC: superior & inferior vena cava respectively; A-V: atrioventricular; PA: pulmonary artery.

3. Hemorheological stock: the right heart circuit contains > 64% of blood volume surrounded by an important mass of endothelial cells. This natural stock of blood volume and endothelial mass can be stimulated by a proper pulsatile CAD, adaptable for right heart circuit's biophysics and physiopathology, for inducing shear stress-mediated endothelial function enhancement. Contrarily, to current evidence of high mortality of CHF patients associated with right heart failure (Haddad, 2011), the concept of the present therapeutic approach considers the right heart as a physiological backup for management of almost all types of hemodynamic and circulatory disorders, including CHF patients (Nour S, 2009). As been demonstrated on (Table 3), the right heart afterlaod could improve or deteriorates the global cardiac output (CO) and hemodynamic, for example nitrates therapies that could improve left ventricular MI by lowering the systemic afterload, may worsen and be fatal in case of RV ischemia (Haji, 2000).

Vascular Resistances	Status	Right heart	Left heart
Systemic	Low	Bad hemodynamic[1]	Good hemodynamic
Systemic	Elevated	Good hemodynamic[2]	Bad hemodynamic
Pulmonary	Low	Good hemodynamic	Good hemodynamic
Pulmonary	Elevated	Bad hemodynamic	Bad hemodynamic

Table 3. Dominancy of the right heart over the left heart through pulmonary vascular resistances (Nour, 2008):1= i.e. nitrates therapy in right ventricular ischemia; 2= i.e. epinephrine therapy with cyanotic spells

4. Pulmonary afterload: the influence of the right heart on hemodynamics is observed by the immediate postnatal drop of the pulmonary vascular resistances, triggered by the external shear stress-mediated endothelial function induced by the respiratory pump

(creating an indirect internal pulse pressure closer to Newton's law). Another example is observed in patients in squatting position during cyanotic spells of Tetralogy of Fallot (TOF) that increases the systemic vascular resistances (Senzaki, 2008) and increases the intrapulmonary flow and shear rates in a retrograde manner through the malaigned VSD to lower the pulmonary vascular resistances, followed by global hemodynamic improvement. The increased intrapulmonary shear rate that can be induced by adrenaline injection as well during the cyanotic TOF spells (Table 3), provides shear stress-mediated endothelial function approaching Bernoulli's law. Reduction of pulmonary vascular resistances is an immediate target for hemodynamic improvement that can be achieved by shear stress-mediated endothelial function enhancement directly with an intrapulmonary shear rate enhancement device (e.g. pulsatile catheter); or indirectly with an external pulsatile device (e.g. pulsatile suit).

5. Microcirculation: as is known, human being is a multicellular organism in which cellular biology performs a main role in terms of development, maintenance, proper operation and also failure of vital organs (Vincent, 2008). Maintaining good operation of organs by means of microcirculation in the organ constitutes a characteristic effect of the proposed concept. Microcirculations are controlled by plurality of endothelial mediators of vasodilators, which are dependent on shear stress (Koller, 1993) (Poelmann, 2008). Under normal hemorheological condition, microcirculation behavior approaches that of Newton's law. A symbolic example observed in athletics, high physical performance, which means shear stress-mediated endothelial function, could be achieved with slow heartbeat (shear rate) and increased stroke volume (pulse pressure). In contrast, in any abnormal hemorheological state, microcirculation presents behavior that approaches that of Bernoulli's law, as interpreted by the Fahraeus-Lindqvist effect in which plasma stuck at the inner vascular boundary layers while erythrocytes move faster at the center (Fahraeus & Lindqvist, 1931; Neri Serneri, 1981). This could explain absence of cyanosis in anemic patients with low hematocrite, unlike those patients with high hematocrite, as erythrocytes aggregations at microcirculations induce cyanosis with clinical signs finger clubbing (drumsticks fingers).

2.1 Cardiovascular pathogenesis

Endothelial dysfunction is responsible for almost all types of cardiovascular pathogenesis whatever congenital or acquired (Endemann et al., 2004)

The dependency of the endothelium on shear stress stimuli starts by the placental angiogenesis since the 6th gestational day, once there are normal hemorheolgical maternal factors (Heilmann, et al, 2005). Troubled shear stress forces due to an increased blood pressure (e.g.,preeclampsia) or low hematocrit (anticoagulant drugs), induces congenital anomalies and could interrupt the course of pregnancy (Aron, et al., 2003).

By the 8th gestational day of the intrauterine life, the embryonic vasculogenesis starts due to shear stress enhanced endothelial function, creating the first blood vessels followed by the appearance of the first fetal heartbeat by the 21st day (Meyers, 2007).

Furthermore, disturbed flow dynamics in the prenatal period, could induce congenital anomalies (Al-Ghazali, et al., 1989). Some symbolic examples of cardiac malformations are resumed on (Table 5) of cardiac malformations on (Table 4).

Flow disturbances	Congenital malformations
No flow → no grow	Hypoplastic left heart syndrome (Rao, 1994)
Homogenous flow	Heterotaxy syndrome (Prendiville, 2010).
Excessive flow	Agenesis pulmonary valves (Yeager, 2002).
Modified flow	Conotruncal defects: TGA, TOF, DORV, DOLV, (Rothenberg, 2003).

Table 4. Congenital malformations with troubled flow dynamics: TGA = transposition of great arteries; TOF= tetralogy of Fallot; DORV, DOLV= double outlet right or left ventricle respectively.

In the postnatal period, endothelial dysfunction is a major predisposing factor to hemodynamic troubles, circulatory disorders such as diabetes (Kapur A, De Palma R., 2007), arterial hypertension (Martini, et al., 2006), atherosclerosis (Chatzizisis, et al., 2007) and life-threatening conditions (e.g. cardiogenic shock, multiple organ failure). This could be induced by disturbed flow dynamics due to pump failure and/or elevated vascular resistances. As a symbolic example, right ventricular (RV) failure can occur either due to elevated pulmonary vascular resistances caused by pulmonary oligemia, pulmonary hyperemia; or due to RV pump failure caused by ischemia, congenital anomalies, arrhythmia, valvulopathy, and/or accessory circulatory driving forces failure like with failed Fontan's operation (Pereira & Shirali, 2005).

2.2 Types of endothelial dysfunction

Practically, and in a matter to facilitate the therapeutic approach for cardiovascular pathologies, endothelial dysfunctions could be classified into three categories as follows (Nour, 2009):

- **Type A**: endothelial dysfunction manifested with heart failure.
- **Type B**: includes endothelial dysfunction patients with endothelial dysfunction with normal heart function (e.g. diabetic, systemic arterial hypertension, PAH, erectile dysfunction, etc).
- **Type C**: represented by healthy individuals, liable for endothelial dysfunction pathogenesis under certain circumstances like disturbed atmospheric pressure and gravity (e.g. Astronauts, professional scuba divers, bedridden); fatigue, increased inflammatory responses, increased apopotosis (e.g. athletics, early aging processes).

2.3 Endothelial dysfunction vs. current CVD therapies

Usually, endothelial dysfunction occurs as a consequence of pathological and/or interventional cardiovascular conditions, unfortunately with bad prognosis as there is no real curative option. A symbolic example, as been schematized in (Figure 3), regarding the current management of ischemic heart disease (IHD), which is still the leading cause of death so far. Except cracking or bypassing atheroma nothing has been done effectively until present.

As been resumed in (Figure 3): there are three symbolic "R" therapeutic options of myocardial ischemia which means: Reperfusion through an interventional and/or surgical approach; Rehabilitation, with physical exercise or CAD; Replacement with cellular therapy

(WU KH, et al., 2006) or heart transplants. Also there are three conflictual therapeutic factors "F": F1 due to patients clinical varieties like with unstable angina; silent ischemia; ST-elevated myocardial infarction (STEMI) or non-ST elevated myocardial infarction (NSTEMI); mechanical complications of IHD; cardiogenic shock (Berger PB, et al., 1999); age or sex. This is complicated by anatomical variation; variations in myocardial damage that affects the septum, right or left ventricular regions (Haji SA & Movahed, 2000); and variable coronary pathology, including normal, spasmodic, vasculitis, (Newburger, et al., 2004), or classical coronary atherosclerosis. Second factor (F2) is related to therapeutic defects like with nitrates tolerance (Abrams J, 1988); finally the most important factor (F3) is the maintained endothelial dysfunction (e.g. atheroma).

Unfortunately, all those therapeutic options could not resolve the problem, means to restore the main cause of dysfunctional endothelial atherosclerotic plaques (Davignon , et al., 2004). In addition, there are several varieties of MI due to other endothelial dysfunction pathogenesis rather than atherosclerosis such as coronary spasm (Kusama, et al., 2011) or congenital anomalies (McCrindle, et al. 2007), that could not be managed easily with angioplasty or coronary grafts (Gershlick & Thomas, 2007).

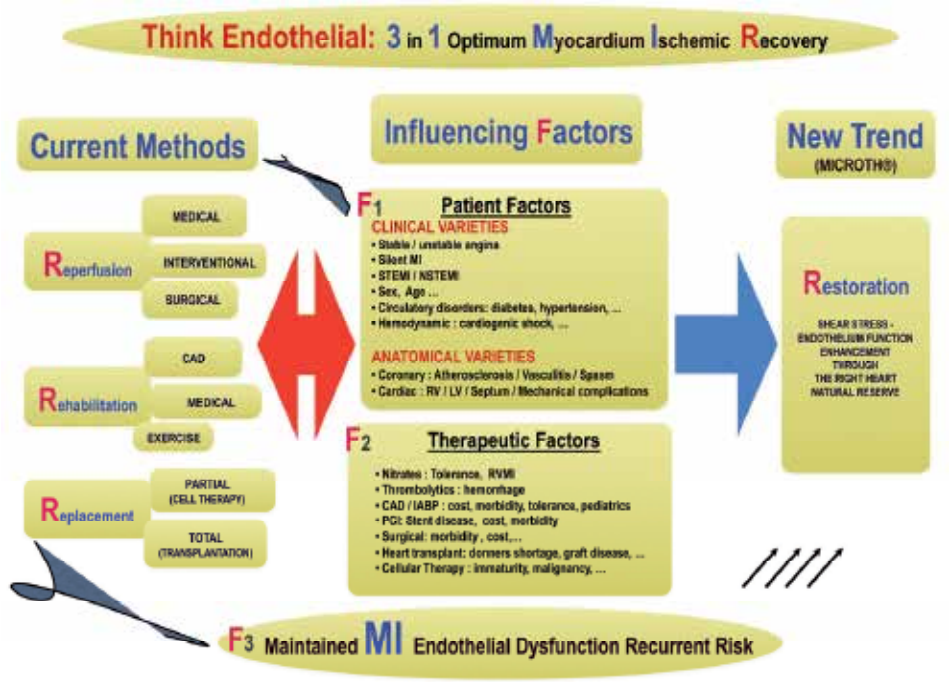

Otherwise, restorations of the endothelial function could be provided by the present concept (3R-in-one).

Fig. 3. Current therapeutic options for Myocardial infarction (MI)

3. Current CADs and endothelial dysfunction

In case of disturbed hemodynamic with heart failure, additional circulatory driving forces might be needed such as: a) Bio-assists with surgical procedures like the aortomyoplasty (Bolotin, et al (2001), cardiomyoplasty (Chachques, et al.,2005), and heterotopic heart

transplants (Onuzo, et al., 2000); and/or b) mechanical assists devices: like the cardiopulmonary bypass (CPB), left ventricular assist device (LVAD) (Seyfarth, et al., 2008)or right ventricular assist device (RVAD), and the artificial heart (Unger, et al.,1988).

In general, the present arts of cardiac assists devices can be classified in two categories:

1. Devices that increase coronary blood flow during diastole, in order to improve the oxygenation and thus the performance of the myocardium. This category includes the intra-aortic balloon pump (IABP), (Burkhoff , et al., 2006) and the enhanced external counterpulsation pump (EECP), (Bonetti, et al. 2003). These devices must be synchronized with heartbeat and unsuitable in case of cardiac arrhythmia; and
2. Devices that unload and bypass the heart pump: either partially as achieved by left ventricular assist devices (LVAD), right ventricular assist devices (RVAD), and by extracorporeal membrane oxygenation (ECMO); or completely like with biventricular assist devices, extracorporeal circulation (CBP), hetertopic heart transplant. It should be emphasized that ECMO partially deviates some of the venous blood to an external membrane oxygenator. ECMO does not completely unload the right ventricle (RV) and that may explain its successful applications in pediatrics patients who are more frequently vulnerable to RV failure (Wilmot, et al. 2011).
   As a matter of fact, development of CAD remains controversial due to the induced momentum energy losses with the tasks of increased morbidity and mortality.

Most probably, CAD may aggravate hemodynamics, leading to multiple organ failure and death due to several factors that could be directly linked to devices themselves or indirectly due to patients' related factors as follows:

1. Devices related factors:
   a. *Concept and design*: a CAD is typically a lumped model constructed according to laws of physics for driving a Newtonian compressible fluid inside a closed pressurized hydraulic circuits (Roselli RJ & Brophy, 2003), implementing rigid tubes with fixed diameter. Meanwhile in practices a CAD is confronted with a non-Newtonian fluid (blood, running in flexible vessels with different geometries). This confrontation between two opposite pressurized hydraulic circuits (Figure 4) creates a vicious circle of momentum energy losses manifested clinically by increased vascular resistances with endothelial dysfunction (e.g. hemorrhage, thromboembolism, inflammatory response, apoptosis, etc.), up till multiple organ failure.
   b. *Driving forces' drawbacks*: more precisely, roller or centrifugal pumps are usually used to circulate and perfuse blood between the patient and the external circuit most commonly in a steady flow mode of perfusion (Gravlee, 2008). Unfortunately even with biocompatible, materials the effect of sucking and pumping a fragile fluid like blood mechanically with impellers, propellers, or pulsed reservoir, inside narrow rigid conduits create a zone of turbulence and vortices with important energy losses (Geankoplis, 2005). This improper simulation of a ventricular function with current CAD, as it is practically impossible to replace a type III passive pump like the heart, by type II, or I pump (Anderson,1999).
   c. *Installations systems*: usually conduits of tubes, and cannula, made of biocompatible materials (e.g. PVC®, Dacron®, PTFE®, etc.), are used for connection between patient and CAD. In addition, those conduits need to be securely stitched to

cardiovascular tissues, diverted under the skin (tunnelization) to allow proper chest closure, then to be de-aired and checked for leakage or gas emboli before finally connected to their corresponding CAD. Furthermore, the distance between a CAD and the patient' inlet/outlet sites gives rise to dead space, creating an additional momentum energy losses zone(please refer to Figure 8). Finally, the procedures for installing such conduits need to be carried out by experienced surgeons in specialized centers on patients who are fragile, and who have usually already been operated on several times in the past, increasing the risks of morbidity and mortality (e.g. hemorrhages, vascular complications, infections, multiple organ failure).

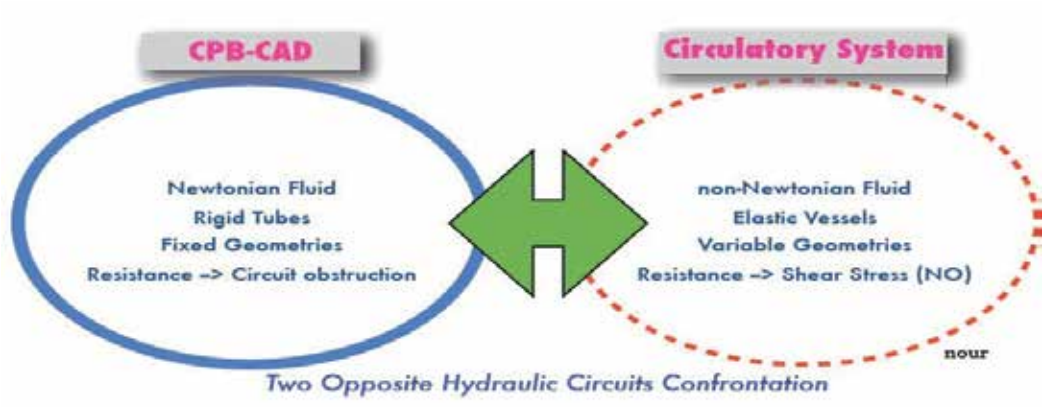

Fig. 4. Circulatory system and CAD create two opposite hydraulic circuits dilemma

2. Patients related factors: The aggravating factors inherent to the patients themselves can be of several kinds such as:
   a. Age, sex: most CAD devices are unsuitable for patients with small body surface area (e.g. children, female) since more than 80% of CAD devices are designed for body areas of more than 1.5 m^2, i.e. corresponding to adult heart patients. In addition CAD are generally first designed for management adult heart diseases and then miniaturized to cope with pediatric populations. However; pediatric patients are more vulnerable to hemodynamic disturbances caused by right heart failure due to congenital anomalies and they are vulnerable to vascular complications caused by small vessels geometries in content (Potapov, et al 2007). Adults usually suffer from ischemic left ventricular heart diseases with atherosclerotic vessels and they are therefore more vulnerable to vascular complications (Nour S, 2008).
   b. Etiology: fate of CHF patients with severe right ventricular (RV) failure (CVP>16mmHg) is worse, compared with those patients with left heart sided pathologies. Current therapies employing CAD to treat CHF patients with severe RV failure (Prutkin et al. 2008), still exhibit a high mortality rate (65%-95%), most probably due to insufficient understanding of the great difference between the right and left heart circuits (Sollano, 1998).
   c. Preclinical studies: in particular, the role of animal models in therapeutic evaluation, which is an extremely essential procedure before proceeding to clinical

applications of new CAD. However, there is still a gape between the chosen animal model and clinical realities as presented in the following examples:

i. Current models of myocardial infarction are unfortunately, driven by costs rather than clinical resemblance. For example, rat as a most popular selected model is far from human physiopathology with a heart rate> 400 bpm.
ii. Models of acute pulmonary hypertension (PAH), as often done either by hypoxia, monocrotaline, or systemic-pulmonary shunt. However, a lack of robust models of PAH, is still missing due to different spectra of lung tissue between species and humans (Robbins, 2004), (Bauer, et al. 2007).
iii. The biventricular heart failure models, often called for testing of cardiac assist devices, which remain difficult to achieve in animals. The most part of these mechanical assists devices are usually tested in computational version (Querzoli, 2011) or WindKessel models, away from the pathophysiological aspect in humans (Olufsen & Nadim A, 2004).

d. Miscellaneous: finally, the shortage of donors, immunosuppressive drugs drawbacks (e.g. malignancy); coronary atherosclerosis, follow up costs and surgical complications, all contribute to limiting the generalization of such treatments in practice.

4. Proposal

The present concept proposes clinical applications of these tangential forces of shear stress in order to regulate the endothelial function so as to improve the hemodynamic of patients, the overall microcirculation of vital organs, and, when it has failed, to reestablish normal operation of the cardiac pump in a manner that is as physiological as possible, without replacing any organs and without any traumatic intrusion, to provide a method that is as minimally invasive as possible.

Development of a CAD* with an optimum function, which means improving hemodynamics, increasing organ microcirculation, restoring and preserving deficient endothelial function in a diseased human being, should compromise the following steps: maintaining the circulatory flow dynamics in the patient's systemic and pulmonary circulations; and temporarily relieving the heart of its pumping function.

** CAD is referred to a "circulatory assist device", instead of the commonly applied term "cardiac assist device".*

More precisely there are three manners to stimulate the endothelium with a mechanical assist device as follows (Figure 5):

1. Direct internal endothelial stimulation that will be induced by an intravascular catheter device.
2. Indirect internal endothelial stimulations with a pulsatile perfusion flow generated by a pulsatile pipe (tube) device at the left heart side.
3. External stimulation (pulsatile suit) at the right heart side endothelial with gentle rhythmic squeezing of the venous and lymphatic capacitances reservoirs at the superficial veins and capillaries.

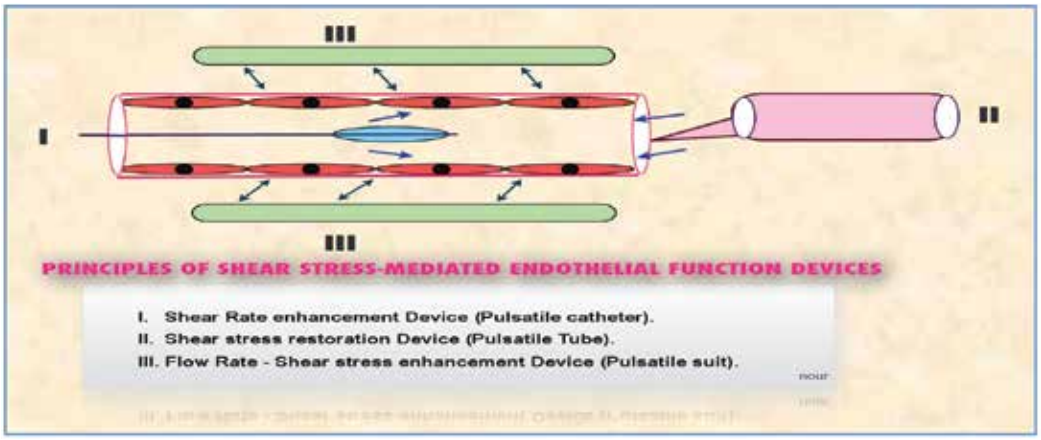

Fig. 5. Methods for shear stress-mediated endothelial function stimulations

According to the present concept, the method consists in using at least one device external to the patient's body and connected by at least a pipe and/or a specific connection element to:

1. Increase the preload of the right ventricle so as to improve myocardial oxygenation and so as to improve its contractility; and/or
2. Unload the left ventricle and diffuse regular pulsatile flow in the proximity of the aortic root so as to improve the hemodynamics of the left ventricle of the heart; and/or
3. Stimulate the endothelium mechanically by shear stress enhancement so as to release several mediators of endothelial vasodilators like nitric oxide (NO), to reduce the systemic and pulmonary vascular resistances (afterload).

5. Synchronization with the diastolic phase

The synchronization of these new pulsatile CAD with the heartbeat is strictly guided by the therapeutic indications according to types of endothelial dysfunction as follows (Nour S, 2009):

- Type A: this means in case of heart failure, CAD's synchronization is unnecessary and must be unsynchronized with heartbeat.
- Type B: synchronization of CAD with the heart is necessary to restore the endothelial function.
- Type C: synchronization of CAD is relative, because according to the Starling's law (Katz, 2002), the cardiac output (CO) adapts to the venous return (RV preload).

6. Devices

In known manner, the prior art constituted in particular by circulatory assistance systems such as LVAD, RVAD, Biventricular AD, etc., simulate the ventricular pump by complex driving forces.

In a manner that is very different, and indeed that is opposite in the physical sense of the word, the devices and methods of the present concept are designed to maintain circulation

in columns of blood within their own physiological containers as constituted by veins and arteries. The idea is to maintain a pulsatile blood stream complying with the biophysical and physiological standards of pulmonary and systemic circulations, by applying mechanical endothelial stimuli of shear stress.

One aspect of the devices and methods of the present concept enables shear stress endothelial stimuli to be increased, thereby enabling a microcirculation opening to be created in various organs of human body by means not only of conventional mediators of vasodilators such as nitric oxide, but also by means of other new vasodilators processing.

6.1 Pulsatile suit

In one aspect of the present method, blood is compressed from the outside of the body by means of a special suit referred to as a 'pulsatile suit", of the kind described in patents applications (WO/2008/000111) and (WO 2010/070018), which suit is used primarily to provide circulatory assistance to the right heart and secondarily as a device that makes it possible to obtain an overall hemodynamic improvement. The pulsatile suit is composed of three layers and must be suitable for the postoperative situations and provided with security features as following:

1. Inner layer made of elastic material (e.g. neoprene) to insure smooth tight massage like pulsed surge at the skin. 2. Middle sandwiched layer filled with gelatinous fluid, to alleviate the vigorous inflation/deflation, power induced by the driving force. 3. External layer made from tougher materials to keep the pulsed wave inwards toward the body. This part is equipped by security air releasing valve to prevent over inflation accident in case of mechanic defect. 4. Holes are previewed in the suit body, in order to facilitate medical administrations and prevent bedsores. 5. Layers thickness and design are modified according to age, body weight and indication of the patient. 6. The back portion of the trunk part of the suit (vest and belt) must not be inflatable in order to avoid any spinal, or back injuries. 7. Blood must be pulsed back from periphery towards the heart in a sloping progressive wave in longitudinal axis. Except at the chest part, pulsations must be started backward - forward towards the front, in a horizontal axis in such a manner to increase venous return within respect of the respiratory movement.

Naturally, this pulsatile suit has detachable parts and may take on various forms such as a hood, a pair of trousers, a jacket, a glove, a boot, or a sock. The parts could be reassembled together in one unit and wrapped tightly around the patient body through straps and zippers, as shown in (Figure 6) and as patents descriptions.

Figures 12 show such suit covering the bottom portion of the human body, which the therapist (doctor, nurse, or even the patient) can put into place without effort. The suit may be connected directly to an external pump, it may be actuated by the therapist himself or herself.

The structure serves advantageously to guide the pulsations it generates, progressively in the venous return direction. It thus constitutes a circulatory assistance device for the right ventricle (RVAD).

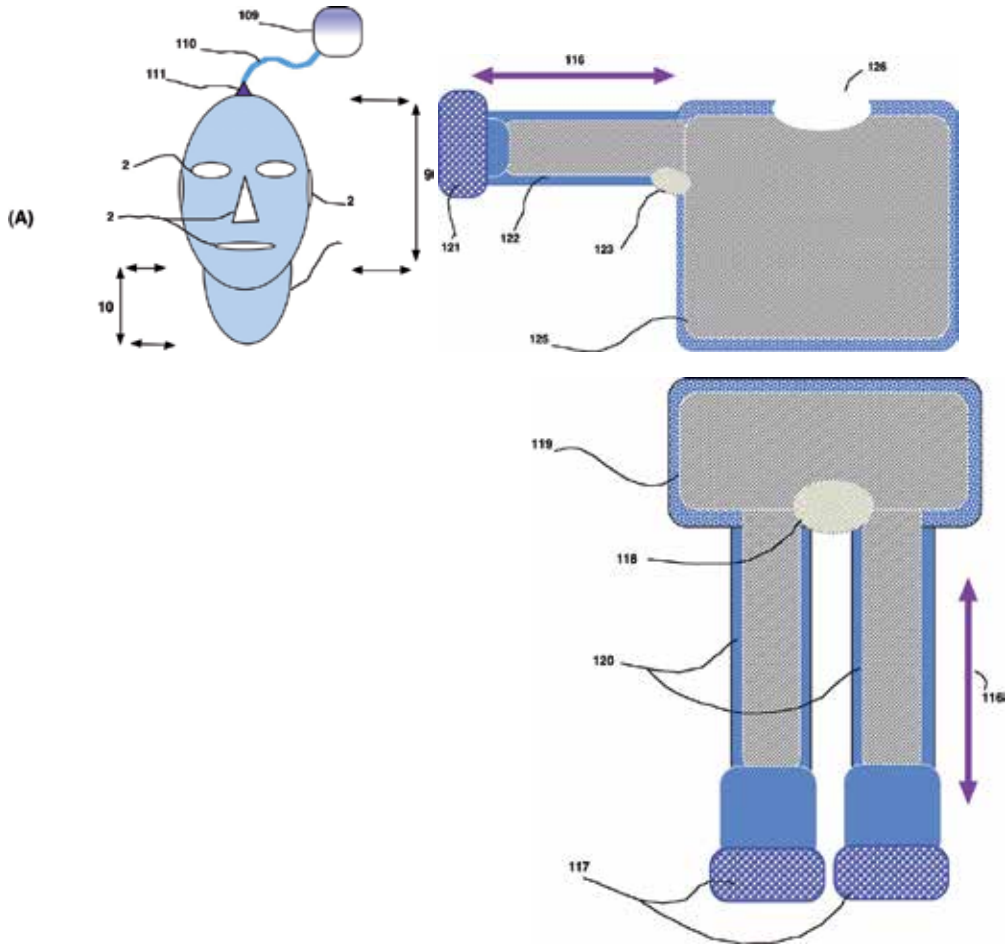

Fig. 6. Pulsatile suit CAD

6.2 Pulsatile tube

In another of its aspects shown in (Figure 7), the method implements at least one specific "pulsatile pipe" that serves to impart pulses to columns of blood, and that is preferably used in the context of providing circulatory assistance to the left ventricle (LVAD). Such a pipe is described in particular in patents applications (WO/2008/000110) and (WO 2010/066899). It may form part of a pulsatile medical kit that also includes a conventional pump (with or without oxygenator) placed at one end of the pipe, and an aortic cannula is placed by surgeon as close as possible to the patient's aorta. It is preferably prefilled in its intermediate space with an inert fluid such as helium, CO_2, etc. This diminishes the risk of embolism since the gas initially present in the pipe is discharged outside the circulation. In addition, the pressure forces required for operating the pulsatile device are reduced. It can readily be understood that this device is invasive to a very small extent. It generates pulsations in most effective manner and it is very easy to implement. It may be put into place surgically via a mini-incision or via a percutaneous approach and then synchronized with the patient's electrocardiogram.

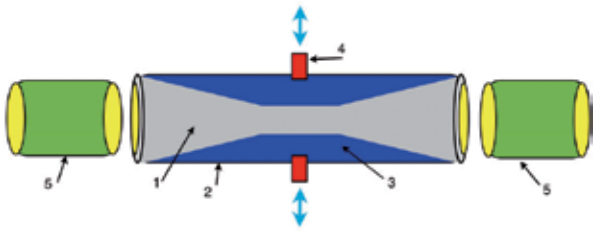

1= Flexible inner tube; 2 = Rigid external tube; 3 = Intermediate chamber; 4 = Ports; 5 = Connectors

Fig. 7. Disposable pulsatile tube (pipe)

A disposable double lumens' tube, which is designed according to the principles of the "Bernoulli" 3rd equation: propagated pulsatile impacts transferred from the intermediate chamber (blue color), would move up the stagnant fluid boundaries' layers at the inner flexible tube (grey color), and push them towards the center in a mater to diminish the traumatic effects of blood and its components. Both tubes (inner & external) are sealed together at their extremities creating a sandwiched space between them with double central orifices connected to a pulsatile console. The tube is adaptable to a conventional CPB arterial line circuit through two standard connectors wedged at each end of the inner tube.

Practically, circulatory perfusing systems create a state of momentum energy losses that could be identified in 6 main zones (Z0-Z5) (Nour S 2008), as follows (Figure 8): (**Z0**) it represents the pre-oxygenator zone, where momentum energy losses depend on types of driving forces (e.g. (e.g. roller or centrifugal pump) to be deleted as well as the oxygenator, which is a major constant site of energy losses; (**Z1)** it is the zone downstream to the oxygenator, where energy losses depend on circuit conduit types (length, width, materials) and fluid viscosity; (**Z2)** it is represented by the pulsatile tube wedged at the arterial perfusion line between the oxygenator and aortic cannula; (**Z3)** it represents the pre-aortic cannula zone, which is the first effective pulsatile zone; (**Z4)** it represents the aortic cannula zone, where the effect of convergent (at the entrance) and divergent (at the tip) energy losses plays an important role (Cutlera D 1999); (**Z5)** it represents the perfused tissues started from the tip of the aortic cannula, causing important divergent momentum energy losses.

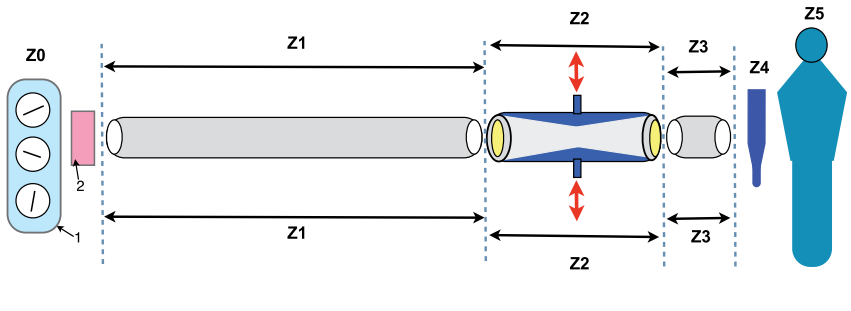

Fig. 8. Main momentum energy losses zone in a circulatory perfusion circuit

Accordingly, the pulsatile tube receives the steady flow from (Z1) downstream to the oxygenator, till (Z2) where the homogenous pulsations from the inner tube's walls move the stagnant laminar boundaries layers towards the center within total respect of Bernoulli's principle, with less vortices and better conservation of blood components.

At (Z3) where the effective pulsatile flow starts, theoretically this pre-aortic cannula zone represents a convergent diffuser with low momentum energy losses at the entrance of the aortic cannula. Meanwhile, a short (Z3)'s distance is requested to reduce turbulence and vortices that might occur due to strong-pulsed flow within a fixed geometries' tube. Furthermore, the pulsatile tube serves to reduce the empty space between monitor system and the tube itself, thereby giving rise to optimized operation with minimum pulsatile pressure; it is thus possible to envisage miniaturizing the device and correspondingly reducing the energy needed for its operation.

As seen in (Figure 12) a pulsatile pipe may be placed between the left subclavian artery and the right subclavian vein.

6.3 Pulsatile catheter

Another aspect of the present method comprises a "pulsatile catheter" comprising a conventional catheter that is surrounded by an inflatable element over a portion of its length (Figure 9). Such a catheter is disclosed in patent applications (US/2011/021987) and (WO 2009/136035).

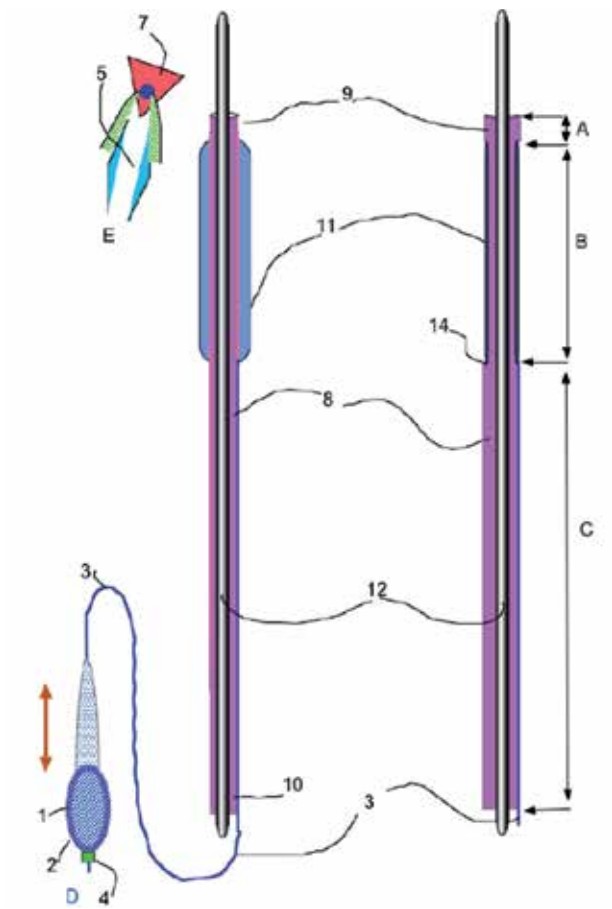

Fig. 9. Intravascular shear rate enhancement device

According to (Figure 9), the invention relates to a device for creating a pulsating inflation of an inflatable component (11) of a catheter (8), comprising: a bag (1) that can be filled with fluid (2); a bag compression means (5) capable of compressing said bag (1) in a pulsed manner; and a connection means (3) connecting said bag (1) to said inflatable component (11) of the catheter (8) and allowing the fluid (2) to move between said inflatable component (11) and said bag (1).

Advantageously, the inflatable element in place around the catheter presents in the deflated state an outside diameter that is less than that of the remainder of the catheter. Naturally, the inflatable element is connected to external inflation means suitable for generating pulsations during inflation. The device advantageously makes it possible to avoid excessively enlarging of the point where the catheter is inserted into a blood vessel.

Such a device is used in particular for PAH with increase in the afterload of the right ventricle (right ventricular failure); the catheter is placed in the trunk of the pulmonary artery by a percutaneous venous approach, preferably in association with a pulsatile suit.

6.4 Pulsatile console

An example of the pulsatile console (Figure 10), is described in patent application (US 2011166515) that console is very simple in design and easy to use. The console enables determined pulsatile pressure to be created and applied to a pipe, a catheter, or ay other equivalent means. A simple source of fluid under pressure such as a bottle of an inert fluid, or of liquid under high pressure constitutes the continuous source that is transformed into a pulsatile source by the pulsatile console as disclosed therein.

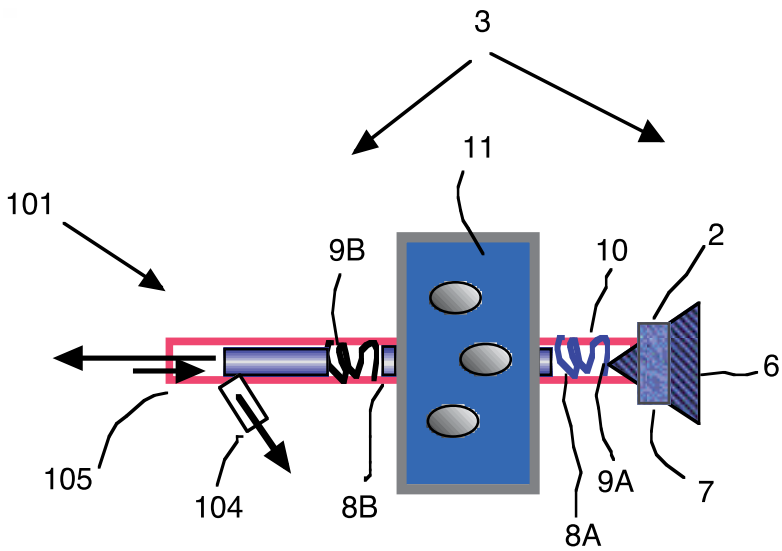

Fig. 10. Portable pulsatile console (Tu-Master).

The invention relates to equipment for applying a determined pulsatile pressure to a medical device, comprising: a withdrawing means (2) designed to withdraw fluid from a source of fluid in continuous flow at high pressure; a conversion means (3) designed to convert said fluid into a fluid in a pulsatile flow at low pressure; at least one application means (105) for applying said fluid, as a low-pressure pulsatile flow, to said medical device; and a means (104) for removing said fluid.

6.5 Smartcan

According to yet another aspect of the present method, a secure and almost non-invasive connection is provided between the patient and external mechanical systems for providing circulatory assistance (Figure 11). This aspect may be achieved by a device of the kind described in patent application (WO 2011/089162).

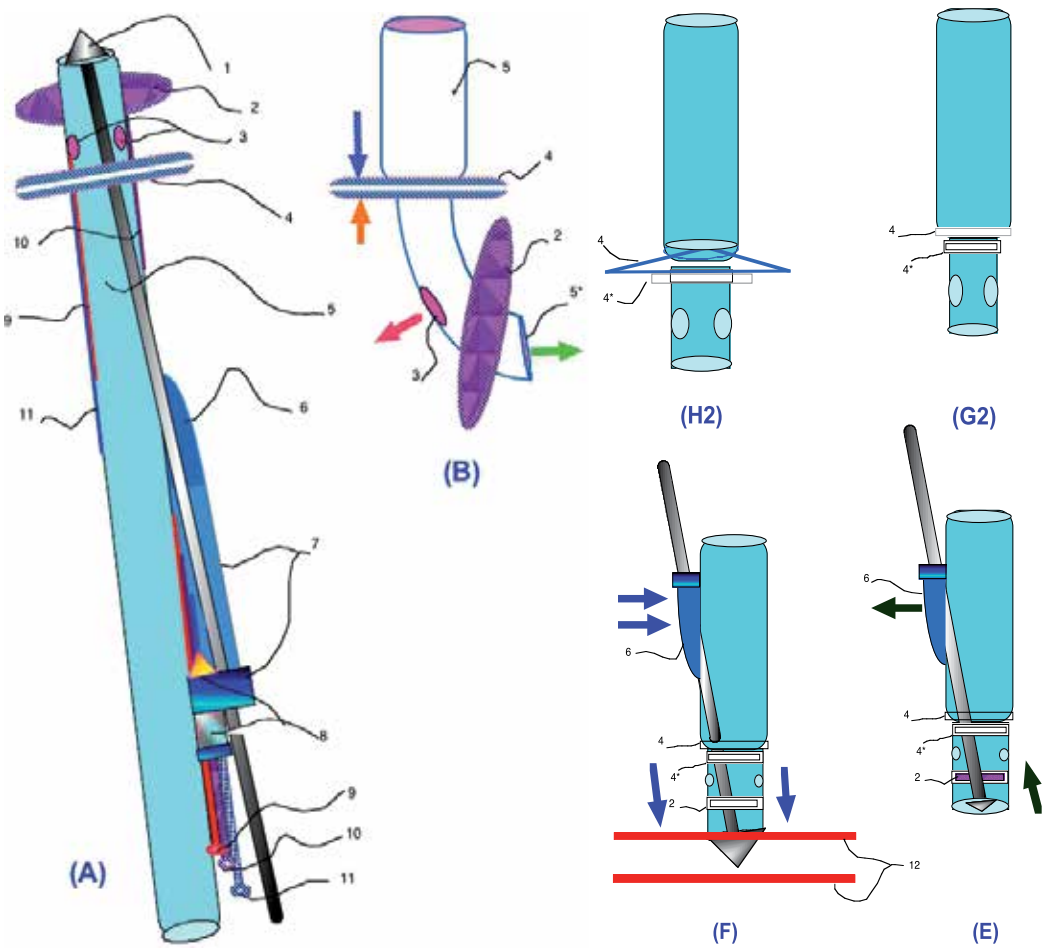

Fig. 11. The Smartcan conduit device

That device entitled the "Samartcan", makes it possible advantageously to group together all of the tools that make it possible to obtain a cardiovascular approach that is effective, fast, safe, and inexpensive. Thus, the tool enables a single operator, makes it possible to avoid all of the traditional steps such as incision, suture stitches, purse strings, etc. That simplifies the operation. Operating costs are thus significantly reduced.

Such a tool may be put into place and moved with assistance and remote guidance, e.g. echocardiography. This avoids blind guidance under the patient's skin for connecting the patient with an external circulatory assistance machine as with prior art methods. Such a connection gives rise to complications for the patient such as infections, hemorrhages, problems of closing the chest, etc.

In an advantageous manner, such a tool can be used as an aortic cannula, a cardiac cannula, a vascular catheter, or indeed as tubing for cavity drainage.

Such a tool, and more precisely the body of the device, is preferably prefilled with a liquid such as heparinized serum in order to reduce the risks of gaseous embolism and in order to shorten operating time.

In a novel and advantageous manner, the distance between such a tool and the patient is very small. In other words, the distance between a circulatory assistance machine (CAD) and the puncture sites (on the patient) is very short; in particular when implantation is performed close to the subclavian artery. This characteristic greatly reduces the energy losses that are inherent to existing devices.

The present invention relates to a single-use device to be used in surgery each time that a vascular approach by means of cannulation or catheterization is deemed indispensable (cardiopulmonary bypass, anesthesia, emergencies, resuscitation), particularly during cardiac surgery or interventional cardiology. Said novel device substantially includes a body (5), a sealing system consisting of two inflatable diskettes (4), a control connector for inflating and deflating the diskettes (4), a tubular unit (6) and a flexible guide (1). Upper right panel: shows a Smartcan with folded (G2) and unfolded (H2) external diskettes. Lower right panel: shows the Smartcan manually controlled guide wire before (E) and after penetrating a blood vessel (F). Left panel global schema of the Smartcan (A) and the proximal end (B) with the intraortic obstructive dikette (2), the cardioplegia delivery holes (3).

6.6 l'Orthèse cardiaque

According to another US patent application in pending, the various devices (pulsatile pipe, suit, and catheter, in particular) implemented in the present disclosure are synchronized together or separately as a function of the patient's hemodynamic parameters.

It relates to a novel therapeutic technique and method of providing mechanical circulatory assistance using a CAD that is minimally invasive. The CAD improves hemodynamics and microcirculation, and restores the endothelial function when it is insufficiently stimulated, particularly for a patient suffering from congestive heart failure (CHF).

The device complies with the patient's hemodynamic parameters as a function of breathing frequency and cardiac rhythm. Heart rhythm is detected by the electrocardiogram or by pacemaker as a function of variation in arterial pressure and/or in systemic and pulmonary resistances.

Synchronizing the pulsatile suit, thereby increasing venous return (preload) and reducing afterload, needs to be performed without hindering the frequency of breathing and without increasing central venous pressure above 16 mmHg. The pulsatile frequency of the suit may be less than the cardiac frequency of the patient (one-third to two thirds of the heartbeat).

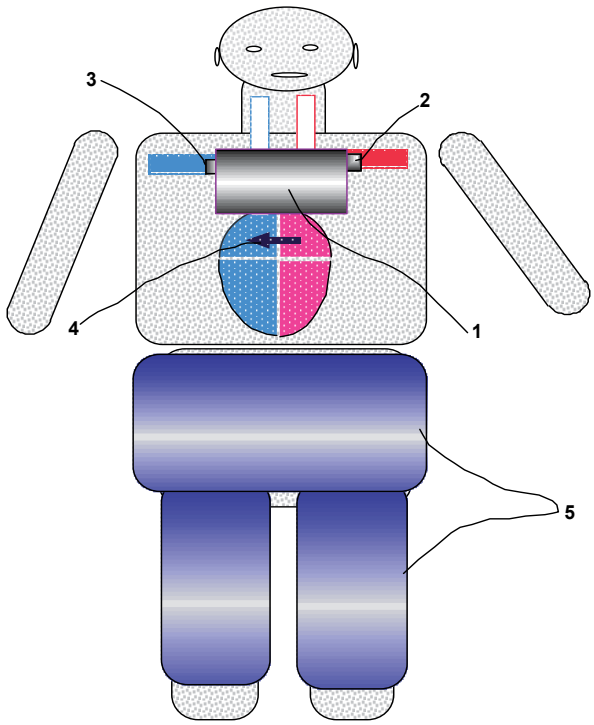

Right panel: l'orthèse with complete suit (full throttle option); left panel: l'orhèse with bottom trouser; 1= pulsatile pipe set; 2 = left subclavian artery tip; 3 = right subclavian vein tip; 4 = arrow defines intraseptal drainage; 5 = pulsatile trouser set; 14 = vest; 15 = sleeves.

Fig. 12. l'Orthèse Cardiaque

In contrast, the pulsatile pipe associated with the patient's electrocardiogram may be synchronized with cardiac rhythm and the pulsatile catheter may be faster than heart rate.

In particular, the devices and methods of the present CAD avoids problem associated with blood circulation through two well-separated circuits (systemic and pulmonary) that are constituted by the vessels and arteries of the patient and by the mechanical circulatory assistance device (s).

All of those pulsatile means enable variations in blood pressure to be created in vessels in application of the physical laws that apply to non-Newtonian fluids. They allow stagnant blood to be moved in compliance with Bernoulli's law, i.e. from the walls towards the insides of the vessels. This therefore gives minimizes the traumatic effects on erythrocytes.

When the heart pump, and in particular the left ventricle, is to be relieved (unload), the practitioner will use a Smartcan device in a version that enables an incision via the tip of the left ventricle or a left intra-atrial transeptal incision.

Similarly, when regular pulsations are to be produced and diffused close to the aortic root, the same device may be inserted as an arterial perfusion cannula in the root of the aorta or in the subclavian artery via a percutaneous approach or by echocardiographic guidance.

Figure 12 shows a patient fitted with a pulsatile suit that covers the bottom portion of the body; in addition, a pulsatile jacket is placed around the patient's thorax and pulsatile sleeves are placed on each of the patient's upper limbs. In this embodiment of the invention a pulsatile pipe is placed between the subclavian artery and the subclavian vein.

Furthermore, the present CAD is suitable for managing various types of heart failure, regardless of the right or left etiology.

On the right heart, by putting pulsatile suit into place, the device makes it possible to reduce the stagnation of venous capacitances; by implementing a pulsatile catheter, it is possible to reduce the pulmonary afterload.

On the left heart putting a pulsatile pipe into place enables physiological pulse pressure to be maintained and directly serves to improve overall hemodynamics by reducing systemic vascular afterload.

Thus, the methods and devices according to the present disclosure may be defined as a circulatory orthosis, as opposed to prosthesis. Unlike orthotopic transplantation, the present disclosure makes it possible to keep the patient's heart in place, thus allowing the patient to wait in relative comfort for a histocompatible donor.

The present method provides bridging treatment prior to transplantation, thereby improving prognosis and morbidity by restoring patient's hemodynamics. As a reminder, present-day mortality is higher for right ventricular failure it lies in the range of 65% to 95%.

The present disclosure makes it possible to restore the endothelial function progressively by maintaining quasi-physiological shear forces on the endothelium; consequently, there is a significant improvement in the function of myocardium, thus making it possible avoid subsequent transplants.

The present disclosure provides and approach that is invasive to a very small extent, since it avoids risky surgical acts, in particular, the invention avoids sternotomy and/or thoracotomy which can be put off until subsequent transplantation.

The devices and method of the present disclosure thus makes it possible to cope with the shortage of donor and with the numerous problems that are associated with antirejection treatments.

In addition, the present CAD is adapted to all age categories, from newborns to patients of great age and/or patients that are most clinically fragile.

7. Experiments

These devices were evaluated in vitro, as well as with clinical volunteers. The in vivo study was approved by the Animal Research Facility at Sun Yat-Sen University and conformed to the Guide for the Care and Use of Laboratory Animals (NIH Publication No.85-23, Revised in 1996). In original pediatric animal models of acute cardiogenic shock state, created in

piglets. We have avoided any premedication or any prophylactic medical support that may interfere with the endothelial function (e.g. atropine, β-blockers, etc.). Only mechanical cardiac support was provided with the evaluated device compared to traditional therapies in control groups. The clinical volunteers were medical doctors included the author.

7.1 Evaluation of the pulsatile tube device

Perfusions of the circulatory system with devices like the cardiopulmonary bypass (CPB) and CAD disturb endothelial shear stress (ESS), which is responsible for the post-cardiotomy syndrome, increasing liabilities of clot formation, bleeding, disseminated syndrome, etc (Bick et al., 1976)) (Abshire, 2009). This endothelial dysfunction syndrome is most probably occurred due to steady flow, foreign surfaces and the severe momentum energy losses. To overcome these side effects different therapeutic strategies are currently applied (Nour S, 2003), such as: *a) pharmacological supports* using antifibrinolytic (Cooper, 2006), inotropes, vasodilators, platelets, etc. (Nardell, 2009), but with some side effects as well (Ishida, zt al., 2004); b) *normothermia:* that becomes more practiced in CPB with some proven advantages over hypothermia (Pouard, et al., 2006), which may be explained because blood is nearly Newtonian at 37.2°C (Box, et al. 2005). Meanwhile, the benefits of normothermia on myocardial protection and microcirculation improvements remain controversial (Rastan, et al., 2008), as the myocardium is already protected with doses of cardioplegia, while the perfusion of microcirculation is more or less helped by the Fahraeus-Lindqvist effect due to hemodilution; c) *total or partial absenteeism* of CPB: that becomes popular with proven postoperative hemodynamic advantages, *but* it is still a challenging technique reserved for selected groups of patients (Shroyer, et al., 2009); d) *pulsatile perfusion flow devices:* in a matter to keep ESS some pulsatile CPB have proven advantages clinically and experimentally (Ündar, et al.,1999); (Undar, et al. 2006). Despite that, recent studies recommend the unphysiological steady flow (Voss, et al., 2010). This may be explained by pulsatile CPB inadequate curves with the necessity of a double perfusion pumps system to compensate the oxygenators momentum energy losses. Instead associating an intra-aortic balloon pump (IABP) with a conventional CPB, as a cost-effective manner (Onorati, et al., 2007), creates turbulent zones of vortices (Geankoplis, 2005), with vascular complications (Sanfelippo, et al.,1987) and controversial effectiveness (Kadoi Y & Saito, 2000).

Alternatively, the pulsatile tube represents a potential solution for those aforementioned CPB and CAD drawbacks

The pulsatile tube device (Figure 7), was evaluated as a potential solution for these CPB and CAD drawbacks. A device prototype was tested in vitro (a mock circuit) for energy losses studies and in vivo as a LVAD, also the tube prototype was associated in the in vivo study of a Bi-ventricular assist device (l'orthèse).

7.1.1 In vitro study

Materials and methods: a double lumen tube prototype as shown in (Figure 13), composed of: a) external polyvinyl chloride (PVC) (20 cm length, ½ inch diameter). b) Internal Polytetrafluoroethylene (PTFE) (18 cm length, 12mm diameter), reinforced with latex membrane (condom), as a protector against the PTFE micropore. c) 2 connectors (¼ inch) introduced at each end of inner tube and wedged to the PVC tube and securely sealed by

external adhesive straps and rings. A small animal ventilator (HX-300 TaiMeng Technologies Inc®), was applied as a pulsatile generator.

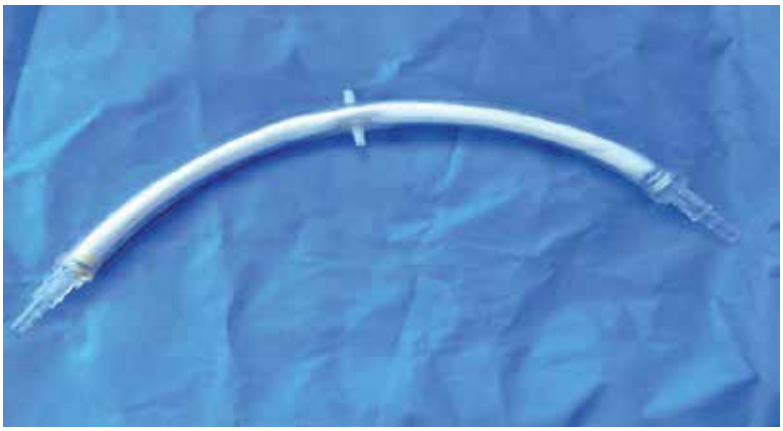

Fig. 13. Pulsatile tube prototype (Dr. Nour)

Mock circulation: with slight modifications from the literatures (Undar et al;, 2006), (Wang, et al., 2009), it was composed of (Figure 14): a roller head pump (Cobe® Cardiovascular Inc.), pediatric oxygenator (Sorin® Lilipput 2 Ecmo) and filter (Sorin® Group hemoconcentrators), primed with fresh piglet's blood mixed with dextrane in concentration of (2/3) and (1/3) respectively. A pediatric arterial line circuit, PVC tube (1.5 m length), 14 FR aortic cannula (DLP® Medtronic, Inc.), venous line (1.5 m length) and simulating vascular resistance partial clamp, positioned downstream to the aortic cannula.

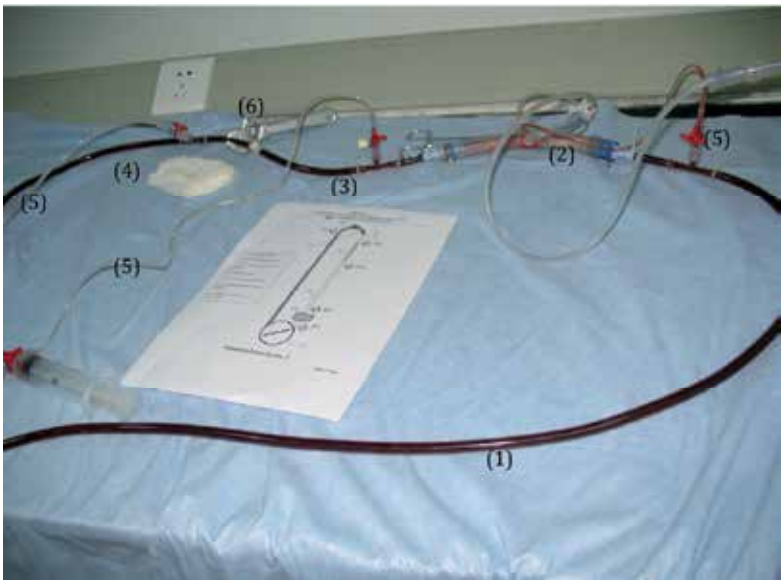

1 = arterial perfusion line; 2 = pulsatile tube; 3 = aortic cannula; 4 = venous line; 5 = pressures lines; 6 = partial tube clamp (simulated resistance).

Fig. 14. Mock-circulation: energy losses circuit (I)

7.1.2 Methods

With variant pump flow rate (400, 600, 800 and1000 ml/min) and fixed pulsation rate (110 bpm), we have compared circuit momentum energy losses during steady and pulsatile flows in 3 different tube positions as following:

- Energy losses I: the tube was positioned downstream to the oxygenator at 6 cm from the aortic cannula (Figure 15-I).
- Energy losses II: the tube was positioned downstream to the oxygenator at 150 cm from the aortic cannula (Figure 15-II).
- Energy losses III: the tube was positioned between pump and oxygenator (Figure 15-III). This position conceptually simulates current devices of pulsatile CPB.

Recorded pressure curves: first in a steady mode, then pulsatile by switching the tube's generator on, were collected at 5 remote distances spots: up and downstream: to oxygenator (P1, P2); to tube (P3, P4) and to resistance (P5) which simulated a systemic arterial perfusion curve in patients.

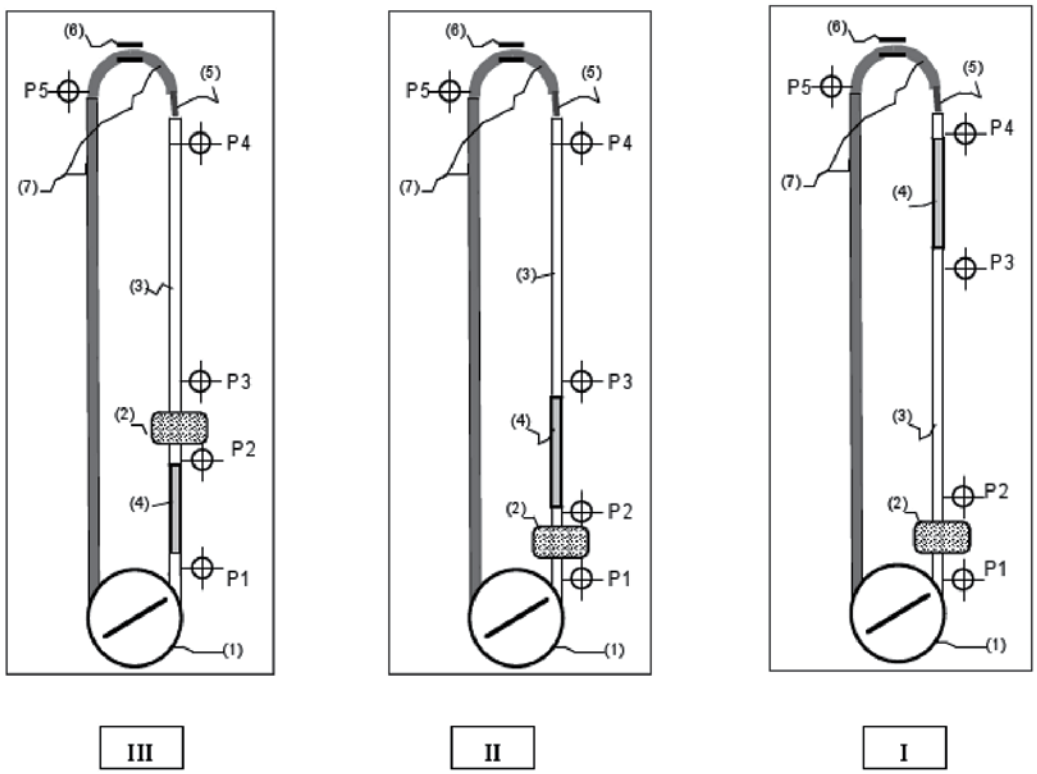

{I} = Pulsatile tube was positioned at *6 cm* distance from aortic cannula; {II} = Pulsatile tube positioned at *150 cm* distance from aortic cannula; {III}. Pulsatile tube wedged between roller pump and oxygenator. 1 = roller pump; 2 = oxygenator; 3 = arterial line; 4 = pulsatile tube; 5 = aortic cannula; 6 = resistance (tube clamp); 7 = venous line. P1, P2, P3, P4, P5 = perfusion pressures recording spots.

Fig. 15. Mock-circulations with 3 different tube positions

7.1.3 Statistics

Continuous variables are expressed as the mean±SEM. Comparisons between groups of independent samples were performed with student t-test hemodynamic data. P with a value less than 0.05 was considered statistically significant. GraphPad Prism® software was applied for all the statistical analyses in this study.

7.1.4 Results

As been resumed in (Table 5) and (Figures: 16 & 17), momentum energy losses were significantly increased with the pulsatile tube in positions: III and II, compared to position I. Furthermore, there were observations of an increased perfusion pressure at P5 from the initial P1 of those groups (II and III), signifying severe turbulence at the post-cannula zone, which theoretically, corresponds to patient's aorta. There were minimum momentum energy losses with the steady flow in position. I, In contrast to positions II and III, there were important vortices with obstructive zones that created a sort of retrograde flow even before pulsations.

	Groups	P1	P2	P3	P4	P5
	NP (I)	32,5 ±1,3	31,3 ± 1,3	30,3 ± 0,5	30,3 ± 0,5	30,8 ± 0,5
1 -	NP (II)	36,3 ±1,3	37,8 ± 1	39,5 ± 0,6	38,5 ± 0,6	39,3 ± 0,5
	NP (III)	40,3 ±1	42,3 ± 1	43 ± 0,00	42,3 ± 0,6	43 ± 0,00
	Pm. (I)	34,5 ± 1,7	34,5 ± 1,3	33,5 ± 1,7	32,3 ± 1	31,8 ± 1
2 -	Pm. (II)	39,3 ± 0,5	40 ± 0,8	40,8 ± 0,6	40,5 ± 0,6	40,3 ± 0,5
	Pm. (III)	43 ± 1,2	46 ± 2,2	46,3 ± 1,5	44 ± 0,8	44,8 ± 0,5
	Ps. (I)	72 ± 3,5	81 ± 11	92,8 ± 4,9	98 ± 11,5	92,8 ± 5,6
3 -	Ps.(II)	97,3 ± 7	92,3 ± 6	90 ± 11,2	81,3 ± 7,5	82,3 ± 8,4
	Ps. (III)	84,3 ± 6,6	79,8 ± 5,9	79,8 ± 5,5	69 ± 3,9	69 ± 4,2
	Pd. (I)	(-)4,4 ± 3,2	(-)6,5 ± 7,4	(-)13,6±11,7	(-)35,3±8	(-)33,5±13,3
4 -	Pd. (II)	(-)1,1 ± 6,2	(-)7,8 ± 4,4	(-)0,8±9,4	5,6 ±8,4	13 ±3,2
	Pd. (III)	0,5 ± 10	5,3 ± 5,3	7,5 ± 7,5	20,3 ± 3,8	20,3 ± 0,5
	PP (I)	76,4 ± 3,4	87,5 ± 11,8	106,4 ± 15,9	133,3 ± 17,7	126,3±18,6
5 -	PP (II)	98,3 ± 7,9	1OO ± 10,4	100,3 ± 10,3	75,7 ± 15,4	66 ± 6,1
	PP (III)	83,8 ± 9,2	74,5 ± 8,7	72,3 ± 12,6	48,8 ± 7,1	48,8 ± 4,7

P = pressures in (mmHg); I,II,III: correspond to each different 3 circuits; NP: non-pulsatile pressure; Pm: mean pulsatile pressure; Ps: systolic pulsatile pressure, Pd: pulsatile diastolic pressure; PP: pulse pressure; ($p<0.001$).
Pulse pressure was higher at P5 with position I, compared to position II & III. Pm was higher at P5 compared to NP with position I.
N.B. For further details please refer to the following experimental movies site:
http://www.nourmd.com/

Table 5. Results of momentum energy losses, obtained in 3 different mock circuits.

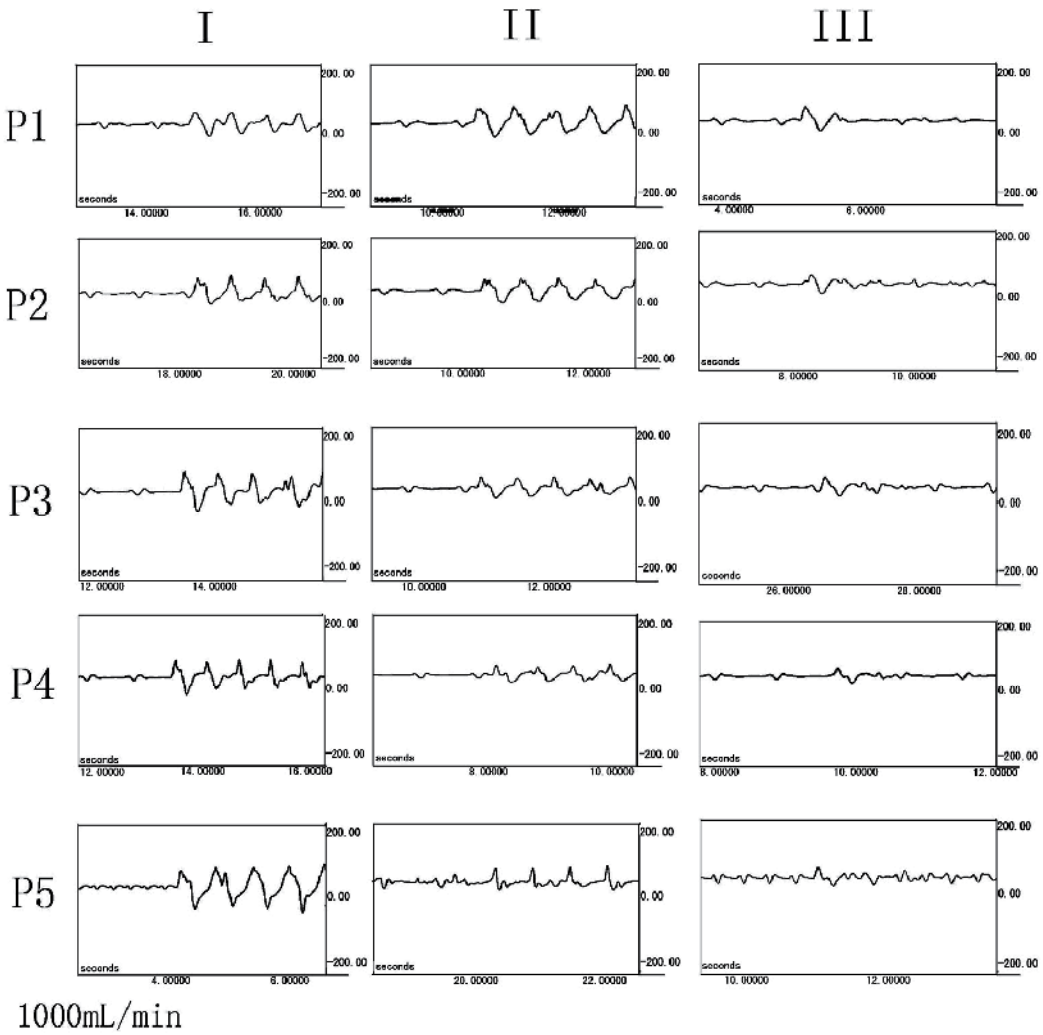

Fig. 16. Perfusions curves obtained in vitro

Perfusion curves (in mmHg) obtained at different circuit sites in 3 different pulsatile Tube positions: I, II, III close & distant from aortic cannula and pre-oxygenator respectively. The perfusion curve amplitude was significantly higher at P5 with position I, compared to positions II & IIII.

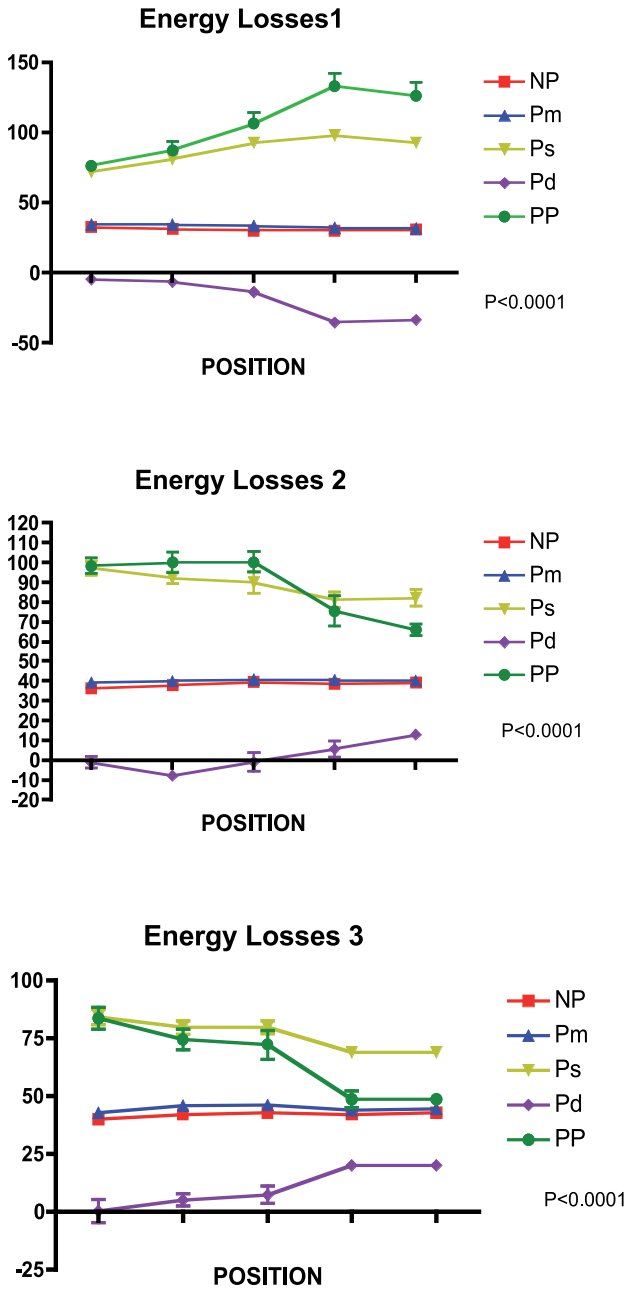

Energy losses 1 (upper panel) = pulsatile tube at 6 cm from aortic cannula; Energy losses 2 = pulsatile tube at 150 cm from aortic cannula; Energy losses 3 = pre-oxygenator pulsatile tube position. P1-P5 = distant circuit spots for perfusion pressure records (mmHg). NP= non-pulsatile; Pm = mean pulsatile pressure, Ps = systolic pressure; Pd = diastolic pressure; PP = pulse pressure. The pulse pressure (green color) was significantly higher with position I compared to positions II & III.

Fig. 17. comparative steady and pulsatile flow perfusion curves obtained from 3 different circuits

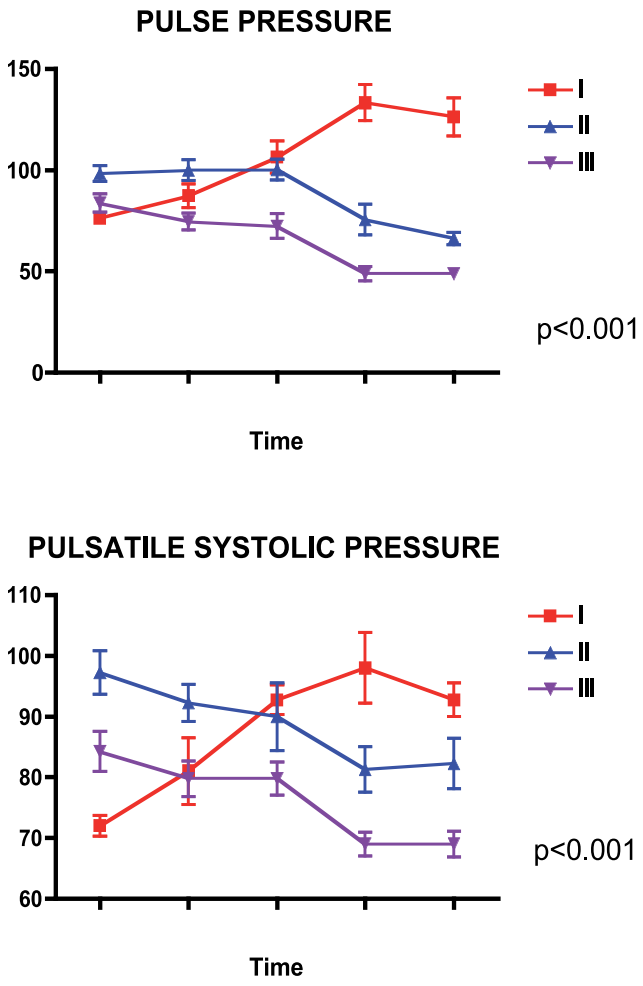

Energy losses with different tube positions: I = pulsatile tube at 6 cm from aortic cannula; II = Pulsatile tube at 150 cm from aortic cannula; III = Pulsatile tube pre-oxygenator. P1-P5 = perfusion pressure records (mmHg) at main circuit energy losses spots. At P5 the pulse pressure (upper panel) as well as the systolic pressure (lower panel) were significantly higher in position I (red color) compared to other positions: II (blue color), and III (violet color).

Fig. 18. Pulsatile flow pulse pressure (upper panel) and systolic pressure (lower panel8)

7.1.5 Comments

In this study, a steady perfusion flow was transformed successfully into pulsatile flow with a simple double lumen tube integrated into the arterial perfusion line of a conventional CPB circuit. According to our previous explanations (Figures 4 and 8), quantification of circulatory perfusion devices (CPB, CAD) depends on their momentum energy losses. The Bernoulli's principles of energy losses could be applied with accuracy in vitro to quantify lumped models like CPB (Undar et al., 2007). In vivo vessels elasticity and vascular tone bring CPB quantification more closer to Newton's law of shear stress as a major stimulant for endothelial NOS / resistances control.

The resulted energy losses have proven the importance of the pre-cannula zone represented in position I by P4, compared to P3 and P2 with positions II and III respectively showing severe turbulent flow with important vortices constitutions at this zone or (Z 3). Finally, the prototype by its position downstream to oxygenator could avoid an important obstructive zone of energy losses, which is almost constant with current CPB necessitating a double perfusion pump system and special low resistance oxygenator.

Conclusion CPB induces momentum energy losses with severe endothelial dysfunction. Current pulsatile devices induce inadequate curves with high costs. Pulsatile tube, adaptable to a conventional driving system could induce homogenous, downstream and nearly physiologic pulsatile perfusion flow with low momentum energy losses. This is a cost-effective method, promising low mortality and morbidity, especially in fragile cardiac patients.

7.2 In vivo study (study in progress)

The pulsatile tube device was tested as a left ventricular assist device (LVAD), in pediatric animal models (piglets) with acute myocardial ischemia.

Materials and methods: in the pulsatile group: a prototype of a pulsatile tube was realized in the same manner as the in vitro study, then a short piece of 14 Fr. PVC tube was modified as a aortic cannula (Figure 19), in a matter to avoid the conastant energy losses caused by current cannulae length with narrow tips. Same a small LV vent was attached to the other end of the tube. The whole system was connected to a pulsatile generator console (HX-300 TaiMeng Technologies Inc®). In the control group: a centrifugal pump (Sorin group Revolution ®), was connected to a standard aortic cannula (12 Fr. DLP®-Medtronic, Inc.) and apical vent (14 Fr. DLP®-Medtronic, Inc.).

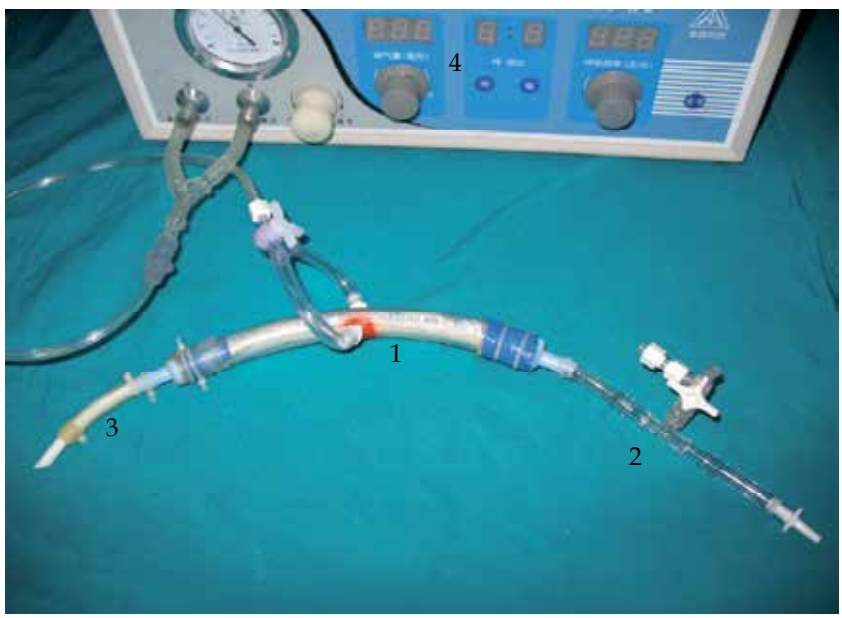

Tube (1) is connected to aortic cannula (2), LV vent (3) and console (4).

Fig. 19. Pulsatile tube prototype used as LVAD

Steps	Maneuvers
1	Anesthesia / sternotomy / pericardectomy / dissection of great vessels.
2	Insertion of an infundibular Swan-Ganz, aortic and apical pursestrings.
3	Hemodynamic measurement / blood test data for Time 1 (T1).
4	Heparin injection (2ml/kg) LAD coronary artery mid-term ligation (snugger).
5	Time 2 (T2) = after 1 hr of ischemia without any medical support
6	LVAD System switched on for 1hr.
7	Time 3 (T3) data collection after 1 hr of assistance with LAD ligation.
8	Removal of LAD snugger (coronary reperfusion + LVAD assistance) for 1hr.
9	Time 4 (T4) data collection before animal sacrifice

Table 6. Summary of the surgical steps

Operative schema and steps of surgical protocol are resumed in (Figure 20) and (Table 6) respectively.

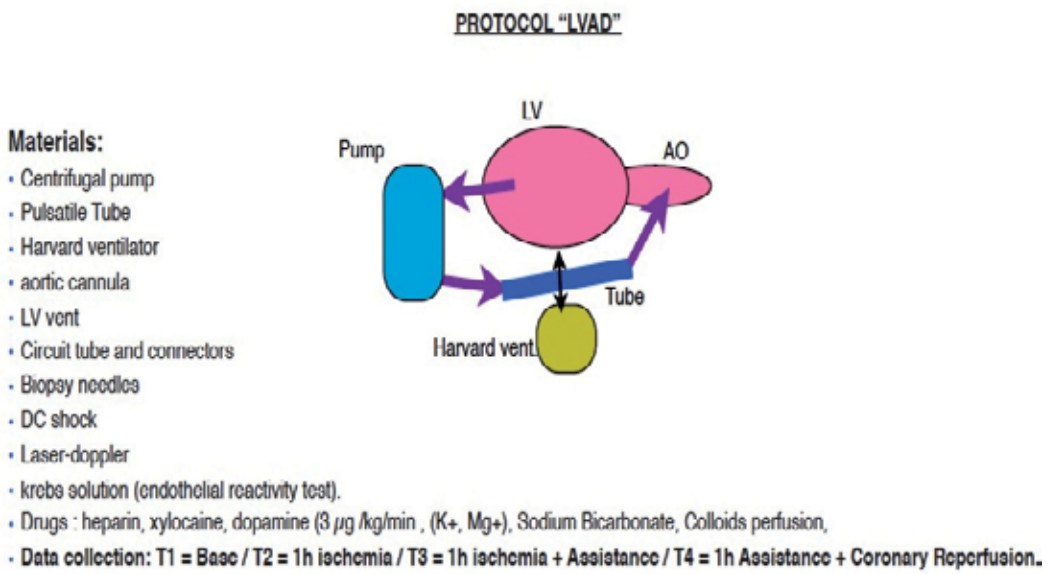

(Ao=aorta, LV=left ventricle, vent. = ventilator)

Fig. 20. Schema representing the pulsatile tube as a LVAD

7.3 Results

This ongoing study results showed better hemodynamic with lower cardiac enzymes in the pulsatile group compared to control (Figure 21) and (Table 7).

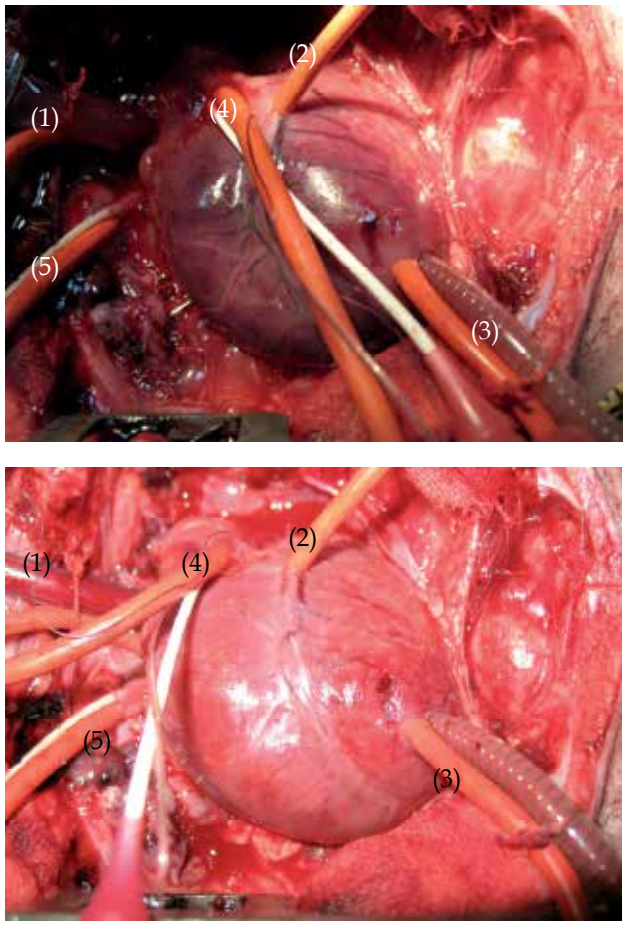

Upper panel: shows a massive myocardial ischemic zone after LAD ligation; Lower panel: ischemic zone after 15 min of pulsatile tube assistance. 1 = Aortic cannula; 2= LAD snugger (permanent coronary occlusion); 3 = left ventricular apical vent; 4 = trans-infudibulum pulmonary artery & Millar right ventricular pressure catheters; 5 = right atrium pressure line.

Fig. 21. Pulsatile tube as LVAD in piglet ischemic model

Test	**T1**		**T2**		**T3**	
	P	**NP**	**P**	**NP**	**P**	**NP**
cTnT*	0.036	0.06±0.07	-	021±0.1	0.029	1.31±0.61
CK-MB*	0.92	0.56±0.41	-	0.89±0.85	0.100	100±4
PLT	351	487±100	-	245±128	47	80±3
Htc	0.27	0.32±0.06	-	0.28±0.08	26	33±7
Lac (v)	1.23	3.3±3.1	-	4.9±4.1	0.6	0.4±0.1

Table 7. Biochemistry results: cardiac enzymes*; P: pulsatile group; NP: non-pulsatile (control group); Plt: platlets: Htc: hematocrit; Lac (v): venous lactate. T1: baseline; T2: 1h of ischemia; T3: after 2h of myocardial assistance.

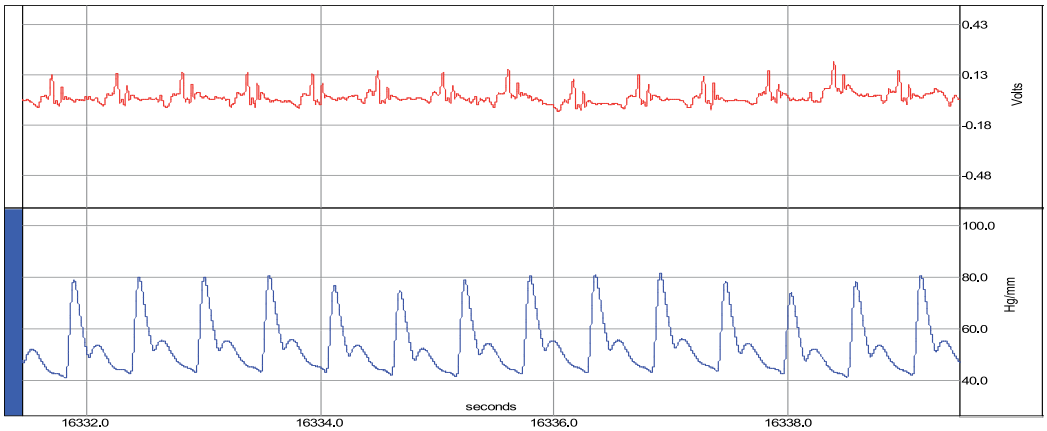

Fig. 22. Pulsatile tube perfusion curve in vivo, as a LVAD in acute MI piglet

The pulsatile tube's perfusion curve was nearly physiologic with complete discharge of the LV and unsynchronized with heartbeatt, as have been demonstrated on the operative movies.

7.4 Operative movies of the pulsatile Tube (LVAD):

- Pulsatile as a LVAD associated with a conventional roller pump (Cobe® Cardiovascular Inc.): http://www.nourmd.com/
- Pulsatile tube as a main LVAD, without any other associating driving systems: http://www.nourmd.com/
- Control group movie, LVAD by (Sorin Group Revolutionary centrifugal pump®): http://www.nourmd.com.

7.5 Comments

The exposed results proved the feasibility as well as the effectiveness of the pulsatile tube as a LVAD. These preliminary results have shown hemodynamic improvement and myocardial recoveries, lower cardiac enzymes in the pulsatile group, compared to control. This hemodynamic improvement was significant in the pulsatile tube group and despite the maintained coronary obstruction in a fragile pediatric model, with very poor coronary collaterals. Interestingly we've tested the tube alone without a perfsuion pump and LV vent, as an endocardial stimulator. Myocardial recovery and macroscopic disappearance of the ischemic zone were obvious after few minutes (< 5min), of unsynchronized pulsations (please refer the attached movie). This was ended by severe vasodilatation and cardiac arrest. Currently, we are trying to overcome these drawbacks, particularly, the inner tube (PTFE) microporosity and vasodilatations, with a new generation of pulsatile tube prototypes.

8. Evaluation of the pulsatile catheter device (in vivo)

Prototype: a standard IABP catheter (8 Fr., 30 cc) was modified. Briefly, its original balloon membrane was peeled off and replaced with a small piece of commercial rubber balloon, secured and tied manually at each end of the catheter. This created an inflatable

compartment of 1×1 cm. The distal part of the prototype was connected to a cardiorespiratory monitor (BIOPAC® physiology monitoring system, ECG channel). For a pneumatic rhythmic driving force, it was attached to a small animal ventilator (HX-300 TaiMeng Technologies Inc®). It was tested for leakage while pulsating in a heparinized saline bath. Once the prototype was inserted into the pulmonary trunk, the circuit inflation volume was adjusted (usually between 50-90 ml) to avoid right ventricular outflow tract obstruction. The ventilator was pulsed at a frequency of 110 cycles/min. The prototype device was tested in two animal model studies for acute MI and acute PAH as follows:

8.1 Acute myocardial ischemia model

(part of the results was presented at the 17th conference of ACTVS, Nour, 2009)

Material and methods: Twelve piglets (8.3 ± 1.5 kg) were given either pulsatile (P: n=6) or non-pulsatile (NP: n=6) nitrates treatment. Both groups underwent permanent left anterior descending coronary artery (LAD) ligation with a median sternotomy (Figure 23). After 1 h of ischemia, heparin was injected (150 IU/kg). In group P, a prototype CAD, driven by a small ventilator, was introduced into the pulmonary trunk and pulsated intermittently over 1 h at 110 bpm, irrespective of heart rate (73 ± 16 bpm). In group NP, nitrates were given (7±2 μg/kg/min) for 1 h. Animals survived ischemia for 2 h in group P vs. 93±30 min in group NP.

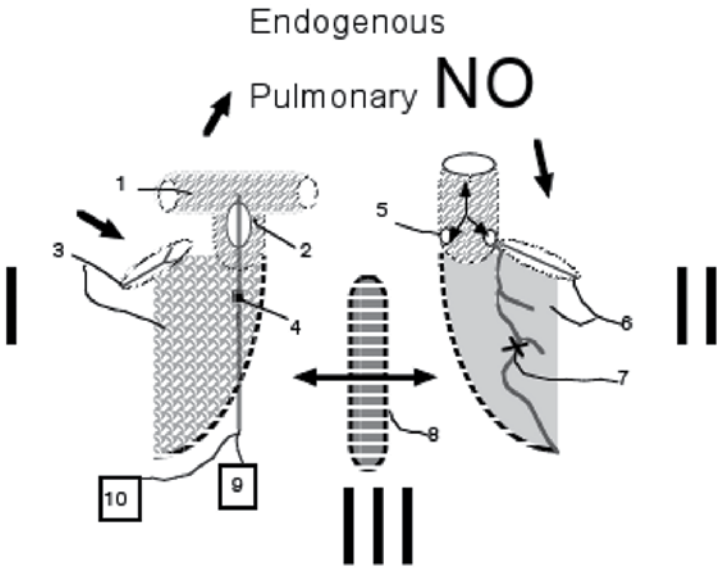

1 = Pulmonary artery (PA); 2 = pulsatile catheter fitting PA trunk; 3 = right ventricle (RV) inlet-outlet compartments; 4= infundibular site of pulmonary catheter insertion; 5 = arrows showing presumed passage of pulmonary eNOS (backward through coronary ostia and/or forward through systemic circulation); 6 = left ventricle (LV) inlet-outlet compartments; 7 = permanent ligation of the left anterior descending coronary artery distal to the second diagonal branch; 8 = interventricular septum; 9 = cardiorespiratory monitor; 10 = pneumatic driving force. I = pulmonary eNOS primarily induced at PA zone with catheter pulsation; II = pulmonary eNOS natural passage through the left heart circuit; III = presumed pulmonary eNOS involvement in myocardial recovery most probably through microcirculation and/or the RV interseptal coronary network.

Fig. 23. Presumed mechanism and passage of induced pulmonary eNOS

With the macroscopic disappearance of infarction (Figure 24), group P exhibited improved hemodynamics (Figure 25) and significantly lower myocardial apoptosis (0.66±0.07) compared to group NP (4.18±0.27), (Figure 26). Vascular resistances (dyne.sec/cm^{-5}.kg^{-1}) were significantly lower (P<0.01) in group P vs. group NP: pulmonary resistance was 119±13 vs. 400±42, and systemic resistance was 319±43 vs. 1857±326, respectively. Myocardial endothelial NO synthase mRNA expression (Figure 27), was higher in group P (0.90±0.09) than in group NP (0.25±0.04; P<0.01), probably due to endogenous pulmonary NO secretion.

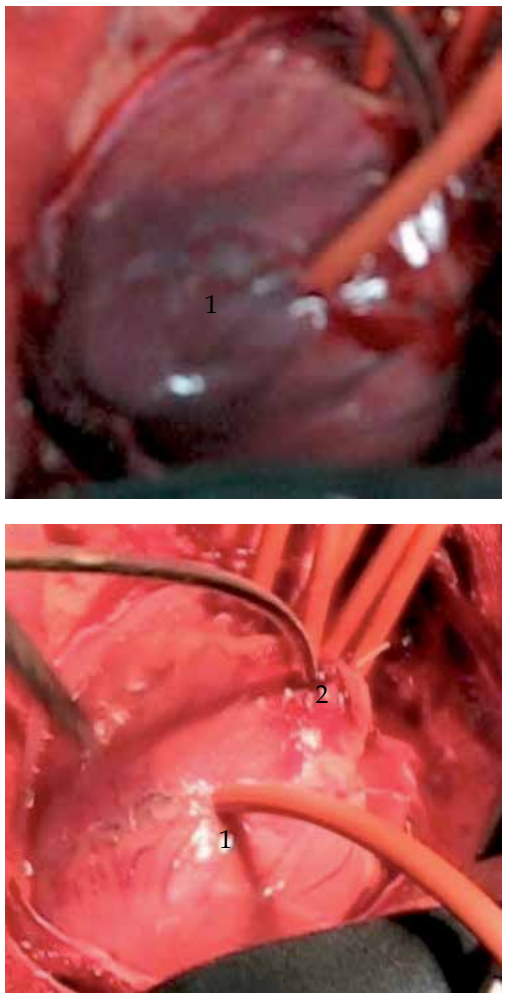

Left panel figure showing dark infarcted myocardial after 50 min of ischemia; right panel figure showing significant reduction of ischemic myocardial zone after 10 min of pulsation; 1 = left anterior descending coronary artery snugger; 2 = infundibular site of the intrapulmonary pulsatile catheter insertion.

Fig. 24. Macroscopic disappearance of the ischmeic zone in group P

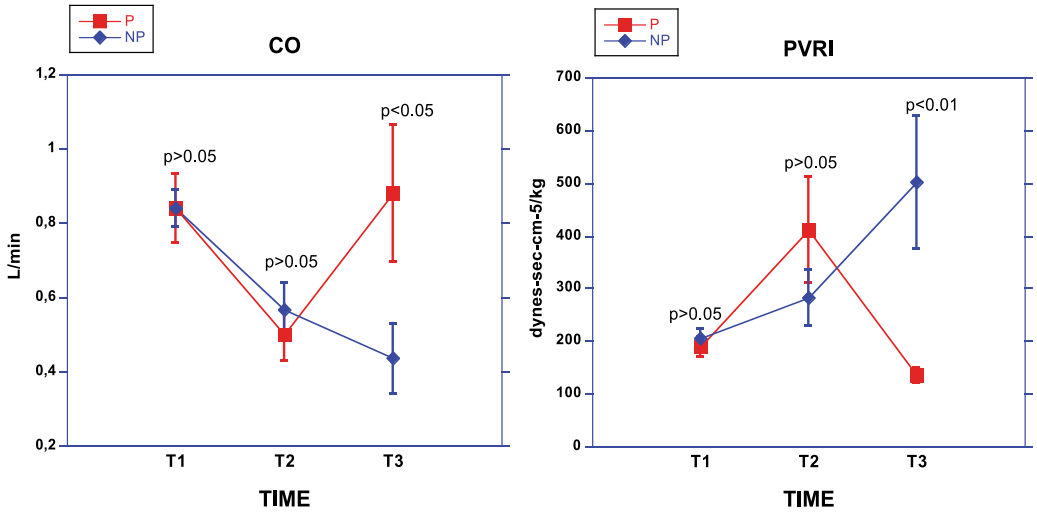

Right panel showing the pulmonary vascular resistances index (PVRI) calculated from pulsatile group (P; red color) and non-pulsatile group (NP; blue color) at three predetermined time: T1= baseline; T2 after 1H of shunt and T3= end of 1h therapy. at T1 (baseline) and the end (T3). PVRI (dynes.sec.cm^{-5}/kg) were significantly lower ($p<0.01$) were significantly lower at T3 in group P compared to group NP. Left panel showing the cardiac output (CO) from both groups P and NP. CO (L/min) was with significantly improved at T3 in group P compared to group NP ($p<0.01$), in group P (red color) compared to group NP (bleu color).

Fig. 25. Hemodynamics improvement with the pulsatile treatment in group P

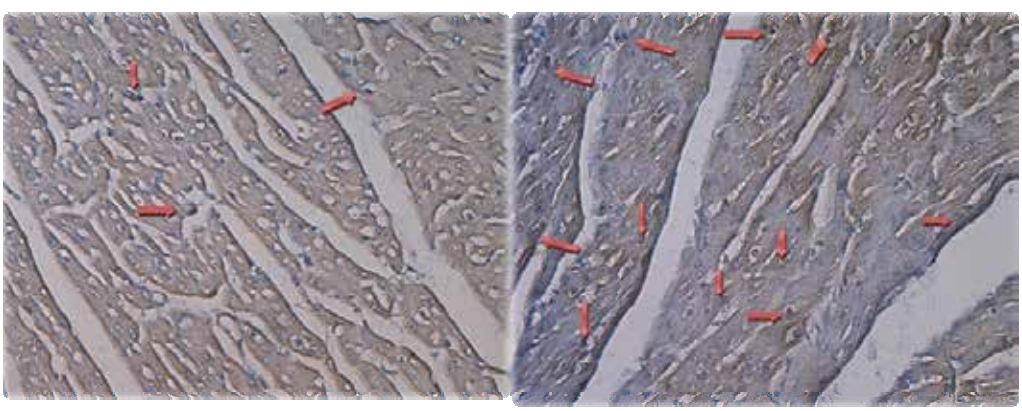

Fig. 26. Myocardial apopotosis (TUNEL test)

Representative figures from both groups showing apoptotic cells manifestations (red arrows), from both groups: group P (left) and group NP (right). The apoptotic index (AI) in group P was significantly lower than that in group NP ($P<0.01$).

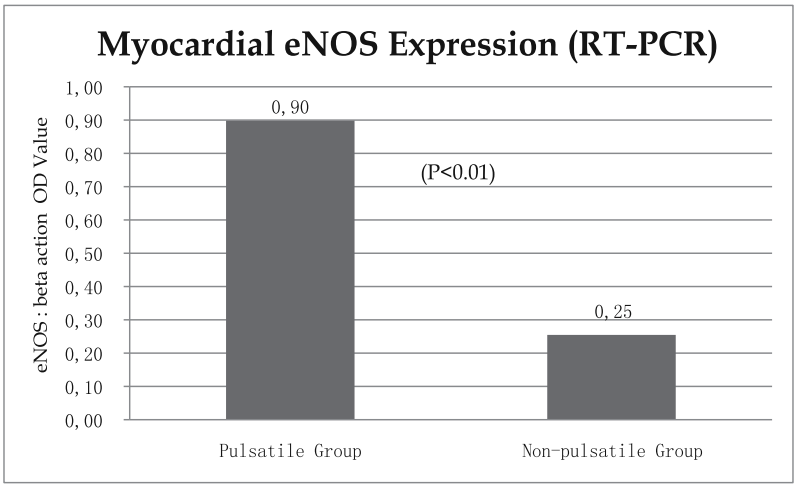

RT-PCR results shown with statistics, in which myocardial eNOS expression was significantly higher in group P (left) compared to group NP (right). (p<00.01).

Fig. 27. Myocardial eNOS mRNA expression

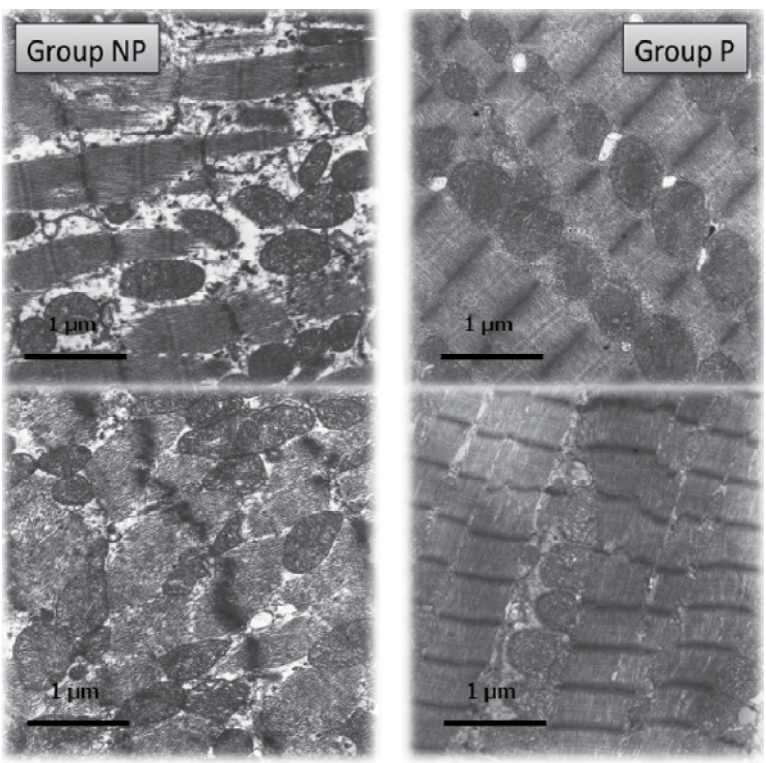

Left panels: samples from the non-pulsatile, nitrate treatment group (NP); right panel: sample from the pulsatile treatment group (P). Notice the relatively well-preserved myocardial microstructure in group P. Bar scale on each graph equals one micrometer.

Fig. 28. Myocardial microstructure visualized with transmission électron microscopy

8.2 Comment

Decalogue of original observations emanated from the present preliminary study as follows:

i. Hemodynamic improvement, with significant recovery of the myocardial contractility and cardiac output (CO), despite maintained coronary obstruction. This was obvious macroscopically, and confirmed by low myocardial apoptosis manifestation, and relatively well-preserved cardiomyocytes organelles in the pulsatile group P.
ii. Intrapulmonary shear stress enhancement, that was induced successfully and for the first time according to literatures, as that was practiced with uncertain results, using an intra-aortic balloon pump (IABP) (Letsou et al. 1993). The uncertainty is probably due to differences between vessel geometries and catheters diameters, in addition the right heart side has specific morphological particularities that must be considered (Burton, 1954), (Huang W & Yen RT, 1998).
iii. Endogenous vs. exogenous nitric monoxide (NO): generally, NO has an important effects on the cardiovascular system as a potent vasodilator, inhibitor of platelets aggregation and myocardial contarctility (Jones SP & Bolli, 2006). Shear stress induces endogenous NO production by activating endogenous nitric oxide synthase (eNOS). (Chatzizisis et al., 2007), like during physical exercise Walsh et al., 2003). Also exogenously administered NO donors like Nitrates, can to be deleted induce eNOS (Ignarro, et al.,2002). Therefore, the study results showed that physiologically induced NO was superior to exogenous nitrates in acute IHD syndrome.
iv. Microcirculation vs. collaterals, in group P, the increased expression of myocardial eNOS mRNA (Depre, et al. 1997); with fewer apoptotic cells (Mital, et al., 2002) could be explained by endogenous NO due to the intrapulmonary catheter pulsation. Meanwhile the exact mechanisms of action remain to be explored. However several conditions supported the role of microcirculation, as the subendocardial resistance vessels are more sensitive to mediators of vasodilatation and endothelium dependent dilators (Pelc, 1987). In consideration of the short biological lifetime of NO (Doherty et al., 1998), and the maintained coronary ligation, the chosen model is known for poor coronary collaterals, in addition to the immature myocardium in young pig model (Gorge, et al. 1989). This may be explained by an undiscovered endothelial mediator(s) that improved myocardial microcirculation in the group P. in group P.
v. Reperfusion injury syndrome to be deleted, interestingly the study results showed that immediate myocardial reperfusion might be unnecessary. The procedure, provides stabilization as well as myocardial and hemodynamic recoveries without the urgent need of reperfusion with the well known consequences of the reperfusion injury syndrome (Heinzel, et al., 2008). This was confirmed with our ongoing study, using an intrapulmonary catheter device induced percutaneously through the jugular vein.
vi. Right heart vs. left heart endothelium, this study suggested that the right heart endothelium responded rapidly, to shear stress stimuli, compared to the left heart endothelium, which is most frequently, stimulated with devices like IABP and EECP, known for tolerance and long with long term effectiveness respectively (Pagonas, 2010). We found that the PA endothelium was hypersensitive; a few minutes of intrapulmonary pulsations were more than sufficient to drop systemic and pulmonary pressures. At the beginning of our trials, have observed severe vasodilation with

continuous intrapulmonary catheter pulsation (2 animals were expired). We then shifted from continuous to intermittent pulsation controlled by hemodynamic readings (5-10min pulsation) interrupted by pause intervals (10-15 min).

vii. Venous vs. arterial approach, the systemic arterial approach is most commonly practiced in IHD management, typically with IABP and/or PCI procedures. However, these require specific operative environments with high risks of risk vascular complications (Busch, et al. 1997); (Dangas, et al., 2001). Instead, the study provides a safer and cost-effective venous approach for IHD management that could be done by an ER therapist without the need to specific cardiac centers facilities.

viii. Diastolic CAD synchronizations vs. unsynchronized pulsatile catheter, contrarily to present synchronized cardiac assist devices (CAD), like the IABP, EECP, etc., we believe that unsynchronized catheter pulsation simplifies and broadens its application as an efficient cost-effective method for IHD management. Recorded pressure curves showed that the delivered catheter pulsation was faster than the heart rate; Nevertheless, it did not disturb right ventricular hemodynamic or obstruct the outflow tract.

ix. Suitable for almost all kinds of myocardial ischemia, as been observed, hemodynamic stabilization could be achieved after a few minutes of device pulsation without any pharmacological supports. Positioned inside the PA trunk, the device can reduce pulmonary afterload without jeopardizing preload in case of RV ischemia. Its small dimensions allow applications in pediatrics and other cases of non-atherosclerotic IHD (e.g. congenital, spasm, or vasculitis, induced MI. Moreover, in preconditioned (Bolli R, 2001), hibernating, stunned myocardial or permanent ischemic lesions (Vroom MB & van Wezel, 1996), long term intermittent intrapulmonary or intracoronary sinus catheter pulsation could restore myocardial tissues and dysfunctional endothelial coronary lesions.

x. The pulsatile catheter device vs. CAD, compared to current CAD drawbacks, an autonomous small catheter driven by a portable or implantable pacemaker-like generator, could be safely inserted into the circulatory system of any patient or chosen vessel, including arterial, venous or umbilical. And most probably, it could restore atherosclerotic endothelial lesions and endothelial dysfunction with the pulsatile catheter insertion into the intrapulmonary or intracoronary sinus in coronary atherosclerosis or into the main lumen of a diseased systemic artery (e.g. carotid, renal, femoral, etc.). An enhanced external counter pulsation studies in animal models have shown that regular application of endothelial shear stress stimuli could improve conditions related to atherosclerotic endothelial dysfunction (Zhang, et al., 2007). This could be a supportive argument for the concept.

In summary, An intrapulmonary pulsatile catheter device could improve hemodynamics and recover acute myocardial ischemia efficiently, compared to nitrates. This could be induced with an appropriate intrapulmonary catheter device, adaptable to vessel geometries, regardless of coronary occlusion and irrespective of the heartbeat. The procedure represents an innovative and cost-effective method for IHD management, particularly through an intravenous percutaneous approach (ongoing study).

Operative movie site: http://www.nourmd.com.

9. Acute pulmonary arterial hypertension*

Pulmonary arterial hypertension (PAH) is a dysfunctional endothelium disease with increased pulmonary vascular resistances (PVR) and poor prognosis. Current therapies are still insufficient. Alternatively, we propose a the pulsatile catheter device as a more effective for PAH management compared to traditional treatments.

Material and Methods: *Twelve* piglets (10.3 ± 3.8 kg) were given either intrapulmonary pulsatile (P: n=6) or non-pulsatile (NP: n=6) Tadalafil treatment. After median sternotomy and heparin injection (250 IU/kg), both groups underwent aorto-pulmonary surgical shunt during 1 h then removed (Figures 29 and 30). Over a second 1 h period: in group P, a catheter prototype, driven by a small ventilator, was introduced into the pulmonary trunk and pulsated intermittently at 110 bpm, irrespective of heart rate (90.6±10.74 bmp). In group NP, Tadalafil were given orally (1 mg/kg).

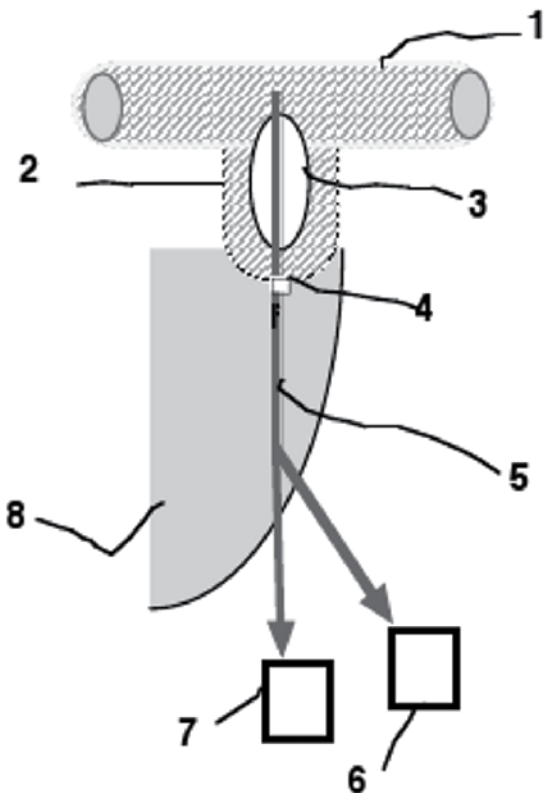

1 = pulmonary artery branch; 2 = pulmonary artery trunk; 3 = inflated balloon in place; 4 = infudibular snugger; 5=catheter shaft; 6= cardiopulmonary monitor; 7 = pulsatile driving system (small animal ventilator); 8 = right ventricular cavity.

Fig. 29. Intrapulmonary pulsatile system

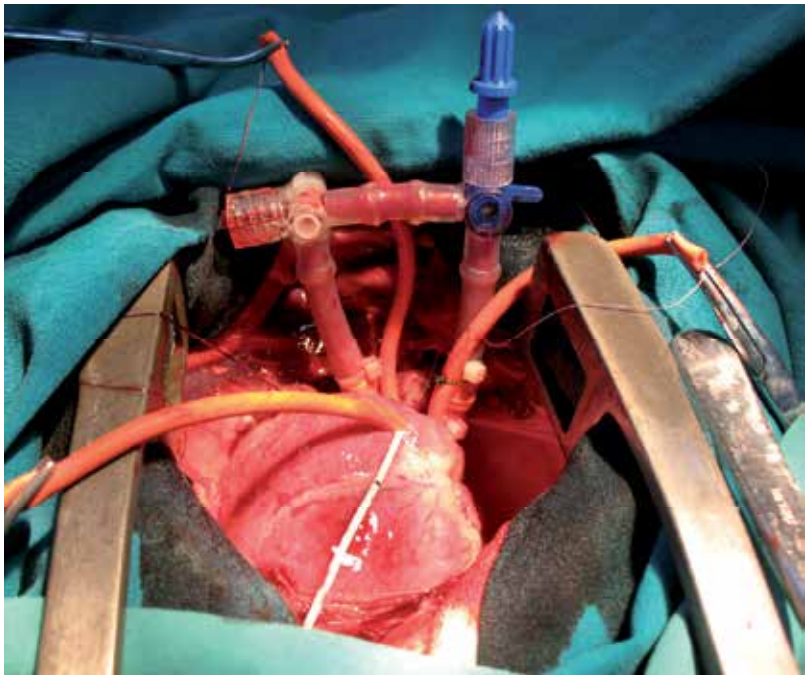

Assembled shunt showing: 2 PVC limbs unequally cut with ½ cm; connected together with silicone tube and equipped with 2 stopcocks and pressure lines connectors, prefilled with heparinized saline and clamped ready before insertion. Aorto-pulmonary shunt in place with infundibular intrapulmonary artery pressure line (white color).

Fig. 30. Aortico-pulmonary "U" shape external shunt system.

Statstics: Continuous variables are expressed as the mean±SEM. Comparisons between groups of independent samples were performed with student t-test for eNOS and a 2-way ANOVA for hemodynamic data. P with a value less than 0.05 was considered statistically significant. GraphPad Prism® software was applied for all the statistical analyses in this study.

Results: hemodynamic and cardiac output (CO) were significantly ($p<0.05$) better in group P compared to group NP: CO was 0.56±0.0.26 vs. 0.54±0.11 (L/min) respectively. Mean pulmonary artery pressure (PAP) was significantly dropped in group P compared to group NP: PAP was 9.6±2.97 vs. 32.25.07 respectively. Vascular resistances (dynes.sec/cm^{-5}.kg^{-1}) were significantly lower in group P vs. group NP: pulmonary resistance (Figure 31), was 85±42.12 vs. 478±192.91, and systemic resistance was 298.8±172.85 vs. 1301±615.79, respectively. The endogenous NO synthase expression in PA segments with Western blot analysis was higher from group P (0.81±0.78) vs. (0.62±0.35) in group NP ($p>0.05$).

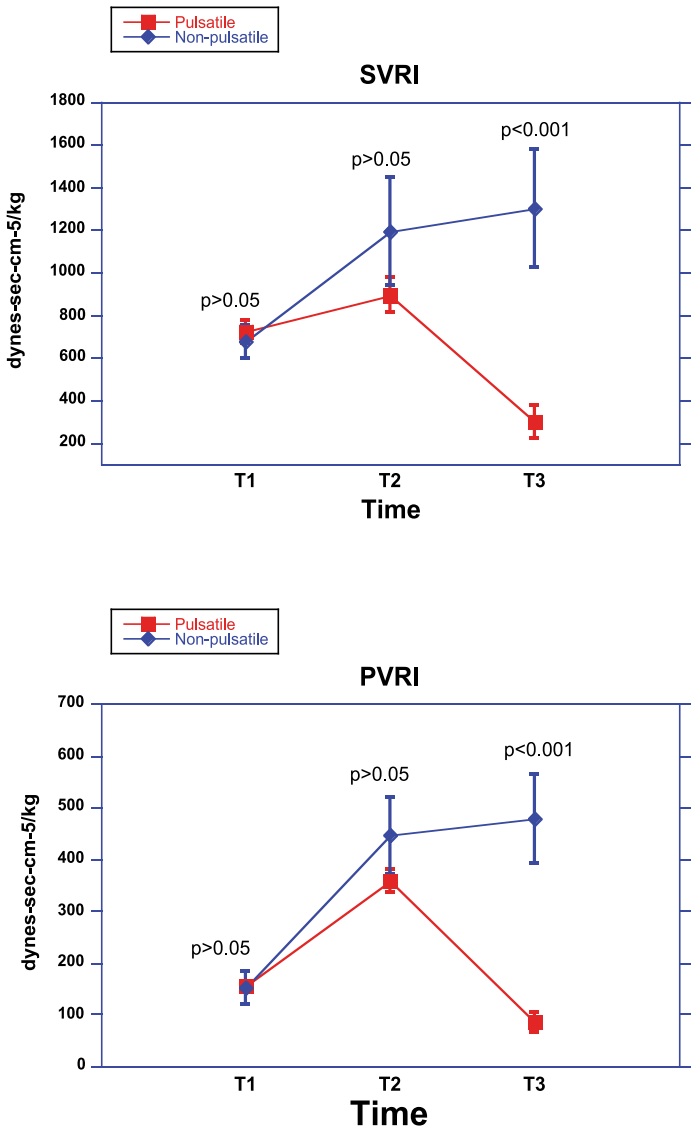

Fig. 31. Systemic and pulmonary vascular resistances indexes

Upper panel: showing data of the systemic vascular resistances index (SVRI) calculated from pulsatile group (P; red color) and non-pulsatile group (NP; blue color) at three predetermined time: T1= baseline; T2 after 1H of shunt and T3= end of 1h therapy. at T1 (baseline) and the end (T3). Lower panel: showing data of the pulmonary vascular resistances index (PVRI) calculated from pulsatile group (P; red color) and non-pulsatile group (NP; blue color) at three predetermined time: T1= baseline; T2 after 1H of shunt and T3= end of 1h therapy. at T1 (baseline) and the end (T3). Both SVRI and PVRI (dynes.sec.cm^{-5}/kg) were significantly lower ($p<0.001$) were significantly lower at T3 in group P compared to group NP.

Comment This study confirms the dominancy of the right heart over the left heart and hemodynamic through PVR

The effect of intrapulmonary shear stress enhancement was immediate upon both PVR and SVR in the group P. The significant improvement of hemodynamic with rapid reduction of pulmonary pressure in group P compared to the group NP, confirms the dominancy of shear stress-mediated endothelial function enhancement method over traditional therapies*. Also this confirmed what we have mentioned with the ischemic models regarding the hypersensitivity of the right heart side endothelium of the pulmonary artery compared to systemic arteries.

Conclusions: Induced with an appropriate device, intrapulmonary shear stress-mediated endothelial function enhancement, provides a more effective nearly physiological therapy for PAH.

* Abstract of the study concept was presented at the 16th conference of ACTVS - Singapore, Nour, 2008). Paper in press, submitted to the Pediatric Cardiology Journal (Nour, S 2012).
Operative movies: http://www.nourmd.com.

10. Evaluation of the pulsatile suit device

This concerns the non-invasive devices (pulsatile suit) that were tested in vivo and healthy volunteers (the author and medical doctors colleagues).

10.1 Animal model of acute RV failure*

Cardiac assists devices (CAD) for right ventricular (RV) failure remain controversial with poor results. The purpose of this study was to evaluate a pulsatile suit CAD in an acute RV failure model vs. current therapies.

Material and methods (Figure 32): twelve piglets, divided in two equal groups: pulsatile group P and non-pulsatile group NP. Acute pulmonary incompetence was created surgically through median sternotomy. Management started once severe RV failure observed (48.1±24.5 min): in group P, a pulsatile trouser, driven by pneumatic generator was pulsated intermittently at 40 bpm, irrespective of heart rate (104±27 bmp). Group NP, was treated with oral Tadalafil (1 mg/kg), IV fluids and adrenaline (0.3μg/kg).

Results (Figure 33 & Table 8): after 1 h of therapy, hemodynamic and cardiac output (CO) were significantly ($P<0.05$) better in group P compared to group NP: CO 1±0.2 vs. 0.7±0.2 (L/min) respectively. Mean RV pressure (RVP) and pulmonary arterial (PAP) pressure were dropped in group P compared to group NP: RVP 16±6 vs. 24±2 and PAP 22±1 vs. 31±2 (mmHg) respectively. Vascular resistances indexes ($dyne.sec/cm^{-5}.kg^{-1}$) were dropped in group P vs. group NP: pulmonary resistance was 174±60 vs. 352±118, and systemic resistance was 611±70 vs. 1215±315, respectively. Western-blot analysis of pulmonary arteries shown higher endogenous NO synthase (eNOS) expression ($p>0.5$) in group P :0.90±0.71 vs. 0.66±0.52 in group NP.

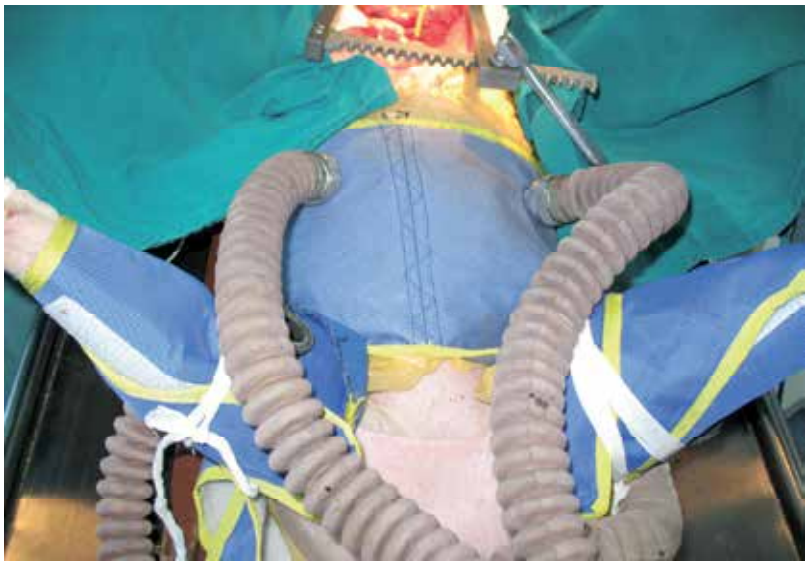

Fig. 32. Pulsatile trouser (intraoperative view)

	Group	PAP	RVP	PVRI	CO
T1	P	24±3 / 15±2	29±4 / 14±5	168±27	0.8±0.3
	NP	23±4 /15±3	34±3 / 7±2	182±42	0.9±0.1
T2	P	41±2 / 27±3	43±2 / 16±5	314±17	0.7±0.2
	NP	42±3 / 25±2	46±2 / 12±3	385±51	0.7±0.2
T3	P	27±2 / 17±2	28±2 / 6±3	174±27	1±0.2
	NP	39±3 / 23±2	42±1 / 7±1	352±52	0.7±0.2

Table 8. Therapeutic response of the right heart hemodynamic parameters (Trouser vs. TadalafilTM): Systolic and diastolic pressures (mmHg) of the right ventricle (RVP) and pulmonary artery (PAP); PVRI: pulmonary vascular resistances index (dynes•sec/cm5/kg); CO: cardiac output (L/min); T1: baseline; T2: nearly 1 h after pulmonary valve disruption; T3: end. P: pulsatile group; NP: non-pulsatile group; ($p<0.05$).

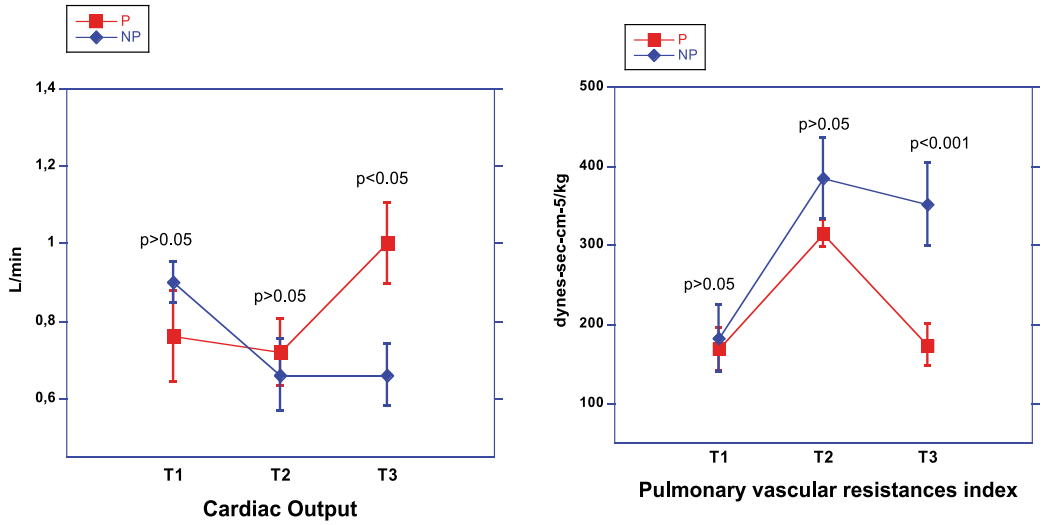

P: pulsatile group (red color), NP: non pulsatile group (blue color); left panel showing cardiac output panel showing pulmonary vascular resistances index (PVRI); right panel showing cardiac output (CO) results obtained from both groups P and NP in three. Data were obtained from both groups (P & NP) at three predetermined time: T1= baseline; T2: nearly 1 h after pulmonary valve disruption and T3= end of 1h therapy. CO (L/min) was significantly improved ($p<0.05$) at T3 in group P compared to group NP. PVRI (dynes.sec.cm^{-5}/kg) were significantly lower were significantly ($p<0.01$) lower at T3 in group P compared to group NP. (Two ways ANOVA test)

Fig. 33. Hemodynamic figures

*Paper was submitted to the Asian Cardiovascular & Thoracic Annals Journal (in press Nour, S 2012).

Operative movies: http://www.nourmd.com.

10.2 Clinical volunteers (study in progress)

10.2.1 Mask

Pulsatile mask was tested in healthy volunteers (n=8) from both sex (age:19-68 ys), subjected to 20 minutes of low pressure (0.2-0.6 bars) pulsatile mask, synchronized with diastolic heart rate. *Statistics:* Continuous variables are expressed as the mean±SEM. Comparisons between groups of independent samples were performed with student t-test hemodynamic data. P with a value less than 0.05 was considered statistically significant. GraphPad Prism® software was applied for all the statistical analyses in this study.

Results: hemodynamics and cerebral blood flow was significantly improved ($p<0.05$), as manifested by Doppler flow measured at the common carotid artery (Figure 35): carotid output: 246±41.73 vs. 294±50.42 (ml/min), and velocity 18±2.4 vs. 21±2.8 (cm/sec). Microcirculation measured from the tip of the nose (Perimed®-PeriScan 3 System), was

45.5±14.6 vs. 89.2±31.1 ($p<0.001$) with unsynchronized mask pulsations (Figure 34); and from the mandibular angle (measured with Perimed® - PeriFlux System 5000), was 28±12.5 vs. 87±35.2 ($p<0.05$), with synchronized mask pulsations (Figure 35).

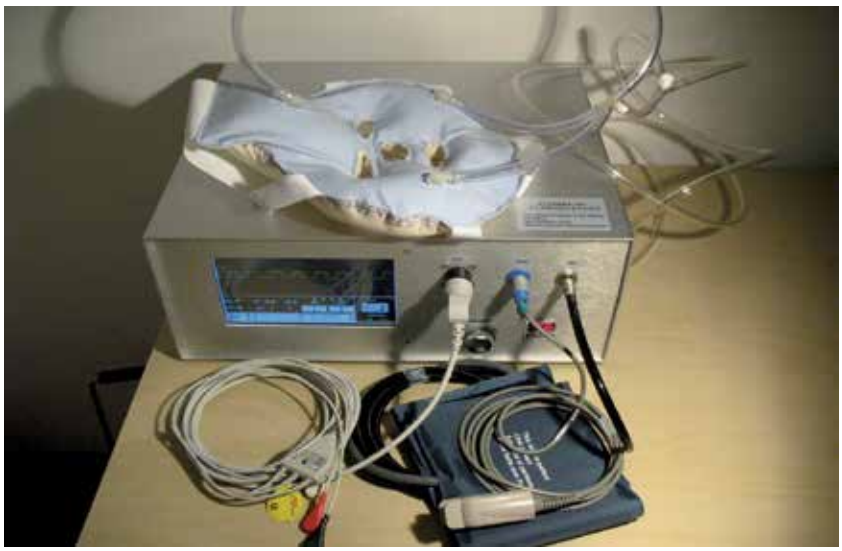

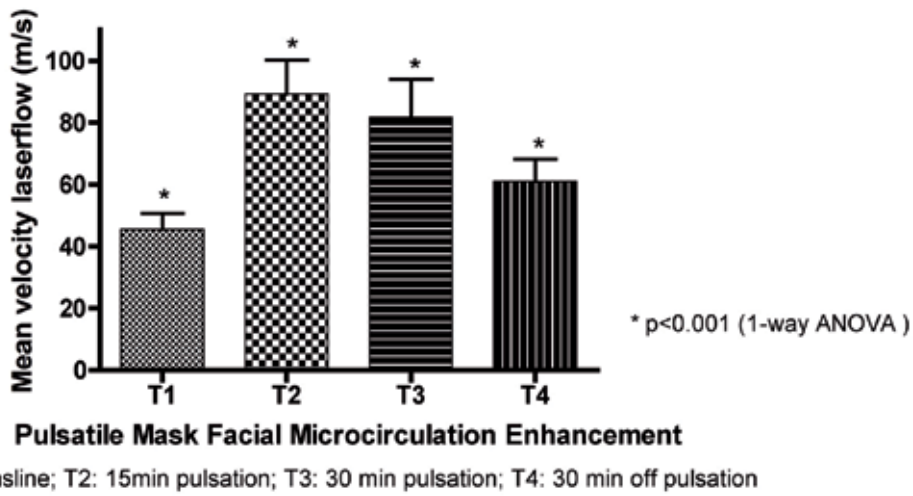

Upper panel, showing mask device inflated and connected to a generator equipped with a set for hemodynamic measurements (ECG, BP, SaO2); lower panel showing cutaneous microcirculation measured from the tip of the nose at T1: baseline; T2: after 15 min of low pressure pulsation (0.2-0.4 bar) unsynchronized with heart rate; T3: by the end after 30 min of pulsation. T4: 30 min after the end.

Fig. 34. Pulsatile mask improving facial microcirculation

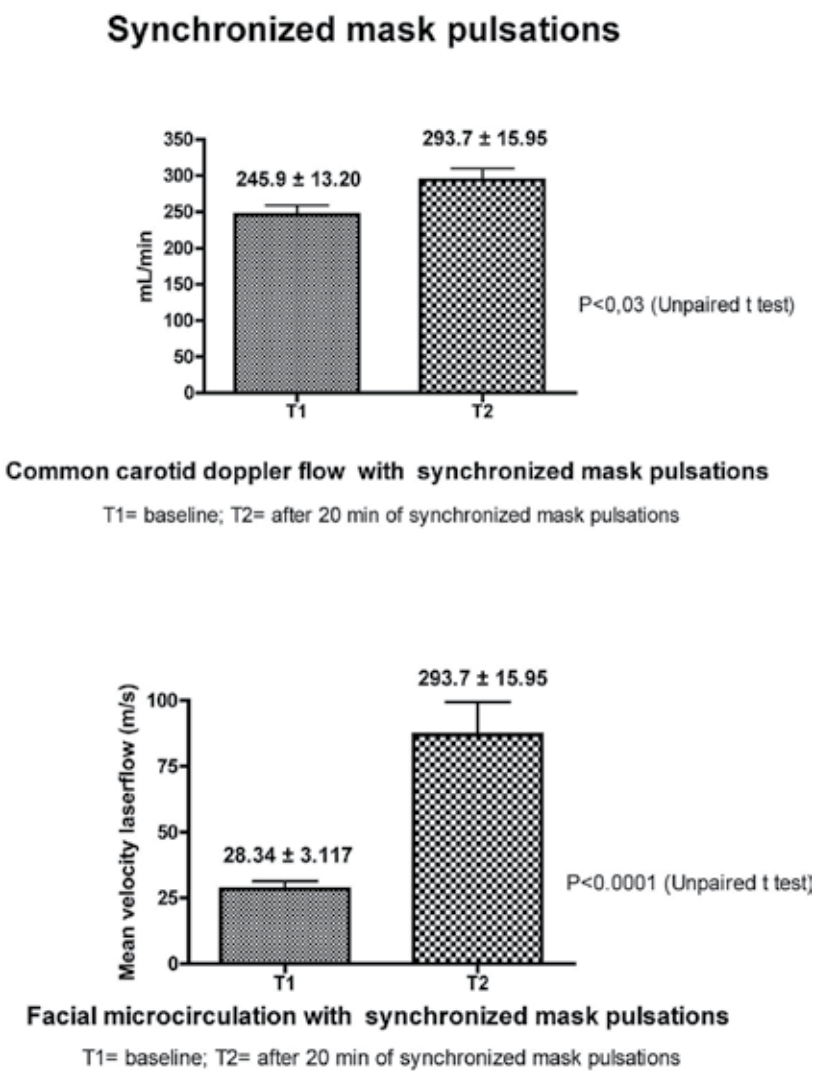

Upper panel carotid flow measured by echo Doppler; lower panel: facial microcirculation (from the mandibular angle)

T1: baseline; T2: after 20 min of pulsations

Fig. 35. Synchronized pualstile mask results

N.B. interestingly the microcirculation's flow shown in (Figure 34), was rapidly increased after 15 min of pulsations, then dropped slightly to pass in plateau over the second 15 min of stimulation. This proves the physiological effect of the device that does not stun endothelial biology, allowing self-cellular regularization in response to induced endothelial vasodilators mediators and unlikely to exogenous NO donors vasodilators (e.g. nitrates).

Movies demonstration of the pulsatile mask:

http://www.nourmd.com.

10.2.2 Trouser

Pulsatile trouser, that covering almost the trunk, was tested in healthy adult volunteers (the author and medical colleagues) (n:6), were subjected to a low pressure (1.2 bars) fixed pulsations (60 bpm) and without synchronization of heartbeat (72± 17 bpm). Results (Figure 36); after 20 min of pulsations, the peripheral microcirculation was measured with laser flowmeter (Perimed®-PeriScan 3 System) at the tip of the finger was significantly improved: 93.5±31.3 vs. 222.4±35.8 ($p<0.003$).

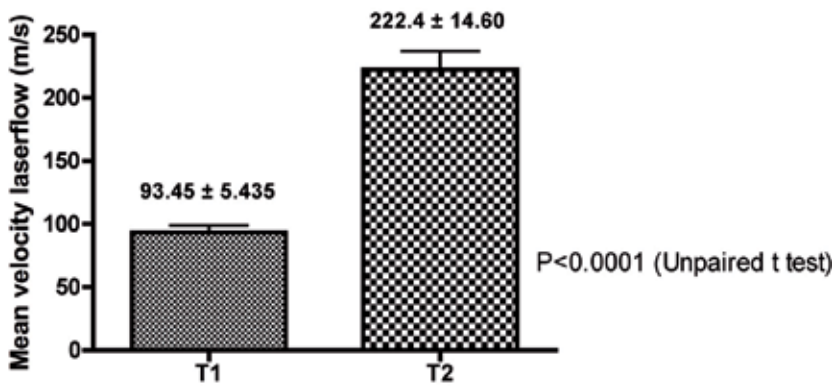

Microcirculation of the index tip with unsynchronized trouser pulsations

T1:Basline; T2: end after 20 min of pulsation

Upper panel: pulsatile trouser's prototype; lower pannel: increased peripheral microcirculation, measured at the tip of the right index (laser flowmeter: Perimed®-PeriScan PIM 3 System)

Fig. 36. Hemodynamic results after 20 min pulsation in 6 volunteers

Movie demonstration http://www.nourmd.com.

11. Evaluation of the Biventricular assist device "L'Orthèse cardiaque" (study in progress)

11.1 In vivo

The device was tested in an acute ischemic biventricular failure (piglet). This was created by mid ligation of the LAD, and elecrocauterization of the RV coronary artery branches, for details refer to the attached operative movies site. The preliminary results shown better hemodynamic responses with the biventricular assist device combing the pulsatile tube as a LVAD and the pulsatile trouser as RVAD (Figure 36).

Fig. 37. Biventricular CAD (l'Orthèse cardique) in ischemic model (piglet)

Operative movies: http://www.nourmd.com.

Comment: in this study the device (l'Orthèse cardiaque) was tested as well in total cardiac arrest followed and acute ischemic biventricular failure and cardiogneic shock. The device was successfully capable to circulate the stagnant blood columns within the respect of the biophysical conditions of each heart circuit biophysiological conditions (please refer to the attached movie). The study pending new pulsatile tube constructions. The object is to maintain circulatory flow dynamics and cellular metabolism in case of acute biventricular failure until improvement of hemodynamic or arrangement for heart transplants with compatible donors in nearly physiological condition.

11.2 In clinical volunteer

The pulsatile trouser was indicated in a CHF patient, (a medical consultant from the UK), as an ultimate therapeutic option, according to a consensual patient's request. The patient was short-listed for both heart and kidney transplant, then been removed due to severely deteriorated hemodynamics: EF ≈ 15%, systolic pulmonary arterial pressure >65 mmHg,

and elevated BNP (1100 pg/ml). He was on renal dialysis (6 days/ week), chronic constipations and oxygen sleep dependent. The pulsatile trouser was applied for 2O minutes daily, in a posture position* with fixed frequency (40 bpm), irrespective of patient's pacemaker (78 bpm) and low inflation / deflation pressure (1.4 bar). The patient recovred regular bowl, and became less dependent on oxygen during the first week of treatment. After two months there was hemodynamic improvement: EF≈ 20%; systolic PAP ≈ 41mmHg and BNP ≈ 500 pg/ml. The patient reintegrated the NHS transplant program. Despite, hemodynamic improvement, the procedure was interrupted because a cholecystectomy was urgently, needed for biliary lithiasis, which may promote to shower pancreatitis with the trouser pulsations.

*N.B. In CHF patients, it is preferred to apply trouser therapy in a posture position, rather than supine position to amplify the gravity effect as an enhancement factor of shear stress with more voluminous columns of venous capacitance.

Movie demo: http://www.nourmd.com.

11.3 Comment

These aforementioned preliminary results have proven the feasibility of the concept as a promising therapeutic approach for CVD. On other word, proven the efficiency of the right heart endothelial reservoir as a physiological therapeutic backup compared to optimum traditional therapies in addressing acute cardiogenic shock state.

The pulmonary endothelium, stimulated with a small size pulsatile catheter that can be introduced intravenously and percutaneously, open a new era in cardiology as almost all types of ischemic heart disease as well as pulmonary arterial hypertension (PAH). Macroscopic disappearance of the ischemic zone confirmed with low myocardial apoptosis and that despite permanent ligation of the coronary artery means improved hemodynamic is more related to open myocardial microcirculation in neonate animal model known with poor coronary collaterals.

A significant drop in the pulmonary vascular resistance was the key of hemodynamic improvement. This can be induced with the proposed pulsatile systems after short period of intermittent shear stress-mediated endothelial function stimulations at the splanchnic and hepatic venous capacitance, or at the pulmonary artery, and irrespective to heart rate.

Pulsatile suit concept results that have been obtained in volunteers also open a new era of therapeutic approach in nearly all types of endothelial dysfunctions pathogenesis as follows: with (Type A), endothelial dysfunction with heart disease patients; in Type B, with endothelial dysfunction and normal heart function (e.g. diabetic, systemic arterial hypertension, PAH, erectile dysfunction, etc); and Type C, as prophylactic in healthy individuals, liable for endothelial dysfunction pathogenesis (Astronauts, bedridden, etc) as well as a circulatory hemodynamic physiological stimulus (e.g. athletics, anti-aging, etc).

The pulsatile mask can improve the cerebral circulation directly through the cavernous venous systems, and systematically through the jugular vein system, current studies show enhancement of the retinal artery flow as well as diameter, which ca be effective in treating early neurodegenerative diseases and stroke patients.

This improvement is observed at points remote from the pulsating zone, i.e. where the suit was being worn.

A clear improvement in microcirculation has also been observed at the fingertips as a result of putting a pulsatile suit (trouser) on the bottom portion of a patient's body as shown in (Figure 36).

Practically, delivery of shear stress stimuli at the compliant pulmonary artery (PA) zone (zone5), can be induced according to the Bernoulli's principles with a small size pulsatile catheter adaptable to the pulmonary trunk geometries for shear rates enhancement at the inner boundaries layers, irrespective of heartbeat without obstructing the right ventricular outflow tract. Meanwhile at the superficial venous capacitance (zone1) shear stress enhancement could be achieved externally with the pulsatile suit.

At the left heart side, an endothelial shear stress will be induced by the pulsatile tube. The pulsatile tube could adapt whether a conventional CPB or CAD, provides a nearly physiological pulse pressure with lowest momentum energy losses, particularly in association with the Smartcan. It will considerably reduce the distance between CAD and the perfused artery (Z3).

Similarly, an improvement in the microcirculation of the myocardium has been observed in an ischemic model by permanent ligation of the left anterior descending coronary artery (LAD), after applying shear forces generated by pulsatile catheter inserted in the pulmonary artery forming part of the right circuit of the heart.

Given the very short lifetime of nitric oxide, it cannot reach zone that are remote from the site where it is secreted, since it is necessarily absorbed by hemoglobin before reaching said remote zones. Thus, it has been found that at least one mediator mechanism other than those that are already known and secreted by the endothelium is capable of triggering the opening of microcirculation. The devices and methods of the present concept advantageously enable such secretion to take place.

As a priority, assistance should be provided to the right portion of the heart. It is known that the right heart "dominates" the left heart and controls hemodynamics by pulmonary resistances (Nour S 2008). Isolated ventricular assistance, on the left or right, can then be envisaged in accordance with the present disclosure; and after that assistance for the left heart.

The method makes it possible to restore the endothelial function progressively by maintaining quasi-physiological shear forces on the endothelium; consequently, there is a significant improvement in the function of myocardium, thus making it possible avoid subsequent transplants.

Alternatively, the pulsatile catheter prototype, when applied in the clinic, could be implanted into the pulmonary artery through a central venous line (ongoing study), in hospital settings, it could be connected to a small portable-implantable driving device. Patients with catheter device set implants would benefit from real-time hemodynamic measurements and simultaneous therapeutic pulmonary pulsation. Thus, this approach promises to be cost-effective.

By providing immediate improvement of myocardial microcirculation, the device could become a first priority in IHD as well as PAH managements.

In future investigations, the device could be inserted through the PA (ongoing study) or coronary sinus, either associated or not with an absorbable stent, to test for enhancements in the restoration of endothelial function.

Over the long term, shear stress-induced endothelial regulation, alone or in combination with progenitors and angiogenic factors could promote cardio-circulatory rehabilitation and accelerate cardiogenesis. This approach might eliminate the need for interventional or surgical procedures.

Finally, as far as the concept has been proven therapeutic efficiencies, there were some study limits that should be resolved in the future. This includes the severe vasodilatation as a result of direct intravascular endothelial stimulations by the intrapulmonary pulsatile catheter as well as the pulsatile tube as a LVAD.

Interestingly, the application of the pulsatile tube alone as a LVAD without perfusion pump induced severe vasodilatation after impressive improvement of MI (please refer to operative movie). This is proving the hypersensitivity of the pulmonary endothelium as well as the LV endocardium that were responded rapidly to the unsynchronized tube pulsations.

A similar phenomenon has been observed with Nicorandil, an exogenous NO donor used for angina pectoris relief (Falase BA, et al., 1999), (Blanc P, et al., 2001).

Meanwhile, vasodilatation that could be induced by exogenous NO donors, leads to hypovolemic-cardiogenic shock. In contrast, the observed study hypovolemia, was preceded by general improvement of hemodynamic and organ microcirculation. This was manifested by the increased renal output manifested by a vesical globe that was released spontaneously in the pulsatile group animal models, which could be easily compensated by IV fluids. Currently we reduced the frequencies of pulsatile time (5-10 min), interrupted by interval pause guided by hemodynamic monitors, particularly systemic BP.

There was no observed severe vasodilatation with the externally stimulated endothelial devices (the pulsatile trouser and mask). By caution, as the mechanism of vasodilatation is still undiscovered, also the improved microcirculation became almost steady after 15-20 min of external endothelial stimulations, our recommendation for the pulsatile suit sessions is: 20-30 min. Furthermore, it is unnecessary to apply high-pressure pulsatile volume. A low pressure (1.2-2 bars) is sufficient to stimulate the superficial intravascular blood volume, covered by their endothelial stocks.

Contraindications of the pulsatile suit, are more or less relatives as a non-invasive device, meanwhile cautions may be considered with some patients (e.g. hepatic cirrhosis, malignancy, open fractures, 3rd degree burns, colostomy, cerebral accidents, malignancy). Under all circumstances, Clinicians will determine contraindications according to the obtained results.

Currently, clinical programs of the non-invasive devices will start very soon, with (Type A, & C) endothelial dysfunction patients (e.g. CHF, resistant arterial hypertension, cerebral atherosclerosis, etc.) and others with healthy persons (Type C) e.g. bedridden, athletes.

12. Conclusion

A promising therapeutic approach for CVD and circulatory disorders management with more physiological cost effective manners compared to current therapies. According to physics, it consists of: a shear rate intravascular enhancement device (catheter); a steady flow transformer device (tube) and an accessory circulatory driving forces enhancement and/or replacement device (suit). Drawbacks of the invasive devices could be overruled through accurate mathematical calculations of the induced momentum according to individual body surface area and the stimulated sites (blood column). Means, optimum devices performances could be achieved with computational models and biomedical engineering, to define the accurate device geometries as well as materials.

13. Acknowledgements

We would like to express our gratitude for the great help of the laboratory teamwork at the Sun Yat-sen University (GZ-China): Drs. Wu Guifu, Wang Qinmei, Mr. G Dai. The Biosurgical Research Lab (Foundation A Carpentier) Paris-France: Drs. Alain Carpentier, JC Chachques. Marie-Lannelogue Hospital (Plessis-Robinson- France): Drs. Cl. Planché, G Mazmannian. Particular acknowledgment for Mrs. Ana Skalamera for the edition of this work.

14. Sources of funding

Centre Francilien de l'Innovation (75012 Paris); Centre d'Innovation - Oseo Centre (45074 Orléans) and Cardio Innovative Systems (75012 Paris) – France. The Key Laboratory on Assisted Circulation, The First Affiliated Hospital, Sun Yat-sen University, Ministry of Health, 510080 Guangzhou - China.

15. References

Abrams, J (1988). A reappraisal of nitrate therapy. *JAMA, Vol.*259, No.3, (January 1988) 396-401.

Al-Ghazali, W (1989). Evidence of redistribution of cardiac output in asymmetrical growth retardation. *Br J Obstet Gynaecol*, Vol. 96, No. 6, (June 1989), pp.697-704.

Anderson, RM. (1999). *The Gross Physiology of the Cardiovascular System,* Racquet Press 4625. San Carlos PL. Tucson, Arizona 85712, USA.

Aron EA, et al (2003). *Angiogenesis. Genetics and Embryology Textbook*. Australia; pp.83.

Adamo L. (2009). *Biomechanical control of hematopoiesis,* Ph.D., HARVARD UNIVERSITY. ISBN: 3385549, Boston, USA.

Abshire, TC (2009). Bleeding risks with cardiac disease.Transfusion Medicine and Hemostasis, Academic Press, (April 2009), pp. 577-580. ISBN. 9780123744326

Burton, AC (1954). Relation of structure to function of the tissues of the wall of blood vessels. *Physiol Rev*, Vol.34, No.4, (October 1954), pp. 619-42.

Bick, RL (1976). Alterations of hemostasis associated with cardiopulmonary bypass. *Thrombosis Research*, Vol.8, No.3, (March 1976), pp. 285-302.

Busch, T (1997). Vascular complications related to intraaortic balloon counterpulsation: an analysis of ten years experience. *Thorac Cardiovasc Surg,* Vol.45, No.2, (April 1997), pp. 55-59.

Berger, PB (1999). One-year survival among patients with acute myocardial infarction complicated by cardiogenic shock, and its relation to early revascularization: results from the GUSTO-I trial. *Circulation,* Vol. 99, No.7, (February 1999), pp. 873-8.

Bolotin, G (2001). Hemodynamic evaluation of descending aortomyoplasty versus intraaortic balloon pump performed in normal animals: an acute study. *Eur J Cardiothorac Surg*, Vol. 19, No. 2, (February 2001), pp.174-8.

Bolli, R (2001). Cardioprotective function of inducible nitric oxide synthase and role of nitric oxide in myocardial ischemia and preconditioning: an overview of a decade of research. *J Mol Cell Cardiol,* Vol.33, No.11, (November 2001), pp.1897-1918.

Bonetti, PO (2003). Enhanced external counterpulsation improves endothelial function in patients with symptomatic coronary artery disease. *J Am Coll Cardiol*, Vol. 41, No.10, (May 2003), pp.1761-8.

Box, FM (2005). The influence of flow, vessel diameter, and non-newtonian blood viscosity on the wall shear stress in a carotid bifurcation model for unsteady flow. *Invest Radiol*, Vol.40, No.5, (May 2005), pp. 277-94.

Buckberg, GD. (2006). The ventricular septum: the lion of right ventricular function, and its impact on right ventricular restoration. *Eur J Cardiothorac Surg*, Vol.29, No.1, (Apr 2006), pp.272–8.

Burkhoff, D (2006). A randomized multicenter clinical study to evaluate the safety and efficacy of the Tandem Heart percutaneous ventricular assist device versus conventional therapy with intraaortic balloon pumping for treatment of cardiogenic shock. *Am Heart J,* Vol. 152, No. 3, (September 2006), pp. 469.e1-8.

Bauer, NR (2007). Rodent models of PAH: are we there yet? *Am J Physiol Lung Cell Mol Physiol*, Vol. 293, No.3, (September 2007), pp. 580–582.

Clark, EB. (1987). Mechanisms in the pathogenesis of congenital cardiac malformations. In: *The Genetics of Cardiovascular Disease,* Pierpont MEM, Moller JH, editors. Nijhoff Publishing, Boston, 1987:3–11.

Calvert, JB. (2000). Bernoulli's Equation « The most useful relation in engineering hydraulics is really three ». (August 2000), (11/09/20011), available from: <http://www.du.edu/~jcalvert/tech/fluids/bernoul.htm>

Chachques, JC (2005). Cellular cardiomyoplasty for myocardial regeneration. *Asian Cardiovasc Thorac Ann*, Vol.13, No.3, (September 2005), pp. 287-296.

Cooper, JR Jr (2006). Fatal pulmonary microthrombi during surgical therapy for end-stage heart failure: possible association with antifibrinolytic therapy. *J Thorac Cardiovasc Surg*, Vol.131, No.5, (May 2006), pp. 963-968.

Chatzizisis, YS (2007). Role of endothelial shear stress in the natural history of coronary atherosclerosis and vascular remodeling: molecular, cellular, and vascular behavior. *J Am Coll Cardiol,* Vol.49, No.25, (June 2007), 2379-2393.

Couzens, GF (2009). Surviving a Heart Attack, Succumbing to Heart Failure. *The New Yourk Times*-Iside Health, (January 2009), available from: http://www.nytimes.com/ref/health/healthguide/esn-heart-failure-ess.html

Carpentier, A. (2011). Building human hearts on an assembly line (CARMAT). *European hospital*, (Aug 2011), available from: http://www.european-hospital.com/en/article/8917-Building_human_hearts_on_an_assembly_line.html

Dhombres, J. (1989). "La théorie de la capillarité selon Laplace: mathématisation superficielle ou étendue" (in French). Revue d'Histoire des sciences et de leurs applications, Vol.42, No.42 (1989), pp. 43–70, available from: <http://www.persee.fr/web/revues/home/prescript/article/rhs_0151-4105_1989_num_42_1_4134>

Depre, C (1997). Activation of nitric oxide synthase by ischaemia in the perfused heart. *Cardiovasc Res*, Vol. 33, No.1, (January 1997), pp. 82-87.

Doherty, DH (1998). Rate of reaction with nitric oxide determines the hypertensive effect of cell-free hemoglobin. *Nat Biotechnol,* Vol.16, No.7, (July 1998), pp. 672-676.

Dangas, G (2001). Vascular complications after percutaneous coronary interventions following hemostasis with manual compression versus arteriotomy closure devices. *J Am Coll Cardiol,* Vol.38, No.3, (September 2001), pp. 638-641.

Davignon, J (2004). Role of endothelial dysfunction in atherosclerosis. *Circulation*, Vol.109, No.23 Suppl 1, (June 2004), pp. III27-32.

D'Alto, M. (2007). Long term effects of bosentan treatment in adult patients with pulmonary arterial hypertension related to congenital heart disease (Eisenmenger physiology): safety, tolerability, 1 clinical, and haemodynamic effect. *Heart, Vol.93, No.5, (May* 2007), pp. 621-625.

Endemann, DH. (1983). Endothelial Dysfunction. *J Am Soc Nephrol,* Vol.15, No.8, (August 2004), pp. 1983-92.

Gorge, G. (1989). Microvascular and collateral adaptation in swine hearts following progressive coronary artery stenosis. *Basic Res Cardiol,* Vol.84, No.5, (September-October 1989), pp. 524-35.

Geankoplis, CJ. (2005). Principles of Momentum Transfer and Applications. 4th edition, ISBN 13: 9780131013674;

Gershlick, T.(2007). PCI or CABG: which patients and at what cost? *Heart, Vol.*93, No.10, (October 2007), pp.1188-90.

Gravlee, GP. (2008). Cardiopulmonary bypass: principles and practices. Lippincott Williams & Wilkins, a Wolters Kluwer business. ISBN 978.0.7817.6815.3.

Fahraeus R, Lindquist T (1931). The Viscosity of the blood in narrow capillary tubes. *Am J Physiol,* Vol. 96, No.3 (March 1931), pp. 562-568.

Furchgott, RF. (1980). The obligatory role of endothelial cells in the relaxation of arterial smooth muscle by acetylcholine. *Nature,* Vol.288, No.5789, (November 1980), pp. 373–376.

Feynman, R P. (2005). The Feynman Lectures on Physics. Vol. 1 (2nd ed.). Pearson/Addison-Wesley. ISBN 0805390499.

Humbert, P (1947). L'OEuvre scientifique de Blaise Pascal, Paris, Albin Michel, '1947), available from: <http://www.persee.fr/web/revues/home/prescript/article/rhs_0048-7996_1948_num_1_3_2649>.

Hutchins, GM. (1988). Development of the coronary arteries in the embryonic human heart. *Circulation,* Vol.77, No.6, (June 1988), pp. 1250-7.

Hoeks, APG. (1995). Noninvasive Determination of Shear-Rate Distribution Across the Arterial Lumen. *Hypertension,* Vol.26, No.1, (July 1995), pp. 26-33.

Huang, W (1998). Zero-stress states of human pulmonary arteries and veins. *J Appl Physiol*, Vol.85, No.3, (September 1998), pp. 867-73.

Haji, SA. (2000). Right ventricular infarction--diagnosis and treatment. *Clin Cardiol,* Vol.23,No.7, (July 2000), pp. 473-82.

Heilmann, L. (2005). Fetal hemorheology in normal pregnancy and severe preeclampsia. *Clinc Hemorheol Microcirc*, Vol.32, No.3, (2005), pp. 183-90.

Heinzel, FR. (2008). Inducible nitric oxide synthase expression and cardiomyocyte dysfunction during sustained moderate ischemia in pigs. *Circ Res,* Vol.103, No.10, (November 2008), pp.1120-7.

Haddad, F. (2011). Characteristics and outcome after hospitalization for acute right heart failure in patients with pulmonary arterial hypertension. *Circ Heart Fail*, Vol.4, No.6, (Nov 2011), pp. 692-9.

Ignarro, LJ. (2002). Nitric oxide donors and cardiovascular agents modulating the bioactivity of nitric oxide: an overview. *Circ Res,* Vol.90, No.1, (January 2002), pp. 21-28.

Ishida, K. (2004). Heparin-induced thrombocytopenia after coronary artery bypass grafting with cardiopulmonary bypass: report of a case. *Surg Today*, Vol.34, No.12, (2004), pp. 1041-1043.

Jones, SP. (2006). The ubiquitous role of nitric oxide in cardioprotection. *J Mol Cell Cardiol,*Vol.40, No.1, (January 2006), pp. 16-23.

Koller, A. (1993). Role of shear stress and endothelial prostaglandins in flow- and viscosity induced dilation of arterioles in vitro. *Circulation Research*, Vol.72, No.6, (June 1993), pp. 1276-84.

Kessler, DP. (1999). Momentum, Heat, and Mass Transfers Fundamentals. Marcel Dekker, Inc. ISBN 0-8247-1972-7.

Kadoi, Y (2000). Balloon pump-induced pulsatile perfusion during cardiopulmonary bypass does not improve brain oxygenation. *J Thorac Cardiovasc Surg*, Vol. 11ç, No.1, (January 2000), pp. 189-90.

Kozák-Bárány, A. (2001). Development of left ventricular systolic and diastolic function in preterm infants during the first month of life: a prospective follow-up study. *J Pediatr*, Vol.139, No.4, (October 2001), pp. 539-45.

Katz, AM (2002). Ernest Henry Starling, his predecessors, and the "Law of the Heart". *Circulation*, Vol. 106, No.23, (December 2002), pp. 2986-92.

Kapur, A. (2007). Mortality after myocardial infarction in patients with diabetes mellitus. *Heart,* Vol.93, No.12, (December 2007), pp. 1504-1506.

Kusama, Y. (2011). Variant angina and coronary artery spasm: the clinical spectrum, pathophysiology, and management. *J Nihon Med Sch*, Vol.78, No.1, (2011), pp. 4-12.

Letsou, GV. (1993). Pulmonary artery balloon counterpulsation: safe after peripheral placement. *Ann Thorac Surg,* Vol.55, No.3, (March 1993), pp.741-746.

Lam, CF (2006). Increased blood flow causes coordinated upregulation of arterial eNOS and biosynthesis of tetrahydrobiopterin. *Am J Physiol Heart Circ Physiol,* Vol.290, No.2, (February 2006), pp. H786-793.

Limaye, V. (2007). The vascular endothelium: structure and function. Mechanisms of Vascular Disease: A Textbook for Vascular Surgeons. ISBN: 9780521860635.

Mital, S. (2002). Endogenous endothelium-derived nitric oxide inhibits myocardial caspase activity: implications for treatment of end-stage heart failure. *J Heart Lung Transplant,* Vol.21, No.5, (May 2002), pp. 576-585.

Martini, J. (2006). Mechanotransduction and the homeostatic significance of maintaining blood viscosity in hypotension, hypertension and haemorrhage. *J Intern Med*, Vol.259, No.4, (April 2006), pp. 364-72.

McCrindle, BW. (2007). Coronary artery involvement in children with Kawasaki disease: risk factors from analysis of serial normalized measurements *Circulation*, Vol.116, No.2, (July 2007), pp. 174-9.

Meyers, K. (2007). Fetal Development: 10 Stages. Biology 156: Online Lab Seven. 2OO7. 1-6. http://desertfiddlekate.blogspot.com/2007/07/online-lab-seven-fetaldevelopment-10.html

Neri Serneri, GG. (1981). Pathophysiological aspects of platelet aggregation in relation to blood flow rheology in microcirculation. *Ric Clin Lab*, Vol.11, No.1, (1981), pp.39-46.

Nour, S. (2003). Étude préliminaire sur un nouveau dispositif de circulation extra corporelle pédiatrique pulsée. DEA de Sciences Chirurgicales . Université de Paris XI (Octobr 2003).

Newburger, JW. (2004). Diagnosis, treatment, and long-term management of Kawasaki disease: a statement for health professionals from the Committee on Rheumatic Fever, Endocarditis and Kawasaki Disease, Council on Cardiovascular Disease in the Young, American Heart Association. *Circulation,* Vol.110, No.17, (October 2004), pp. 2747-2771.

Nour, S. (2008). DISPOSABLE PULSE PIPE. Patent application, WO 2008/000110, available from:
http://worldwide.espacenet.com/searchResults?bookmarkedResults=true&submitted=true&DB=EPODOC&locale=en_gb&IA=NOUR+SAYED&sf=q&FIRST=1&CY=gb&LG=en&&st=IA&kw=NOUR+SAYED&Submit=SEARCH&=&=&=&=&=

Nour, S. (2008). NEONATE OR INFANT PULSATING WEAR. Patent application, WO 2008/000111 available from:
http://worldwide.espacenet.com/searchResults?bookmarkedResults=true&submitted=true&DB=EPODOC&locale=en_gb&IA=NOUR+SAYED&sf=q&FIRST=1&CY=gb&LG=en&&st=IA&kw=NOUR+SAYED&Submit=SEARCH&=&=&=&=&=

Nour, S. (2008). Shear stress, energy losses and costs: the resolved dilemma of pediatric heart lung machines with a pulastile tube (abstract). The 16th annual meeting of the Asian Society for Cardiovascular & thoracic surgery. Singapore 14-16 March.

Nour, S. (2008). De l'ECG au coeur artificiel (Lecture). Module Instrumentation Biomédicale. Ecole Central de Paris. 10/03/2008.

Nour, S. (2009). Instrumentation pour les secteurs de cardiologie et de chirurgie cardiaque (Lecture). Module Instrumentation Biomédicale. Ecole Central de Paris. 17/02/2009.

Nour, S. (2009). Flow and rate: almost all we need to trigger, restore and maintain the Cardio-endothelial system (video presentation). The 17th annual meeting of the Asian Society for Cardiovascular & thoracic surgery. Taipei, Taiwan 5-8 March.

Nour, S. (2009). The forgotten driving forces in right heart failure: new concept and device. *Asian Cardiovasc Thorac Ann*, Vol.17, No.5, (October 2009), pp. 525-30.

Nour, S. (2009). NOVEL PULSATING MEDICAL DEVICE. Patent application, WO 2009/136035, available from:

http://worldwide.espacenet.com/searchResults?bookmarkedResults=true&submitted=true&DB=EPODOC&locale=en_gb&IA=NOUR+SAYED&sf=q&FIRST=1&CY=gb&LG=en&&st=IA&kw=NOUR+SAYED&Submit=SEARCH&=&=&=&=&=

Nardell, K. (2009). Risk factors of bleeding in pediatric post-cardiotomy patients requiring ECLS. *Perfusion*, Vol.24, No.3, (May 2009), pp. 191-197.

Nour, S. (2010). PULSATILE AND NON-INVASIVE DEVICE FOR CIRCULATORY AND HAEMODYNAMIC ASSISTANCE. WO 2010/070018, available from:
http://worldwide.espacenet.com/searchResults?bookmarkedResults=true&submitted=true&DB=EPODOC&locale=en_gb&IA=NOUR+SAYED&sf=q&FIRST=1&CY=gb&LG=en&&st=IA&kw=NOUR+SAYED&Submit=SEARCH&=&=&=&=&=

Nour, S. (2010). PULSATILE MEDICAL DEVICE DESIGNED TO BE USED IN EXTRACORPOREAL SURGERY. Patent application WO 2010/066899, available from:
http://worldwide.espacenet.com/searchResults?bookmarkedResults=true&submitted=true&DB=EPODOC&locale=en_gb&IA=NOUR+SAYED&sf=q&FIRST=1&CY=gb&LG=en&&st=IA&kw=NOUR+SAYED&Submit=SEARCH&=&=&=&=&=

Nour, S. (2011). SINGLE-USE CARDIOVASCULAR DEVICE FOR MEDICO-SURGICAL OPERATION. Patent application, WO 2011/089162, available from:
http://worldwide.espacenet.com/searchResults?bookmarkedResults=true&submitted=true&DB=EPODOC&locale=en_gb&IA=NOUR+SAYED&sf=q&FIRST=1&CY=gb&LG=en&&st=IA&kw=NOUR+SAYED&Submit=SEARCH&=&=&=&=&=

Nour, S. (2011). EQUIPMENT THAT MAKES IT POSSIBLE TO APPLY A DETERMINED PULSATILE PRESSURE TO A MEDICAL DEVICE. Patent application, US 2011/166515, available from:
http://worldwide.espacenet.com/searchResults?bookmarkedResults=true&submitted=true&DB=EPODOC&locale=en_gb&IA=NOUR+SAYED&sf=q&FIRST=1&CY=gb&LG=en&&st=IA&kw=NOUR+SAYED&Submit=SEARCH&=&=&=&=&=

Nour S (2011). NOVEL MEDICAL PULSATING DEVICE. Patent application, US 2011/021987, available from:
http://worldwide.espacenet.com/searchResults?bookmarkedResults=true&submitted=true&DB=EPODOC&locale=en_gb&IA=NOUR+SAYED&sf=q&FIRST=1&CY=gb&LG=en&&st=IA&kw=NOUR+SAYED&Submit=SEARCH&=&=&=&=&=

Nour, S. (2011). A THERAPEUTIC AND SURGICAL TREATMENT METHOD FOR PROVIDING CARDIOPULMONARY AND CIRCULATORY ASSIST DEVICE. US patent application in pending.

Nour, S. (in press). Forgotten driving forces in right heart failure (Part II): experimental study. Asian Cardiovasc Thorac Ann. DOI: 10.1177/0218492312440567.

Nour, S. (in press). Intrapulmonary Shear Stress Enhancement: a New Therapeutic Approach in Pulmonary Arterial Hypertension. Pediatr Card [PEDC-D-11-00290R1].

Onuzo, OC. (2000). Heterotopic cardiac transplantation and Batista operation. *Ann Thorac Surg*, Vol.70, No.1, (July 2000), pp. 285-287.

Olufsen, MS. (2004). On deriving lumped models for blood flow and pressure in the systemic arteries. *Math Biosci Eng*, Vol.1, No.1, (June 2004), pp. 61-80.

Onorati, F. (2007). A randomized trial of pulsatile perfusion using an intra-aortic ballon pump versus nonpulsatile perfusion on short-term changes in kidney function

during cardiopulmonary bypass during myocardial reperfusion. *Am J Kidney Dis*, Vol.50, No.2, (August 2007), pp. 229-38.

Pelc, LR. (1987). Preferential increase in subendocardial perfusion produced by endothelium dependent vasodilators. *Circulation*, Vol. 76, No. 1, (July 1987), pp. 191–200.

Petrovic, D. (2000). Apoptosis and proliferation of cardiomyocytes in heart failure of different etiologies. *Cardiovasc Pathol,* Vol.9, No.3, (May-June 2000), pp.149-152.

Palmieri, V. (2001). Aortic root dilatation at sinuses of valsalva and aortic regurgitation in hypertensive and normotensive subjects: The Hypertension Genetic Epidemiology Network Study. *Hypertension*, Vol37, No.5, (May 2001), pp.1229-35.

Pereira, NL (2005). Cardiac transplant following failed Fontan or Glenn procedures. J Am Coll Cardiol, Vol.46, No.7, (October 2005), pp. 1374-5; author reply 1375-6.

Park, SJ. (2005). Left ventricular assist devices as destination therapy: a new look at survival. *J Thorac Cardiovasc Surg,* Vol.129, No.1, (January 2005), pp. 9-17.

Pouard, Ph. (2006). Normothermia becomes more practiced during CPB perfusion with less morbidity normothermic cardiopulmonary bypass and myocardial cardioplegic protection for neonatal arterial switch operation. *Eur J Cardiothorac Surg, Vol.30, No.5, (November* 2006), pp. 695-699.

Potapov, EV. (2007). Ventricular assist devices in children: current achievements and future perspectives. *Pediatr Transplant*, Vol.11, No.3, (May 2007), pp. 241-55.

Poelmann, RE. (2008). The development of the heart and microcirculation: role of shear stress. *Med Biol Eng Comput*, Vol.46, No.5, (May 2008), pp. 479-84.

Prutkin, JM. (2008). Percutaneous right ventricular assist device as support for cardiogenic shock due to right ventricular infarction. *J Invasive Cardiol*, Vol.20, No.7, (July 2008), pp. E215-E216.

Prendiville, TW. (2010). Heterotaxy syndrome: defining contemporary disease trends. *Pediatr Cardiol*, Vol.31, No.7, (Oct 2010), pp. 1052-8.

Pagonas, N. (2010). Assessment of the effect of external counterpulsation on myocardial adaptive arteriogenesis by invasive functional measurements--design of the arteriogenesis network trial 2. *Int J Cardiol*, Vol.145, No.3, (December 2010), pp. 432-7.

Rao, PS. (1994). Hypoplastic left heart syndrome. In: Kambam J (ed.). *Cardiac Anesthesia for Infants and Children*. St. Louis, MO: Mosby-Year Book,; 1994:296-309. ISBN0801672899, 9780801672897

Rothenberg, F. (2003). Sculpting the cardiac outflow tract. *Birth Defects Res C Embryo Today*, Vol.69, No.1, (Feb 2003), pp. 38-45.

Roselli, RJ. (2003). Redesigning a biomechanics course using challenge-based instruction. *IEEE Eng Med Biol Mag*, Vol. 22, No. 4, (July-August 2003), pp.66-70.

Robbins, IM (2004). Advancing Therapy for Pulmonary Arterial Hypertension : Can Animal Models Help? *Am J Respir Crit Care Med*, Vol.169, No.1, (January 2004), pp. 169:5-6.

Rastan, AJ. (2008). Moderate vesrsus deep hypothermia for the arterial switch operation: experience with 100 consecutive patients. *Eur. J. Cardiothorac. Surg*, Vol.33, No.4, (April 2008), pp. 619 – 625.

Roussel, JC. (2009). CardioWest (Jarvik) total artificial heart: a single-center experience with 42 patients. *Ann Thorac Surg*, Vol.87, No.1, (January 2009), pp. 124-9.

Stern Lc (1875). Ebers G. ed (in German). *Papyros Ebers: Das hermetische Buch uber die Arzeneimittel der alten Ägypter in hieratischer Schrift, herausgegeben mit Inhaltsangabe und Einleitung versehen von Georg Ebers, mit Hieroglyphisch-Lateinischem Glossar von*

Ludwig Stern, mit Unterstutzung des Königlich Sächsischen Cultusministerium. 2 (1 ed.).Leipzig: W. Englemann. Retrieved 2010-09-18.

Sanfelippo, PM. (1987). Vascular complication associated with the use of intra-aortic ballon pumping. *Texas Heart Inst J*, Vol.14, No.2, (June 1987) pp.187-5.

Sollano, J. (1998). Do we need another cardiac assist device? Assessing the feasibility of a new cardiac compression device for the treatment of cardiogenic shock. Paper presented at: Annu Meet Int Soc Technol Assess Health Care Int Soc Technol Assess Health Care Meet, 1998.

Samet, I. and Lelkes, PI. (1999): "Mechanical Forces and Endothelium"; 2-11; Harwood academic publishers; The Netherlands.

Schmauss, D. (2008). Cardiac allograft vasculopathy: recent developments. *Circulation,* Vol.117, No.16, (April 2008), pp. 2131-2141.

Senzaki, H. (2008). Sedation of hypercyanotic spells in a neonate with tetralogy of Fallot using dexmedetomidine. *J Pediatr (Rio J)*, Vol.84, No.4, (Jul-Aug 2008), pp. 377-80.

Seyfarth, M. (2008). A randomized clinical trial to evaluate the safety and efficacy of a percutaneous left ventricular assist device versus intra-aortic balloon pumping for treatment of cardiogenic shock caused by myocardial infarction. *J Am Coll Cardiol,* Vol.52, No.19, (November 2008), pp. 1584-1588.

Shroyer, AL. (2009). On-pump versus off-pump coronary-artery bypass surgery. *N Engl J Med*, Vol.361, No.19, (November 2009), pp.1827-37.

Samady, H. (2011). Coronary artery wall shear stress is associated with progression and transformation of atherosclerotic plaque and arterial remodeling in patients with coronary artery disease. *Circulation*, Vol.124, No.7, (August 2011), pp. 779-88.

Thom, Th. (2006). Heart Disease and Stroke Statistics—2006 Update: A Report From the American Heart Association Statistics Committee and Stroke Statistics Subcommittee. *Circulation*, Vol.113, No.8, (February 2006), pp. e85 - e151.

Tumkosit, M (2007). Left ventricular spherical remodeling and apical myocardial relaxation: cardiovascular MR imaging measurement of myocardial segments. *Radiology*, Vol.244, No.2, (August 2007), pp. 411-8.

Unger, F. (1988). Artificial heart and cardiac transplantation: report on the first European combined procedure. *Artif Organs.* Vol.12, No.1, (February 1988), pp. 51-55.

Ündar, A. (1999). Effects of perfusion mode on regional and global organ blood flow in a neonatal piglet model. *Ann Thorac Surg*, Vol.68, No.4, (October 1999), pp.1336-43.

Ündar, A. (2001). Comparison of six pediatric bypass pumps during pulsatile and nonpulsatile perfusion. *J Thorac Cardiovasc Surg*, Vol.122, No.4, (October 2001), pp. 827-9.

Undar, A. (2006). Quantification of perfusion modes in terms of surplus hemodynamic energy levels in a simulated pediatric CPB model. *ASAIO J*, Vol.52, No.6, (November-December 2006), pp. 712-7.

Undar, A. (2007). Pulsatile Perfusion During Cardiopulmonary Bypass Procedures in Neonates, Infants, and Small Children. *ASAIO J*, Vol.53, No.6, (November-December 2007), pp. 706 –709.

Vroom, MB. 1996). Myocardial stunning, hibernation, and ischemic preconditioning. *J Cardiothorac Vasc Anesth,* Vol.10, No.6, (October 1996), pp. 789-799.

Vincent, JL. (2008). Defining sepsis. *Clin Chest Med*, Vol.29, No.4 (Dec 2008), pp. 585-90.

Voss, B. (2010). Cardiopulmonary bypass with physiological flow and pressure curves: pulse is unnecessary!. *Eur J Cardiothorac Surg,* Vol.37, No.1, (January 2010), pp. 223—232.

Wilmot, I. (2011). Effectiveness of mechanical circulatory support in children with acute fulminant and persistent myocarditis. *J Card Fail*, Vol.17, No.6, (June 2011) pp. 487-94.

Walsh, JH. (2003). Exercise training improves conduit vessel function in patients with coronary artery disease. *J Appl Physiol,* Vol.95, No.1, (July 2003), pp. 20-25.

Wu, KH. (2006). Cellular therapy and myocardial tissue engineering: the role of adult stem and progenitor cells. *Eur J Cardiothorac Surg.* Vol.30, No.5, (November 2006), pp. 770-781.

Yacoub, MH. (1995). Two hearts that beat as one. *Circulation*, Vol.92, No.2, (Jul 1995), pp.156-7

Yeager, SB. (2002) Prenatal role of the ductus arteriosus in absent pulmonary valve syndrome. *Echocardiography*, Vol. 19, No.6, (Aug 2002), pp.489-93.

Zickmund, SL. (2006). Congestive heart failure patients report conflict with their physicians. *J Card Fail*. Vol.12, No.7, (September 2006), pp. 546-53.

Zhang, Y. (2007). Enhanced external counterpulsation inhibits intimal hyperplasia by modifying shear stress responsive gene expression in hypercholesterolemic pigs. *Circulation,* Vol.116, No.5, (July 2007), pp. 526-534.

3

Microtools for Microsurgery of a Single Cell in Field of Cellular Engineering

Vladimir A. Nikitin
Institute of Cell Biophysics Russian Academy of Sciences,
Institutskaya 3, Pushchino, Moscow Region,
Russia

1. Introduction

Almost all main problems of natural science lead to necessity of studying the processes occurring in single cell. At present intensive work is going on in order to improve the technology of reconstruction of cells, and after that of the whole organism. At the level of an individual cell it is possible to change its biochemical processes, its physiology and morphology, its genetic status. Microsurgery of a single cell, replacing its elements, the introduction of foreign genetic material makes this area of medicine, agriculture, basic and experimental biology especially relevant. Appearance in the hands of microsurgeon of a single cell of the new microtools that have the ability of active interference in functioning of the cell without causing a significant damage to it have changed the experimental biology. The cellular engineering solves a wide range of problems, extensively using microsurgical methods and approaches, which include microinjection into the cell and its organelles - for nuclear transfer and transfer of the individual chromosomes, transgenesis, dividing of early preimplantation embryos for twinning, etc.

2. Microtools

Microtools for microsurgery of single cells are microscopic things comparable in their dimensions with a cell or its organelles; microtools are made with a microforge on the tip of a round forged out glass micropipette or of a glass blank of some other profiles (Fig. 2). The figure shows a diagram of the micropipette, which can serve as a blank (foundation) for many microtools.

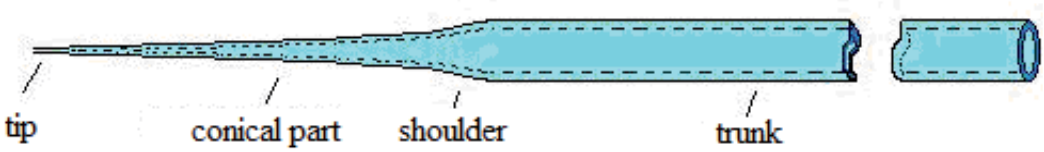

Fig. 1. Scheme of a micropipette – a blank for manufacture of many microtools

Round capillary, from which microtools are manufactured, can be presented in form of a blank of various profiles. Drawn tip of a capillary or other profile is, in fact, a blank for microtools manufacture.

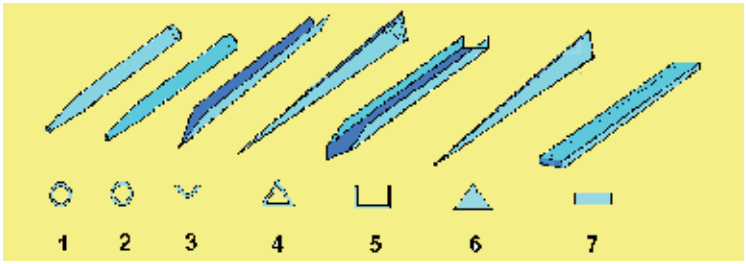

Fig. 2. Types of glass profiles for microtools manufacture

Using specialized microtools has many advantages. For example, a triangular profile of a micropipette allows to produce micropipettes, which do not leave long-lived perforations on a cell; two-channel pipettes enable to transplant organelles and to enucleate cells with single puncture, etc.

Further microtools will be shown according to the chart:

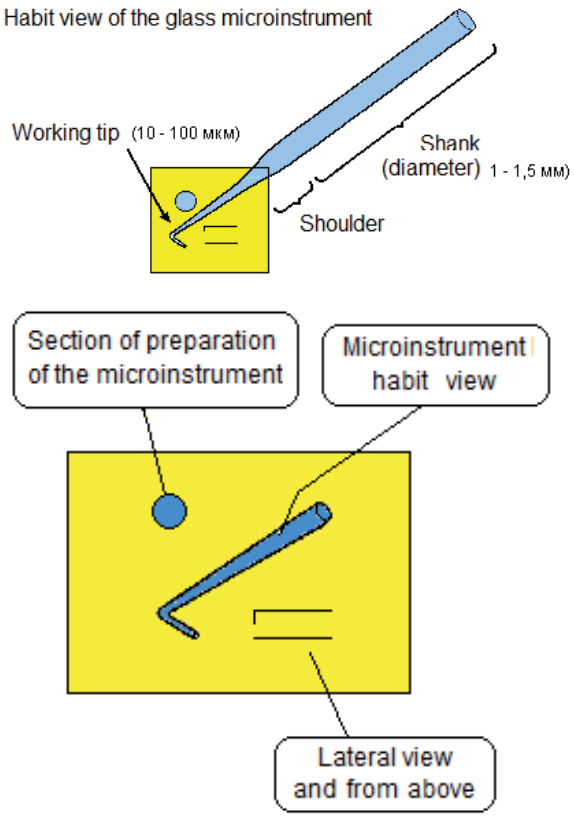

Fig. 3. Scheme of a microtool tip

Microtools for micromanipulation on cells can be distributed into several groups according to their functions: fixing and keeping; actually operating; auxiliary and special purpose microtools. Such a distribution is convenient from a practical point of view, since it allows making the right choice from a variety of microtools. This greatly reduces time of an operation and enables to make it with minimal damage to cells. For example, a seemingly simple task of cells fixing appears not a simple problem. For protoplasts, spheroplasts or individual organelles in cases when they should not be exposed to negative pressure, inevitable at aspiration or at microsucker fixation, microtools like microspatula-holder or capsule-holder are recommended (Fig. 4).

Use of such tools allows to fix an object without negative pressure, merely by a shape of tool itself.

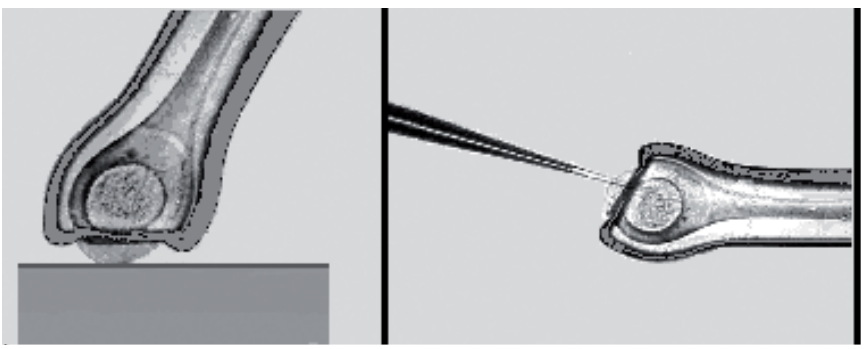

Fig. 4. Capsule-holder

Microtools must be separated by the nature of their use in active and passive. By active, we usually mean those able to damage a cell to a greater or lesser degree (operating and some special purpose instruments, such as microexpander, microprobe, microloop, etc.). Passive microtools usually only contact cells and have little possibility to damage it (fixing and auxiliary tools, such as microhook, capsule-holder, spatula-holder, etc.).

3. Microtools for single cell microsurgery

3.1 Microneedles, microhooks, microloops

Microneedle is an oldest microtool that emerged from the practical work with cells. The most important mission of microneedles was first manipulations with cells. However, using it one could perform various simple and complex operations: cell cutting; its destruction; perforation of a cell wall or membrane. Nowadays role of microneedles in microsurgery became much more important because of development of technology for production of monozygotic genetically identical twins of laboratory and farm animals. Microneedles are actively used for preparation of a given size incisions in zona pellucida of early mammalian embryos during retrieval of blastomeres from them and for preservation of integrity of transparent envelope for its further use.

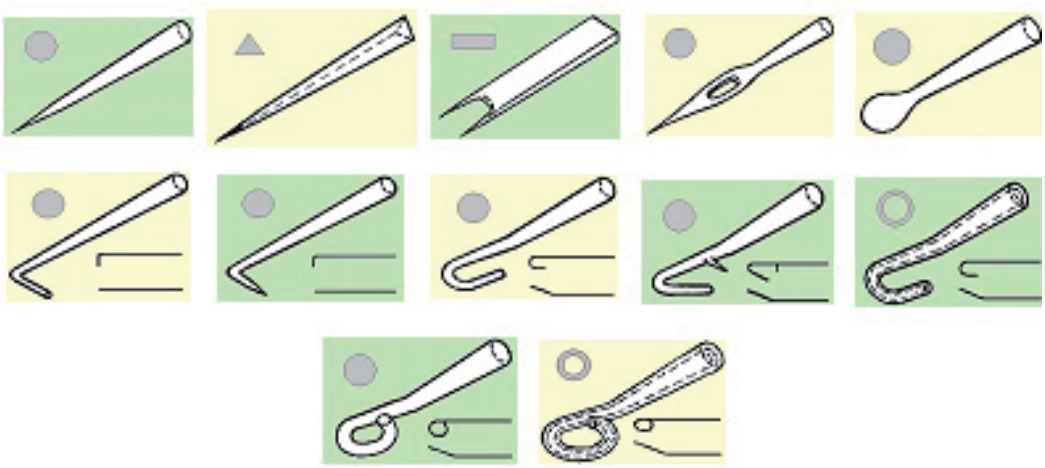

Fig. 5. Microneedles, microhooks, microloops

According to our findings, change of section profile of microneedles, for example, for triangular one, can greatly expand field of its activity at atraumatical separation of blastomeres and their further separation. In addition, perforations made with triangular microneedle (the same as with a micropipette) are repaired much faster than those made with rounded microtools.

Using of flat section profiles allows making special forks for retention of large cells, tissues, capillaries.

Microneedles with a hole enable to apply microligatures relatively easy on small capillaries, spermatic cord, etc., surrounded by tissues. These are made from carefully soldered microloop on microforge it until piercing tip is formed. A hole shape and size depend on ratio of internal to external holes of a microloop and its dimension in whole.

Microspheres at the end of microneedles are made on microforge at very high temperature of the filament and used to keep cells and manipulate with them and to hold tissues or organs; use of them minimizes mechanical damages.

Different types of microhooks are used primarily to hold cells; to isolate them from cell mass; to isolate individual cells from tissue. Hollow semicircular microhook, holding cells, allows to change solutions.

3.2 Microtools: Microloop with variable diameter

Application of microligaturing method for small size early embryos of mice, for instance, appeared far simple. The method was firstly used by Spemann on embryos of Triton with a newborn baby hair. We improved this method and made it much easier, having designed a special micromanipulator for microligaturing. Even simpler became a method of microligaturing with variable diameter microloops, at that we used Nylon thread with of 5-7 microns diameter as a loop. With the help of such microloopscan one can not only separate blastomeres, but can cut early embryo into two halves as well. These loops may be used

repeatedly. For this purpose it is necessary to insert a Nylon thread into a loop before the beginning of the work: this thread will repeatedly return a loop into its start position.

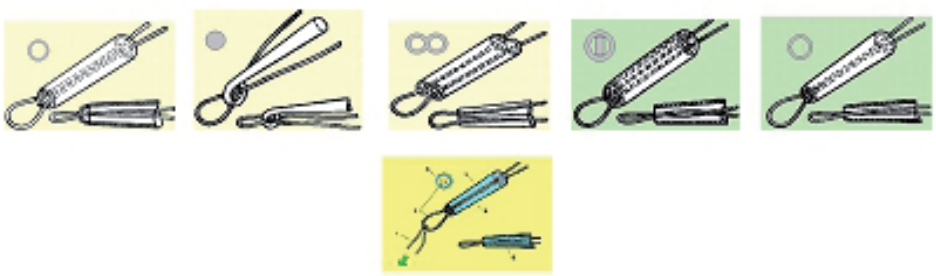

Fig. 6. Micro-loops with variable diameter

To reuse a microloop, a thread was inserted into them, as shown for a microloop; free ends of the thread enabled returning of the loop at its start position. We used some of microtools designed for single cell microsurgery/: microneedle and microspatula of profile glass and a special polyvinyl microsucker for unilateral removal of a tadpole eyes with the so-called "waist" method (the same as production of monozygotic twins "halves" from blactocyst) in series of morphogenesis studies on amphibian Mauthner cells; it showed possibility of using these tools for microoperations at organ level as well. This technology has dramatically increased the viability of the tadpoles.

3.3 Microsupports for cells holding

When working with isolated, single cells it may be necessary to fix them for the microsurgical operations. Capsule-holder (Figure) allowed holding a cell without application of negative pressure (suction), which made it possible to practically avoid damage to the cell at its fixation.

Fig. 7. Clamping stops of different profiles

Cells holding during operation is always an important issue and can somehow affect a result of the operation and integrity of operated cells.

First, you need to avoid excessive deformation of cells during holding. If you do not use microsuckers aspirating cell contents and serving as "hidden factor" of cell damage, you can use end and clamping stops as shown in the figure. The stops must be bent in a way allowing it only to contact a cell but not deform it in general. End stop is used for holding cell near a Petri dish wall or some piece of objective or cover glass. Profile of such a stop can be round or rectangular. These stops are convenient for holding large cells like amphibian or fish eggs.

Profile microhook and profile microloop can be good stops when it is necessary to use a cover glass or microspatula. It is practically impossible to damage a cell placed under such microtools.

These unique microtools allow to place a cover glass on them and hold the cell during microscopy. In addition, profile microloop allows to work in a flow microchamber.

3.4 Microspatulas for cells

Microtools - microspatulas have various profiles and serve for pressing, dissection, separation and holding cells in microchamber. They are necessary for work with tissues or with cells clusters. Microspatulas are applied to press cells to the bottom of a microchamber and to hold it. In addition microspatula-hemisphere is used to crush cells, scraping and cell preparation. They have various configurations and help to solve specific problems of cells fixing at special experimental situations. Various spatulas that can successfully hold and manipulate single cells are presented further.

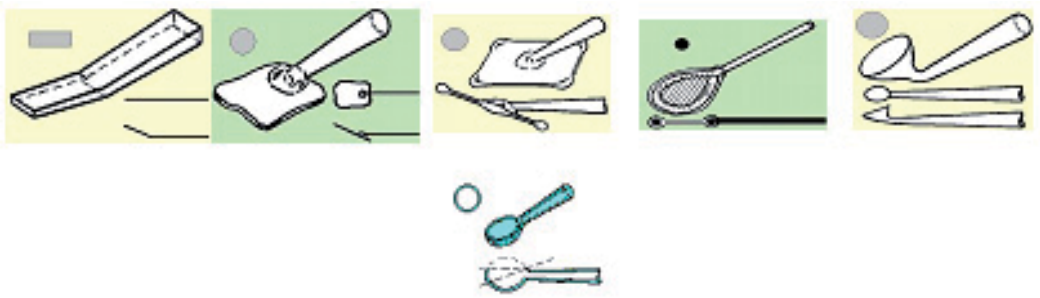

Fig. 8. Microspatulas of different profiles

Cell microsurgery often meets situations when a cell must be held with a microtool to immobilize it, or, conversely, move it along the surface of a microchamber object-slide, or, finally, to reduce its thickness uniformly, thus facilitating detailed study of its internal structure. For this purpose, flat or convex or concave micropress-spatulas may be useful.

The Figure 8 shows the spatulas scheme (left to right):

Microspatula from fragments of plane cover glass for pressing cells to the bottom of the microchamber, holding of one or several cells.

Profile microspatula for preparation, pressing, separation and holding of cells in microchamber.

Microspatula from fragments of plane cover glass with stops.

Microspatula from glass melted in platinum microloop.

Microspatula-semisphere to separate cells, scrapings, preparation of cells and tissues, pressure of cells or tissue to the bottom of a microchamber.

Microspatula-holder for holding cells, fixing it during microsurgery, quick change of solution around the cell (part of the sphere is polished). The universality of this

microspatula-holder is obvious, since the cell can be transferred and held without use of negative pressure, making a variety of saw cut (abrasion), and fixing it additionally with negative pressure, sticking a cell rigidly to a holder. There are some operations that do need such a fixation.

3.5 Microspatulas-microscrapers for cell culture and flattened cells

Single cells can be isolated from the culture by scraping them from a substrate on which they are cultivated. This eliminates the effect of lytic enzymes or substances weakening cell adhesion to the substrate. Scraping cells with sharpened microtools can damage cells themselves. A cell must be not cut but very carefully "peel off" from substrate, and only after that it becomes "spall", isolated and may be used for work.

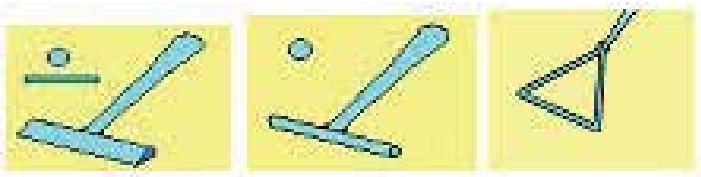

Fig. 9. Microscrapers of different profiles (left to right): Triangular profile microscraper; Round profile microscraper; Microscraper of platinum wire

3.6 Microscalpels

Microscalpels are the most common and frequently used microtool for division of early embryos; for removal of zona pellucida; for dissection of the chromosomes, etc. Microtools end are made from profiled glass blanks. This somewhat extends and simplifies manufacturing of microscalpel with simple cleavage or sharpening with an abrasive disk.

Since a cell reconstruction is in one way or another related with microsurgical operations of varying degrees of complexity, we have paid great attention to various kinds of scalpels.

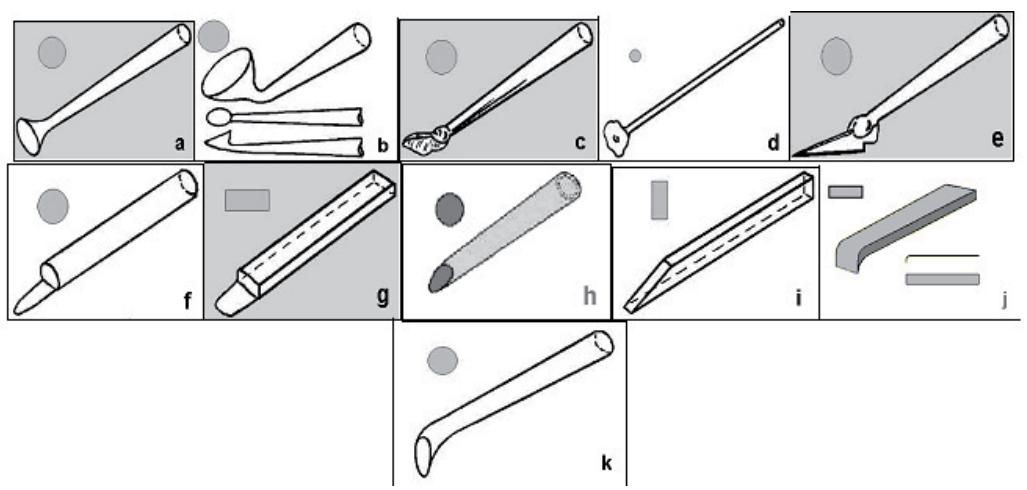

Fig. 10. Microscalpels of different kinds

Later on, we began to use them for microsurgical operations less frequently as cutting tools cause the most severe damages. Sometimes, however, these tools cannot be avoided, for example, at work with plant cells and various tissues.

A scalpel is the most common tool in surgery. However, in the case of a single cell it should be reasonably applied only in exceptional circumstances. A scalpel is a cutting tool and it can severely damage integrity of cells during operation. Nevertheless, a scalpel is indispensable at preparative manipulation with a study object or at preparation for surgery.

Let us review various types of microscalpels for work with single cells and cell tissues.

a. Circular microscalpel for cutting cells of early embryos or tissues. This microscalpel is made with a microforge, producing a separation of the weld microbead technology, perfectly described in the monograph.
b. Microscalpel-hemisphere for cell cutting, scrapings, cell preparation and tissue surgery. By making technique this knife is similar to the previous one with the only difference being that position of a hemisphere can be changed by bending of microforge neck at any angle. To use such a scalpel is much more convenient because you can cut with a top section or with lateral parts of the hemisphere.
c. Microscalpel from a crystal to cut cells or tissues of early embryos (crystal is glued). Reliable and easy microscalpel can be made by using of finest pieces of artificial crystals of ruby, sapphire or quartz. Only water-resistant glue should be used for this purpose.
d. Circular microscalpel for cutting cells or tissues (at a platinum wire). If a thin platinum wire is inserted into molten bead, and then torn on cooling of glass, you can get round microscalpel. It requires besides a scalpel holder in form of a glass capillary in which a platinum wire is welded to install it on a micromanipulator. It should be noted that according to, Shouten showed excellent qualities of this instrument, cutting with it such small objects, as bacteria, into three or four parts.
e. Microscalpel preparative to cut a cell or tissue (from a piece of the blade). Preparation works with biological samples are easy to carry with a simple knife blade made of pieces of blade glued with water resistant glue to a holder.
f. End microscalpel to cut cells or tissues. Tempered glass (glass after heating and cooling) with a transverse fracture sometimes gives a sharp cutting edge, which can act as an end microscalpel.
g. End microscalpel from profile blank to cut cells or tissues. Glass, depending on their composition on the Mohs scale, can be scaled 5 to 7 (diamond is 10). The hardest are quartz glass and "Pyrex" type glass. Profile blanks from such glasses can be used for the manufacture of end microscalpel by cleavage.
h. End microscalpel (micro-engraver, oval) from a large rod for cutting cells or tissues (sharpened and polished).
i. End microscalpel profile (narrow) to cut cells or tissues (sharpened and polished).
j. Microscalpel bent from profile blank (with given different sharpening angles) to cut a cell or tissue (can be sharpened at a different angle, as shown below).
k. Microscalpel bent from profile blank (can be sharpened at a different angle, as shown below).

The last microscalpel in this table (bottom right) is offered by Fonbrun. We have found a way to make cutting edges of it with different bevel angles (Fig.11).

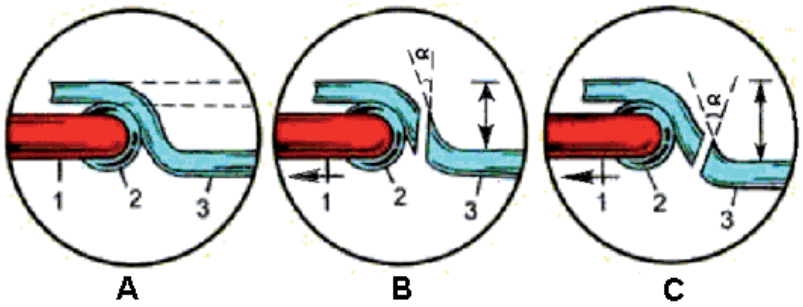

Fig. 11. Technology of manufacture of microscalpels with different angles of grinding with the help of microforge 1 - microforge filament, 2 - a drop of molten glass, 3 - a tip of drawn glass rod,α - angle of grinding. Position B and C - /cooling of the filament

3.7 Micropipettes

The micropipetes proposed in the paper and used in experiments, have different construction. These are:pipettes with inserts and triangular ones, that are used for microinjection to puncture a cell; a micropipette with a limiter allowed to microinject into tissue at a certain depth, for example, at embryo transplantation into horn of an animal uterus. Using microsurgical pipette we performed nuclear transfer in mice. It is four-sided, sharpened by special technology, with the aid of an original device for microtools sharpening, and has the shape of a pupil pen. Many micropipettes were used for the selection of eggs and other isolated cells and organelles, including nuclear transfer. Various profile inserts, limiting cell advance into a micropipette pot, were made inside the micropipettes.

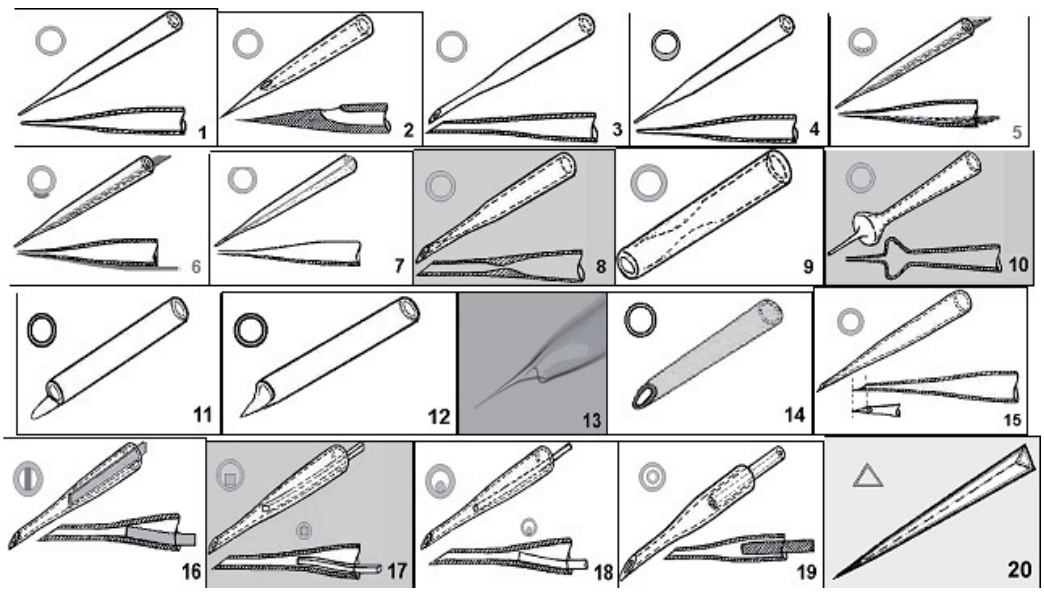

Fig. 12. Micropipettes of different kinds

The most part of microsurgical operations and all kinds of micromanipulation are made with the help of a well - known micropipette.

1. Micropipette for microinjections of solutions and organelles into cells, microelectrophoresis, may be used as microelectrode.
2. Micropipette-needle for perfusion, isolation of organelles from cell
3. Micropipette with a bevel for nuclear and other organelles transfer
4. Micropipette with non-co-axial profile for microinjections of solutions into cell, microelectrodes, microelectrophoresis, iontophoresis
5. Micropipette with inserts (filaments)
6. Micropipette with an external insert
7. Micropipette with abrasion
8. Micropipette with a "waist" (sharpened)
9. Micropipette with a "waist" (melted) and slightly melted tip
10. Micropipette with a limiter for microinjections into the tissue and vessels
11. Micropipette with a cutting edge
12. Micropipette with a piercing tip
13. Micropipette with a polished tip
14. Microsurgical micropipette (four-sided sharpened) for nuclear transfer and intracellular organelles
15. Micropipette with a flat rectangular insert – stop
16. Micropipette with an inner profile
17. Micropipette with an inner square stop
18. Micropipette with an inner circular stop
19. Micropipette with a calibrated capillary – stop
20. Micropipette profile (triangular) for injection, organelle transplantation, cutting, preparation of cells or tissues

3.8 Microtweezers

Rarely used for work with the single cell microtweezers are presented to give an idea that they are easy in manufacturing but hard in use, as they require special micromanipulators or various devices with micrometer displacement of tweezers tips.

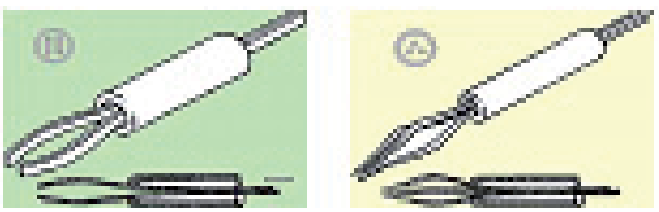

Fig. 13. Microtweezers

3.9 Microsyringes

Microsyringes are widely used in cell microsurgery, even a microinjector by itself is a complex Microsyringe, consisting of microneedles, conductive wire for compressed air or hydraulics, and pressure source.

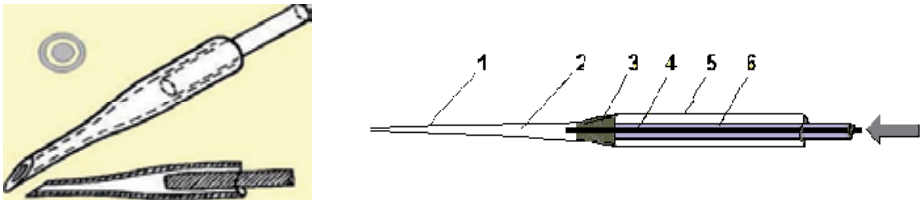

Fig. 14. Micropipette with a plunger inserted into its cavity. 1 - tip of the micropipette, 2 - injectable solution, 3 - seal (silicone tube), 4 - metal plunger, 5 – micropipette body, 6 - capillary sealing silicone tube and plunger guide.

The figures show two nearly identical microsyringes with the only difference being that the first

Movement of a plunger in an injectable solution enables to make multi-dose injections or, vice versa, to produce suction micropipette and then a micropipette itself serves for transfer of organelles.

3.10 Profile microtools

For solving various problems in the field of microsurgery of single cell, depending on the complexity of operations, one should always seek to expand microtools species. Round capillaries and glass solid rods practically exhausted their potential. Therefore, a further step can be choice of different types of profile available for making them both as over the burner flame and at special pull devices as well.

Different profile of a blank allows to produce cutters of different shapes. Their distinctive difference from other penetrating microtools is that perforations on a cell are closed immediately after microtools leaves a cell.

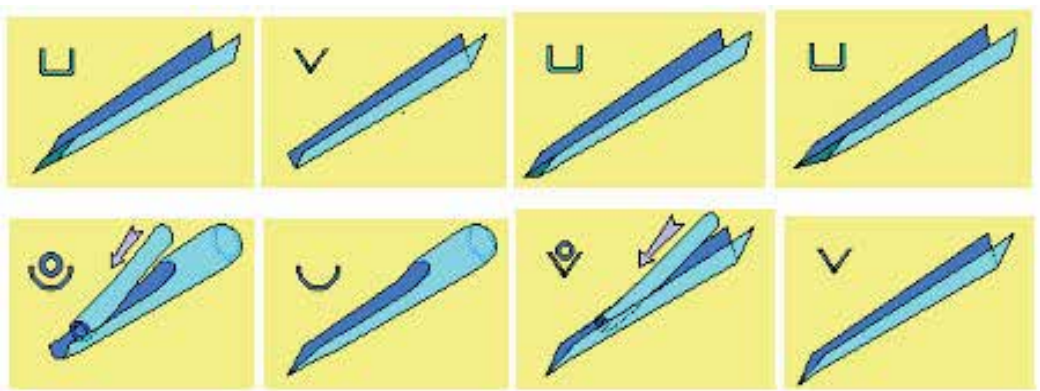

Fig. 15. Microcutters of different configurations

4. Microtools from paired capillaries

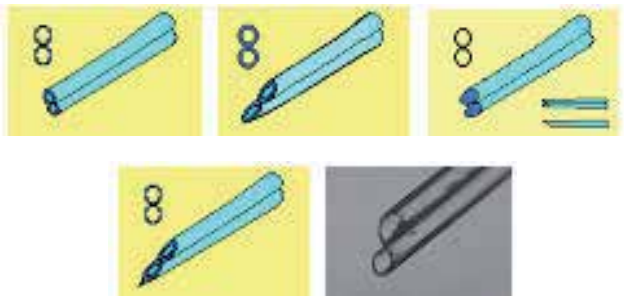

Fig. 16. Paired microcapillaries

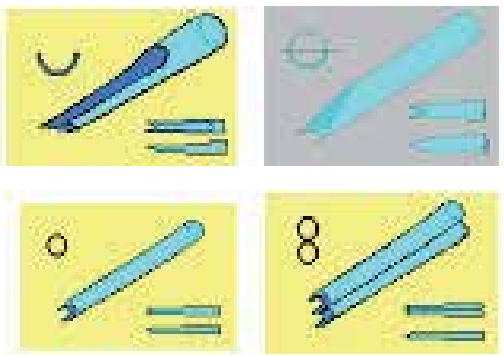

Fig. 17. Microtools for work with chromosomes and tissue microcapillaries

5. Microprobes

The demonstrated flexible microprobes are universal. Microaspirator-irrigator, made from polyethylene tubing (high pressure) over a spirit lamp flame or on a microforge, was used for washing of eggs out from oviducts or uterine horns of animals. They were also used for washing of organs cavities, for perfusion, for change of solutions in the flow microchamber. Microprobes with side and end holes were used for transplantation of eggs into uterine horns of laboratory animals.

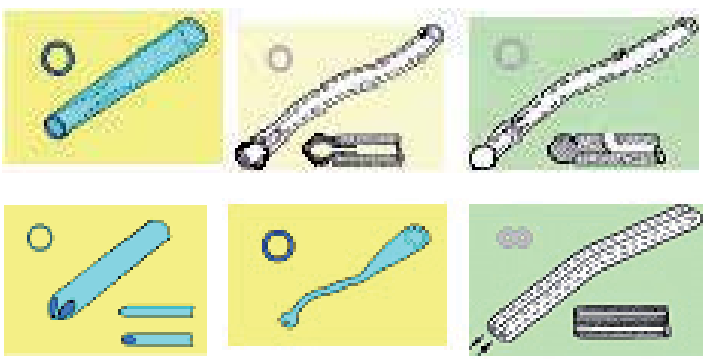

Fig. 18. Microprobes of different material and different configuration

6. Microsuckers and holders

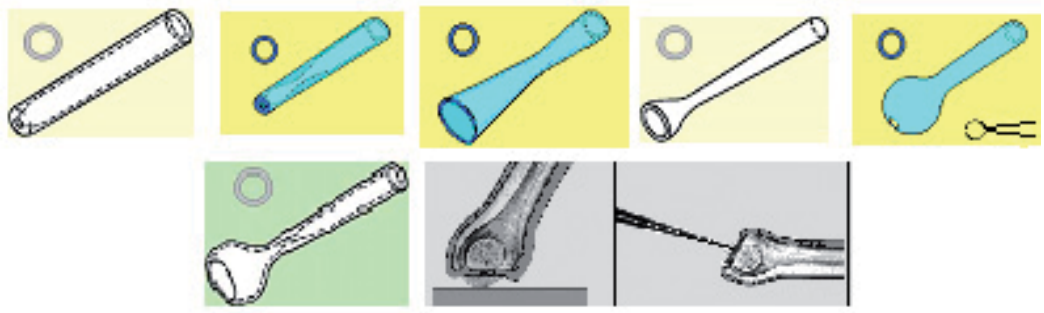

Fig. 19. Microsuckers and Holders

7. References

[1] Spemann H (1938) Embryonic Development and Induction. Yale University Press: New Haven, Connecticut.

[2] Schouten SL (1931) Die Nadeln des Mikromanipulator. Acta brevia neerl. de phys. pharm. microb. E. A., 1, 2, 1, 3.

[3] De Fonbrune P (1949) Technique de micromanipulation. Masson et C. Editeurs, Paris: 203 p.

[4] Chaĭlakhian LM, Veprintsev BN, Sviridova TA, Nikitin VA (1987) Electrostimulated Cell Fusion in Cell Engineering. Biofizika. 32(5): 874-887.

[5] Bezgina EN, Moshkov DA, Nikitin VA, Savel'eva LN, Uteshev VK (1999) Morphogenesis of Mauthner neurons of Xenopus laevis Tadpoles Following Early Unilateral Eye Enucleation. Morfologiia. 115 (3): 49-52.

[6] Bezgina EN, Moshkov DA, Nikitin VA, Savel'eva LN, Uteshev VK (2000). The Morphogenesis of Mauthner neurons in Tadpoles of the Common Frog after Early Unilateral Enucleation of the Eye, Neurosci. behav. physiol. 30(5): 521-524.

[7] Bezgina EN, Moshkov DA, Savel'eva LN, Nikitin VA, Uteshev VK, Ledneva VN (2000) The Reaction of Endoplasmic Reticulum of Mauthner Cells of Xenopus laevis Tadpoles in Response to the Partial Denervation. Tsitologiia. 42 (5): 508-515.

[8] [8] Nikitin VA, Fesenko EE (2006). Biophysical Aspects of Reconstruction of a Single Cell by the Methods of Cell Engineering. Biofizika. 51(4): 673-678.

[9] Grishin AF, Ivanov EG, Nikitin VA, Popov YuA, Khokhlov AM, Tsalkovich AE. Method for Grinding Glass Micropipettes and Device for its Realization. Author certificate № 1315248.

[10] Nikitin VA, Chochlov AM, Larin VT, Fichte BA Verfahren zur Durchfuhrung von Mikrooperationen an Zellen und Einrichtung zu dessen Verwirklichung Patentschrift DE 3390499 C2.

[11] Nikitin VA, Khokhlov AM, Larin VT, Fikhte BA Proc'ed'e d'intervention microchirurgicale sur les cellules et dispositif pour sa mise en oeuvre N de publication: 2 553 432.

[12] Bondarev VA, Ivanov UG, Nikitin VA, Popov UA, Chochlov AM, Tsalkovitch AE, Gazar'yan KG (pioneer invention) The Way of Embryo Bisection and the Device for Realization of this Technology, Author certificate № 1327333.
[13] Nikitin VA (2010) Mystery and Problems of cloning. Biofizika. 55(3): 434-444.

4

An Interfacial Thermodynamics Model for Protein Stability

Donald J. Jacobs
University of North Carolina at Charlotte
USA

1. Introduction

Proteins are important macromolecules that exhibit thermodynamic and kinetic properties that are highly tuned to facilitate biological function within limited ranges of environmental conditions. Despite having a wealth of understanding of the interactions that affect protein stability [Dill, 1990; Pace, et al. 2004], such as the hydrophobic effect, hydrogen bonding, packing, solvation and electrostatic effects: Predicting thermodynamic properties of proteins is difficult because these interactions simultaneously work together within the molecular structure comprising of heterogeneous microenvironments that change dynamically as the conformational state of the protein changes. Consequently, a protein is truly a *complex system* [Bar-Yam, 1997] where thermodynamic and other emergent physical properties are sensitive to small perturbations in protein structure or its environment. It remains an open problem to develop models that can accurately predict protein stability, ligand-protein binding affinities and allosteric response, all of which are critical to the function of a protein [Petsko & Ringe, 2004; Klepeis, et al. 2004; Bray & Duke, 2004].

1.1 Available computational approaches

A rigorous brute force method that can in principle computationally predict thermodynamic properties of proteins is through all-atom molecular dynamics (MD) simulation in explicit solvent [Lindorff-Larsen, et al. 2009]. In this approach, the equations of motions for all atoms must be integrated over femtosecond time-steps out to timescales extending to hours or more. Then the emergent properties governing how a protein functions must be extracted from the massive amount of atomic coordinates contained in the MD trajectory. Invoking the ergodic hypothesis to determine thermodynamic averages of physical quantities by time averaging over many such long trajectories makes this approach painstakingly slow, especially when one would like to scan over large numbers of possible what-if scenarios for the purpose of finding conditions that yield a desired "engineered" response, such as identifying specific mutations, ligands or solvent composition. Unfortunately, it is not yet possible to reduce statistical errors by employing MD simulations to a point where they are negligible, especially in the context of high-throughput applications.

Despite practical limitations in sampling, MD has proven indispensible for gaining insight into protein function over limited timescales [Gunsteren, et al. 2006]. Furthermore, a coarse-

grained MD approach with implicit solvent is faster, and multiscale modelling can be fast while achieving good accuracy [Nielsen, et al. 2010]. While multiscale MD is promising, substantial computer resources are required that preclude high-throughput applications, including studies that systematically vary temperature, pressure, pH, and concentration of co-solvents. Therefore, it is not yet feasible in engineering design applications to calculate free energy and other thermodynamic properties of proteins from MD simulations.

There are alternative approaches that represent the fold of a protein in terms of an Ising-like model involving discrete "spin" variables assigned to residues [Hilser & Freire, 1996; Muñoz 2001; Bakk & Hoye 2002; Zamparo & Pelizzola, 2006]. By discretizing macrostates, conformational ensembles that include native, unfolded and partially unfolded states can be generated efficiently [Jacobs, 2010]. Moreover, calculating thermodynamic properties is feasible as a result of the approximations used to reduce *degrees of freedom* (DOF). One such critical approximation common to Ising-like models is that the three-dimensional native structure is used as a *template*. Spin variables decorate the template to partition the protein at the residue level into native-like (spin up) and disordered (spin down) regions. For N residues, the 2^N possible spin configurations retain only topological significance because geometrical information beyond the native state structure is not considered. The models are simple enough that for practical purposes exact thermodynamic properties (of the model) can be calculated. However, because non-native interactions are not accessible, the ensemble of conformational states generated (expressed by microscopic "spin" configurations) is not complete physically. Consequently, Ising-like model predictions can be made *rapidly*, they are *precise*, but *accuracy* becomes questionable because the models tend to be oversimplified.

1.2 Identifying a fundamental problem

Most Ising-like models that describe protein stability are based on the concept of *free energy decomposition* (FED), where the free energy of a system is partitioned into parts by assigning enthalpy and entropy contributions to subsystems. Assuming transferability, a ledger is created to account for the gain or loss of enthalpy and entropy relative to a reference state. The naïve method is to sum over all enthalpy and entropy contributions to arrive at the total free energy of the protein in a specific macrostate. This approach is extremely fast, and it is accurate when all subsystems are essentially independent of one another. Unfortunately, errors occur when DOF within subsystems couple. Since cooperative behaviour is typically found in proteins, the assumption of additivity generally fails [Mark & van Gunsteren, 1994; Dill, 1997], causing inaccurate predictions and/or model parameters to be non-transferable.

The application of FED and assumption of additivity is commonly employed to interpret single site mutations and ligand binding affinities. One reason why it is not obvious that the assumption of additivity is flawed is because non-transferability of model parameters also derives from a lack of completeness in modelling interactions, and, Ising-like models are notoriously incomplete. Nevertheless, the fundamental problem is in treating subsystems as independent, which is tantamount to assuming all internal DOF are independent, and this leads to a dramatic overestimate of conformational entropy in the native-state relative to the unfolded state. Fortunately, this problem can be largely overcome by keeping track of the correlations between DOF using concepts of *network-rigidity* (also called *graph-rigidity*).

1.3 The distance constraint model

The challenge of accurately predicting protein stability lies in developing a model that can account for all essential types of interactions while demanding the model is computationally tractable for high-throughput applications. Toward this goal, I describe a *Distance Constraint Model* (DCM) that is an Ising-like model that employs a FED, but the assumption of additivity is not used. The total free energy is calculated through the process of *Free Energy Reconstitution* (FER) to account for coupling of DOF between subsystems. The critical component of the FER is to employ network-rigidity as a long-range mechanical interaction to govern the non-additive nature of conformational entropy.

The DCM has been employed in various forms (differences in model details and methods to solve the DCM) to describe the helix-coil transition [Jacobs, et al. 2003; Jacobs & Wood, 2004; Lee, et al. 2004; Vorov, et al. 2009; Wood, et al. 2011], the hairpin-coil transition [Jacobs & Fairchild, 2007a] and protein stability [Livesay, et al. 2004; Jacobs & Dallakayan, 2005; Jacobs, et al. 2006a; Vorov, et al. 2011]. Moreover, the DCM predicts substructures within a protein that are rigid or flexible, and identifies sets of atoms that are co-rigid or co-flexible within a correlated motion. Many studies on proteins using a *minimal* DCM (mDCM) have elucidated stability/flexibility relationships important to function [Livesay & Jacobs, 2006; Livesay, et al. 2008; Mottonen, et al. 2009; Verma, et al. 2010] including the study of allostery [Mottonen, et al. 2010]. The DCM provides a good estimate for conformational entropy in simple loop systems compared to exact calculations [Vorov, et al. 2008]. This body of work has been reviewed previously [Jacobs, 2006b; Jacobs, et al. 2012]. The success of the DCM across disparate systems indicates that it is well suited for high-throughput applications that include macromolecular design, large-scale comparative analysis and drug discovery.

1.3.1 Advantages of the DCM and its limitations

The DCM offers several advantages over other models for protein stability, listed in order of importance: 1) Network-rigidity is employed to account for the coupling of DOF between subsystems for better estimates of conformational entropy, thereby restoring the utility of a FED. 2) Structural characteristics are linked to thermodynamic properties by associating mechanical constraints to enthalpy-entropy compensation mechanisms. 3) Molecular structure is represented at the all-atom level. 4) The DCM is not restricted to use template structures, although use of templates allows rapid calculation of the partition function. 5) Relationships between flexibility and stability are quantified, which gives insight into the mechanisms of protein function [Luque, et al. 2002]. 6) The DCM can be solved efficiently in multiple ways. 7) The DCM is a general approach that is not restricted to proteins.

Limitations of the DCM include: 1) Calculation of conformational entropy is *approximate*. Errors are introduced when the geometrical problem is simplified to a topological one (explained below), and because loop corrections are neglected. 2) Long-range electrostatic interactions are not considered. To acknowledge these limitations, the DCM is formulated as an empirical spin-model. 3) Moreover, in the mDCM, mean-field approximations are used to replace many essential enthalpy-entropy compensation mechanisms that are not explicitly modelled, especially in regards to solvation effects. Thus, effective parameters are required to compensate for mDCM inadequacies, suggesting that non-transferability in parameters observed across diverse proteins largely derives from discretionary oversimplifications.

1.3.2 Generalization of the DCM

Despite several studies indicating the mDCM is useful for predicting flexibility and stability of proteins, the merits and limitations of the DCM paradigm remain to be assessed. Many limitations can be substantially reduced by generalizing the form of the DCM to provide a more accurate estimate for conformational entropy without much more computational cost. With the goal of establishing an accurate high-throughput empirical approach, adding terms to model solvation effects offers the least amount of effort for the greatest improvement in accuracy, parameter transferability and retaining rapid calculations. Here, I will redevelop the DCM in the context of interfacial thermodynamics, which has not been done before.

The DCM has four key elements each of which will be discussed separately. First, network-rigidity is explicitly considered as a long-range mechanical interaction to account for the non-additive property of conformational entropy. Second, the FED provides a complete set of elementary subsystems and interaction types that are uniquely identified based on the three dimensional structure of the protein and its macrostate. Third, order parameters are used to define the macrostate of a protein that include the composition of protein-solvent interactions and the number of native-like intramolecular interactions. Forth, applying the FER to each macrostate allows the *free energy landscape* (FEL) to be calculated.

2. Linking network-rigidity to conformational entropy

As the amplitude of motion of a flexible molecular structure increases, the conformational entropy will increase accordingly. By ascribing an entropic measure to distance constraints, the DCM posits a quantitative link between network-rigidity and conformational entropy [Jacobs, et al. 2003]. This link requires assigning and characterizing tolerances to constraints.

2.1 Draconian view of network-rigidity

A draconian view of network-rigidity in proteins is that *some* interactions can be modelled by placing a distance constraint between certain pairs of atoms, while the distances between all other pairs of atoms are not fixed. Given a network of distance constraints, the program FIRST (Floppy Inclusion and Rigid Substructure Topography) gives a detailed mechanical analysis of protein structure [Jacobs, et. al. 2001] that includes rigid cluster decomposition (RCD). A RCD defines all rigid substructures where the distance between all pairs of atoms is fixed within a substructure. As such, a protein is modelled as a collection of rigid bodies, where conformational change is through relative motions between rigid substructures.

The RCD depends on the set of distance constraints modelling various types of interactions. Covalent bonds are always modelled as distance constraints, while other interactions may or may not contribute to distance constraints. For example, the hydrogen bond (H-bond) has a wide variation of strength. In FIRST, a *dilution* analysis is employed to represent a H-bond as 5 distance constraints when its energy is lower than some cut-off energy. By *lowering* this cut-off, more H-bonds are identified as *weak*, which do not contribute distance constraints. As such, a protein will undergo a mechanical transition from being mostly a rigid structure with flexible pockets (all H-bonds contribute to distance constraints whether weak or strong) to a globally floppy structure interconnecting many small rigid clusters (only the strongest H-bonds contribute distance constraints). This dilution idea [Jacobs, et al. 1999] was later interpreted as a *kinetic* mechanism for protein unfolding [Rader, et al. 2002].

The notion of a rigid substructure is an idealization. For example, FIRST often identifies a long alpha-helix as a rigid substructure, but an alpha-helix actually bends and twists (just like a metal bar can do!). Nevertheless, the RCD is useful to understand long-time scales, where small amplitude conformational deviations in substructures within a protein are neglected, such as the compression, elongation, bending or twisting of an alpha-helix. The rapid calculations for the RCD by FIRST (requiring tiny fractions of a second) has proved to be useful in making comparative studies across protein families, and to elucidate common structural features regarding flexibility important to function [Hespenheide, et al. 2002; Rader, et al. 2004; Fuxreiter, et al. 2005; Costa, et al. 2006; Radestock & Gohlke 2008; Mamonova et al. 2008; Rader, 2010; Heal, et al. 2011; Radestock & Gohlke 2011]. It has also been shown there is a statistically significant correlation between the propagation of rigidity between two mutation sites within a protein to non-additive effects in free energy cycles describing double mutant studies [Istomin, et al. 2008].

If all weak interactions are allowed to contribute to distance constraints, FIRST will predict a completely rigid protein, failing to be of any use. Instead, excluded volume effects due to van der Waals interactions are included in geometrical simulation that allows rigid clusters to wiggle about without violating any distance constraint, or without atoms passing through one another. FRODA (Framework Rigidity Optimized Dynamics Algorithm) is one method [Wells, et al. 2005; Farrell, et al. 2010], among others [Lei, et al. 2004; Thomas, et al. 2007; Jimenez-Roldan, et al. 2011; Yao, et al. 2012] that uses FIRST to identify a native RCD that is preserved during the simulation. FRODA efficiently explores the native state ensemble of conformations [Jacobs, 2010; David & Jacobs 2011]. The main limitation is that the native state structure defines the distance constraints, and once set, they never break. This *athermal* mechanical description of a protein cannot account for non-native contacts, making large-scale conformational change between different conformational states impossible if native-contacts in either state must be broken along the pathway. However, pathways between conformational states can be achieved by using a common collection of distance constraints between native conformations [Farrell, et al. 2010].

2.2 Liberated view of network-rigidity

The draconian view suffers from three awkward problems. There is no prescription for (1) *how* to determine the proper number of distance constraints to model an interaction, and for (2) *when* an interaction will contribute distance constraints. Also, (3) the selection threshold that determines whether distance constraints are placed in the network causes artificial discontinuities. A discontinuity is illustrated by two nearly identical H-bonds having a small energy difference slightly above and lower than the cut-off energy. The H-bond with higher energy is modelled as *infinitely weak* (not present) while the other is *infinitely strong*!

By assigning tolerances to configuration *variables*, the accessible range for each variable can be quantified. The distinction between a DOF and a constraint is reflected in the process of *before and after* a tolerance is assigned. That is, a variable *acts* as a DOF before its tolerance is assigned. Once the range of a variable is restricted, it acts as a generic distance constraint. Applying graph-rigidity algorithms determine if a generic distance constraint is redundant or independent. A redundant distance constraint has zero tolerance because its length is determined by independent constraints. The length of independent distance constraints can vary within their tolerances. After all variables are analysed, a system of N atoms is

generically rigid (having 0 internal DOF) consisting of $3N-6$ independent distance constraints all with finite tolerances that quantify the accessible geometrical embedding of the constraint topology. In other words, for a given constraint topology there will be an entire ensemble of geometrical realizations that are consistent with the accessible tolerances. The conformational entropy is then related to the logarithm of this geometrical degeneracy.

In this view, the three awkward problems mentioned above are eliminated. A system of N atoms consists of $3N-6$ internal DOF. Similarly, a subsystem with n atoms for $n \geq 3$ has $3n-6$ internal DOF, and for $n=2$ has 1 internal DOF. A proper description of a subsystem should only be in terms of independent configuration variables that need to be assigned tolerances. Therefore, the number of contributing constraints for a subsystem of n atoms is just equal to the number of its internal DOF. For example, regarding a H-bond as a 3 atom subsystem (the donor, hydrogen and acceptor) requires 3 internal DOF to specify its configuration. Thus, a H-bond will contribute 3 generic distance constraints whenever it forms, and it will randomly form or break based on a probability that is appropriate for the system to be in thermodynamic equilibrium, which removes arbitrary thresholds.

2.2.1 Illustration: A two dimensional quadrilateral

To illustrate the points discussed above, consider 4 particles confined to a plane as shown in Fig. 1A. Quenched central-force interactions are between particles (1,2), (2,3), (3,4) and (4,1) with respective relative distances: ℓ_{12}, ℓ_{23}, ℓ_{34} and ℓ_{41}. The word "quenched" indicates that the interaction is always present within the network. Fluctuating interactions can also form between particles (1,3) and (2,4) with respective distances ℓ_{13}, ℓ_{24}. Quenched torsion-force interactions are between particles (4,1,2), (1,2,3), (2,3,4) and (3,4,1) with respective angles θ_1, θ_2, θ_3, θ_4. The potential energy for the *central* (c), *fluctuating* (f) and *torsion* (t) interactions are given as: $V_c = E_c + g\left(\frac{\ell - a}{\Delta L_c}\right)^2$, $V_f = E_f + g\left(\frac{\ell - b}{\Delta L_f}\right)^2$ and $V_t = E_t^k + g\left(\frac{\theta - \theta_k}{\Delta\theta}\right)^2$ where E_c, E_f, E_t^k are reference energies, g is a scaled spring constant, ΔL_c, ΔL_f, $\Delta\theta$ are configuration variable tolerances, a and b are equilibrium lengths, θ_k is an equilibrium angle, and the index, k, labels bins that partition the angle range. Four cases are compared below that differ only in g and b, each assigned two distinct values with common parameters held fixed. Common parameters are set to: E_c = -20 kcal/mol, E_f = -5 kcal/mol, $E_t^1 = E_t^3 = E_t^5$ = 2 kcal/mol, $E_t^2 = E_t^4$ = 0, a = 1 Å, ΔL_c = 0.04 Å, ΔL_f = 0.09 Å, $\Delta\theta$ = 15° and k = 1, 2, 3, 4, 5 to define five bins for the respective angle ranges (15°, 45°), (45°, 75°), (75°, 105°), (105°, 135°), (135°, 165°) and for corresponding θ_k = 30°, 60°, 90°, 120°, 150°.

The four cases to be considered are: g = 8 kcal/mol or 0, and $b = \sqrt{2}$ Å or 1.5321 Å. For the *harmonic* potential where g = 8 kcal/mol; the quadrilateral defines an elastic network. A *flat* potential (g = 0) has a constant energy as lengths or angles vary within a tolerance, but an infinite energy outside the tolerance. A sketch of how much the quadrilateral can deform for a flat potential is shown in Fig. 1B. Shaded regions define accessible geometries for each angular range (5 rows) and distinct constraint topology (4 columns) due to the fluctuating

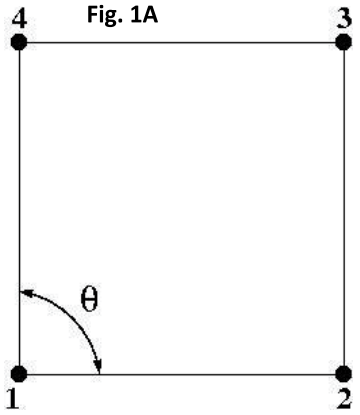

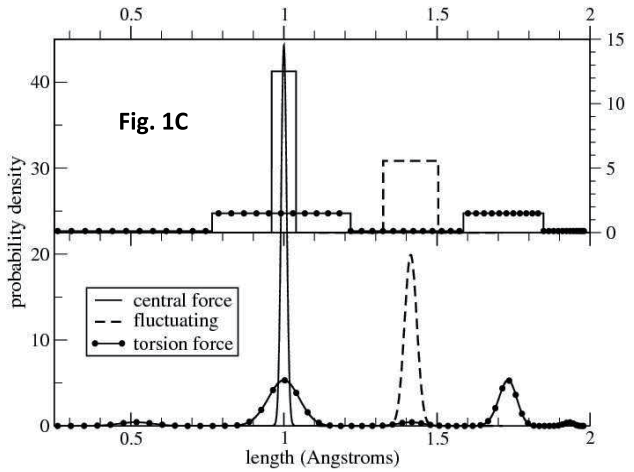

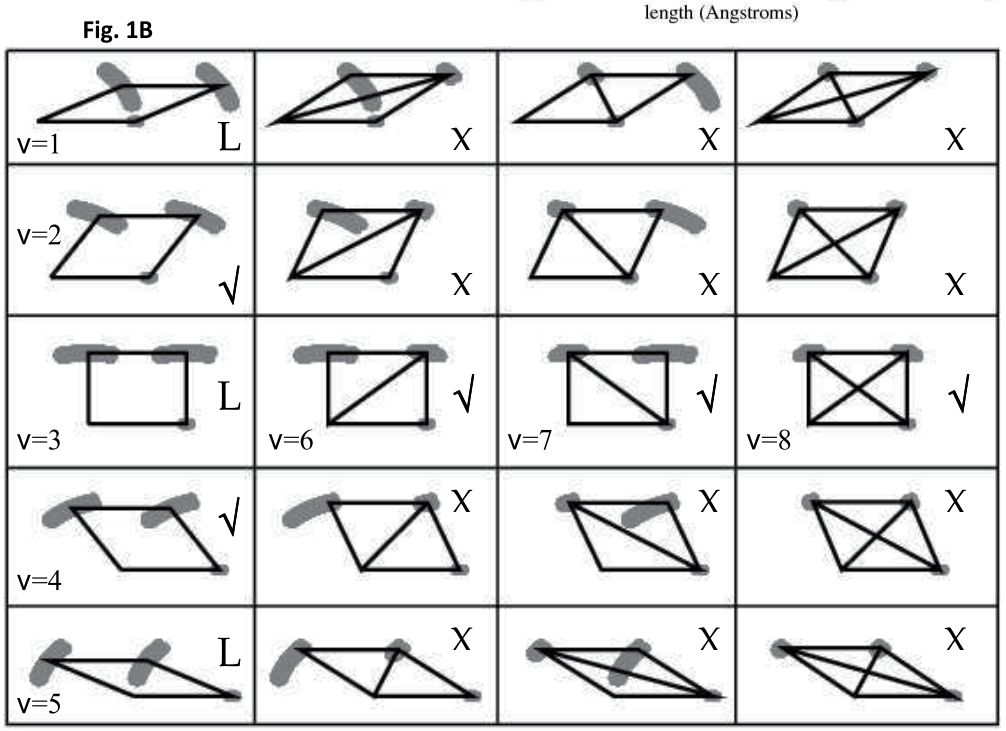

Fig. 1. (A) Definition of the quadrilateral network. (B) The accessible range of motion for each coarse-grained configuration is shown in grey. The middle two columns show how the more limited range of motion along a diagonal interaction compared to the range allowed by the torsion-forces is the determining factor restricting the motion. The symbols (√, L, X) indicate which configurations are (very probable, improbable, inaccessible). The index, ν, is used to label all accessible configurations. In the example considered here, the inaccessible configurations essentially have infinite energy, but in a more refined model they could have a finite energy. (C) Treating interactions as *independent*, the probability density, $\rho(\ell)$, for the length of a distance constraint is plotted for central-, fluctuating- and torsion-interactions, where the lower and upper graphs correspond to the cases: g = 8 kcal/mol and g = 0.

interaction along the diagonals. Fluctuating interactions break and form to reflect hidden DOF in the system not modelled. For example, a fluctuating interaction along a diagonal of the quadrilateral could model a H-bond that may appear or not depending on the details of the electronic structure of the donor, hydrogen and acceptor atoms.

2.2.2 Free energy decomposition and reconstitution

The configuration integral, $Q_\nu = \delta^{-5}\int\cdots\int \exp(-\beta V_\nu)\, dx_2 dx_3 dy_3 dx_4 dy_4$ is calculated where V_ν is the potential energy of the system in the ν–th coarse-grained configuration, $\beta = (RT)^{-1}$, where R is the ideal gas constant, T is absolute temperature, and $\delta = 0.002$ Å is a length scale factor (in classical statistical mechanics entropy is defined up to an arbitrary constant). Since rigid body DOF are not of interest, the quadrilateral is translated and rotated so that particle 1 is at the origin while particle 2 is along the x-axis, requiring a five dimensional integral. From Q_ν, the total internal free energy is given as $F_\nu = -RT\ln(Q_\nu)$, thermal energy is $U_\nu = \langle V_\nu \rangle$, and entropy is $R\tau_\nu$, where $\tau_\nu = \beta(U_\nu - F_\nu)$ is the total *pure* entropy. Similarly, the FED defines $\{Q_x, F_x, U_x, \sigma_x\}$ for each interaction type when *treated* as an independent subsystem. For the quadrilateral: $x \to c, f, t1, t2, t3, t4, t5$ denotes central-, fluctuating-, and torsion interactions for bin 1,2,3,4,5 respectively. Taking care to maintain the spatial length scale, $Q_c = \delta^{-1}\int \exp(-\beta V_c)\, d\ell$, $Q_f = \delta^{-1}\int \exp(-\beta V_f)\, d\ell$, and $Q_{tk} \approx \delta^{-1}\int \exp(-\beta V_k)\, \frac{d\ell}{d\theta}\, d\theta$ where a Jacobian is inserted to convert from an angle to a length measure using an approximation that constrains $\ell_{12} = \ell_{23} = \ell_{34} = \ell_{41} = a$. Consequently, a slight underestimate of the entropy is incurred because the angle is actually defined without imposing these length constraints. The probability density, $\rho(\ell)$, for finding the distance between a pair of particles (the plot is for T=400K) for a particular interaction is shown in Fig. 1C, which is given by the Boltzmann factor normalized by the corresponding partition function.

For each interaction type, x, the thermal energy, U_x, and pure entropy, σ_x, are plotted in Fig. 2A and Fig. 2B respectively for a flat potential energy, and in Fig. 2C and Fig. 2D for a harmonic potential energy. Notice that σ_x decreases when the peak width in the probability density, $\rho(\ell)$, decreases as shown in Fig. 1C. Interestingly, transforming from an angle to a length variable to describe torsion interactions causes σ_{tk} to decrease as the angle increases (larger k) because a smaller length variation results from the same angular deviation. This difference is important when network rigidity is used to calculate conformational entropy.

For an *additive* FER: The free energy for the ν–th configuration is: $F_1 = -RT\ln(Q_c^4 Q_{t1}^2 Q_{t5}^2)$, $F_2 = -RT\ln(Q_c^4 Q_{t2}^2 Q_{t4}^2)$, $F_3 = -RT\ln(Q_c^4 Q_{t3}^4)$, $F_4 = F_2$, $F_5 = F_1$, $F_6 = F_7 = -RT\ln(Q_f Q_c^4 Q_{t3}^4)$ and $F_8 = -RT\ln(Q_f^2 Q_c^4 Q_{t3}^4)$. Recall that a product of partition functions corresponds to adding the free energies over independent subsystems. Thus, in the additive approach, the total free energy of a configuration is simply a sum over all free energy components, such as $F_1 = 4F_c + 2F_{t1} + 2F_{t5}$ or $F_8 = 2F_f + 4F_c + 4F_{t3}$.

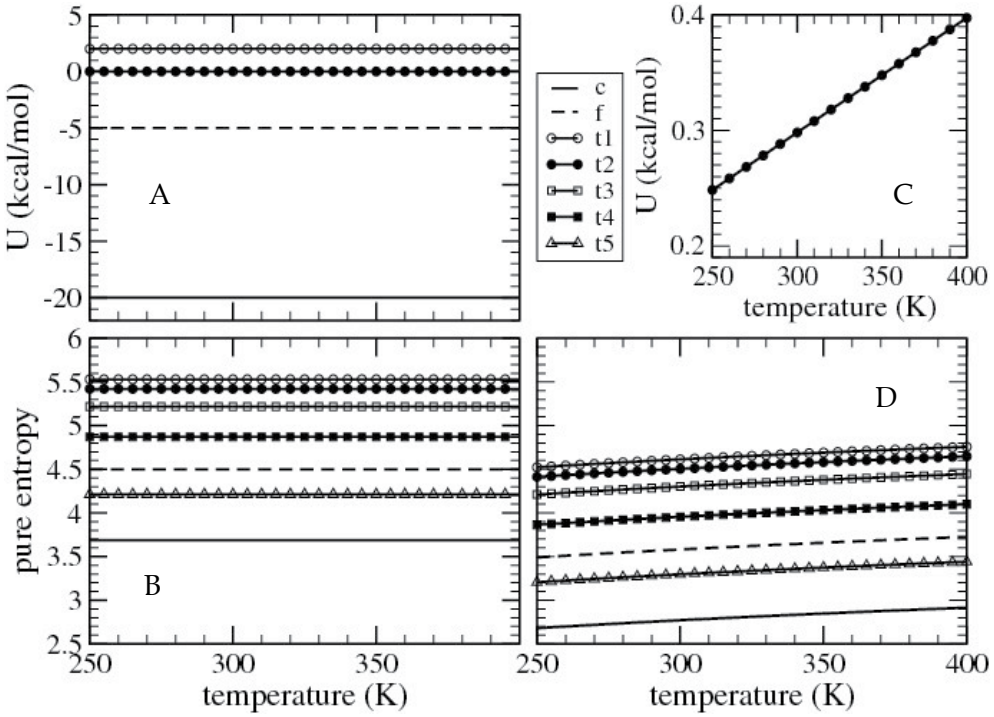

Fig. 2. The legend (middle-top) applies to all four graphs. For a flat potential: (A) Thermal energy has no temperature dependence. Note $U_{t1} = U_{t3} = U_{t5}$ and $U_{t2} = U_{t4}$. (B) The pure entropy also has no temperature dependence. For a harmonic potential: (C) Thermal energy has temperature dependence according to the equipartition theorem, but this cannot be seen using the energy scale of graph-A. Therefore, only U_{t2} is shown on a magnified scale. (D) The pure entropy monotonically increases, but it has a limiting plateau of the flat potential. Note that graph-D uses the same vertical axis as graph-B to assist in direct comparisons.

To proceed further, a more general indexing is needed to label *specific interactions*. For the quadrilateral network, there are four torsion-force, two fluctuating and four central-force interactions. Let j=1,2,3,4 label the angle variables $\theta_1, \theta_2, \theta_3, \theta_4$. Let j=5,6 label the fluctuating interactions between particles (1,3) and (2,4). Let j=7,8,9,10 label the central-force interactions between particles (1,2), (2,3), (3,4) and (4,1). The j index identifies a particular interaction within a configuration that is labelled by the ν index. In application to proteins, the ν index labels a particular accessible coarse-grained geometry that a subsystem can explore. Thus, the index-pair, νj, is a general indexing scheme used to uniquely label energy and entropy contributions. In this example, each νj maps to the x index, where $x \to c, f, t1, t2, t3, t4, t5$.

For a *non-additive* FER: The free energy of configuration, ν, is given as:

$$F_\nu = U_\nu^{cnf} + U_\nu^{vib} - TR\tau_\nu \tag{1}$$

where U_ν^{cnf} is the lowest possible energy of the selected basin, and U_ν^{vib} describes the energy associated with vibrations within the basin. Furthermore, the conformational entropy, $R\tau_\nu$,

is associated with any continuous deformation that is able to take place within a basin over a constant (or nearly constant) energy surface. The three functions are explicitly given as:

$$U_\nu^{cnf} = \sum_{\{j\}} n_{\nu j} E_{\nu j} \quad U_\nu^{vib} = \sum_{\{j\}} n_{\nu j} q_{\nu j} \langle \delta E \rangle_{\nu j} \quad \tau_\nu = \sum_{\{j\}} n_{\nu j} q_{\nu j} \sigma_{\nu j} \tag{2}$$

where the non-additive contributions can be identified by the terms containing the $q_{\nu j}$ variables. The $E_{\nu j}$ define reference energies, $\sigma_{\nu j}$ define pure entropies as plotted in Figs. 2B and 2D, and, $\langle \delta E \rangle_{\nu j}$ define the difference between thermal and reference energies. For a flat potential energy, $\langle \delta E \rangle_{\nu j}$ = 0, and for the harmonic potential with g = 8 kcal/mol, the *equipartition theorem* applies, which yields $\langle \delta E \rangle_{\nu j} = \frac{1}{2} RT$. Quantities for individual interactions, such as $E_{\nu j}$, $\sigma_{\nu j}$ and $\langle \delta E \rangle_{\nu j}$ are to be worked out in advance and stored in *lookup tables* to define the FED. The variable $n_{\nu j}$ can equal (1 or 0) when the j-th interaction is (*present* or *not present*) in the ν–th configuration. For quenched interactions, $n_{\nu j}$ = 1 $\forall \nu$. The variable $q_{\nu j}$ can equal (1 or 0) when the j-th interaction is represented by (an *independent* or *redundant*) distance constraint. It is important to notice that the assignment of which distance constraints are independent or redundant is not unique. Therefore, τ_ν will also not be unique! However, because distance constraints with smaller tolerances restrict motion more than those with greater tolerances (see Fig. 1B and view the middle two columns), the *lowest* value that can be obtained for τ_ν yields the best estimate for the *net* conformational entropy in the basin. Therefore, $q_{\nu j}$ are determined by augmenting a *preferential rule* to the graph-rigidity algorithm that manifest as building the network by placing one distance constraint at a time in the order defined by the sorted *set* of $\sigma_{\nu j}$ from *smallest to largest*.

As can be seen from Fig. 2B and Fig. 2D, the *rank ordering* of pure entropies from smallest to largest values when considering all interaction types does not depend on temperature. The same rank ordering is obtained whether flat or harmonic potentials are considered. The values for $n_{\nu j}$, $q_{\nu j}$ and corresponding $\nu j \to x$ labels are listed in Table 1 to enable explicit hand calculation of F_ν. Note that an additive FER is obtained by setting all $q_{\nu j}$ = 1, so that all interactions are considered independent, despite being *inconsistent* with network rigidity. Regardless of the FER employed, the free energy of the system with n fluctuating interactions *present* is given by: $F(n) = -RT \ln[Z(n)]$, where $Z(0) = \sum_{\nu=1}^{5} Q_\nu$, $Z(1) = Q_6 + Q_7$, $Z(2) = Q_8$ and of course $Q_\nu = \exp(-\beta F_\nu)$. The $F(n)$ are calculated in three different ways: (1) Exact answers are obtained by numerically performing the 5 dimensional configuration integral for each Q_ν , and approximate answers are obtained by employing an (2) additive and (3) non-additive FER. In Fig. 3, $F(n)$ are plotted for the four cases g = 8 or 0 kcal/mol, and $b = \sqrt{2}$ or 1.5321 Å. Table 2 summarizes the relative errors for the additive and non-additive FER predictions for the thermal energy and entropy of the system separately.

Comparing to the exact answers using Fig. 3 and Table 2, it is seen that the predictions of the non-additive FER are good for the harmonic and flat potential energy cases when b= $\sqrt{2}$ a. This is because the geometry of the fluctuating-interaction is *commensurate* with the torsion-interaction. Conversely, when b=1.5321a, the predictions breakdown because geometrical *frustration* between these two interactions cause large *strain energy* in the network. The additive and non-additive FER procedures are now juxtaposed. The results for this simple quadrilateral network example highlight the key concepts that are applied to proteins.

j=	1	2	3	4	5	6	7-10
ν	(n,q) - x	(n,q) - x	(n,q) - x	(n,q) - x	(n,q) - x	(n,q) - x	(n,q) - x
1	(1,0) - $t1$	(1,1) - $t5$	(1,0) - $t1$	(1,0) - $t5$	(0,0)	(0,0)	(1,1) - c
2	(1,0) - $t2$	(1,1) - $t4$	(1,0) - $t2$	(1,0) - $t4$	(0,0)	(0,0)	(1,1) - c
3	(1,1) - $t3$	(1,0) - $t3$	(1,0) - $t3$	(1,0) - $t3$	(0,0)	(0,0)	(1,1) - c
4	(1,1) - $t4$	(1,0) - $t2$	(1,0) - $t4$	(1,0) - $t2$	(0,0)	(0,0)	(1,1) - c
5	(1,1) - $t5$	(1,0) - $t1$	(1,0) - $t5$	(1,0) - $t1$	(0,0)	(0,0)	(1,1) - c
6	(1,0) - $t3$	(1,0) - $t3$	(1,0) - $t3$	(1,0) - $t3$	(1,1) - f	(0,0)	(1,1) - c
7	(1,0) - $t3$	(1,0) - $t3$	(1,0) - $t3$	(1,0) - $t3$	(0,0)	(1,1) - f	(1,1) - c
8	(1,0) - $t3$	(1,0) - $t3$	(1,0) - $t3$	(1,0) - $t3$	(1,1) - f	(1,0) - f	(1,1) - c

Table 1. The variables n_{vj} , q_{vj} and corresponding x - indices are specified for all allowed configurations (for ν=1-8) and interactions (for j=1-10). The vj pair-index for the n_{vj} and q_{vj} variables is suppressed. Note that q_{vj} can be determined by first placing the four x=c type of interactions in the network. Once the very next constraint is added, it will reduce one more DOF to make the network rigid. Therefore, the total number of independent distance constraints is 5 for all configurations, which can be checked by inspection.

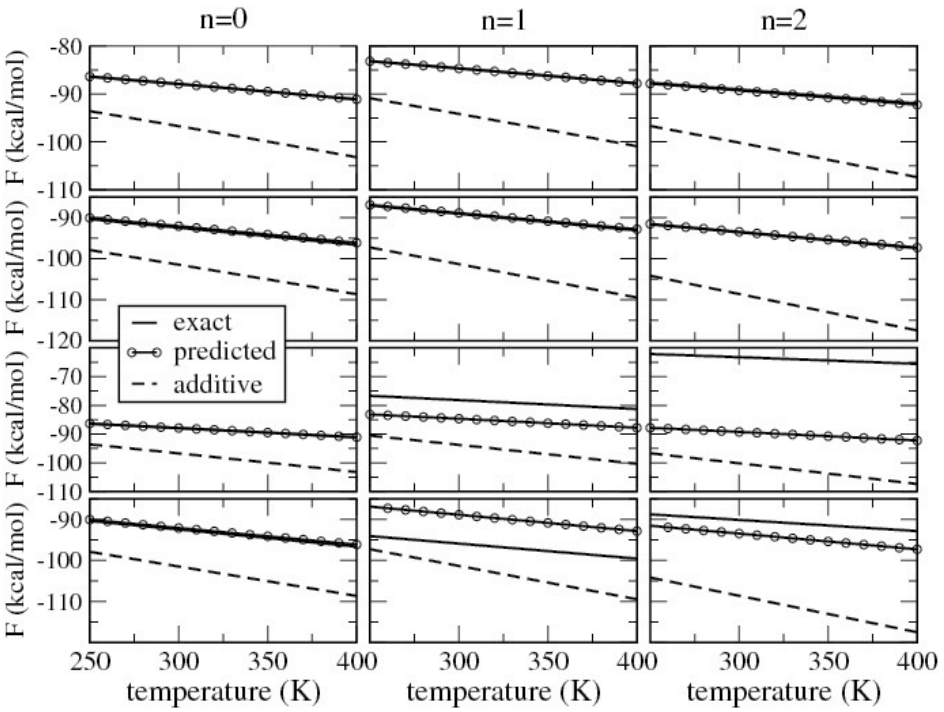

Fig. 3. The legend (left column and between middle rows) applies to all 12 graphs. The rows from top to bottom correspond to $b=\sqrt{2}$ Å for harmonic and flat potential energies, and then for b=1.5321 Å again for harmonic and flat potential energies. The columns show the free energy, $F(n)$, for n=0, 1, 2 fluctuating interactions present in the system. Note that the predicted and exact free energies for the $b=\sqrt{2}$ Å cases are nearly on top of one another.

Specs:		b= $\sqrt{2}$ a				b=1.5321a			
g	# fip	a-E-%e	a-S-%e	p-E-%e	p-S-%e	a-E-%e	a-S-%e	p-E-%e	p-S-%e
8	0	-1.8	77.8	0.0	-0.5	-1.8	77.8	0.0	-0.5
8	1	1.6	112.8	0.0	0.4	-7.6	112.9	-9.4	0.4
8	2	1.9	147.3	0.0	2.3	-39.9	213.0	-42.5	29.5
0	0	0.0	72.1	0.0	-3.0	0.0	72.1	0.0	-3.0
0	1	0.0	101.0	0.0	-1.7	9.4	122.3	9.4	8.7
0	2	0.0	129.4	0.0	-1.0	0.0	226.7	0.0	40.9

Table 2. The relative percent errors (denoted as %e) are given for energies (denoted as E–) and entropies (denoted as S–) for the additive FER (denoted as a–) and the non-additive FER prediction (denoted as p–) for when the system has 0, 1, 2 fluctuating interactions present (denoted as # fip) for $g =$ 8 kcal/mol and 0 on the top and bottom three rows respectively. Also the ($b = \sqrt{2}a$ and $b = 1.5321a$) cases are shown on the (left and right) sides of the table. These percent errors apply to T=300K, and reflect typical values at all other temperatures.

The additive approach is *completely wrong* for predicting conformational entropy because it predicts conformational entropy of a network increases as more constraining interactions appear. Thus: *The conformational entropy of a protein in its native state will always be predicted to be greater than that of the unfolded protein when using an additive model.* Although energy estimates from the additive FED are good, there are two sources of errors that occur for harmonic potentials (not for flat potentials). Part of this discrepancy is directly caused by over counting thermal energy contributions (i.e. $\frac{1}{2}RT$) for all quadratic DOF, rather than just the independent ones. This problem is more severe with respect to entropy estimates, and these errors cause relative statistical weighting of the various configurations in the ensemble to error, thereby indirectly leading to errors in average energies.

A non-additive FED *naturally* models energy-entropy compensation mechanisms that link atomic structure characteristics to thermodynamic response. As interactions form within a *protein*, such as from H-bonds or packing, more constraints are placed on conformational motions, leading to a decrease in conformational flexibility and entropy. In particular, if an energetically favourable interaction forms in an *otherwise flexible region*, it will constrain motions and decrease conformational entropy. However, if the interaction forms within an *otherwise rigid region*, no entropic cost is incurred because the constraint that is imposed is redundant. This effect is the underlying source of non-additivity. Thus, network rigidity is an interaction between entropic contributions that provides a simple mechanism for groups of interactions that constrain conformational flexibility to form and break cooperatively.

Errors appear in the non-additive FER primarily due to three reasons: (1) The Jacobian that *should* be part of the reconstitution of free energy components to account for *how subsystems interface geometrically is ignored* by assuming independent constraints are orthogonal. For example, the very skewed configurations shown in Fig. 1B have smaller conformational entropy than the configurations with all θ_k approximately 90 degrees. The coarse-graining into restricted angular bins was required to capture this difference. (2) *The energy landscape of*

a subsystem cannot change as it interacts with other subsystems. The two harmonic potential energy examples violate this assumption, but this approximation fails badly for a frustrated network. (3) *Information is lost by coarse-graining structure into local configurations* (identified by the ν index). For example, when $b = 1.5321a$ the flawed prediction in energy (~ ±10% relative error as listed in Table 2) occurs because when *just one* fluctuating-interaction is present it can stretch between multiple configurations. In addition, the building blocks are not commensurate, leading to strain energy. When *both* fluctuating interactions are present in the system, only the problem of strain energy remains.

Partitioning local structure into *finer* coarse-grained bins to define accessible configurations with *more restricted range of motion* systematically diminishes all three sources of error. A high degree of accuracy can be obtained by *finely* coarse-graining the energy landscape (such as a harmonic well) by a *large* number of flat energy tiers differing by tiny increments (say 0.01 kcal/mol). As the quantities $\{Q_x, F_x, U_x, \sigma_x\}$ are further refined for each interaction type, x, this will create more binning labels that comprise the FED. Although defeating the objective of *rapidly* calculating absolute free energies, it is important to note that errors can be reduced to low levels in principle. Also important is that the computational cost for the non-additive FER scales linearly with respect to the number of atoms in the network, N, with a pre-factor that is proportional to the number of coarse-grained bins used. Since exact integration scales as δ^{-3N}, consideration of a sophisticated FED may be worth the effort.

The errors caused by large strain energies in frustrated configurations can be identified and *removed* from the ensemble in applications to proteins based on the empirical justification that proteins exhibit folding funnels because they are minimally frustrated [Onuchic & Wolynes, 2004]. In practice, this is *accomplished* by considering only native contacts with respect to a specified template structure that is obtained experimentally (say from X-ray crystallography) or from a model structure that is fully relaxed. This leads to a FED scheme that classifies protein structure in terms of a finite number of local energy basins such as accessible backbone conformations within a Ramachandran plot and sidechain rotamers for residues. Moreover, a variety of different types of H-bonds can be classified. The complete classification of local structure defines the set of all possible subsystems that can appear within a protein. Then, the minimum of the potential energy of a basin is used to obtain the conformational part of the free energy, with the free energy contributions from modes of vibration augmented. Consequently, the U_x and σ_x parameters for the various basins are *temperature independent*. Notice that for the quadrilateral example, the temperature dependence in U_x and σ_x appears because of the harmonic potential energy, as seen in Fig. 2C and 2D. Thus, the free energy of a subsystem is separated into conformational and vibrational parts, such that $F_x^{net} = F_x^{cnf} + F_x^{vib}(\omega_x)$ where ω_x is the frequency of oscillation. Only when $\hbar\omega_x << RT$ does the equipartition theorem apply. More generally, $F_x^{vib}(\omega_x)$ is empirically modelled as the free energy of a quantum harmonic oscillator with natural frequency, ω_x. An observation that can be seen by comparing the harmonic and flat potential energy example cases is that the free energy contributions from vibration originate only from independent modes. A subsystem (in three dimensions) with n atoms for $n \geq 3$ has $3n-6$ independent modes of vibration, and one independent mode when $n = 2$. At this point, an empirical interfacial thermodynamic model can be developed.

3. Interfacial thermodynamics model for protein stability

The previous section showed how to reconstitute conformational free energy for a given constraint topology or *framework* using network rigidity. The staring information is that all energy and entropy components for accessible subsystems are stored in lookup tables. The focus was on *internal* DOF of the system. Now the affect of solvent on a protein will be included. Solvent DOF are *external* to the protein and need not be kept track of because they are part of a *reservoir*. Therefore, treating all free energy components from a reservoir as additive is consistent with a thermodynamic hypothesis. The problem that is at hand now is to determine the partition function of a protein, which takes the generic form:

$$Z = \sum_{\psi} Q_{\psi}^{slv} Q_{\psi}^{cnf} Q_{\psi}^{vib} = \sum_{\psi} Q_{\psi}^{slv} \exp\left(-\beta \sum_{\{\nu j\}_{\psi}} \left(n_{\nu j} E_{\nu j} - RT q_{\nu j} \sigma_{\nu j} \right) \right) \exp\left(-\beta \sum_{\{\nu j\}_{\psi}} q_{\nu j} F^{vib}(\omega_{\nu j}) \right) \quad (3)$$

The index, ψ, defines an accessible configuration that is generated from a template structure decorated with Ising-like spin variables to specify the local environment of each residue. Through coupling, the template decoration helps define a mechanical framework, which is specified by energy basins, labelled by ν, and its member distance constraints labelled by j, across all subsystems. The placement of distance constraints is specified by the $n_{\nu j}$ values. Topological information about the mechanical framework that is contained in ψ serves as input to a graph-rigidity analysis that yields the $q_{\nu j}$ values. Because the *number* of distance constraints and modes of vibration are equal within a subsystem, the j index is reused to label modes[1]. In Eq. (3) involving *random variables*, it is understood that whenever $n_{\nu j}$=0, so does $q_{\nu j}$=0, since if a distance constraint is not present, it cannot be independent. The $q_{\nu j}$ in the last term are necessary because the free energy of vibration is reconstituted by adding only *independent* modes of vibration. The term, Q_{ψ}^{slv}, takes on a form similar to many FED schemes commonly employed in the literature that relate transfer free energies to estimate changes in free energy of residues and other designated chemical groups based on whether they are exposed or buried in the protein through solvent exposed surface area.

3.1 Free Energy Decomposition (FED)

The FED accounts for enthalpy[2] and entropy contributions from solvent, conformation and vibration. The geometry of a protein is defined by one or more template structure(s). Given any template structure, all its atoms are partitioned into contiguous groups of atoms that are classified and parameterized by the FED. As such, each atom within a system must map to one and only one *molecular constituent*, which also serves as a primary subsystem. Molecular constituents in proteins define the residues, as illustrated in Fig. 4.

---

[1] Each mode of vibration can be represented by a distinct set of distance constraints to better capture the local atomic motions within a subsystem, but this requires another sub-index for distance constraint labeling that is suppressed for this discussion.

[2] Enthalpy is considered to be a function of pressure using standard pressure as a reference point, about which a Taylor expansion is employed. At standard conditions, the terms enthalpy and energy are considered synonymous in this discussion.

The FED considered here consists of 1) residues, 2) covalent bonds that link residue pairs, 3) H-bonds and 4) hydration interactions that together constitute a constraint network, and, the additive contributions consist of 5) residue solvation and 6) hydrophobic interactions that together model solvent effects. To account for protonation states on titratable residues, an additional solvent dependent partition function, Q_{ψ}^{ion}, must be inserted in Eq. (3), but this is not discussed here because it introduces technical complexity without offering anything more conceptually. Packing interactions are implicitly included. Because the FED can divide a system up in different ways, and because of the empirical assignments, different effects can be lumped together in various terms. Here packing effects are included in the residue states that are identified as *native-like* or *disordered*, corresponding to good or poor atomic packing with respect to the strain free template. With exception of long-range electrostatic interactions, and electing to work with a fixed protonation state, the six listed types of contributions encompass all essential enthalpy-entropy compensation mechanisms.

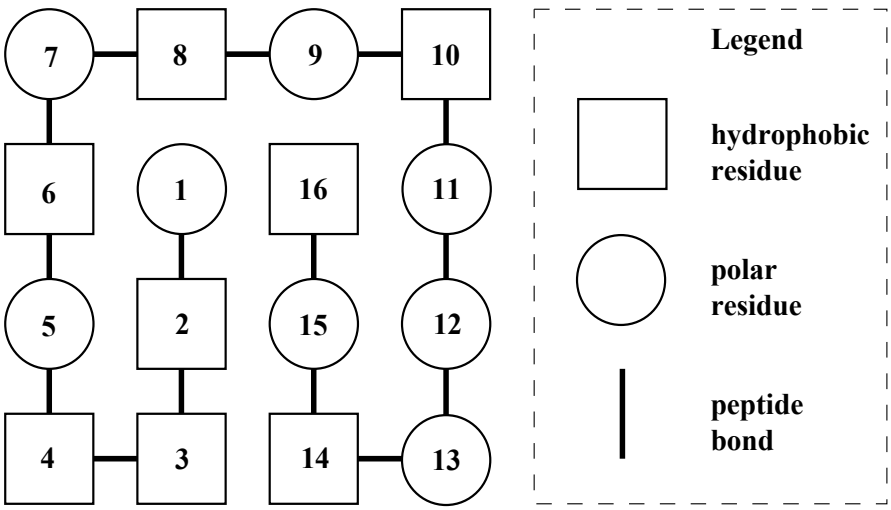

Fig. 4. A schematic of a protein template structure is shown consisting of 16 residues. Each residue defines a subsystem that includes all atoms from its backbone and sidechain. The model can include a sufficient number of probable low energy basins for each residue type covering the most frequently occurring conformations identified in the Ramachandran plot and the sidechain rotamers. The degree of coverage depends on the level of coarse graining, which ultimately controls the accuracy of the model and speed of the calculations.

3.2 The free energy functional

Solving Eq. (3) poses insurmountable challenges. Therefore, Eq. (3) is reformulated as a *free energy functional* (FEF) that can be efficiently solved numerically using self-consistent mean field theory. The FEF in generic form is written in a format that is germane to the concept of a FED, where various types of contributions can be identified.

$$G_{FEF} = \left(G_{slv}^{res} + G_{slv}^{hph} + G_{slv}^{shb} + G_{slv}^{etc}\right) + \left(G_{cnf}^{res} + G_{cnf}^{lnk} + G_{cnf}^{ihb} + G_{cnf}^{hyd} + G_{cnf}^{etc}\right) + G_{vib} \qquad (4)$$

Terms are grouped together to reflect contributions that involve solvent, conformation and vibration. Terms involving *solvent* effects (subscripted by *slv*) are: G_{slv}^{res} for residue solvation; G_{slv}^{hph} for the hydrophobic effect, G_{slv}^{shb} for solvent-protein H-bonds, and G_{slv}^{etc} indicates the model can be extended if needed, such as including a G_{slv}^{ion} contribution. Similarly, terms involving the *conformation* contributions (subscripted by *cnf*) are: G_{cnf}^{res} for the set of primary subsystems where residues define molecular constituents; G_{cnf}^{lnk} for peptide bonds linking residues together along the backbone and crosslinking disulphide bonds when present; G_{cnf}^{ihb} for intramolecular H-bonds within the protein; G_{cnf}^{hyd} for conformational constraints that are *externally imposed* on the protein structure due to solvent molecules --- often described as forming a clathrate-structure, and G_{cnf}^{etc} indicates that the model can be extended if needed, such as modelling packing interactions explicitly.

The FEF is expressed in terms of a set of a priori unknown probability functions describing the microstates of the protein. The exact nature of what the microstates are will depend on the FED. In addition to the various FED terms that make up the FEF, order parameters are employed to define the macrostate of a protein that reflect sub-ensembles of microstates. By minimizing the FEF under the global constraints imposed by the order parameters, a *free energy landscape* (FEL) is calculated. The first step is to define the FED based on microscopic mechanisms deemed important to model, which naturally leads to defining variables and their associated probability functions. The second step is to define the order parameters that will be used to define the FEL. The third step is to solve the FEF. How to solve the FEF will be explained below in a specific context of the FED. The task at hand now is to define the FED in terms of enthalpy-entropy compensation mechanisms essential to protein stability.

3.2.1 Solvent related enthalpy-entropy compensation mechanisms

Residue solvation: A residue can be *buried* (b) in the core of a protein without solvent contact, or it can be *exposed* to solvent. When exposed, the solvent molecules surrounding the residue might be *mobile* (m) or structured *clathrate* (c). Each residue is assigned a solvation state, s, to characterize its local environment, where $s = \{b, m, c\}$. Residue solvation together with the given template structure is used to specify a microstate of the protein. The ensemble of all accessible solvent states for a given template with n residues consists of 3^n configurations. The solvent state *decorates* the template structure. For example, Fig. 5 illustrates a decoration of the template structure shown in Fig. 4 by one such solvent state configuration.

Let p_{rs} be the probability that residue, r, is in solvation state, s. Then G_{slv}^{res} is given by:

$$G_{slv}^{res} = \sum_{r=1}^{n} \sum_{s} \left[\varepsilon_{rs}^{slv} + v_{rs}^{slv} \left(P - P_o \right) - TR\, \alpha_{rs}^{slv} + TR \ln\left(p_{rs} \right) \right] p_{rs} \tag{5}$$

where the parameters, $(\varepsilon_{rs}^{slv}, \alpha_{rs}^{slv})$, give the (energy, entropy) contributions for residue, r, in solvation state, s, which are scaled by solvent accessible surface area as determined from the template. The parameters, v_{rs}^{slv}, are first order Taylor expansion coefficients for the solvation enthalpy with respect to pressure, P. For purposes of simplicity, the parameters are treated as constant over the temperature range of interest. Moreover, by limiting the calculations to the reference pressure, $P = P_o$, the v_{rs}^{slv} parameters are not needed. The model parameters

can be expanded in terms of pressure and co-solvent concentrations. Notice that with the exception of the extra $-RT\,\alpha_{rs}^{slv}$ term, the form of Eq. (5) is the standard expression for the free energy of a system comprised of independent subsystems, where the mixing entropy is accounted for in the last term. At this point, each residue is able to independently explore three solvation states in thermodynamic equilibrium. However, as more terms are added to the FEF, these states will become coupled in the same way spin-spin coupling occurs in Ising or Potts models. In the FED considered here, the set of functions $\{p_{rs}\}$ will form the basis for completely representing the FEF as an Ising-like model with generalized spin-spin coupling terms. The coupling terms that are described next account for interactions at the interface between subsystems, which are the molecular constituents defined by the residues.

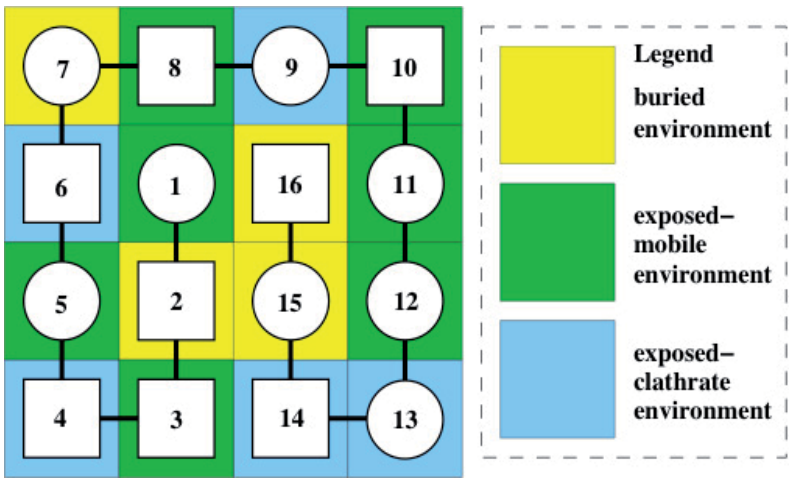

Fig. 5. A schematic of a protein template that is decorated by specifying one of three possible solvation states for each residue. Buried means that some part of a residue is not in contact with solvent. The contributions of free energy, enthalpy and entropy in the buried state are proportional to the solvent accessible surface area of the residue. Exposed solvation states have maximum solvent accessible surface area. The difference in these quantities between buried and exposed states will be less for corner residues {4,7,10,13} compared to the other surface residues {3,5,6,8,9,11,12,14}. A maximum difference occurs for core residues {1,2,15,16}, which can become exposed to solvent due to solvent penetration. Recall the template defines a fixed topology, but not a fixed geometry. This type of coarse-grained description of solvation is common to Ising-like models.

Hydrophobic interaction: The change in free energy to transfer water from an *interface* that separates neighboring molecular constituents into bulk solvent is *how* the hydrophobic effect is modeled in the FEF. This interface term is illustrated in Fig. 6A. Then G_{slv}^{hph} is given by:

$$G_{slv}^{hph} = \sum_{r1=1}^{n} \sum_{r2=1}^{n} \left[\varepsilon_{r1,r2}^{hph} - TR\,\alpha_{r1,r2}^{hph} \right] p_{r1,b}\; p_{r2,b} \tag{6}$$

where $\varepsilon^{hph}_{r1,r2} = n^{wat}_{r1,r2}\,\varepsilon^{hph}$, $\alpha^{hph}_{r1,r2} = n^{wat}_{r1,r2}\,\alpha^{hph}$ and $n^{wat}_{r1,r2}$ is an estimate for the number of water molecules that could reside at the interfacial surface between residues $r1$ and $r2$ based on the geometry of the template structure. Note that $n^{wat}_{r1,r2}$ is the interfacial surface area divided by the *specific area* covered by a single water molecule. The parameters, $(\varepsilon^{hph}, \alpha^{hph})$, represent the (energy, entropy) contributions to the free energy for transferring one water molecule from a generic non-polar reference environment to bulk solvent.

An interesting property of Eq. (6) is that the accumulated *strength* of the hydrophobic effect is proportional to the total surface area of the buried-buried interfaces that snake through a protein. The nature of these interfaces depends on the solvation state of the protein. Also a significant part of the overall strength of the hydrophobic effect is due to the *chemical nature* of the bulk solvent (i.e. affecting chemical potential), which is reflected in the parameters $(\varepsilon^{hph}, \alpha^{hph})$ by expressing them as *functions of co-solvent concentrations*. In aqueous solution a thermodynamic force is generated to expel water from the core of a globular protein, thereby resisting water penetration. The hydrophobic effect competes against the desire for residues of all types (hydrophobic or polar) to be solvated. The nuanced details of the solvation properties of each residue type combined with where residues are located in the template structure determines the amount of "dry" or "wet" interfacial surface area, and this directly relates to water penetration pathways associated with partial unfolding events.

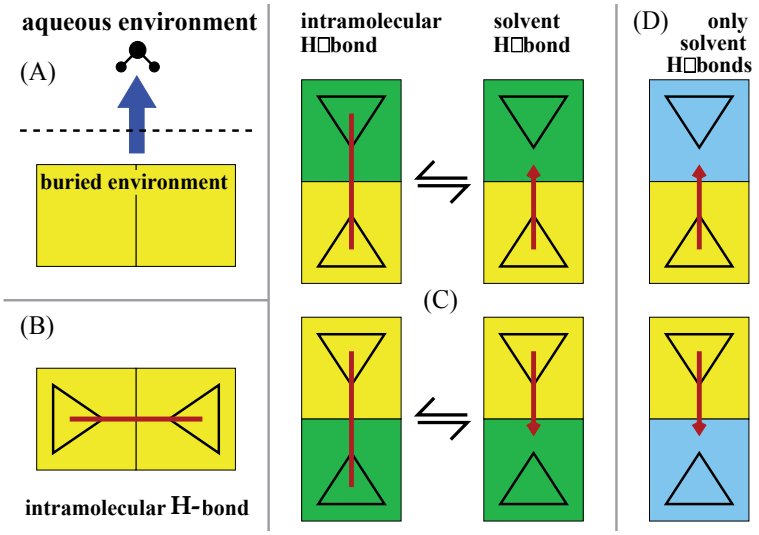

Fig. 6. (A) Schematic of a water molecule transferring from a non-polar environment to bulk solvent. (B) Intramolecular H-bonds (red line) identified in the template are present when both residues are buried (yellow block). Triangles represent residues and indicate a relative orientation. (C) Neighboring pair of residues in buried and exposed-mobile (green block) states is shown. When mobile solvent surrounds an exposed residue; a *fluctuating* intramolecular H-bond (red line) can form between it and a buried residue, or a *fluctuating* solvent-protein H-bond can form (short red arrow) between the buried residue and solvent. (D) An exposed residue surrounded by clathrate water (blue block) prevents a H-bond to form between it and a neighbouring buried residue because the immobile water molecules cannot properly rearrange, and thereby shields the residue from intramolecular H-bonding.

Solvent-protein H-bond: H-bonds appear in the FEF in both the solvation and conformational parts of the FED. When a H-bond forms between two neighboring residues in a template structure, the model must account for nine cases corresponding to each of the residues being in one of its three possible solvation states. First, the intramolecular H-bond will be present when both residues are buried, making it impossible for another H-bond to form between solvent and to that particular buried region of the protein. If both residues are exposed, the question about solvent-protein H-bonding to these residues is irrelevant because the residue solvation free energy fully accounts for theses interactions. The cases that generate a solvent-protein H-bond are when one residue is exposed to solvent, while its neighboring residue is buried. The discontinuity in local environment creates a surface term at a wet-dry interface between the two subsystems. In particular, the intramolecular H-bond can remain in tact, or be replaced by a solvent-protein H-bond that forms between solvent and the buried residue.

In all, Fig. 6B, 6C and 6D summarizes 7 cases. The three cases that involve intramolecular H-bonding will be addressed below when considering the conformational part of the FED. However, because two cases are coupled dealing with fluctuations between solvent-protein and intramolecular H-bonds (see Fig. 6C), another probability function must be introduced to determine if a solvent-protein H-bond or an intramolecular H-bond will form when both options are accessible. Let p_h^{ihb} be the probability that the *h*-th *intramolecular H-bond* (ihb) identified in the template structure is present. Although it is not difficult to associate the *h*-index of an identified intramolecular H-bond to its residues that provide donor and acceptor atoms, it does require *cumbersome notation* to explicitly show this correspondence. Therefore, in formulas that involve the *h*-index and two residue indices (r_1 and r_2) this correspondence is *implied*. Then, as another *interface* term in the FEF, G_{slv}^{shb} is given by:

$$G_{slv}^{shb} = \left(\varepsilon^{shb} - TR\,\alpha^{shb}\right)\left\langle N_{shb}\right\rangle + RT\sum_h \left(\ln(p_h^{ihb})p_h^{ihb} + (1-p_h^{ihb})\ln(1-p_h^{ihb})\right) \tag{7}$$

$$\left\langle N_{shb}\right\rangle = \sum_h p_h^{shb} \text{ where } p_h^{shb} = \left(p_{r1,b}\,p_{r2,c} + p_{r1,c}\,p_{r2,b}\right) + \left(p_{r1,b}\,p_{r2,m} + p_{r1,m}\,p_{r2,b}\right)\left(1-p_h^{ihb}\right) \tag{8}$$

In Eq. (7) the parameters $(\varepsilon^{shb}, \alpha^{shb})$ characterize the energy and entropy contributions from solvent-protein H-bonds. These parameters *should be* dependent on local structural details of the solvent and protein, but the model is based on an *implicit solvent*. Including myriad structural details would be intractable, but as effective parameters, they depend only on the *chemical nature* of the bulk solvent. Thus, all that matters is the total number of H-bonds between solvent and the protein, given by $\left\langle N_{shb}\right\rangle$. This average is over the ensemble of microstates that represent all fluctuations taking place between intramolecular H-bonds and solvent-protein H-bonds. Therefore, the second term is the mixing entropy associated with intramolecular H-bonds forming and breaking. The average number of H-bonds in Eq. (8) is expressed as a simple sum over the probability of finding a solvent-protein H-bond, which is then expanded out in detail corresponding to the four terms shown in Fig. 6C.

3.2.2 Entropy spectrum for molecular constituents and interfacial subsystems

As outlined in section 2, subsystems are coarse-grained into configurations corresponding to low energy basins, each with the same number of distance constraints but with *particular*

characteristics. The number of distance constraints is just enough for the subsystem to be *isostatically rigid*, meaning no distance constraint is redundant when the subsystem is isolated. Suppose subsystems 1 and 2 with n_1 and n_2 atoms are connected together to form a larger rigid system with $(n_1 + n_2)$ atoms through an interaction at their interface involving n atoms from each subsystem. This *interfacial interaction* is modelled using $3(2n) - 6$ distance constraints[3] so it too is *isostatic* when isolated. Within the combined system, there will be $3(n_1 + n_2) - 6$ independent distance constraints. However, the two subsystems together with the interfacial interaction produce $3(n_1 + 2n + n_2) - 18$ constraints, leading to $6n - 12$ redundant constraints in the combined system. Therefore, *interfacial subsystems will generally create redundant constraints* as molecular constituents are coupled through interactions. Interestingly, peptide bonds along the backbone that join residues together do not generate redundant constraints. Thus, a random coil (no crosslinks) has no redundant constraints.

A *complete entropy* assignment to all distance constraints can be made for each basin by performing a local all-atom sampling using a quasi-harmonic approximation. This means that absolute entropies are estimated from the Schlitter entropy formula based on the covariance matrix of atomic fluctuations (Andricioaei & Karplus, 2001) that is obtained from an all-atom MD simulation using an accurate molecular mechanics force field. Afterwards, by considering contributions from all accessible basins, the intrinsic free energy of a subsystem can be reconstituted. This method applies to residues (Wang, et al. 2011) and all interfacial subsystems. While it is important that a *robust procedure* to determine entropy and energy parameters for the conformational part of the FED has been established, for my discussions here it suffices to know that the parameters concretely exist with entropy values on an absolute scale! Furthermore, it is possible to model each mode of vibration within an energy basin of a subsystem using a specific distribution of distance constraints. However, a surprisingly simple description can be made without invoking any details about *how* the distance constraints are distributed.

For the purpose of explaining the interfacial thermodynamics paradigm, network rigidity will be described in terms of *Maxwell constraint counting* (Whitely, 2005). Maxwell constraint counting (MCC) is a mean field approximation to graph-rigidity. As shown previously, the application of MCC to solve the mDCM yields results that capture the correct qualitative thermodynamic response in beta-hairpins (Jacobs & Fairchild, 2007a), alpha-helices (Vorov, et al. 2009) and proteins (Vorov, et al. 2011). The advantage of using MCC is that concepts can be calculated easily without obfuscation because all topological details about how the constraints are distributed in the network are ignored. The only specification required is that a subsystem with n atoms has $3n - 6$ distance constraints, each assigned an entropy value of σ_j for j=1 to n, such that $\sigma_j \leq \sigma_{j+1}$. This ordered set of values from lowest to greatest defines an *entropy spectrum* for a subsystem. All of the different types of subsystems that make up the conformational part of the FED are now described.

3.2.3 Conformation related enthalpy-entropy compensation mechanisms

Molecular constituents: Residues are molecular constituents that define subsystems involving a certain number of atoms. Each residue, r, in a specific energy basin, ν, has its own entropy

[3] The special case n=1 is not considered in this discussion because no subsystem is employed that contains less than 3 atoms.

spectrum. While it is possible to have a detailed description of each residue by using a large number of energy basins, an Ising-like model similar to the mDCM is described here, where each residue is classified as *native-like* or *disordered*. A conditional dependence as to whether a residue is native-like (ν=n) or disordered (ν=d) is tied to its solvation state. If a residue is exposed to solvent, it is modelled as disordered. However, a buried residue can be native-like or disordered. Native-like implies the local geometry of a residue will be similar to the template structure, and disordered implies poor atomic packing that is reflected by higher energy and entropy. Respecting conditional dependences on solvation, G_{cnf}^{res} is given by:

$$G_{cnf}^{res} = \begin{cases} \sum_{r=1}^{R} \left(\varepsilon_{rd}^{cnf} - TR \sum_{j} q_{rdj}\, \sigma_{rdj}^{cnf} \right) \left((1 - p_{rb}) + p_{rb}\,(1 - p_r^{nat}) \right) + \\ \sum_{r=1}^{R} \left(\left[\varepsilon_{rn}^{cnf} - TR \sum_{j} q_{rnj}\, \sigma_{rnj}^{cnf} \right] p_r^{nat} + TR \left[p_r^{nat} \ln\left(p_r^{nat} \right) + (1 - p_r^{nat}) \ln\left(1 - p_r^{nat} \right) \right] \right) p_{rb} \end{cases} \tag{9}$$

In Eq. (9) the top term contributes when residue, *r*, is exposed with probability $(1 - p_{rb})$ or when it is buried *and* disordered with probability, $p_{rb}(1 - p_r^{nat})$. The energy contribution is ε_{rd}^{cnf} and the *maximum* possible entropy contribution is given by $R\sum_j \sigma_{rdj}^{cnf}$ when all distance constraints are independent (i.e. $q_{rdj} = 1$). The set of pure entropies, $\{\sigma_{rdj}^{cnf}\}$, define the entropy spectrum for residue, *r*, when it is in the disordered state, *d*. Once residue, *r*, couples to other residues within the protein, some of its distance constraints may become redundant. Recall redundant constraints do not contribute to conformational entropy. Therefore, q_{rdj} is the probability that distance constraint, *j*, in residue, *r*, and in its disordered state, *d*, is independent. The probability for residue, *r*, to be native-like when it is buried, is given as p_r^{nat}. Similarly, the bottom term in Eq. (9) contributes ε_{rn}^{cnf} energy and $R\sum_j q_{rnj}\sigma_{rnj}^{cnf}$ is the net entropy when the residue is buried *and* native-like with probability, $p_r^{nat} p_{rb}$. The native-like entropy spectrum is given by $\{\sigma_{rnj}^{cnf}\}$, and q_{rnj} is the probability that distance constraint, *j*, in residue, *r*, and in its native-state, *n*, is independent. The last term involving the square brackets is the mixing entropy for the buried residue, *r*, to be either native-like or buried.

Taken together, G_{cnf}^{res} supports the following possibilities: A large number of buried residues that are mostly disordered correspond to a collapsed state driven by the hydrophobic effect. As more native-like residues form, but with high variance, the protein will transition to a molten globular state with fluctuating secondary structure. When the majority of buried residues are native-like, the protein will be in its native-state with some degree of flexibility. Thus, all common known phases can be described by the accessible microenvironments.

Covalent bond linkers: When a covalent bond links two residues, it involves two atoms in each of the two residues. Therefore, the covalent bonds are modelled as an interfacial subsystem containing 4 atoms connected by 6 distance constraints. The parameterization of the distance constraints for a covalent bond with a flexible dihedral angle such as a

disulphide bond, or a peptide bond with a fixed dihedral angle within a *trans* or *cis* basin will have distinct energy and entropy parameters. Since chemical reactions involving the breaking or forming of a covalent bond is not considered here, these interactions are *quenched*. Moreover, only one energy basin for each type of covalent bond is considered here. Then, G_{cnf}^{lnk} is given by:

$$G_{cnf}^{lnk} = \sum_{k=1}^{K} \left(\varepsilon_k^{cnf} - TR \sum_j q_{kj} \, \sigma_{kj}^{cnf} \right) \tag{10}$$

Here ε_k^{cnf} is the energy, $\{\sigma_{kj}^{cnf}\}$ is the entropy spectrum, and, q_{kj}^{cnf} is the probability that the *j*-th distance constraint for the *k*-th covalent bond in the protein is independent. It is worth noting that for peptide bonds, the entropy spectrum will consist of such low entropy values that a graph-rigidity analysis augmented by the preferential rule of placing lowest entropy distance constraints first, yields q_{kj}^{cnf} = 1 *always*. In this case, a constant contribution will always come from peptide bonds, rendering its affect on thermodynamic response. As such, the parameters for peptide bonds are unnecessary to specify. In contrast, for a rotatable covalent bond, usually 5 out of 6 distance constraints can be "frozen" out. However, the sixth distance constraint characterizes tolerances in the torsion-angle. Note that even using one energy basin to model a rotatable covalent bond can affect thermodynamic response because depending on other distance constraints in the network, the q_{k6}^{cnf} probability need not be 1 always, and thus not frozen out. For more accuracy, more than one basin can be considered of course, which would also provide variation in the energy if the energy basins correspond to frequent and rare angular ranges.

Intramolecular H-bonds: An intramolecular H-bond (IHB) identified in the template structure between residues r_1 and r_2 (labeled by the *h*-index) will be present when both residues are buried. When one residue is buried and the other is exposed to mobile solvent there is a probability p_h^{ihb} for this IHB to be present, otherwise it will be broken as shown in Fig. 6C. When both residues are buried as shown in Fig. 6B, there are four cases to consider because each buried residue may be native-like or disordered. Consolidating the four cases into two leads to either both residues are native-like, which defines a native IHB, otherwise a disordered IHB forms. The *h*-th native IHB will have energy, ε_{hHB}^{cnf}, and entropy spectrum, $\{\sigma_{hHBj}^{cnf}\}$, characteristic of the local geometry of the template structure. When one or both of the residues are disordered, the native geometry is disrupted, creating a disordered IHB. Therefore, it is natural to define two basins: A basin reflecting properties specific to the native geometry of the *h*-th IHB, and a basin with common properties for all disordered IHB. A disordered IHB is modeled with an energy, ε_{dHB}^{cnf}, and entropy spectrum, $\{\sigma_{dHBj}^{cnf}\}$, independent of location in the template. Since a H-bond has 3 atoms (donor, hydrogen acceptor) and there are *3n-6* distance constraints, all IHB subsystems will have j=1,2,3. Taking the conditional dependencies into account, G_{cnf}^{ihb} is given by:

$$G_{cnf}^{ihb} = \begin{cases} \sum_{h=1}^{H} \left[\left(\varepsilon_{hHB}^{cnf} - TR \sum_{j} q_{hnj}\, \sigma_{hHBj}^{cnf} \right) p_{r1}^{nat}\, p_{r1}^{nat} + \left(\varepsilon_{dHB}^{cnf} - TR \sum_{j} q_{hdj}\, \sigma_{hHBj}^{cnf} \right) \left(1 - p_{r1}^{nat}\, p_{r1}^{nat} \right) \right] p_{r1,b}\, p_{r2,b} \\ + \sum_{h=1}^{H} \left(\varepsilon_{dHB}^{cnf} - TR \sum_{j} q_{hdj}\, \sigma_{dHBj}^{cnf} \right) \left(p_{r1,b}\, p_{r2,m} + p_{r1,m}\, p_{r2,b} \right) p_{h}^{ihb} \end{cases} \tag{11}$$

The form of Eq. (11) follows a *general pattern* that applies to all conformational interactions. That is, there is a probability for the interaction to be present, possibly in a specific state, and under this local condition modelled by a particular basin, it contributes energy that adds to the system. Moreover, the conformational entropy that it contributes is non-additive due to network rigidity, which is used to calculate the probabilities for distance constraints to be independent. In the top term of Eq. (11), the q_{hnj} and q_{hdj} give the probabilities for the *h*-th IHB in the native and disordered basins respectively. Notice that the q_{hdj} in the lower term is the same as in the top term. When Eq. (11) is considered together with Eq. (7) and Eq. (8), we see the protein structure must balance enthalpy-entropy compensation in the hydrogen bond network of the protein versus forming H-bonds to solvent.

Hydration interaction: The hydration interaction is introduced to model the affect of aqueous solvent on a residue when it is exposed to a clathrate environment. In this case, the water molecules surrounding a residue form a *rigid motif* that manifests itself as a *mechanical clamp* on the residue. Many distinct molecular configurations can lead to a rigid motif. As such, a large number of basins are needed to fully characterise the structure of water molecules around a residue. However, this detailed information is difficult to obtain, and considering the level of coarse-graining that has been made in regards to residue solvation, and to the native-like and disordered classifications of a residue with respect to a template structure, it is appropriate to employ a single basin. Following the general pattern, G_{cnf}^{hyd} is given by:

$$G_{cnf}^{hyd} = -TR\, \sigma_{hyd} \left(\sum_{r=1}^{R} \sum_{j} q_{rcj} \right) p_{r,c} \tag{12}$$

In Eq. (12) the energy term is not included because it is already accounted for in the clathrate solvation energy parameter. The additive part of the solvation entropy parameter accounts for the solvent DOF having a reduction in conformational entropy. But *mechanical clamping* from the clathrate structure reduces conformational flexibility and entropy of the residue. This clamping is modelled by *3n-6* distance constraints to ensure the residue of *n* atoms is isostaticly rigid. A degenerate conformational entropy parameter is given by σ_{hyd}, and q_{rcj} gives the probability for the *j*-th distance constraint to be independent, where the *c*-subscript denotes clathrate. A reduction in conformational entropy at low temperatures is a critical mechanism to understanding cold denaturation, as shown in previous work [Jacobs & Wood, 2004]. Technically, this clamping effect could also be present for an exposed-mobile environment, and using the same modelling scheme but with different parameters would allow for different types of clamping depending on the details of the local water structure. Again, as found previously, breaking up this complicated many body interaction of water molecules on the protein into two simple states (mobile verses clathrate) proves sufficient.

Network rigidity: The non-additive reconstitution of total conformational entropy involving all entropy components is a critical aspect of the FEF. First note that the labelling scheme for component entropies across various interaction types is quite cumbersome, although useful for distinguishing their roles. In regards to network rigidity calculations, it is convenient to define a *parallel indexing scheme*. Let σ_c be the pure entropy of distance constraint, *c*, which runs from *1* to *C* to account for all accessible interactions. Note that the total number of distance constraints in a protein is *not equal* to *C*. Rather, if all identified subsystems were present *simultaneously*, which is not physically possible, *C* is the sum of the numbers of distance constraints in all subsystems defined by the template structure. The labelling of all these accessible entropies fall in sorted order such that $\sigma_c \le \sigma_{c+1}$. That is, $\{\sigma_c\}$ will play the role of an entropy spectrum for a template structure, but not all *levels* can be occupied.

As part of a general pattern, there is a probability for an interfacial subsystem to be present, and tracing over a chain of conditions as products of probabilities translates to an *occupation probability*, p_c, for an individual distance constraint. Similarly, q_c, is the probability that a distance constraint is independent given it is present. With this generic labelling scheme, the network rigidity part of the FEF is *compactly* stated by the following three formulas:

$$N_c = \sum_{c=1}^{C} p_c \quad I_c = \sum_{c=1}^{C} q_c\, p_c = 3n - 6 \quad \tau = \sum_{c=1}^{C} \left(q_c\, \sigma_c\right) p_c \tag{13}$$

The average number of constraints within a protein is N_c, which will generally be greater than the *3n – 6* DOF required to position all atoms in a protein. The minimum value that N_c can be is *3n – 6* corresponding to a protein in an *ideal* random coil state without any disulphide bonds (i.e. only residues and peptide bonds). Starting from a random coil, as intramolecular H-bonds crosslink the backbone, the number of constraints will increase. Yet the total number of independent constraints, I_c, that are present in the protein is *conserved* across all accessible constraint topologies to maintain a *rigid* protein. The condition of a rigid protein is required because it means that everything that can be specified is specified within tolerances. This property reflects the *completeness* of the FED. With the liberated view of rigidity, $R\tau$ provides a lowest upper bound *estimate* for the total conformational entropy.

3.2.4 Vibrational contributions

The contribution to the FEF from G_{vib} *would be* straightforward once the frequency is known for all 3n – 6 modes. Unfortunately, determining vibrational frequencies for the entire protein is a task that must be avoided to retain computational efficiency in the interfacial thermodynamics model. Therefore, the frequency spectrum is modelled *empirically* to capture two important features. Vibrational mode frequencies will (increase, decrease) as redundant distance constraints are (added, removed) to a network as it (stiffens, softens). Furthermore, the lowest frequency decreases as the size of the system increases. Assuming a vibrational frequency can be defined for each *c*-index, G_{vib} is given by:

$$G_{vib} = RT \sum_{c=1}^{C} q_c\, p_c \ln\left[1 - \exp\left(-\beta\hbar\omega_c\right)\right] \tag{14}$$

To account for the first feature, the entropy spectrum for the system is employed to define a frequency spectrum where $\omega_c = \omega_{\max}\sigma_{\min}/\sigma_c$ to reflect the generic property that frequency is inversely proportional to pure entropy. This relation would be sufficient if the entire protein was employed as the sole constituent, but the pure entropy spectrum is comprised from many small subsystems resulting in a range for ω_c not reaching sufficiently low frequency. By generalizing the Debye model [Kittel, 1996] for vibrations in a crystalline solid, system size dependence can be better accounted for. In the Debye model, the frequency spectrum is given as: $\omega_m = \omega_{\min} m$ for mode *m*, where $\omega_{\max} = \omega_{\min}(3n-6)$ is the maximum frequency possible assuming a *linear dispersion*, and knowing the total number of vibrational modes in the system. Inverting these relationships leads to $\omega_m = \omega_{\max} m/(3n-6)$. Combining both of these general aspects to model the frequency spectrum yields the empirical model:

$$\omega_c = \omega_{\max}\frac{\sigma_{\min}}{\sigma_c}\frac{\left(3n-5-\sum_{b=1}^{c} q_b\, p_b\right)}{(3n-6)} \tag{15}$$

In Eq. (15), the right-most fraction parallels the Debye model, where the numerator defines an *effective mode number* that ranges from *1* to *3n – 6*. Mode (*3n – 6*) corresponds to *c=1*, or the lowest *c*-index present in the network. As the mode index decreases with increasing *c*-index, the frequency of vibration lowers in the same way as the Debye model. The front scale factor $\sigma_{\min}/\sigma_c$ (i.e. $\sigma_{\min} = \sigma_1$) modifies the dispersion, which is required to span a disparate range of vibrational frequencies typical of proteins. Consequently, as more redundant constraints appear in the network, the lowest frequency mode will be reached sooner on the entropy ladder (smaller *c*-index) so that the lowest lying vibrational frequencies shift higher without affecting high frequencies. The spectrum for a protein in a random coil will reach the lowest possible frequency. Note that upon protein-ligand binding, frequency shifts that take place due to changes in the constraint network and size of the system are roughly accounted for.

4. Self-consistent constraint theory

The essence of constraint theory applied to an interfacial thermodynamics model is to determine how a system responds under certain *global* conditions that are consistent with *microscopic* heterogenous environments. The previous section constructed a FEF to describe protein stability by building up a hefty collection of free energy terms representing specific enthalpy-entropy mechanisms. This process lead to conjuring up the probability functions $\{p_{rs}, p_h^{ihb}, p_r^{nat}, p_c, q_c\}$ that will be determined self-consistently when solving the FEF. In doing so, it is critically important that *heterogeneous micoenvironments* throughout the protein are taken into account. An efficient way to solve the FEF is to introduce a number of *constitutive equations* to transform the functional into a variational problem in parametric form that allows certain global constraints to be imposed. Specifically, a trial function with a number of variables is substituted into the functional to reduce the problem to finding the minimum of a function. These variables correspond to Lagrange multipliers that control the values of selected order parameters. Actually, this method builds upon a previous method used to solve the mDCM (Jacobs & Dallakayan, 2005), but there are critical differences.

First, I highlight key points about the initial method (Jacobs, 2006b) for solving the mDCM. Occupation probabilities $\{p_c\}$ are calculated using Lagrange multipliers to enforce the amount of intramolecular H-bonds and native-like character within a protein. Given $\{p_c\}$, a constraint network is randomly generated, and a rigidity algorithm is applied with the preferential entropy rule to identify the distance constraints as independent ($\tilde{q}_c = 1$) or redundant ($\tilde{q}_c = 0$). After collecting N_s *random samples*, an estimate is given as $q_c = \langle \tilde{q}_c \rangle$. By focusing on distance constraints, all the formulas in Eq. (13) apply, and N_s should be at least 200 to obtain a *useful* estimate for conformational entropy, $R\tau$. The employed trial function for p_c does not depend on whether a distance constraint is independent or not. For this information, p_c must be a function of q_c. In this latter case, the calculation scheme would then be to assume $q_c = 1$, calculate p_c, determine $q_c = \langle \tilde{q}_c \rangle$ from sampling, then recalculate p_c, and iterate this process until the latest values of p_c are nearly equal to the previous values of p_c within some tolerance to obtain self-consistency.

To simply implement this self-consistent approach using averaging does not work because convergence will not occur when the precision in q_c is low. To ensure convergence, N_s *should be at least 500,000*, suggesting a self-consistent calculation is not tractable! Recently, a new algorithm to calculate average network rigidity properties as a *probability flow* problem describing independent DOF and where DOF absorb onto constraints has been successfully developed [Gonzalez, et al. 2011a, Gonzalez, et al. 2011b]. Now q_c is calculated to within numerical precision, making the self-consistent calculation feasible. Also different from the mDCM: The FEF described above has almost all conformational subsystems that involve distance constraints coupled to the solvation states of residues, as well as other interfacial surface terms between the residues that reflect local microenvironments. Tracking these additional details goes far beyond the mean field treatment invoked in the mDCM. Consequently, a very different set of order parameters need to be considered.

4.1 Order parameters and the free energy landscape

The free energy of a protein is numerically calculated while subjected to global constraints imposed by order parameters that define a specific macrostate. Scanning over the entire range of order parameters produces the FEL. Since a protein is of finite size, the minimum free energy is not the only point on the FEL of interest. Rather, the entire FEL is of interest because it maps out all the low-lying basins and saddles. The natural variables of the FEF that describe microstates dictate the form of the macrostates, and this determines what order parameters need to be considered. The solvent environment of the residues and whether they are native-like when buried is the only information needed to completely define the microstate of a protein. Therefore, order parameters B, M and N are introduced to specify the macrostate of a protein, giving the total number of residues that are respectively *Buried*, exposed to *Mobile* solvent and *Native-like*. Note that the number of residues in the exposed clathrate state[4], H, is not an independent variable, since the total number of residues, R, is given by: $R = B + M + H$. Furthermore, there is a restriction on N, such that $0 \le N \le B$. As such, the FEL is expressed as $G(B, M, N \mid T, \cdots)$ where the triple dots are a reminder that in

[4] The more natural symbol of C is already used, and the symbol H better reflects the idea of a local hydration shell.

addition to temperature, pressure and pH can be directly considered, although not here, and, many parameters in the FEF depend on solvent composition.

4.2 Hierarchical application of global constraints

The macrostate (B, M, N) is associated with the following three constraint equations:

$$B = \sum_{r=1}^{R} p_{r,b} \quad M = \sum_{r=1}^{R} p_{r,m} \quad N = \sum_{r=1}^{R} p_r^{nat}(1 - p_{r,b}) \tag{16}$$

Instead of solving these three equations simultaneously, the calculations are simplified by assuming B can be solved for first, then M, and finally N. To reflect this hierarchical chain, the constitutive equations for the probability functions are expressed in terms of conditional probabilities when necessary. Let $Z_{rs}^{slv} = \exp(\alpha_{rs}^{slv} - \beta \varepsilon_{rs}^{slv})$ and λ_B, λ_M and λ_N be the Lagrange multipliers for the B, M and N order parameters respectively. With $p_{r,c} = 1 - p_{r,b} - p_{r,m}$, the constitutive equations for $p_{r,b}$ and $p_{r,m}$ are given as:

$$p_{r,b} = \frac{Z_{rb}^{slv} \exp(\chi(r)\lambda_B)}{Z_{rb}^{slv} \exp(\chi(r)\lambda_B) + Z_{rm}^{slv} + Z_{rc}^{slv}} \quad p_{r,m} = \frac{Z_{rm}^{slv} \exp(\phi(r)\lambda_M)}{Z_{rm}^{slv} \exp(\phi(r)\lambda_M) + Z_{rc}^{slv}}(1 - p_{r,b}) \tag{17}$$

The Lagrange multipliers λ_B and λ_M are coupled to propensity functions $\chi(r)$ and $\phi(r)$ respectively. Propensity functions characterize physical and/or chemical properties relevant to their conjugate order parameters in the local environment surrounding residue *r*, based on the template structure. The local propensity for being buried is $\chi(r)$, defined as the number of nearest neighbour contacts to residue, *r*. The greater number of nearest neighbours a residue has in the template structure, the greater resistance to solvent penetration irrespective of its intrinsic solvation character quantified by the Z_{rs}^{slv} factors. For $\phi(r)$, it is set to *1*, so that no differentiation is made between clathrate and mobile exposed microenvironments. The template structure is used to define local microenvironments that individual residues will experience. By adjusting the Lagrange multipliers, the total number of residues buried and exposed to mobile solvent is controlled (at least on average). Note that fluctuations are accounted for in the FEF through the mixing entropy terms. Constraining a protein to macrostate (B, M, N) corresponds to selecting a sub-ensemble of microstates that share the common property that the total numbers of buried and exposed to mobile residues are B and M. It is seen from Eq. (17) that the calculation for $p_{r,b}$ based on the global constraint B is independent of M and N. Then the result for $p_{r,b}$ hierarchically feeds into the next level of calculation for $p_{r,m}$ involving the global constraint M.

The next hierarchical step is to calculate p_r^{nat} with N fixed. The two constitutive equations that come into play are:

$$p_r^{nat} = \frac{\exp(-\beta \varepsilon_{rn}^{cnf} + \sum_j q_{rnj}\, \sigma_{rnj}^{cnf} + \lambda_N)}{\exp(-\beta \varepsilon_{rn}^{cnf} + \sum_j q_{rnj}\, \sigma_{rnj}^{cnf} + \lambda_N) + \exp(-\beta \varepsilon_{rd}^{cnf} + \sum_j q_{rdj}\, \sigma_{rdj}^{cnf})} \tag{18}$$

$$p_h^{ihb} = \frac{\exp(-\beta\varepsilon_{dHB}^{cnf} + \sum_j q_{hdj}\,\sigma_{dHBj}^{cnf})}{\exp(-\beta\varepsilon_{dHB}^{cnf} + \sum_j q_{hdj}\,\sigma_{dHBj}^{cnf}) + \exp(-\beta\varepsilon^{shb} + \alpha^{shb})} \tag{19}$$

The form of Eq. (18) is that it has a Boltzmann factor for a native-like state in the numerator, divided by the sum of Boltzmann factors for the native-like and disordered states. This ratio gives the probability that residue, *r*, will be in the native-state. The Boltzmann factor for the native-like state contains the Lagrange multiplier, λ_N, to enforce the number of native-like residues in the system to be, N, in accordance with Eq. (16). The form of Eq. (19) is similar, except the numerator is the Boltzmann factor for a disordered IHB, and the denominator is the sum of Boltzmann factors for a disordered IHB and a protein-solvent H-bond. These two possibilities compete head to head, but there is no additional Lagrange multiplier, as this process is not tied to an order parameter.

It is clear from Eqs. (18 and 19) that knowing the probability certain distance constraints in the constraint network are independent is necessary. However, these *q*-values are initially unknown, and therefore, an iterative self-consistent calculation must be invoked. Note that the probability for a distance constraint to be present is equal to the probability for the basin that it is a member of to be present in the network. For example, all distance constraints used to model the conformational part of the free energy for residue, *r*, when it is native-like is equal to p_r^{nat}. Conversely, the probability of $(1-p_r^{nat})$ is assigned to all the distance constraints for this residue when it is in a disordered state.

The occupation probabilities, p_c, is 1 for quenched constraints, or it is straightforward to get the probabilities from $\{p_{rs}, p_h^{ihb}, p_r^{nat}\}$ once they are known. There is, of course, a chicken and egg problem because q_c is determined after p_c is known, but q_c must be known before p_h^{ihb} and p_r^{nat} can be calculated. The procedure is to guess the initial values of q_c, calculate p_c, apply a rigidity analysis to obtain q_c and then recalculate p_c. Iterate this process until the values for both p_c and q_c converges. Note that these equations converge to the unique solution independent of initial guess. The type of guesses tried include, for each *c*-index q_c set to 1, set to 0, or set to a value between 0 and 1, or independently assign a random number between [0,1]. Notice that q_c and p_c imply one-dimensional arrays for *c=1* to *C*. In fact, any variable that has one index or more than one index implies an array of values. It is worth mentioning here that convergence is reached typically within 15 iterations using the new rigidity algorithm [Gonzalez, et al. 2011a]. However, MCC yields qualitatively similar results, and as described next, captures the essential features about the role of rigidity.

4.3 The entropy spectrum and maxwell constraint counting

The entropy spectrum for an example set of subsystems that can be found within a protein is schematically shown in Fig. 7. Applying MCC with the preferential entropy rule is equivalent to filling the available levels of the entropy spectrum of the system starting from the bottom until the system becomes isostatically rigid. All the distance constraints that are placed in the network before the protein has the minimum number of constraints to become isostatically rigid are considered independent. As more distance constraints are added to the network, they are all redundant. This global and uniform transition point between where

the constraints are independent and redundant defines the Maxwell level. This means, that $q_c = 1$ for $1 \le c < M_L$ and $q_c = 0$ for $M_L < c \le C$ and $0 < q_c \le 1$ at $c = M_L$. Let q_M be the value of q_c at the Maxwell level. Then the self-consistent calculations described above amounts to finding a solution in the form of a step function, where the only unknown is where the step is located on the entropy spectrum of the system.

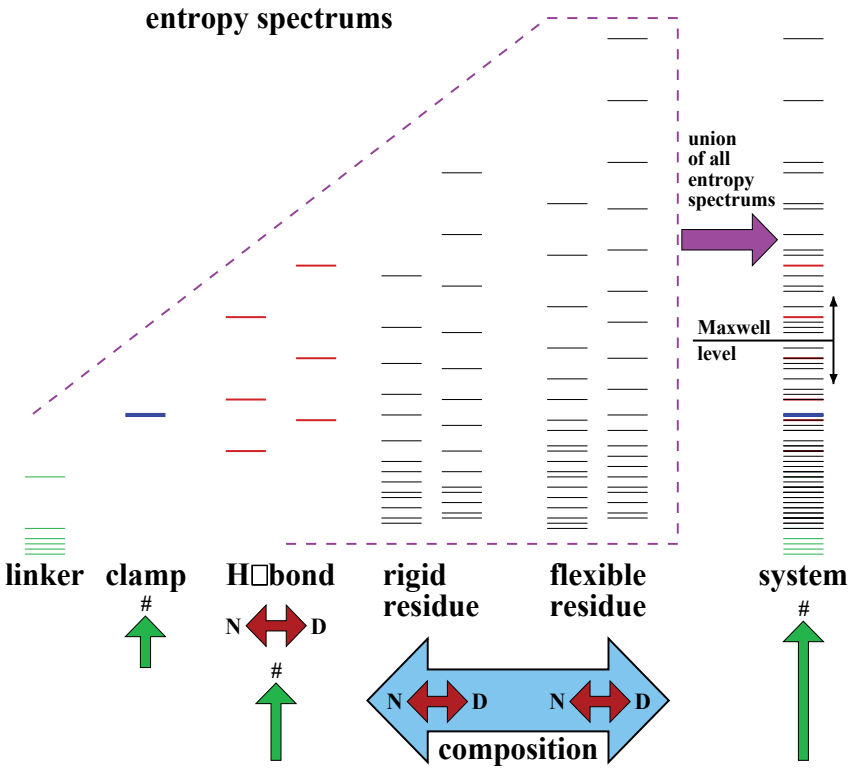

Fig. 7. Schematic of how the entropy spectrums associated with subsystems combine into a single entropy spectrum for the entire system. Green vertical arrows pointing to the # sign indicate that the number of interactions depend on the decorated microstate. The "clamp" interaction derives from clathrate water. The horizontal dark red double arrow indicates a certain number of interactions can be native like (N) or disordered (D), and their respective entropy spectrums are shown. Each residue has a unique entropy spectrum. Residues with (smaller, larger) entropy values are more (rigid, flexible). The protein sequence defining the residue composition is represented as the large horizontal blue double arrows. The system entropy spectrum is characterized by the variables (p_c, q_c). From Eq. (20) distance constraints with entropy less than the Maxwell level are independent, and this level slides up and down the spectrum depending on numbers and types of interactions present in the system.

For a given specification of p_c the Maxwell level is determined by solving the equation:

$$3n - 6 = \sum_{c=1}^{M_L - 1} p_c + D_{M_L} q_{M_L} \tag{20}$$

In Eq. (20) the variable D_{M_L} is the degeneracy for the number of distance constraints having the same entropy value at the Maxwell level. Notice that Eq. (20) reflects the step nature of q_c. Despite the simplicity of the global constraint expressed in Eq. (20), the self-consistent solution results in a dramatic impact on the thermodynamic response of the system. This is because in general every constraint in the network is competing against all other constraints that are present in the network. What changes is the number of distance constraints that appear within the protein for different macrostates. As more constraints are added to the network, the entropy drops.

4.4 Response of local environments to global demands

The type of intramolecular interactions and their locations within a protein depends on the solvation state of the residues and local environments encoded by the amino acid sequence and template structure. For example, using the fold architecture shown in Fig. 4, and for the solvation decoration shown in Fig. 5, a hydrophobic homo-polymer (HH), a heterogeneous protein (HP) and a polar homo-polymer (PH) are shown in Fig. 8.

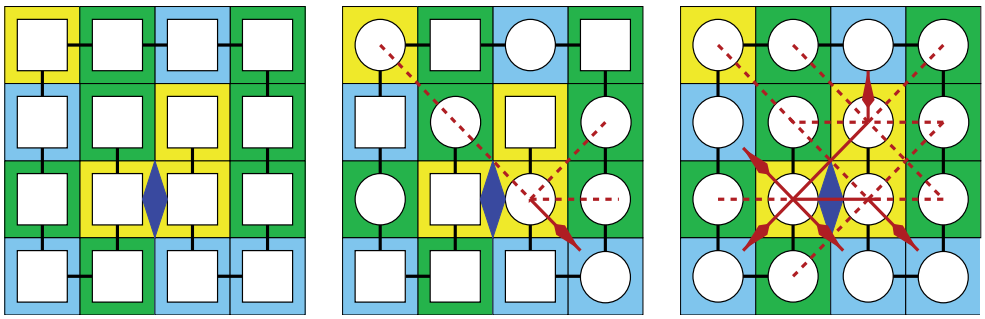

Fig. 8. Schematic illustration of three sequences with the same architecture and solvent decoration. Hydrophobic residues (squares) do not participate in H-bonding. H-bonding is only allowed between polar residues (circles) that are nearest or next nearest neighbours not linked by covalent bonds. Because of the solvent decoration there is only one hydrophobic interaction, shown as a dark blue diamond. Non-fluctuating intra-H-bonds are shown as solid red lines, and red dashed lines indicate fluctuations between intra- and solvent-protein H-bonds. From left to right the three panels show the HH, HP and PH cases, respectively exhibiting (no, limited, many) intramolecular H-bonds for this solvation microstate. The hydrophobic interactions are identical across the three sequences because they only depend on the transfer of water from buried regions to bulk solvent, which is the same in all cases.

In water, HH will form a collapsed state much like an oil droplet. PH will be soluble and will resemble a random coil because few crosslinks form. HP can potentially produce a rich phase diagram. In the next section, stability curves for all three of these *toy* polymers will be shown based on model parameters that were adjusted to produce heat and cold denaturation in HP for the purpose to facilitate general discussions. The same parameters are used for all three cases, and they are in a physically reasonable range. However, the toy models are not structurally realistic, therefore, the parameter values (not given here) are not important. Rather, the *critical issue* at hand is developing a tractable paradigm that can

accurately model the complexity of all the coupled interactions within/on a protein, and do this in a computationally efficient way.

Self-consistent constraint theory applied to the FEF determines the microenvironments that emerge as *most probable*. Although Eq. (3) and Eq. (4) *at face value* appear to be additive, the myriad coupling between interactions will cause two interactions of identical type placed in different microenvironments and/or under different solvent and thermodynamic conditions to respond differently. In particular, the coupling through network rigidity *renormalizes* the conformational entropic contributions (via the q_c values), and this strongly affects where and how solvent penetrates the protein; thus changing the properties of local environments, which impacts the constraint network. For example, a cluster of H-bonds can form a strong nucleation barrier causing a localized buried region to be highly resistant to solvent penetration compared to a similar buried region without a H-bond cluster. Consequently, *non-additive response derives from a chemicophysical feedback loop*. This is captured in the *process of minimizing the free energy* to determine the optimal constraint topology and solvent decoration under the specified thermodynamic and solvent conditions for a given template structure while satisfying Eq. (16) and Eq. (20) for a particular macrostate (B, M, N).

4.5 The Gibbs triangle

The algorithm that is applied to solve the FEF takes the following steps.

1. Scan over the temperature, T, and other thermodynamic and solvent conditions.
2. Calculate $p_{r,b}$ while the variable B is looped over.
3. For given B: Calculate $p_{r,m}$ and $p_{r,c}$ while the variable M is looped over.
4. For given B and M:
   a. Self consistently solve for all p_c and q_c while the variable N is looped over.
   b. Finalize calculation for all probability functions: $\{p_{rs}, p_h^{ihb}, p_r^{nat}, p_c, q_c\}$.
   c. Calculate the free energy: $G(B, M, N \mid T, \cdots)$.
5. Finish all nested loops over N, M and B.

A high dimensional FEL is obtained once the algorithm finishes. In the example considered here, the FEL is four dimensional, consisting of temperature and the three order parameters, (B, M, N). When the free energy value is included to perform an exploration of the FEL, a five-dimensional space is required! Basins for stable and metastable states and free energy barriers between these states can be identified. Within a basin, information about flexibility and its relationship to stability can be obtained. However, protein stability can largely be understood in terms of its solvation properties. Therefore, it proves convenient to construct a two-dimensional version of the FEL specified only by (B, M) to describe how a protein is solvated. At fixed T, this construction is given as:

$$G_2(B,M) = -RT\ln(Z_2) \quad Z_2(B,M) = \sum_{N=0}^{B} \exp\left[-\beta G(B,M,N)\right] \tag{21}$$

The free energy $G_2(B,M \mid T)$ describes the stability of a protein based on a macrostate that characterizes the solvation property of the protein. For fixed T, it is convenient to look at a

phase diagram in terms of how much the protein is buried or exposed to solvent in different forms. Because of the constraint that $1 = (B + M + H) / R$, a Gibbs triangle is employed so that all solvation states can be viewed simultaneously in terms of percentages, as shown in Fig. 9.

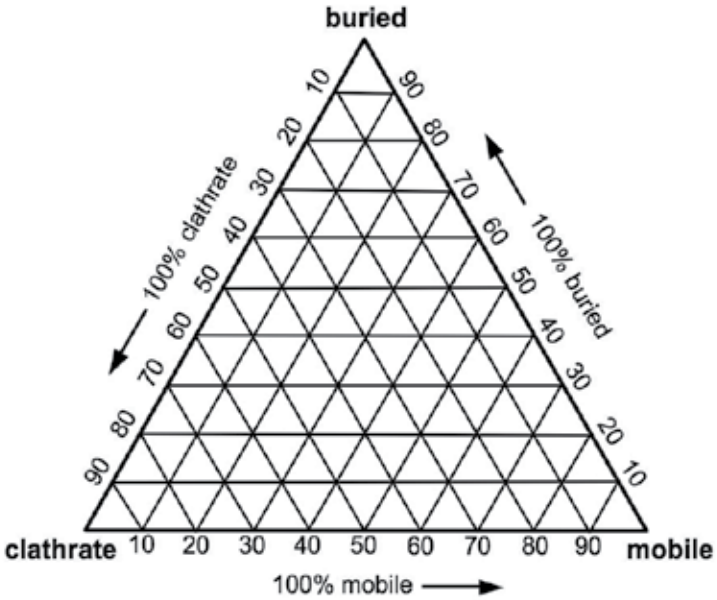

Fig. 9. The Gibbs triangle serves as the base of a three-dimensional FEL that looks like a wedge when viewed at fixed temperature and using the B, M and N order parameters. That is, $N = 0$ on the bottom horizontal line when $B = 0$, and the tip of the wedge is at $B = 1$.

Three stable basins will generically appear in the Gibbs triangle. At low temperatures, it is possible that a free energy minimum will appear when the percent of clathrate structure is dominant. At intermediate temperatures, the number of buried residues in the protein will be dominant, but they can be native-like or disordered. Therefore, a protein may be in either the molten globular[5] or native-fold states. At high temperatures, a molten globular state may remain, or further unfold to allow a majority of residues to become exposed to solvent. Next, the free energy of three representative macrostates is plotted as a function of temperature. Structural phase transitions corresponding to changing free energy basins are like first order transitions, because they occur when stability curves for different states cross one another.

5. Stability curves: Heat and cold denaturation

The stability curves for the toy polymer cases (HH, HP, PH) shown in Fig. 8 are calculated for three macrostates in the Gibbs triangle that correspond to a dominant characteristic of

[5] The degree to which a protein is native-like versus disordered is lost during the process of summing over the native-like order parameter in Eq. (21). However, this information is known from the original 3D free energy landscape.

clathrate, buried or mobile, and these curves are plotted in Fig. 10 A, B, C respectively. In fact, the particular decoration shown in Fig. 8 has a much higher free energy than the lowest free energy state, and is for practical purposes a state of measure zero. Nevertheless, the FEF determines the statistical weights for all macrostates in the high dimensional FEL, and the high free energy states around saddles are important in describing transition states.

As expected, the HH case shows that the buried state is the most stable form over the entire temperature range, and thus there is no phase transition. For the PH case, the structure is always exposed to solvent, but it is interesting to note that there can be a structural phase transition in a protein between low and high temperature without it involving a compact folded structure. This result suggests there is a difference between structural properties in the conformational ensembles of a cold- and heat-denatured polymer. Interestingly, the HP case exhibits both cold and heat denaturation. In all likelihood, a protein of this size (16 residues) would not exhibit a phase transition, however, the parameters were optimized to make this situation occur for the HP case. Although the same set of parameters is used for the HH and PH cases, the competing enthalpy-entropy compensation mechanisms within a heterogenous protein (modelled by HP) make it possible for such a rich phase diagram.

The phenomenon of cold denaturation often does not occur because the temperature at which it *would* take place is too low to be observed. Osmolytes can be used to modify bulk solvent properties to control where the crossing points of the triangle shown in Fig. 10B occur. It is seen in Fig. 10D that the total entropy of a protein increases as a function of temperature. Fig. 10E shows that the order parameter for clathrate solvation content is a monotonically decreasing function of temperature, so that at higher temperatures a greater competition between buried and exposed-mobile states occur. Other order parameters can be easily calculated, such as the number of intramolecular H-bonds or hydrophobic contacts, which are shown in Fig. 10F as tracking one another. Although not shown here, tracking the native contact order parameter allows one to determine if a compact structure is native-like or that of a molten globular. In general, detailed information about solvent penetration and mechanical response of a protein is predicted at fine resolution, and this interplay is very important to protein function [Purkiss, et al. 2001], and these relationships have been more recently been probed experimentally [Kamerzell, et al. 2008; Pais, et al. 2009].

5.1 Conformational ensembles in the native and denatured states

Experiments indicate that native structure *persist* in the denatured states of proteins at low temperature [Shan, et al. 2010] and high temperature in the molten globular state [Shortle, 1999]. Established many years ago, the converse is true: There is appreciable solvent penetration into the native state [Woodward, et al. 1982], while buried secondary structure regions can be very resistant to solvent penetration [DeFlores & Tokmakoff, 2006]. These experimental results suggest to me that using template structures is justified, although this is not to say non-native contacts are negligible. For these cases, multiple templates should be used and these other templates can be computationally generated.

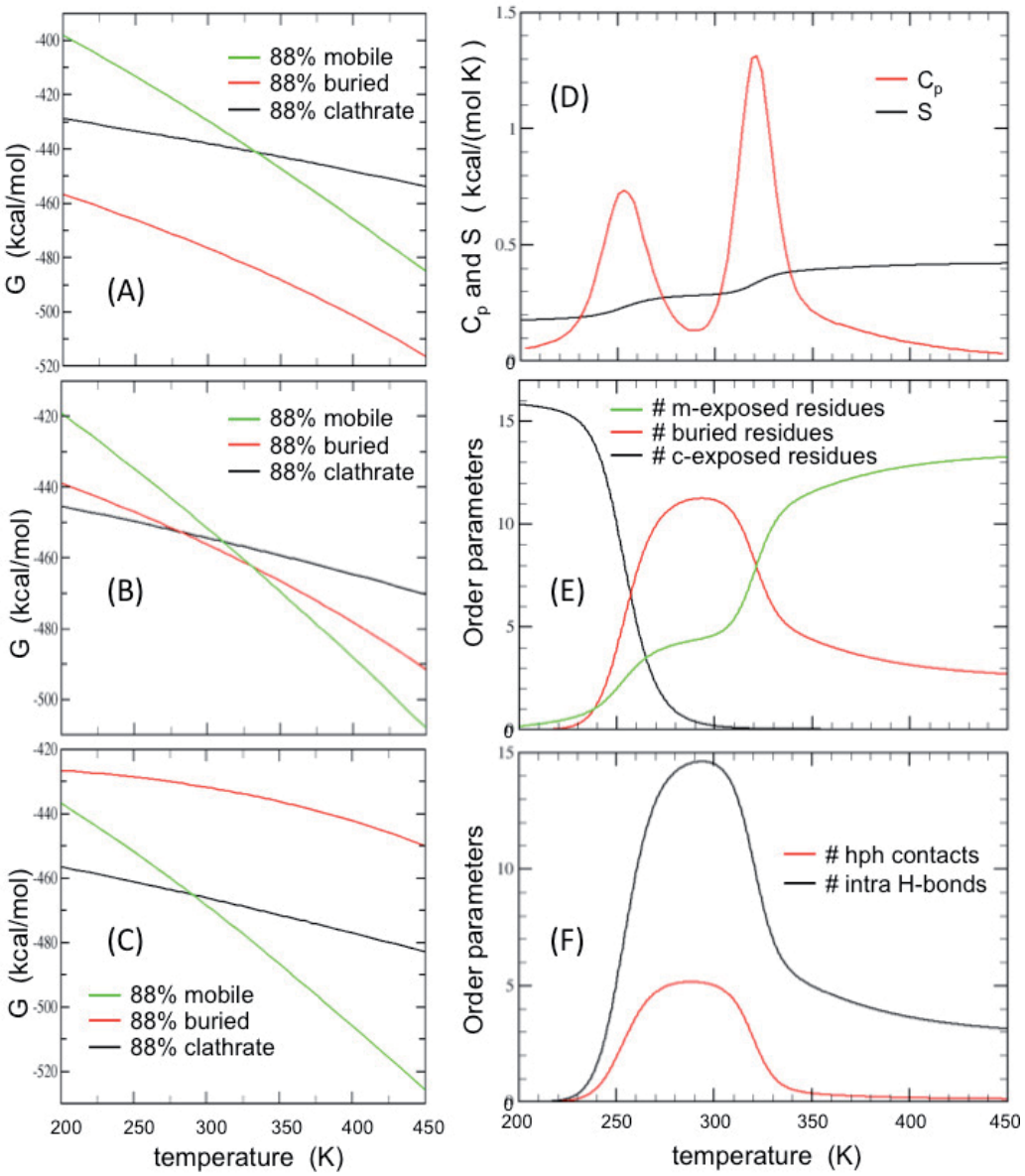

Fig. 10. Left column: The stability curves are shown for macrostates corresponding to a majority of residues that are clathrate (black), buried (red) and mobile (green). In all cases the majority contributor is 88%, and the two minority contributors are each 6%. Thus, the macrostates selected are located at the apex of each corner in the Gibbs triangle. In A, B, C, results are given for HH, HP and PH respectively. Right column: For the HP case only, D) shows the heat capacity and entropy, and E & F show the temperature dependence on five different types of order parameters that respectively correspond to the residue solvation states (clathrate, buried, mobile) and numbers of H-bonds and hydrophobic contacts.

5.2 Phenomenological modeling of protein stability

The standard thermodynamic analysis for protein stability assumes two states describe an unfolded (U) and folded (F) structure. The *mechanism of protein unfolding is hidden* in the temperature dependence of $\Delta G = G_U - G_F$. Specifically, ΔG is a concave quadratic function of temperature with two solutions for $\Delta G(T) = 0$ that yields $T = T_C$ for *cold* denaturation and $T = T_H$ for *heat* denaturation. However, the fact that two transition temperatures exist at all implies a minimum of two order parameters are required to describe the phenomena. The order parameters characterize the emergent behaviour of microscopic properties, which inspired the idea of modelling residue solvation states as three possible states. In a similar way, the molten globular state is distinct from the native state with respect to the degree of disorder, which inspired applying the native-like order parameter to define the FEL. Three independent order parameters appear to me as the minimum number of descriptors to describe protein stability consisting of the exposed unfolded state at low temperature, the compact native and molten globular states, and, the exposed unfolded state with little to no residual secondary structure at high temperature. The results presented in Fig. 10 produced three distinct states[6], indicating the ensemble of conformations of the unfolded state is structurally distinct at low and high temperatures, as demonstrated by the PH example in Fig. 10C. However, the *controversial* clathrate mechanism is invoked and it appears essential.

5.3 Clathrate mechanism for cold denaturation: Fiction or reality?

Models often invoke the clathrate mechanism to describe cold denaturation [Hansen, et al. 1998; Widom, et al. 2003]. The notion of this mechanism is based on *interpretations* of indirect measurements, which has been scrutinized [Graziano, 2004; Lopez, et al. 2009; Oshima, et al. 2009]. However, the critical review on protein hydration dynamics in solution [Halle, 2004] appears to me to dispel paradoxes that result from the controversy. Although the name clathrate may or may not be misleading, the interfacial thermodynamics model is based on general principles of statistical mechanics, which does not depend on a name. All that matters is the affect on the protein from solvent. The interfacial thermodynamics model accounts for native-like and disordered structure, and solvent penetration due to structural deformations. The model requires a partition function for the ensemble of water configurations around a residue, and an empirical contact term representing the affect on the protein's flexibility. This partition function is surely difficult to calculate from first principles, but a partition function can always be partitioned (hence the name) into a sum of terms. Dividing all configurations into two groups that classify the solvent in contact with a residue based on whether there is a small or large reduction in flexibility, no matter how small the difference may be is a valid *mathematical exercise* that does not change the physics because no Boltzmann factors are dropped.

The *exact* partition function, Z, is written as: $Z = Z_c + Z_m$ where Z_c sums over all terms that reduces the flexibility in the residue more than the terms summed in Z_m, no matter how small of a difference there may be. Therefore, Z_m describes a *more-mobile* water-residue

[6] Actually four distinct states are possible: Unfolded at low or high temperature, a native-like fold and a molten globular.

system, and Z_c describes a *less-mobile* water-residue system. Because "more-mobile" and "less-mobile" is cumbersome, I prefer to use the names *mobile* and *clathrate*. However, the important point is that it is not the property of water that is more or less mobile, it is the interaction between the water and residue that cause the residue to be more or less mobile, which is the basis of the classification. In fact, this description has been done for the twenty amino acids found in proteins to arrive at all the necessary solvation parameters [Du, et al. 2011]. Therefore, the notion of a clathrate mechanism is a *reality*, but it may not correspond to the original notion, and it must be calculated in the context of a large ensemble of water-residue configurations, where the flexibility of the residue must be quantified and assessed. Furthermore, a more refined classification scheme is in principle possible.

6. Unifying different perspectives on protein stability

Recent work on the thermodynamic response of a system subjected to geometrical constraints [Chen, et al. 2009] suggests that indirect intermolecular correlations, rather than geometric constraints, are the key to achieving a first-order phase transition. Although this latter conclusion was obtained in a different context, it appears the same idea is implied in the interfacial thermodynamics model. In particular, the template structure provides the native-state geometrical constraints, but all subsequent calculations only involve molecular correlations. That is, terms in the FEF couple intramolecular interactions to residue solvation properties as the protein conformation changes, albeit no new geometries are generated.

I was surprised that the "standard model" for protein stability and folding was criticized with much scrutiny recently [Ben-Naim, 2011] with several misconceptions highlighted. The main concerns raised were: 1) Free energy landscapes must be used to quantify protein stability, not energy landscapes; 2) non-additivity is an inherit property of entropy; 3) stability differences due to the trade off between intramolecular and protein-solvent H-bonds are too weak to drive protein folding; 4) hydrophobic interactions are also too weak to be the *dominant* driving force; whereas 5) the hydrophilic interactions are the strong driving forces that fold a protein. These five points and the clathrate mechanism controversy provide an opportunity to exam the assumptions of the interfacial thermodynamics model.

All solvation effects appear either as volume terms for the primary constituents (residues) or as surface terms between the interfaces of these constituents. The volume and surface terms taken together represent hydrophilic and hydrophobic interactions, the clathrate mechanism and protein-solvent H-bonds interactions using implicit solvent. Non-additivity in entropy components is a primary concern of the approach, and it directly deals with the free energy landscape. Moreover, all parameters have thermodynamic interpretations. For example, the parameters $(\varepsilon^{hph}, \alpha^{hph})$ for the hydrophobic interaction combine into the chemical potential to transfer a water molecule from a buried region in the protein to bulk solvent. In short, the modelling scheme put forth is complete, with the exception of long-range electrostatics.

7. Future direction

The particular FED that has been described above to define all the terms in the FEF, and using the simple MCC in the self-consistent constraint theory calculations is but one possible implementation of the interfacial thermodynamics model for protein stability. Similar to the

strategy described here, but with finer coarse-graining [Jacobs, 2007b], new software called *FAST* is being finalized. *Flexible to Flexibility* proteins to predict myriad thermodynamic and mechanical properties for high-throughput applications. With my collaborator Prof. Dennis Livesay at UNC Charlotte, and our research associates, Dr. Hui Wang and Dr. Chuanbin Du, the software has been designed and coded in C++ from scratch to provide a stable platform to support calculations similar to those described here. The FEF is of a general form that includes accounting for protonation states on titratable residues and explicit packing interactions. Moreover, the FEF is self consistently solved using an accurate rigidity algorithm for which Dr. Luis Gonzalez has helped develop, and he has documented its accuracy over the course of his Ph.D. studies. Many results to be published have been reported at several conferences, such as how model parameters are determined. With the Herculean effort spent on computational methods and optimization by Dr. Wang, *FAST* exceeds the speed of the mDCM and has greater accuracy. Going forward, the main concern is to find support to finish *FAST* so it can be released as free software to academic users.

8. Conclusion

From conception, the interfacial thermodynamics model for protein stability was designed to balance accuracy with computational cost such that it can be applied in high-throughput applications. To meet this *pragmatic objective*, the fundamental problem of non-additivity of conformational entropy that plagues free energy decomposition schemes has been tackled directly by employing the Distance Constraint Model. In particular, network rigidity is invoked as an underlying long-range interaction that couples entropy components between intramolecular subsystems comprising a protein. The problem is formulated as a free energy functional, and it is numerically solved using constitutive equations and self-consistent constraint theory. While the model makes many approximations, it is able to retain essential elements that describe protein thermodynamics and mechanical properties. Perhaps the best aspect of the interfacial thermodynamics model is that every term is intuitive physically and chemically. Different types of enthalpy-entropy compensation mechanisms can be modeled, and their competing effects can be simultaneously calculated with high efficiency.

9. Acknowledgement

This work has been supported by NIH R01 GM073082.

10. References

Andricioaei, I. & Karplus, M. (2001). On the calculation of entropy from covariance matrices of the atomic fluctuations, *J. Chem. Phys.*, Vol.115, pp. 6289-6292

Bakk, A. & Hoye, J. (2003). One-dimensional Ising model applied to protein folding. *Physica A*, Vol.323, pp. 504-518

Ben-Naim, A. (2011). Some aspects of the protein folding problem examined in one-dimensional systems, *J. Chem. Phys.*, Vol.135, No.085104, pp. 1-15

Bar-Yam, Y. (1997). *Dynamics of complex systems*. Addison Wesley Longman, Inc., ISBN 0-201-55748-7

Bray, D. & Duke T., (2004). Conformational Spread: The Propagation of Allosteric States in Large Multiprotein Complexes. *Annu. Rev. Biophys. Biomol. Struct.* Vol.33, pp. 53–73

Chen, Y., Kilburg, R. & Donohue, M. (2009). Thermodynamics of systems with different geometric constraints and intermolecular correlations, *J. Phys. Chem. B,* Vol.113, pp. 12530-12535

Costa, J. & Yaliraki, S. (2006). Role of rigidity on the activity of proteinase inhibitors and their peptide mimics, *J. phys. Chem. B,* Vol.110, pp. 18981-18988

David, C. & Jacobs, D. (2011). Characterizing protein motions from structure, *J. Mol. Graph Model,* Vol.31, pp.41-56

Dill, K. (1990). Dominant Forces in Protein Folding. *Biochemistry,* Vol.29, pp. 7133-7155

Dill, K. (1997). Additivity principles in biochemistry, *J. Biol. Chem*., Vol.272, pp. 701-704

DeFlores, L. & Tokmakoff, A. (2006). Water penetration into protein secondary structure revealed by hydrogen-deuterium exchange two-dimensional infrared spectroscopy, *J. Am. Chem. Soc.,* Vol.128, pp. 16520-16521

Du, C., Wang, H., Livesay, D. and Jacobs, D. (2011). *A Three-State Model of Amino Acid Solvation that Accounts for Hydration at Low Temperatures*, (in review)

Farrell, D., Speranskiy, K., & Thorpe, M. (2010). Generating stereochemically acceptable protein pathways, *Structure, Function, and Bioinformatics,* Vol.78, pp. 2908–2921

Fuxreiter, M., Magyar, C., Juhasz, T., Szeltner, Z., Polgar, L. & Simon, I. (2005). Flexibility of Prolyl Oligopeptidase: Molecular dynamics and molecular framework analysis of the potential substrate pathways, *Proteins: Structure, Function, and Bioinformatics,* Vol.60, pp. 504-512

Gonzalez, L., Wang, H., Livesay, D. and Jacobs, D. (2011a). *A virtual pebble game to ensemble average graph rigidity* (in review)

Gonzalez, L., Wang H., Livesay, D. &Jacobs ,D. (2011b). *Calculating Ensemble Averaged Descriptions of Protein Rigidity without Sampling,* in press, Plos One.

Graziano, G. (2004). Comment on "The hydrophobic effect" by B. Widom, P. Bhimalapuram and K. Koga, *Phys. Chem. Chem. Phys*., 2003, Vol.5, pp.-3085, *Phys. Chem. Chem. Phys*., Vol.6, pp. 4527-4528

Gunsteren, W., Bakowies, D., Baron, R., Chandrasekhar, I., Christen, M., Daura, X., Gee, P., Geerke, D., Glattli, A., Hunenberger, P., Kastenholz, M., Oostenbrink, C., Schenk, M., Trzesniak, D., Vegt, N., & Yu, H. (2006). Biomolecular Modeling: Goals, Problems, Perspectives. *Angew. Chem. Int. Ed.,* Vol.45, pp. 4064-4092

Halle, B. (2004). Protein hydration dynamics in solution; a critical survey, *Phil. Trans. R. Soc. Lond. B*., Vol.359, pp. 1207-1224

Hansen, A., Jensen, M., Sneppen, K. & Zocchi G. (1998). Statistical mechanics of warm and cold unfolding in proteins, *Eur. Phys. J. B*, Vol.6, pp. 157-161

Heal, J., Wells, S., Jimenez-Roldan, J., Freedman, R. & Romer, R. (2011). Rigidity analysis of HIV-1 protease, *J. Phys. CMMP10 conference series,* Vol.286, pp. 012006

Hespenheide, B., Rader, A., Thorpe, M. & Kuhn L. (2002). Identifying protein folding cores from the evolution of flexible regions during unfolding, *J. Mol. Graphics and Modelling,* Vol.21, pp. 195-207

Hilser, V. & Freire E. (1996). Structure-based calculation of the equilibrium folding pathway of proteins. Correlation with hydrogen exchange protection factors. *J. Mol. Biol.*, Vol.262, pp. 756–772

Istomin, A., Gromiha, M., Vorov, O., Jacobs, D. &. Livesay, D. (2008). Insight into Long-Range Nonadditivity within Protein Double-Mutant Cycles, *Proteins: Structure, Function, and Bioinformatics,* Vol.70, pp. 915-924

Jacobs, D., Kuhn, L. & Thorpe, M. (1999). *Flexible and Rigid Regions in Proteins*, Rigidity Theory and Applications, pp. 357-84, Eds: M.F. Thorpe & P.M. Duxbury, Plenum Publishing , New York, USA

Jacobs, D., Rader, A., Kuhn, L. & Thorpe, M. (2001). Graph Theory Predictions of Protein Flexibility, *Proteins: Structure, Function, and Genetics*, Vol.44, No.2, pp. 150-65

Jacobs D., Dallakayan, S., Wood G. & Heckathorne A. (2003). Network rigidity at finite temperature: Relationships between thermodynamic stability, the nonadditivity of entropy, and cooperativity in molecular systems, *Physical Reviews E*, Vol.68, pp. 061109 1-21

Jacobs, D. & Wood, G. (2004). Understanding the α-Helix to Coil Transition in Polypeptides Using Network Rigidity: Predicting Heat and Cold Denaturation in Mixed Solvent Conditions, *Biopolymers,* Vol.75, pp. 1-31

Jacobs, D. & Dallakayan, S. (2005). Elucidating Protein Thermodynamics from the Three Dimensional Structure of the Native State Using Network Rigidity, *Biophysical Journal*. Vol.88, pp. 1-13

Jacobs, D., Livesay, D., Hules, J. & Tasayco, M. (2006a). Elucidating quantitative stability-flexibility relationships within thioredoxin and its fragments using a distance constraint model, *Journal of Molecular Biology*, Vol.358, pp. 882-904

Jacobs, D. (2006b). *Predicting Protein Flexibility and Stability using Network Rigidity: A new Modeling Paradigm*, Recent Research Developments in Biophysics Publisher: Transworld Research Network, Vol.5, pp.71-131 ISBN: 81-7895-215-7, Trivandrum, India

Jacobs, D. & Fairchild, M. (2007a). *Thermodynamics of a beta-hairpin to coil transition elucidated by Constraint Theory*, Biopolymer Research Trends, Ed: Pablo C. Sánchez. Nova Publishers, ISBN: 1-60021-984-5 45-76, New York, USA

Jacobs, D. (2007b). *Computer Implemented System for Quantifying Sability and Flexibility Relationships in Macromolecules*. US Patent Pending, Application: 12232008.

Jacobs, D. (2010). Ensemble-Based methods for Describing Protein Dynamics, *Current Opinion in Pharmacology,* Livesay, D. (Ed.) Vol.10, pp. 760-769

Jacobs, D., Livesay, D., Mottonen, J., Vorov, O. Istomin, A. & Verma, D. (2012). *Ensemble Properties of Network Rigidity Reveal Allosteric Mechanisms, Allostery: Methods and Protocols,* Methods in Molecular Biology, Vol.796, Aron W. Fenton (ed.), Humana Press, Springer Science and Business Media, LLC

Jimenez-Roldan, J., Wells, S., Freedman, R. & Romer, R. (2011). Integration of FIRST, FRODA and NMM in a coarse grained method to study protein disulphide isomerase conformational change, *J. Phys. CMMP10 conference series,* Vol.286, pp. 012002

Kamerzell, T. & Middaugh, C. (2008). The complex inter-relationships between protein flexibility and stability, *J. Pharm. Sci*., Vol.97, pp. 3494-3517

Kittel, C. (1996). *Introduction to Solid State Physics*, 7th Ed., Wiley

Klepeis, J., Gunasekaran, K., Ma, B. & Nussinov, R. (2004). Is allostery an intrinsic property of all dynamic proteins? *Proteins,* Vol.57, pp 433–443

Lee, M., Wood, G. & Jacobs, D. (2004). Investigations on the alpha-helix to coil transition in HP-heterogeneous polypeptides using network rigidity, *Journal Physics, Condensed Matter*, Vol.16, pp. S5035-46

Lei, M., Kuhn, A., Zavodszky, M. & Thorpe, M. (2004). Sampling protein conformations and pathways, *J. Comput. Chem.,* Vol.25, pp. 1133-1148

Lindorff-Larsen, K., Dror, R. & Shaw, D. (2009). Long-timescale molecular dynamics simulations of protein structure and function. *Curr. Opin. Struct. Biol.,* Vol.19, pp. 120-127

Livesay, D., Dallakyan, S., Wood, G. & Jacobs, D. (2004). A flexible approach for understanding protein stability, *FEBS Letters,* Vol.576, pp. 468-76

Livesay, D. & Jacobs, D. (2006). Conserved quantitative stability/flexibility relationships (QSFR) in an orthologous RNase H pair, *Proteins: Structure, Function, and Bioinformatics*, Vol.62, pp. 130-43

Livesay, D., Huynh, D., Dallakyan, S. & Jacobs, D. (2008). Hydrogen bond networks determine emergent mechanical and thermodynamic properties across a protein family, *Chemistry Central Journal*, Vol.2, No.17, pp. 1-20

Lopez, C., Darst, R. & Rossky, P. (2009). Mechanistic elements of protein cold denaturation, *J. Phys. Chem. B.*, Vol. 112, pp.5961-5967

Luque, I., Leavitt, S. & Freire, E. (2002). The linkage between protein folding and functional cooperativity: Two sides of the same coin? *Annu. Rev. Biophys. Biomol. Struct*, Vol.31, pp. 235-56

Mamonova, T., Speranskiy, K. & Kurnikova, M. (2008). Interplay between structural rigidity and electrostatic interactions in the ligand binding domain of GluR2., *Proteins: Structure, Function, and Bioinformatics,* Vol.73, pp.656-671

Mark, A. & van Gunsteren, W. (1994). Decomposition of the free energy of a system in terms of specific interactions. Implications for theoretical and experimental studies, *J. Mol. Biol.*, Vol.240, pp. 167-176

Mottonen, J., Xu M., Jacobs, D. & Livesay, D. (2009). Unifying mechanical and thermodynamic descriptions across the thioredoxin protein family, *Proteins: Structure, Function, and Bioinformatics,* Vol.75, pp. 610-627

Mottonen, J., Jacobs, D. & Livesay, D. (2010). Allosteric Response is Both Conserved and Variable Across Three CheY Orthologs, *Biophysical Journal.*, Vol.99, pp. 2245-54

Muñoz, V. (2001). What can we learn about protein folding from Ising-like models? *Curr Opin Struct Biol*, Vol.11, 212–216

Nielsen, S., Bulo, R., Moore, P. & Ensing, B. (2010). Recent progress in adaptive multiscale molecular dynamics simulations of soft matter. *Phys. Chem. Chem. Phys*., Vol.12, pp. 12401–12414

Onuchic, J. & Wolynes, P. (2004). Theory of protein folding, *Cur. Opin. Struct. Biol.*, Vol.14, pp. 70-75

Oshima, H., Yoshidome, T., Amano, K., & Kinoshitab, M. (2009). A theoretical analysis on characteristics of protein structures induced by cold denaturation, *J. Chem. Phys.*, Vol.131, pp. 205102

Pace, N., Trevino S., Prabhakaran, E. & Scholtz, M. (2004). Protein structure, stability and solubility in water and other solvents. *Phil. Trans. R. Soc. Lond. B*, Vol.359, pp. 1225–1235

Pais, T., Lamosa, P., Garcia-Moreno B., Turner, D. & Santos, H. (2009). Relationship between protein stabilization and protein rigidification induced by mannosylglycerate, *J. Mol. Biol.,* Vol.394, pp.237-250

Petsko, G. & Ringe, D. (2004). *Protein structure and function.* New Science Press Ltd., ISBN 0-9539181-4-9

Purkiss, A., Skoulakis, S. & Goodfellow J. (2001). The protein-solvent interface: a big splash, *Phil. Trans. R. Soc. Long. A*, Vol.359, pp. 1515-1527

Radestock, S. & Gohlke, H. (2008). Exploiting the link between protein rigidity and thermostability for data-driven protein engineering, *Eng. Life Sci.,* Vol.8, pp. 507-522

Radestock S. & Gohlke H. (2011). Protein rigidity and thermophilic adaptation. *Proteins: Structure, Function, and Bioinformatics,* Vol.79, pp. 1089-1108

Rader, A., Hespenheide, B., Kuhn, L., & Thorpe, M. (2002). Protein unfolding: rigidity lost. *Proc. Natl. Acad. Sci.*, USA, Vol.99, pp. 3540-3545

Radar, A., Anderson, G., Isin, B., Khorana, H., Bahar, I. & Klein-Seetharaman K. (2004). Identification of core amino acids stabilizing rhodopsin, *Proc. Nat. Acad. Sci.,* Vol.101, pp.7246-7251

Rader, A. (2010). Thermostability in rubredoxin and its relationship to mechanical rigidity. *Phys. Biol.,* Vol.7, pp. 016002

Shan, B., McClendon, S., Rospigliosi, C., Eliezer, D. & Raleigh D. (2010). The cold denatured state of the C-terminal domain of protein L9 is compact and contains both native and non-native structure, *J. Am. Chem. Soc.,* Vol.132, pp. 4669-4677

Shortle, D. (1999). Protein folding as seen from water's perspective Nature Struct, *Biol. news and views*, Vol.6 pp. 203-205

Thomas, S., Tang, X., Tapia, L. & Amato, N., (2007). Simulating Protein Motions with Rigidity Analysis, *J. Comp. Bio.*, Vol.14, pp. 839-855

Verma, D., Jacobs, D. & Livesay, D. (2010). Predicting the Melting Point of Human C-Type Lysozyme Mutants, *Current Protein and Peptide Science*, Vol.11, pp. 562-572

Vorov, O., Livesay, D. & Jacobs, D. (2008). Conformational entropy of an ideal cross-linking polymer chain, *Entropy*, Vol.10, pp. 285-308

Vorov, O., Livesay, D. & Jacobs, D. (2009). Helix/coil nucleation: A local response to global demands, *Biophysical Journal*, Vol.97, pp. 3000-3009

Vorov, O., Livesay, D. & Jacobs, D. (2011). Nonadditivity in Conformational Entropy Upon Molecular Rigidification Reveals a Universal Mechanism for Affecting Folding Cooperativity, *Biophysical Journal*, Vol.16, pp. 1129-38

Wang, H., Fairchild, M., Livesay, D. & Jacobs, D. (2011). *Intrinsic molecular partition functions for amino acids* (unpublished, to be submitted)

Wells, S., Menor, S., Hespenheide, B. & Thorpe, M. (2005). Constrained geometric simulation of diffusive motion in proteins, *Phys. Biol.,* Vol.2, pp. S127–S136

Whiteley, W. (2005). Counting out to the flexibility of molecules, *Phys. Biol*., Vol.2, pp. S116-126

Widom, B., Bhimalapuram, P. & Koga, K. (2003). The hydrophobic effect, *Phys. Chem. Phys.,* Vol.5, pp. 3085-3093

Wood, G., Clinkenbearda, D. & Jacobs, D. (2011). Nonadditivity in the alpha-helix to coil transition, *Biopolymers*, Vol.95, pp. 240–253

Woodward, C., Simon, I. & Tuchsen, E. (1982). Hydrogen Exchange and the Dynamic Structure of Proteins, *Molecular and Cellular Biochemistry*, Vol. 48, pp. 135-160

Yao, P., Zhang, L. & Latombe J. (2012). Sampling-based exploration of folded state of a protein under kinematic and geometric constraints, *Structure, Function, and Bioinformatics,* Vol.80 pp.25-43

Zamparo M. & Pelizzola, A. (2006). Kinetics of the Wako-Saitô-Muñoz-Eaton model of protein folding. *Phys. Rev. Lett*., Vol.97, pp. 068106 (1-4)

5

Recent Developments in the Study of the Behavior of Fluorescent Membrane Probes in Lipid Bilayers: Molecular Dynamics Approach

Luís M.S. Loura[1,2], A.J. Palace Carvalho[3,4] and J.P. Prates Ramalho[3,4,*]
[1]*Centro de Química de Coimbra, Universidade de Coimbra, Coimbra,*
[2]*Faculdade de Farmácia, Universidade de Coimbra,*
Pólo das Ciências da Saúde, Azinhaga de Santa Comba, Coimbra,
[3]*Centro de Química de Évora, Universidade de Évora, Évora,*
[4]*Departamento de Química, Universidade de Évora, Évora,*
Portugal

1. Introduction

The molecular level organization of biomembranes and the establishment of structure/function relationships of membrane-active biomolecules are topics of crucial importance for the understanding of many phenomena in cell biophysics and biochemistry. This poses challenging problems that most frequently require the use of advanced experimental techniques (Gennis, 1989), among which fluorescence stands out as one of the most powerful and commonly used due to its sensitivity and versatility (Lakowicz, 2006; Royer & Scarlata, 2008). The sub-nanosecond time resolution of fluorescence allows following the kinetics of both fast (fluorophore rotation, conformational changes) and relatively slow (translocation, hindered diffusion) processes, and its extremely high sensitivity (as evidenced in techniques such as single-fluorophore imaging and fluorescence correlation spectroscopy) is almost unrivaled. But, perhaps the most salient feature of fluorescence spectroscopy is its high versatility which allows, through different parameters, the retrieval of complementary molecular information on the system under study. Spectral and fluorescence lifetime/quantum yield variations are informative regarding the polarity and/or solvent accessibility of the fluorophore microenvironment and the extent of partition of a fluorophore-bearing molecule between the aqueous and membrane media, or between coexisting membrane phases or domains. Fluorescence quenching, depending on the underlying interaction mechanism and on the experimental design, can be used to study molecular aggregation, lateral diffusion, compartmentalization, or transverse location in the bilayer. Fluorescence polarization is used to measure the viscosity of the microenvironment and the kinetics of fluorophore rotation. Förster resonance energy transfer (FRET) is useful in many common situations, such as detection and characterization of membrane heterogeneity, determination of the transverse location of protein fluorophores, detection

* Corresponding Author

and quantification of protein/lipid selectivity, and characterization of protein oligomerization. Fluorescence microscopy adds spatial resolution to the canon, and, also because of the non-destructive nature of fluorescence techniques, is widely used in the study of live cells (Royer & Scarlata, 2008; de Almeida et al. 2009). An increasing number of laboratories all over the world are equipped with instruments capable of measuring microscopic fluorescence decays, thus combining spatial and time resolution. In particular, recent developments in multi-wavelength and polarization resolved imaging have led to a widespread use of FRET imaging in studies of functional assemblies in cell membranes (de Almeida et al., 2009).

The basic structural unit of biological membranes is the phospholipid bilayer, and because the vast majority of naturally occurring membrane lipids are non-fluorescent, many of the applications described above require the use of extrinsic membrane probes containing fluorophores with convenient photophysical properties, such as absorption and emission in the visible range and high molar absorption coefficient and fluorescence quantum yield (which is especially convenient for microscopy and single-molecule techniques). Some fluorophores are known for their simple decay kinetics, stability, and invariance of fluorescence parameters, while others are notable for their sensitivity to the local environment. Taking into account the purpose of a given experiment, either one of these types of molecules will be most appropriate (Maier et al., 2002). Some of these fluorescence membrane probes bear no resemblance to lipids, but due to their hydrocarbon-based structure, are sufficiently hydrophobic to partition to the lipid environment. Examples described below are 1,6-diphenyl-hexatriene (DPH) or pyrene (see Fig. 1A and Fig. 1B for structures). Sometimes, synthetic fluorophores are attached to aliphatic chains to increase the extent of partition. In other cases, the probes are phospholipids with a suitable fluorophore covalently attached to either the polar headgroup or one of the acyl chains, or sterols with a fluorophore label bound to either the side chain or the oxygen atom (e.g. cholesteryl esters). In all cases, the probe is a foreign molecule inserted in a host lipid matrix.

Two major issues arise regarding the use of extrinsic probes in membrane studies. First, the behavior of the probe molecule inside the bilayer (e.g. what transverse region of the bilayer is the probe sensitive to, its translational and rotational dynamics) is often not fully understood. Second, when interpreting the results of fluorescence experiments, it can be hard to distinguish between legitimate membrane properties and the perturbing effects resulting from incorporation of the probe (in bilayer structure, dynamics of bilayer components and thermotropic behavior) even in low concentrations (Bouvrais et al., 2010). Whereas the first point can be addressed experimentally using suitable fluorescence techniques (e.g., differential quenching, dynamical self-quenching, time-resolved anisotropy), the latter issue is best dealt with using a methodology able to simultaneously monitor the probe and lipid molecules independently. Given the sheer amount of work that has been carried out using fluorescent membrane probes, it is surprising to note the scarcity of studies that have addressed this fundamental matter.

Molecular dynamics (MD) simulations can provide detailed atomic-scale information, and have been extensively used in the study of lipid bilayer structure and dynamics (Ash et al., 2004; Berkowitz, 2009). This technique has also been established in the past decade as a method of choice to analyze both the location and dynamics of membrane probes and the extent of perturbation they induce in the host bilayer. Fluorophore properties that can be

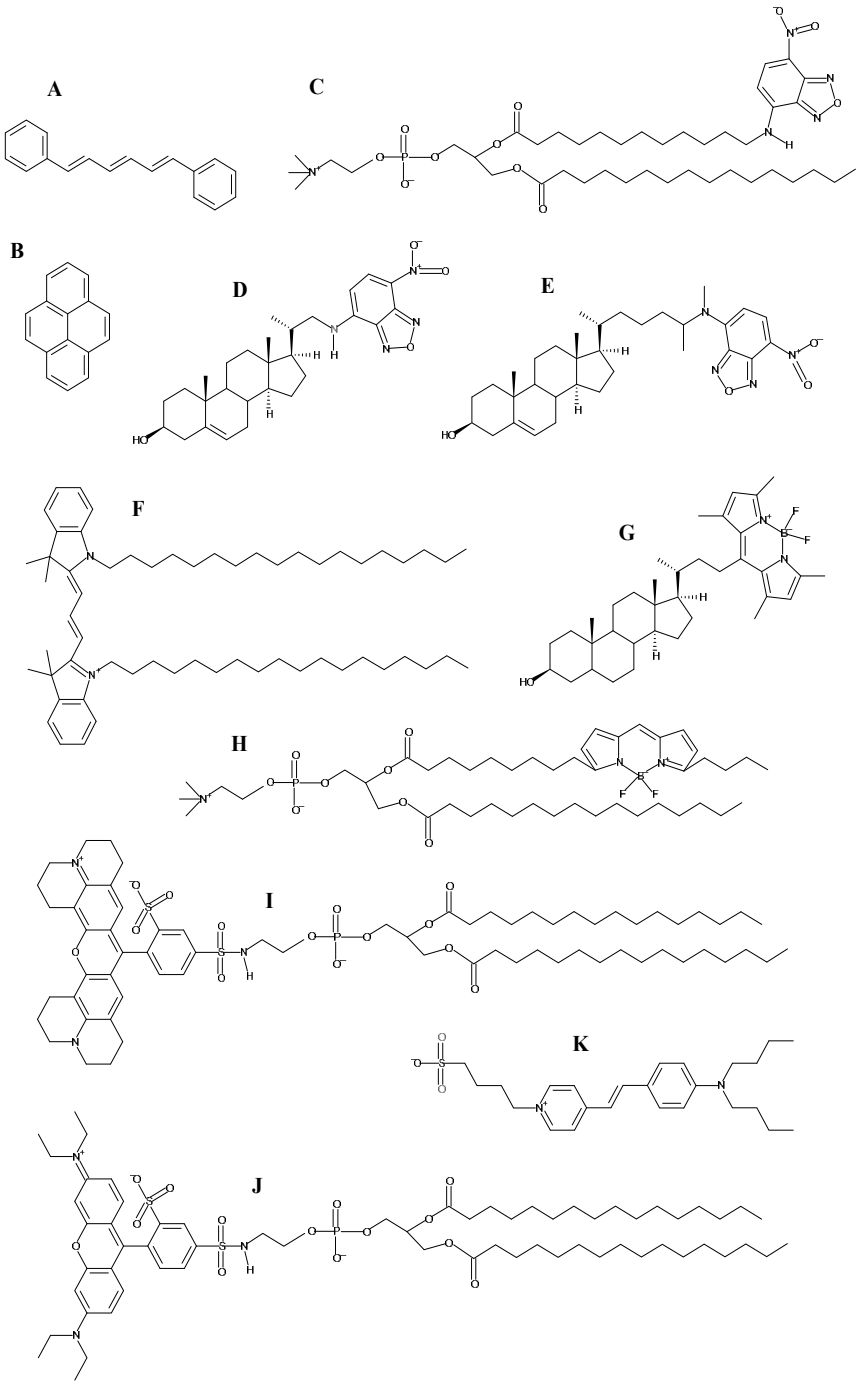

Fig. 1. Structures of membrane probes mentioned in this chapter. (a) DPH; (b) pyrene; (c) C12-NBD-PC; (d) 22-NBD-cholesterol; (e) 25-NBD-cholesterol; (f) DiI; (g) BODIPY-cholesterol; (h) BODIPY-PC; (i) TR-DHPE; (j) Rhod-DPPE; (k) Di-4-ASPBS.

monitored in MD simulations include mass distribution, conformation/orientation, extent of solvation/hydrogen bonding, radial distribution functions, rotational/translational dynamics, and aggregation state. On the other hand, bilayer parameters include area per lipid, density profiles, translational and rotational (headgroup, acyl chain) dynamics, order parameters, orientation of water molecules and lipid headgroups at the interface, and electrostatic potential across the membrane. Comparison between simulations in presence and absence of bilayer-incorporated probe allows evaluation of the perturbation induced by the latter. For the purpose of validating the simulation parameters and protocols, several parameters calculated from simulation can be compared to experimental observables.

The first report of atomistic MD simulations of bilayers containing fluorescent probes dates from 1997 and it was limited to a very short trajectory of less than 1 ns (López Cascales et al., 1997). Over the last decade, studies similar in principle but with much larger scope have focused on several important classes of probes (see Fig. 1 for structures).

Earlier works consisted mostly of atomistic simulations of simple nonpolar (and therefore easier to model) fluorophores in fluid disordered bilayers (easier to simulate). More recent studies have considerably widened the range of studied probes by simulating increasingly more complex fluorophores and extended the simulations to systems consisting of ordered bilayers, e.g. containg cholesterol (which adds considerable biological relevance, given the ubiquity of the latter in the plasma membranes of mammals (Gennis, 1989)). In addition, the recent introduction of coarse-grained force-fields in this field has allowed the study of much longer timescales and larger systems.

This chapter provides a review of this rapidly-evolving subject, which attempts to illustrate the wealth of detailed information that can be made available by these simulations, as well as to present the most recent trends in this field of research.

2. Atomistic simulations of membrane probes in lipid bilayers

2.1 Apolar fluorophores

Because of their relative structural simplicity, the first fluorescent probes simulated in lipid bilayers were small, apolar and highly symmetrical molecules, 1,6-diphenylhexatriene (DPH; Fig 1A) and pyrene (Fig. 1B).

2.1.1 DPH

DPH is a rod-shaped molecule whose fluorescence polarization is very sensitive to the microenvironment viscosity. Its fluorescence quantum yield and intensity decay show little sensitivity to the lipid phase, unlike the fluorescence anisotropy, which decreases threefold upon melting of the lipid acyl chains. For this reason, DPH is the archetypal membrane probe used for assessment of membrane fluidity (Lentz, 1989, 1993).

The most probable location of DPH inside the lipid bylayer was traditionally expected to be within the apolar acyl chain region, on account of its hydrophobicity. However, the question of its orientation remained unanswered for a long time. From analysis of time-resolved fluorescence anisotropy of the bilayer-inserted DPH, Litman and co-workers proposed a bimodal angular distribution of the long molecular axis, one of the two maxima corresponding to an alignment of this axis parallel to the membrane normal whereas the

other corresponded to a perpendicular alignment. Such a distribution is compatible with a location in the bilayer midplane, between the two monolayer leaflets (Straume & Litman, 1987; Mitchell & Litman, 1998). This perspective was challenged by an early report (López Cascales et al., 1997) of a pioneering MD simulation of a 72-molecule 1,2-dipalmitoyl-*sn*-3-glycerophosphocholine (DPPC) fluid bilayer in the presence of either one or three DPH molecules. No partial charges were used in any of the atoms of the DPH molecule and the temperature was set to 350 K, well above the main transition temperature of this phospholipid (T_m=314 K). However, this work was severely restricted by the extremely short time-scale probed (only ≤250 ps were used for analysis). In this study it was observed that the angle between the long molecular axis and the bilayer normal rarely was wider than 60º, and no perpendicular orientations were detected. Fast rotation motions (average correlation times of 0.061 ns for end-to-end tumbling and 0.0051 ns for the vector normal to the phenyl rings in the molecule) were obtained. An abnormally high DPH lateral diffusion coefficient (1.36×10^{-5} cm^2s^{-1}) resulted from this simulation. Significant disordering effects were observed for membranes containing DPH molecules, especially in the region closer to the lipid/water interface. In contrast, no significant probe effects were observed either in bilayer thickness or the area/lipid molecule.

A more conclusive study, employing larger (128-molecule) DPPC fluid bilayers (T = 323 K) labeled with 1 or 3 DPH molecules and simulated for a longer period of 50 ns, revealed broad angular distributions of the DPH long axis, and despite a peak being observed for $f(\theta)\sin(\theta)$ (where f is the orientation distribution function) at $\theta \approx 25°$, significant distribution also occurs around $\theta \approx 90°$ (Repáková et al., 2004). However, perpendicular orientations do not correlate with center of mass locations near the bilayer center. DPH was found to be located mostly deep in the acyl chain region of the bilayer, with its center of mass transverse position located in average at 0.75 nm from the bilayer center, in agreement with fluorescence quenching results (Kaiser & London, 1998). Two different approaches were adopted for attributing charges to DPH atoms, with largely identical results: zero charges on all atoms and partial charges obtained from *ab initio* quantum mechanical calculations. The extended time scale of this study enabled the authors to observe occasional probe translocation (flip-flop) events. Dynamic properties of DPH, such as lateral diffusion and rotational mobility, were also addressed. The correlation function for the long molecular axis had a relaxation time of 4.3 ns, which is in the same order of magnitude of the rotational correlation times measured by time-resolved fluorescence anisotropy. The calculated lateral diffusion coefficient of DPH (20×10^{-8} cm^2s^{-1}) was faster, albeit still in the same order of DPPC's (15×10^{-8} cm^2s^{-1}), possibly reflecting the increased free volume in the lipid acyl region of the bilayer.

A second part of this study (Repáková et al., 2005) focused on DPH effects on the properties of the host DPPC fluid bilayer (again 128 DPPC molecules; T=323 K) but simulation length was extended to 100 ns. The simulation was complemented with experimental differential scanning calorimetry (DSC) and deuterium nuclear magnetic resonance (^{2}H-NMR) measurements. DPH effects on the thermotropic phase behavior of DPPC were minor (very slight decrease of T_m, slight decrease in the corresponding transition enthalpy). ^{2}H-NMR data suggest that DPH has a very small orientating effect on the DPPC acyl chains. This was confirmed by the MD simulations, which were able to establish that, whereas this effect is indeed modest overall, significant increases in the calculated deuterium order parameter $-S_{CD}$ (up to 30–50%) were observed for lipid molecules in close proximity (<1.0 nm) of a

DPH molecule. Ordering effects become negligible for DPPC molecules separated from a DPH probe beyond a distance of 1.5 nm. Thus, by standing mostly upright in the membrane hydrophobic region, DPH produces a local ordering effect on fluid DPPC acyl chains. This is also apparent in the variation of the average area/lipid as a function of the distance to the nearest probe molecule. A ~2% overall decrease is observed, which is significantly more pronounced for DPPC molecules nearby a probe. Also consistent with this picture, there is a similar increase in bilayer thickness upon probe incorporation. DPH has negligible influence on interface properties such as membrane electrostatic potential and P-N tilt angles, but affects both lateral diffusion (halving the coefficient value) and rotation of the P-N axis (relaxation time increases by ~10%) for nearby DPPC molecules. Overall, it was concluded that DPH has a small perturbing effect on DPPC fluid bilayers justifying its wide use as a fluorescent membrane probe, though significant local ordering effects are observed.

More recently, the behavior of DPH was studied in bilayers composed of DPPC and cholesterol (with either 5 mol% or 20 mol% of the latter) (Franová et al., 2010). It was concluded that the increased order and membrane thickness resulting from the presence of cholesterol affects the location and orientation of bilayer-inserted DPH. The distance from the bilayer center to the average transverse location of DPH increased by 0.2 nm for the 20 mol% system, and the orientation distribution of the DPH long axis became narrower, with a single maximum for $\theta \approx 10°$ and essentially zero values for $\theta \approx 90°$. Similarly to the system without cholesterol, though detectable ordering effects were observed for the DPPC acyl chains closest to the DPH molecules, no significant overall perturbations were observed in parameters such as average area/lipid and deuterium order parameters. However, for the system with 20 mol% of cholesterol, the well-known ordering effect of this component is so dominant that the additional role of DPH becomes almost negligible. This paper also focused on a critical evaluation of the fluorophore orientations distribution study by time-resolved fluorescence anisotropy. The latter method allows the recovery of, at most, the first three coefficients ($<P_0>$, $<P_2>$ and $<P_4>$) of the Legendre polynomial series expansion of the orientational distribution function, whereas the complete function is readily available from MD simulation. It is shown that, whereas the truncation to the first three terms is still satisfactory for the more disordered systems (without cholesterol and with 5 mol%), important quantitative disagreement is observed for the cholesterol-rich ordered system.

2.1.2 Pyrene probes

Pyrene (Fig. 1B) is a polycyclic aromatic hydrocarbon which, both in free pyrene form and in pyrene-labeled lipids, has found a common use in membrane biophysics studies (Somerharju, 2002). This is due to its notable spectroscopic properties, including the unusually long fluorescence lifetime (>100 ns in a variety of solvents and membrane systems) and ability to form excimers.

Pyrene has been simulated by MD in 1-palmitoyl,2-oleoyl-*sn*-3-glycerophosphocholine (POPC) fluid bilayers (Hoff et al., 2005; this study combined MD and 2H-NMR measurements) and in both fluid and gel DPPC bilayers (Repáková et al., 2006; Čurdová et al., 2007). The former simulation study spanned 25 ns and the system consisted of 128 POPC molecules with four pyrene molecules inserted inside the membrane and a fifth located, at the start of the simulation, in the water region of the simulation box. The latter pyrene molecule was found to rapidly insert the POPC bilayer in less than 2 ns. Within ~8 ns of the

start, all five molecules were located slightly inside the headgroup region of the bilayer. This somewhat shallow location agrees with a published experimental fluorescence quenching report (Herrenbauer, 2002) and can be attributed to entropic effects. In fact, a considerable acyl-chain ordering and consequent decrease of entropy will result from the accommodation of this large, rigid molecule in the highly disordered middle region of the membrane. No flip-flops were observed in the time-scale of the simulation. The molecules were found to have their long axis essentially aligned (within ±30°) with the bilayer normal. Good agreement between probe order parameter values determined from ^{2}H-NMR and from simulation was verified, seemingly indicating that even 25 ns of simulation seem to be enough to cover all types of motions that pyrene performs inside a lipid bilayer.

The two later studies focused both on probe properties and on its effect on the host bilayer. In the first (Repáková et al., 2006), 1, 4, and 6 molecules of the pyrene-tagged lipid 1-palmitoyl-2-(1-pyrenedecanoyl)-*sn*-glycero-3-phosphocholine (PyrPC) were simulated in a fluid (T=323 K) DPPC bilayer (128 total lipid molecules). In this study, no partial charges were used for the pyrene moiety. Although no significant overall effects were apparent in the average area/lipid molecule, sizeable reductions were detected locally for lipids within a range of 1.5 nm to the nearest PyrPC probe molecule. These effects were as high as ~3–4% for lipids closer than 1.0 nm. In accordance, increases in the calculated acyl chain's $-S_{CD}$ were apparent in the same range of distances. Interestingly, the area/PyrPC molecule was even smaller than that obtained for its nearest DPPC neighbors, and the $-S_{CD}$ value for the unlabeled *sn*-1 chain was notably high. This indicates that the pyrene moiety increases the order of both neighboring DPPC chains and also of the *sn*-1 chain of the lipid molecule to which it is attached. On the other hand, PyrPC incorporation had very minor effects on the DPPC density profiles or bilayer thickness. The label was mostly found ~0.8 nm from the lipid/water interface, in the hydrocarbon region of the bilayer. The fluorophore adopted a broad distribution of orientations, implying a significant fraction of pyrene labels pointing towards the water–lipid interface, causing a kink in the probe's *sn*-2 acyl chain. For molecules that did not present this behavior, the pyrene group often interdigitated to the opposite leaflet (~3–6% of all configurations). According to the authors, this behavior can cause occasional excimer formation involving PyrPC molecules of different leaflets. Another interesting consequence of pyrene interdigitation was an increase in $-S_{CD}$ of the nearest (R<0.5 nm) DPPC acyl chains in the other leaflet.

The second study (Čurdová et al., 2007) concerned free pyrene, in both fluid (0:128, 1:128, and 3:128 pyrene/lipid ratios, T=325 K or 350 K, t=20 ns) and gel (0:120, 1:120 ,and 3:120 pyrene/lipid ratios, T=273 K, t=50 ns) DPPC bilayers. Partial charges of pyrene atoms were obtained from *ab initio* quantum mechanical calculations. In similarity with the previous PyrPC studies, the overall effects of pyrene on area/lipid and $-S_{CD}$ were minor for all systems. However, significant local (for lipids at less than 1.0 nm from the probe) effects were present. In the fluid phase simulations, acyl chain ordering similar to that described for PyrPC above was observed. Concerning the gel phase, the fraction of *trans*/*gauche* defects along the acyl chains of neighboring DPPC molecules increased, meaning pyrene molecules decreased their ordering. However, the presence of pyrene also induced a reduction in the tilt angle of nearby DPPC acyl chains, which would *per se* result in an increased order parameter (as the latter reflects the angle between the chain and the bilayer normal). It is, thus, difficult to make an analysis of $-S_{CD}$ in face of these contradictory effects. Pyrene

incorporation caused a significant reduction and a minor increase of the bilayer thickness in the gel and fluid phases, respectively. This probe presented broad transverse distribution and orientation profiles, with maxima around phospholipid acyl chain carbon 5 (in terms of the transverse distribution) and for θ=90° (corresponding to the normal of the pyrene plane being perpendicular to the membrane normal direction), respectively. Both observations are in agreement with Hoff et al. (2005). In the gel phase, the orientation profile is slightly more complex, with a second maximum being apparent at 50° (probably reflecting the tilt of the DPPC acyl chains). No significant changes in the lateral diffusion coefficient of DPPC were observed upon pyrene insertion. No clustering of pyrene molecules was observed, possibly as a result of time scale limitations.

Similarly to the effects reported by Čurdová et al. (2007) in DPPC gel, recent unpublished data by Loura and Do Canto regarding simulations of pyrene in 80% POPC:20% cholesterol mixed bilayers (see snapshot in Fig. 2) showed that pyrene produces a disordering effect, increasing the area/lipid molecule and decreasing the bilayer thickness and acyl chain order parameter, and thus opposing the ordering effect of cholesterol. Although the overall variations of these parameters were modest, significant local effects were apparent (Fig. 3). This observation is in contrast to that of DPH in DPPC/cholesterol 4:1 (Franová et al., 2010), for which a slight ordering effect was reported, as described above. The difference in behavior of the two probes is probably due to pyrene being substantially bulkier and therefore more difficult to accommodate in an ordered bilayer without inducing perturbation.

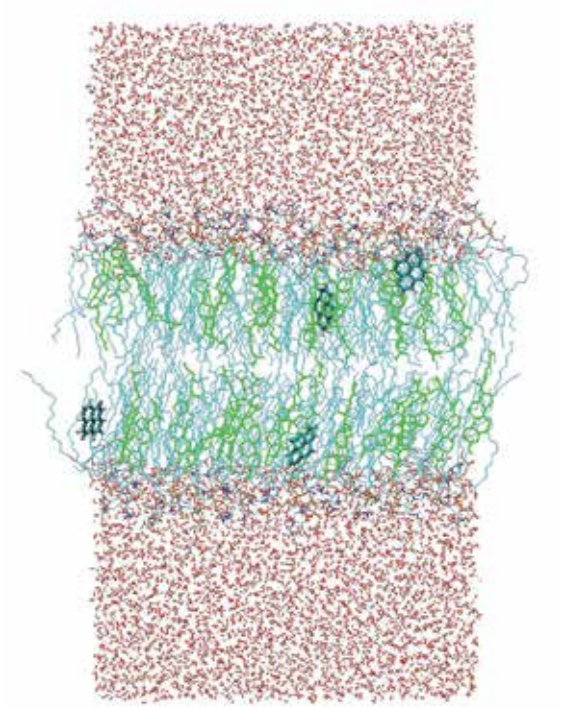

Fig. 2. Snapshot of a POPC/cholesterol 4:1 bilayer containing 4 pyrene molecules.

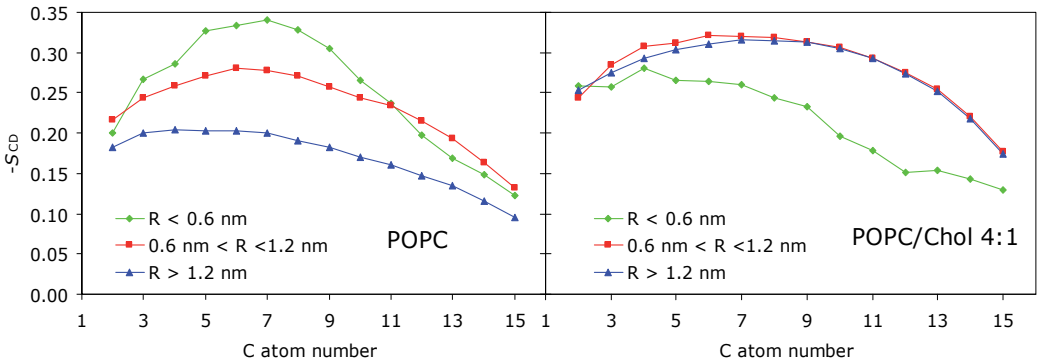

Fig. 3. Deuterium order parameter profile of the POPC *sn*-1 chain for varying proximity to the closest pyrene molecule (R) in the 100-ns MD simulation of (a) POPC/pyrene (128:2) and (b) POPC/cholesterol/pyrene (120:30:2) bilayers. For $R > 1.2$ nm, the profiles are essentially identical to those obtained in absence of probe in both systems (not shown). Significant local ordering is observed for $R < 1.2$ nm in (a), whereas significant local disordering is observed for $R < 0.6$ nm in (b).

2.2 Polar fluorophores

The use of fluorescent membrane probes bearing polar design fluorophores has become very common, especially since the 1980s. Despite having arrived later to the scene, MD simulations of this type of fluorophores are currently outnumbering those involving apolar fluorescent membrane probes.

2.2.1 NBD probes

Among polar fluorophores, a popular family is that of phospholipids labeled with the 7-nitrobenz-2-oxa-1,3-diazol-4-yl (NBD) fluorophore in one of the acyl chains. NBD derivatives are commercially available for all major phospholipid classes, and have been used extensively as fluorescent analogues of native lipids in biological and model membranes to study a variety of processes (Chattopadhyay, 1990; Mukherjee et al., 2004).

Simulations of two of these probes, the acyl chain-labeled phosphatidylcholine derivatives 1-palmitoyl,2-{6-[(7-nitro-2-1,3-benzoxadiazol-4-yl)amino]hexanoyl}-*sn*-glycero-3-phosphocholine (C6-NBD-PC) and 1-palmitoyl,2-{12-[(7-nitro-2-1,3-benzoxadiazol-4-yl) amino]dodecanoyl}-*sn*-glycero-3-phosphocholine (C12-NBD-PC; Fig. 1C), in fluid DPPC bilayers (0:64, 1:63, 4:60 NBD-PC/DPPC bilayers, T=323 K, t=100 ns) have been reported in two complementary studies. The first one addressed primarily the locations and dynamics of the probes (Loura & Prates Ramalho, 2007) whereas the second focused on their effects on the host bilayer properties (Loura et al., 2008). Parameterization of the NBD moiety required energy minimization for geometry and *ab initio* quantum mechanical calculations for partial atomic charges. Simulations were complemented with time-resolved fluorescence anisotropy (Loura & Prates Ramalho, 2007) and DSC (Loura et al., 2008) measurements, which provided experimental information on probe rotational dynamics and perturbation of the thermotropic behavior of DPPC bilayers, respectively. In these two studies it was

observed that NBD fluorophores loop in the direction of the interface. The transversal distribution across the bilayer has a broad profile, with a maximum around the glycerol backbone/carbonyl region, in accordance with fluorescence quenching and ^{2}H-NMR results (Chattopadhyay & London 1987; Huster et al., 2001), and with the nitro group being closest to the interface. It was also observed that the NBD's NH group is involved in H-bonding to PC glycerol backbone O atoms. In terms of the dynamical behavior, the calculated lateral translation diffusion of NBD-PC was found to be identical to that of DPPC and the theoretical rotational dynamics of NBD agreed well with experimental fluorescence anisotropy decays. Whereas important effects were observed for high (~6 mol%) probe content, milder perturbation of fluid PC structure and dynamics is expected for ~1 mol% or lower amounts of probe (the concentrations most frequently used in experimental work). Regarding the range of the induced perturbations, as judged by $-S_{CD}$ values, they occur mostly in molecules in close contact with probes. This is especially true for C6-NBD-PC. Because the labeled *sn*-2 chain of this probe does not extend nearly so much across the bilayer as that of C12-NBD-PC, the disordering effect of the former is mostly concentrated in its immediate vicinity, whereas the large extension of the C12-NBD-PC *sn*-2 chain allows for a more uniform distribution of the perturbation among additional layers of neighbors. Because most fluorescence parameters are dictated by the immediate environment of the chromophore, this implies that C12-NBD-PC may be considered a better reporter of membrane properties than C6-NBD-PC. However, even for these smaller amounts, large alterations (transition temperature shifts, loss of cooperativity), are evident in the themotropic behavior of NBD-PC labeled PC bilayers, as measured by differential DSC.

These 100-ns simulations of NBD-PC in fluid DPPC were also used in a later study to calculate the FRET orientation factor (κ^2) for homo-FRET between these probes embedded in this membrane system (Loura et al., 2010a). κ^2 is a measure of the relative orientation of FRET donor and acceptor transition dipoles and can be calculated according to van der Meer et al. (1994):

$$\kappa^2 = (\cos\theta_T - 3\cos\theta_D \cos\theta_A)^2 \tag{1}$$

where θ_T is the angle between the transition moments of the donor and acceptor and θ_D and θ_A are the angles between the donor and acceptor transition moments and the vector uniting their centres (see Loura et al, 2010a for details). κ^2 can vary between 0 (corresponding to several dipole arrangements) and 4 (collinear dipoles). The value of κ^2 is required for calculating the characteristic distance for the FRET interaction, the so-called Förster radius R_0 as seen in e.g. van der Meer et al. (1994):

$$R_0^6 = \frac{9000(\ln 10)\kappa^2 Q_D J}{128\pi^5 n^4 N_{AV}} \tag{2}$$

where Q_D is the quantum yield of the donor in the absence of any acceptor molecules, n is the refraction index of the medium, N_{AV} is the Avogadro number and J is the normalized overlap integral between the donor emission and the acceptor absorption spectrum.

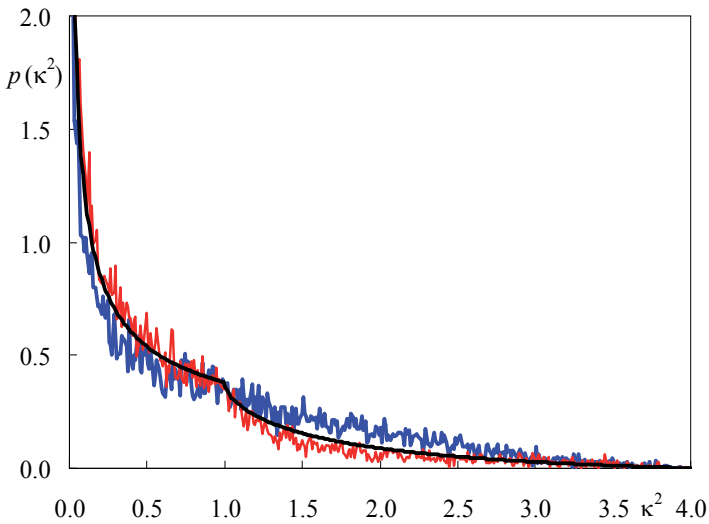

Fig. 4. Calculated probability density $p(\kappa^2)$ for C6-NBD-PC (red) and C12-NBD-PC (blue), compared with the analytical isotropic result of Eq. 3 (black).

R_0 is an essential parameter for the quantitative description of FRET kinetics in membrane systems (Loura et al., 2010b, 2010c) as well as in the classic use of FRET as a spectroscopic ruler (Stryer, 1978). In the preceding equation, whereas Q_D and J may be obtained from straightforward calculations from spectral data, there is no experimental technique suited to a definite measurement of κ^2 (though it was shown by Dale and co-workers (1979) that intervals containing its average value $<\kappa^2>$ can be inferred from adequate fluorescence anisotropy measurents). Most often, the theoretical value for the so-called dynamic isotropic limit ($<\kappa^2> = 2/3$) is used, but the uncertainty in the value of $<\kappa^2>$ is still widely regarded as an inconvenience that may be especially important in membranes, because of their intrinsic anisotropic nature and the restricted rotational mobility experienced by fluorophores incorporated inside the bilayer. However, from the position coordinates in an MD trajectory the calculation of κ^2 for a given FRET donor-acceptor molecular pair is straightforward, and averaging both over pairs and over time is conveniently carried out. Fig. 4 shows the probability densities of κ^2 for the C6-NBD-PC and C12-NBD-PC systems, compared with the theoretical isotropic orientation result which is given by Eq. 3 (van der Meer et al., 1994):

$$p(\kappa^2) = \begin{cases} \dfrac{1}{2\sqrt{3\kappa^2}} \ln(2+\sqrt{3}) & 0 \le \kappa^2 \le 1 \\ \dfrac{1}{2\sqrt{3\kappa^2}} \ln\left(\dfrac{2+\sqrt{3}}{\sqrt{\kappa^2}+\sqrt{\kappa^2-1}}\right) & 1 \le \kappa^2 \le 4 \end{cases} \tag{3}$$

Although the distributions generally resemble the analytical solutions for isotropic dipoles, $<\kappa^2>$ for C12-NBD-PC (0.87 ± 0.06) is ~30% higher than the 2/3 dynamic isotropic limit, whereas $<\kappa^2>$ for C6-NBD-PC (0.61 ± 0.03) is slightly lower than that limiting value. These

values are discussed in the original reference in terms of preferential orientation of the NBD group approximately parallel to the bilayer plane, as well as some extent of probe aggregation in the case of C6-NBD-PC. To our knowledge, this was the first calculation of κ^2 for intermolecular FRET by atomistic molecular simulation methods. A previous study, limited to a 100-ps timescale, focused in intramolecular FRET occurring in a non-membrane dye (Harriman et al., 2006). This methodology provides a way to calculate R_0 with improved accuracy relative to the widespread $<\kappa^2> = 2/3$ assumption, and can also be employed in hetero-FRET κ^2 calculation, provided that bilayers containing both donor and acceptor probes are simulated.

Other NBD membrane probes are currently being studied by MD simulations, including the homologous series of fatty amines NBD-C_n (Filipe et al. 2011), the head-labeled phospholipid 1,2-dipalmitoyl-*sn*-glycero-3-phosphoethanolamine-*N*-(7-nitro-2-1,3-benzoxadiazol-4-yl) (NBD-PE) and some NBD-labeled analogs of cholesterol, namely the 22-(*N*-(7-nitrobenz-2-oxa-1,3-diazol-4-yl)amino)-23,24-bisnor-5-cholen-3β-ol (22-NBD-Cholesterol; Fig. 1D) and the 25-[*N*-[(7-nitro-2-1,3-benzoxadiazol-4-yl)methyl]amino]-27-norcholesterol (25-NBD-Cholesterol; Fig. 1E). Regarding the latter NBD-cholesterol probes, they are among the commercially available fluorescent analogs of cholesterol. This sterol is a major component of mammalian cell membranes, and its action upon the physical properties of lipid bilayers has been studied actively in the last four decades. More recently, its implication in raft domains (Simons & Ikonen, 1997) has further increased this interest. Although both 22- and 25-NBD-cholesterol have been used for characterizing the distribution and dynamics of cholesterol in several systems (for a recent review, see e.g. Gimpl & Gehrig-Burger, 2011), the location and orientation of the NBD group of these probes in lipid bilayers is still a controversial issue. Using time-resolved fluorescence, it has been shown that 22-NBD-cholesterol preferably distributes to the cholesterol-poor liquid disordered (ld) phase rather than to the cholesterol-rich liquid ordered (lo) phase in phase separated PC/cholesterol vesicles (Loura et al., 2001). This displacement from the cholesterol-enriched phase is obviously an anomalous behavior for a probe supposed to mimic the behavior of the cholesterol component. From fluorescence quenching, it was found that the fluorophore of 25-NBD-cholesterol was deeply buried within the bilayer (Chattopadhyay & London, 1987). In contrast, using NMR, it was observed that both NBD-sterols may adopt an upside-down orientation within bilayers (Scheidt et al., 2003). This discrepancy remains unsolved in the literature. The technique of MD simulations is well suited to clarify this question, and both sterols have very recently been simulated in POPC bilayers (Loura & Prates Ramalho, unpublished data). Although complete trajectory analysis is still underway, it is clear from the structures obtained after 100 ns simulation (Fig. 5) that both sterols adopt a conformation where both opposing polar groups (-OH and -NO_2) are simultaneously oriented towards the interface. This behavior is at odds with the well-known orientation of cholesterol, with the hydroxyl group towards the interface, and the long axis approximately perpendicular to the bilayer plane (Franks, 1976; Worcester & Franks, 1976). Therefore, this study seems to confirm that both 22- and 25- NBD-cholesterol are inappropriate cholesterol analogs, probably at variance with BODIPY-cholesterol (see section further ahead), whose orientation in the bilayer resembles that of cholesterol (Hölttä-Vuori et al., 2008).

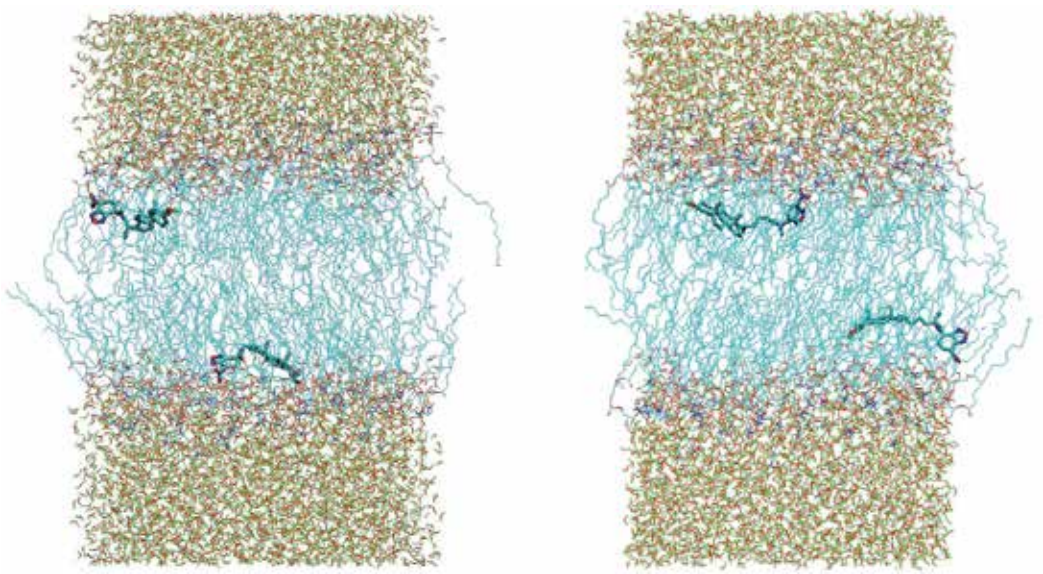

Fig. 5. Final snapshots of 100-ns MD simulations of fully hydrated 128-molecule fluid POPC bilayers with either two 22-NBD-cholesterol (left) or two 25-NBD-cholesterol (right) molecules inserted.

2.2.2 DiI

1,1′-dioctadecyl-3,3,3′,3′-tetramethylindocarbocyanine ($DiIC_{18}$(3) or DiI; Fig. 1F) is the most representative member of the carbocyanine familiy of dyes. These molecules have very high molar absorption coefficients (~$10^5 M^{-1}cm^{-1}$) and are used as membrane potential probes and as stains in cell studies. They have also been extensively used as probes of bilayer dynamics and structure (Wolf 1988). MD simulations have been performed by Gullapalli et al. (2008) to study the behavior of DiI in fluid DPPC bilayers. The simulated systems consisted of 0:128, 2:126, and 4:124 DiI/DPPC bilayers, at a temperature of 323 K, for a simulation length of 40 ns in each case. Partial atom charges on the DiI headgroup (global charge +1) were obtained from *ab initio* quantum mechanical calculations. A fourth simulation, similar to the 4:124 case, but in the absence of any partial charges on the DiI head group, was also performed for the sake of comparison.

It was found that, whereas DiI does not affect the area/lipid molecule significantly, membrane thickness was found to increase by 3–5% (~0.1–0.2 nm) in presence of the incorporated probe. In accordance, DiI was found to induce an increase in $-S_{CD}$ for both *sn*-1 and *sn*-2 DPPC acyl chains. The center of mass of the DiI headgroup was distributed from a distance of 0.3 to 2 nm from the center of the bilayer, with a maximum at 1.26 nm, in the glycerol/upper acyl chain region, and below the phospholipid headgroup region. As pointed out by the authors, this result is in contrast to some popular cartoon representations of DiI but consistent with DiI's increase in fluorescence quantum yield when incorporated into lipid bilayers. Flip-flop was observed in the control simulation with uncharged DiI atoms but not in the other simulation runs, indicating that the overall positive charge prevents the occurrence of probe translocation. The angle between the chromophore long

axis (uniting the two C6 rings) and the bilayer normal had a broad average distribution, with a maximum at 77°, almost parallel to the bilayer plane, in accordance with fluorescence polarization data (Axelrod 1979). Addition of DiI leads to an ordering of the water at the interfacial region (mainly as a consequence of the increase in the bilayer's thickness), decrease in the angle between the P-N vector and the bilayer normal, and a significant variation of the electrostatic potential across the membrane from −0.56 V (DPPC) to −0.69 V (4 DiI:124 DPPC). The latter values can be compared with the above described NBD study (Loura et al., 2008) for which a smaller variation was observed for higher labeling ratios (−0.55 V for DPPC, −0.58 V for 4 C6-NBD-PC:60 DPPC, −0.64 V for 4 C12-NBD-PC:60 DPPC). The decay of the autocorrelation function of the chromophore axis agrees with literature anisotropy decay parameters of related carbocyanines, and DiI has a lateral diffusion coefficient identical to that of DPPC.

2.2.3 BODIPY probes

Recently, a cholesterol derivative bearing the 4,4-difluoro-4-bora-3a,4a-diaza-*s*-indacene (boron-dipyrromethene, BODIPY) fluorophore (BODIPY-cholesterol; see Fig. 1G) was found to partition into ordered domains in model membranes (Shaw et al., 2006). A recent work using BODIPY-cholesterol combined live cell imaging (which established that the probe closely mimics the membrane partitioning and trafficking of cholesterol) with MD simulations (Hölttä-Vuori et al., 2008). Focusing on the latter, systems with both DPPC and *N*-palmitoylsphingomyelin (SM) at T=323 K, were simulated for a duration of ≥60 ns in each case. In a first set of simulations (3.125% sterol), the bilayers were composed of 124 DPPC or SM molecules and 4 sterol molecules. The used sterol was either cholesterol or BODIPY-cholesterol. In a second set (20% total sterol), bilayers of 128 SM or DPPC and 32 cholesterol molecules were simulated, as well as bilayers with 128 SM or DPPC, 28 cholesterol and 4 BODIPY-cholesterol molecules. Since the BODIPY moiety contains a boron atom, and this atom type was not originally included in the used force field, this had to be adapted for the purpose. Partial atom charges in the fluorophore were obtained from *ab initio* quantum mechanical calculations. It was found that the effects of BODIPY-cholesterol on bilayer properties matched those of cholesterol. Differences in the effect of sterol upon the area/lipid and the membrane thickness were not significant. Differences upon $-S_{CD}$, while noticeable, were relatively minor (BODIPY-cholesterol was slightly less efficient in ordering fluid lipid acyl chains than cholesterol; for both molecules the perturbation extended over a range in the order of ~1.0 nm). The distribution of the angle between the vector uniting the ends of the sterol ring system and the bilayer normal showed a predominance of small angles (<45°) in all cases. Distributions of BODIPY-cholesterol were slightly wider and displaced to larger angles as compared to those of cholesterol. On the other hand, the angle between the longer axis of the BODIPY moiety itself and the bilayer is predominantly at >45°. Given that the maximum of the mass distribution profile of the BODIPY moiety is in the middle of the bilayer, one can expect to find the probe molecules with their chromophore located deep along the bilayer midplane. This is the predominant configuration, corresponding to an upright orientation of the steroid ring system (similar to cholesterol); for low sterol bilayers, a significant probe population displays a more tilted steroid ring system, together with a slight upwards loop of the BODIPY moiety.

Remarkably, in more ordered bilayers (containing SM instead of DPPC, or 20 mol% sterol instead of 3.125%), this second population tends to vanish, giving rise to unimodal orientation distributions of BODIPY-cholesterol, as the lipid acyl chains become more ordered. This means that BODIPY-cholesterol is an especially good mimic of cholesterol for more ordered environments, which is an important asset for a raft reporter. The location and orientation of cholesterol itself is not affected by the presence of a smaller amount of BODIPY-cholesterol.

Very recently, a BODIPY-acyl-chain labeled phospholipid probe (2-(5-butyl-4,4-difluoro-4-bora-3a,4a-diaza-s-indacene-3-nonanoyl)-1-hexadecanoyl-*sn*-glycero-3-phosphocholine; see Fig. 1H) was simulated in DPPC monolayers and bilayers in the NPAT (constant pressure, area, and temperature) ensemble (Song et al. 2011). Three area/lipid molecule values were explored, 0.77 nm^2, 0.64 nm^2 and 0.40 nm^2, corresponding to lateral pressures of 5 mN/m, 10 mN/m and 40 mN/m, respectively. From the density profiles it was observed that the BODIPY moiety resided in the hydrophobic region of the bilayer. The calculated distributions of the tilt of BODIPY fluorophore long axis revealed ordering (shifting to narrower distributions, closer to the orientation of the bilayer normal) upon increasing lateral pressure. In any case, even for low and medium lateral pressure, the tilt angle was mostly < 90^o, indicating that snorkeling of BODIPY, while permitted for these lower pressure values, is not predominant. However, the calculated tilt distributions do not agree with the bimodal histograms obtained from analysis of single molecule orientation measurements carried out in a total internal reflection fluorescence microscope. These experimental distributions were consistent with two fluorophore orientations, one normal and another parallel to the membrane plane. In any case, these simulations reinforce the notion that BODIPY might be a better behaved fluorophore (compared to NBD) for reporting the hydrophobic region of membranes.

2.2.4 Headgroup-labeled phospholipid probes

Given the significant degree of perturbation induced by phospholipids labeled at the acyl chain with polar fluorophores (as evidenced by the NBD-PC studies described above), it would be reasonable to assume that headgroup-labeled lipid probes present a potentially less membrane-disturbing behavior. This hypothesis can be tested using MD simulations. Two recent reports address specifically the behavior of phospholipids labeled at the headgroup with rhodamine dyes in fluid DPPC bilayers. Skaug et al. (2009) simulated Texas Red-1,2-dihexadecanoyl-*sn*-glycero-3-phosphoethanolamine (TR-DHPE; Fig. 1I), whereas Kyrychenko (2010a) simulated 1,2-dipalmitoyl-*sn*-glycero-3-phosphoethanolamine-*N*-(lissamine rhodamine B sulfonyl) (Rhod-DPPE; Fig. 1J). As seen from the structures, these probes share an identical phosphatidylethanolamine lipid moiety and present quite similar fluorophores attached to the headgroup. In both cases, fluorophore parameterization involved density functional theory (DFT) quantum mechanical calculations. Although the two fluorophores have similar structures, higher absolute charges were consistently obtained for the Rhod-DPPE case, possibly due to differences in the methodology and details of the two DFT calculations. Perhaps for this reason, the two studies predict different transverse locations for the two fluorophores at equilibrium, with Texas Red in the upper acyl chain region and lissamine rhodamine B sulfonyl in a more external position, near the water/lipid interface (co-localizing with the phosphate and choline groups of DPPC). This

different behavior is not consistent with parallax analysis of experimental fluorescence quenching results, which predicts identical transverse locations of the two fluorophores in 1,2-dioleoyl-*sn*-glycero-3-phosphocholine vesicles (Kachel et al., 1998), despite TR being slightly more hydrophobic than lissamine rhodamine B sulfonyl. The distinct behaviors of the two simulated probes therefore possibly stem from the differences in the model building procedure, which emphasizes the importance of careful parameterization of these polar fluorophores. It could be argued that the combination of different starting positions and incomplete equilibration would be another possible cause for this difference. In fact, the fluorophore of Rhod-DPPE was located outside the headgroup region (into the water region) in the starting structure (Kyrychenko, 2010a), whereas that of TR-DHPE appears to have been placed inside the DPPC headgroups (Skaug et al., 2009). However, both articles report convergence of both average area/lipid and fluorophore transverse position, thus invoking effective equilibration.

In the study by Skaug et al. (2009), both 1 TR-DHPE:127 DPPC and 1 TR-DHPE:511 DPPC systems were simulated, with slightly different fluorophore transverse locations and orientations being obtained from the two simulations. As expected from its location, the bulky Texas Red fluorophore introduces local disordering in the DPPC acyl chains which is apparent from the decrease of $-S_{CD}$ (in both systems) and the increase in the average area/lipid values (in the 1 TR-DHPE:127 DPPC system only) for the DPPC molecules closest to the probe. It was observed that the aryl group of Texas Red and the P atom of a particular DPPC lipid remained in close contact (≅ 0.5 nm of each other) throughout the duration of both 1 TR-DHPE:127 DPPC and 1 TR-DHPE:511 DPPC simulations (Skaug et al., 2009). On the other hand, the core of the fluorophore of Rhod-DPPE presented a tilt of $44^o \pm 8^o$ relative to the bilayer normal, and 2 Rhod-DPPE:126 DPPC bilayers showed reduced (by ~5-10%) $-S_{CD}$ values in all positions of the DPPC acyl chains (Kyrychenko, 2010a). On the whole, a significantly smaller degree of probe perturbation induced by headgroup-labeled lipid probes, compared to acyl-chain labeled lipid probes, could not be verified, as both studies report disordering effects of probe incorporation on the bilayer structure. Especially important effects were recently described in 500 ns simulations of a 24 TR-DHPE:488 DPPC (5 mol%) bilayer (Skaug et al., 2011). These included significant orientation distribution changes, clearly distinct lateral diffusion dynamics of host lipid and probe, and a predicted perturbation of the liquid ordered/liquid disordered phase diagram of a ternary saturated lipid/unsaturated lipid/cholesterol mixture upon incorporation of 1 mol% TR-DHPE.

Whereas the above studies concerned commercially available fluorescent membrane probes that have found previous use in the membrane fluorescence research community, recent works combined fluorescence measurements and MD simulations to address the behaviour of novel environment-sensitive 2-(2′-Pyridyl)- and 2-(2′-Pyrimidyl)-Indoles (Kyrychenko et al., 2010b) and 2,6-bis(1*H*-benzimidazol-2-yl)pyridine (Kyrychenko et al., 2011) in POPC. Spectral shifts and variation of steady-state and time-resolved fluorescence in different environments were measured, and in MD simulations several parameters were calculated, including the kinetics of insertion into the bilayer from the water region, the equilibrium transverse location, the inserted probes' orientations, hydrogen bonding involving water and probe molecules, and the free energy profile of penetration (estimated using the method of potential of mean constraint force (PMF)). From the latter, free energies of probe insertion were calculated that agreed well with the experimental values obtained from fluorescence intensity variation upon titration with lipid vesicles.

3. Coarse-grained simulations of dyes in lipid bilayers

Coarse-grained models represent molecules in a simplified way, e.g. by combining multiple atoms into a single interaction site or bead. This allows the simulation of larger systems for longer times than that sampled in more detailed atomistic simulations. However, this is achieved at the expense of atomic resolution, which is generally critical to many of the aspects that are commonly studied in MD simulation of fluorophores. One sole coarse-grained study of a fluorescent membrane probe (voltage sensitive dye dibutyl-amino-styryl-pyridinium-butyl-sulfonate or Di-4-ASPBS; Fig. 1K) and its derivatives interacting with POPC bilayers has been reported (Hinner et al., 2009), using the MARTINI forcefield (Marrink et al., 2007). In this work, coarse-grain simulations were used to compute the free energy of binding of these dyes to the bilayer. The determination of this parameter from atomistic simulations is highly demanding from the numerical point of view, and coarse-grained methodologies allow its calculation at a fraction of the computational cost. Validation of the MARTINI simulations was achieved by calculation of the fluorophore transverse position and orientation, and the successful comparison with atomistic simulations and experimental data. Constraint options were optimized for the determination of the PMF using umbrella sampling, in order to sample conveniently the water/membrane partition (at the expense of an adequate sampling of flip-flop motions).

Although the study was generally successful, the effects of increasing the lipophilic tail chain length and introducing polar phosphoric acid ester groups at the head or tail of these amphiphiles on the free energy of membrane binding were only semiquantitatively reproduced. Most importantly, the authors observed an overestimation of the free energy increase with increasing chain length of the Di-4-ASPBS derivatives. The underlying reasons for this effect were not clear, as the increment in binding free energy, calculated for a series of alcohols using the same parameterization and simulation protocols, was in agreement with experiment. A possible explanation is that the experimental data might be biased due to dye aggregation in the aqueous phase, especially for the longer-chained derivatives (for which discrepancies are larger). In any case, this study showed that calculation of the partition of membrane-active molecules from careful coarse-grained MD simulations is both fast and sufficiently accurate to provide a useful tool in computational membrane biophysics.

4. Concluding remarks

MD simulations of fluorescence membrane probes interacting with lipid bilayers are still somewhat scarce, but the last few years have seen a dramatic increase and diversification of the use of MD simulations to study the behavior of these systems, indicating that this is fast becoming a very active field within theoretical modeling of membranes. The possibilities offered by this approach are clearly visible from the studies described in this review. Validation of the methodology has frequently been achieved through the verification of several experimental observables. Most importantly, unique information has been retrieved, both on probe properties and regarding their effect on the host bilayer. The combination of simulation of the probes' behavior and experiments designed taking this behavior into consideration has potential to provide accurate insights on membrane structure and function at a molecular level.

Simulation work initially focused in simpler apolar fluorophores (such as DPH or pyrene) in liquid disordered bilayers. Such earlier studies served to show that many of the reported effects of probes in fluid lipid bilayers are minor and most noticeable for lipid molecules close to a probe or for high probe concentration. Recent emphasis has been gradually shifting to more complex design polar fluorophores such as NBD, BODIPY, rhodamine or cyanine groups. The number of studies addressing this type of probes has clearly surpassed those dealing with the traditional small lipophilic compounds during the last two years. Furthermore, simulations of lipid bilayers in liquid ordered and gel phases are also becoming more frequent, which reflects the recognized importance of ordered and even rigid domains such as lipid rafts (Simons and Ikonen, 1997) and ceramide platforms (Zhang et al., 2009), where the problem of finding adequate fluorescent reporters is more critical.

The increase in complexity of the simulated systems has highlighted the importance of adequate parameterization. Methodological differences in parameterization may produce substantially divergent results, as illustrated in the above comparison of the two studies of structurally very similar rhodamine headgroup-labeled phospholipids. For this reason, careful testing against experimentally well-characterized systems is still required.

Recently, the free energy of probe partition into the bilayer was added to the list of calculated parameters. The determination of the extent of interaction of a given compound with bilayers is usually the first step in the characterization of its behavior in membranes. Unless the amounts of compound in the water and lipid media are known, experimental quantitative characterization of many parameters is not feasible. To this effect, determination of PMF using umbrella sampling is an approach made available from MD simulations. Theoretical calculation of the free energy of bilayer partition is particularly advantageous for prediction purposes, as well as in situations where experimental determination is difficult e.g. due to probe aggregation or limited solubility in the aqueous medium. As illustrated by the above described works, where atomistic simulations are too demanding for the size and complexity of the systems of interest, coarse-grained simulations may provide an attractive alternative as they allow for much faster computation. For many parameters, however, atomic resolution is generally essential, and atomistic simulations remain the method of choice.

5. Acknowledgments

We acknowledge support by Fundação para a Ciência e Tecnologia (Portugal) through project PTDC/QUI-QUI/098198/2008, co-funded by FEDER (program FCOMP-01-0124-FEDER-010787).

6. References

Ash WL, Zlomislic MR, Oloo EO, Tieleman DP (2004) Computer simulations of membrane proteins. *Biochim Biophys Acta* 1666:158–189, ISSN 0006-3002

Axelrod D (1979) Carbocyanine dye orientation in red cell membrane studied by microscopic fluorescence polarization. *Biophys J* 26:557–573, ISSN 0006-3495

Berkowitz ML (2009) Detailed molecular dynamics simulations of model biological membranes containing cholesterol. *Biochim Biophys Acta* 1788:86–96, ISSN 0006-3002

Bouvrais H, Pott T, Bagatolli LA, Ipsen JH, Méléard P (2010) Impact of membrane-anchored fluorescent probes on the mechanical properties of lipid bilayers. *Biochim Biophys Acta* 1798:1333-1337, ISSN 0006-3002

Chattopadhyay A (1990) Chemistry and biology of *N*-(7-nitrobenz-2-oxa-1, 3-diazol-4-yl)-labeled lipids: fluorescent probes of biological and model membranes. *Chem Phys Lipids* 53:1–15, ISSN 0009-3084

Chattopadhyay A, London E (1987) Parallax method for direct measurement of membrane penetration depth utilizing fluorescence quenching by spin-labeled phospholipids. *Biochemistry* 26:39–45, ISSN 0006-2960

Čurdová J, Čapková P, Plášek J, Repáková J, Vattulainen I (2007) Free pyrene probes in gel and fluid membranes: perspective through atomistic simulations. *J Phys Chem B* 111:3640–3650, ISSN 1520-6106

Dale RE, Eisinger J, Blumberg WE (1979) The orientational freedom of molecular probes. The orientation factor in intramolecular energy transfer. *Biophys J* 26:161-193 Erratum in: Biophys J 30:365, ISSN 0006-3495

de Almeida RF, Loura LMS, Prieto M (2009) Membrane lipid domains and rafts: current applications of fluorescence lifetime spectroscopy and imaging. *Chem Phys Lipids* 157:61–77, ISSN 0009-3084

Filipe HAL, Moreno MJ, Loura LMS (2011). Interaction of 7-nitrobenz-2-oxa-1,3-diazol-4-yl-labeled fatty amines with 1-palmitoyl, 2-oleoyl-*sn*-glycero-3-phosphocholine bilayers: a molecular dynamics study. *J Phys Chem B* 115: 10109-10119, ISSN 1520-6106

Franks NP (1976) Structural analysis of hydrated egg lecithin and cholesterol bilayers. I. X-ray diffraction. *J Mol Biol* 100:345-358, ISSN 0022-2836

Franová M, Repáková J, Čapková P, Holopainen JM, Vattulainen I (2010) Effects of DPH on DPPC-cholesterol membranes with varying concentrations of cholesterol: from local perturbations to limitations in fluorescence anisotropy experiments. *J Phys Chem B* 114:2704-2711, ISSN 1520-6106

Gennis RB (1989) Biomembranes: molecular structure and function. Springer, New York, ISBN 0387967605

Gimpl G, Gehrig-Burger K (2011) Probes for studying cholesterol binding and cell biology. *Steroids* 76:216-231, ISSN 0039-128X

Gullapalli RR, Demirel MC, Butler PJ (2008) Molecular dynamics simulations of DiI-C_{18}(3) in a DPPC lipid bilayer. *Phys Chem Chem Phys* 10:3548–3560, ISSN 1463-9076

Harriman A, Izzet G, Ziessel R (2006) Rapid energy transfer in cascade-type bodipy dyes. *J Am Chem Soc* 128:10868-10875, ISSN 0002-7863

Herrenbauer M (2002) Biosorption of Polycyclic Aromatic Hydrocarbons (PAH) to microorganisms and liposomes. Shaker, Aachen, ISBN 3826599039

Hinner MJ, Marrink SJ, de Vries AH (2009) Location, tilt, and binding: a molecular dynamics study of voltage-sensitive dyes in biomembranes. *J Phys Chem B* 113:15807–15819, ISSN 1520-6106

Hoff B, Strandberg E, Ulrich AS, Tieleman DP, Posten C (2005) ^{2}H-NMR study and molecular dynamics simulation of the location, alignment, and mobility of pyrene in POPC bilayers. *Biophys J* 88:1818–1827, ISSN 0006-3495

Hölttä-Vuori M, Uronen RL, Repáková J, Salonen E, Vattulainen I, Panula P, Li Z, Bittman R, Ikonen E (2008) BODIPY-cholesterol: a new tool to visualize sterol trafficking in living cells and organisms. *Traffic* 9:1839–1849, ISSN 1398-9219

Huster D, Müller P, Arnold K, Herrmann A (2001) Dynamics of membrane penetration of the fluorescent 7-nitrobenz-2-oxa-1, 3-diazol-4-yl (NBD) group attached to an acyl chain of phosphatidylcholine. *Biophys J* 80:822–831, ISSN 0006-3495

Kachel K, Asuncion-Punzalan E, London E (1998) The location of fluorescence probes with charged groups in model membranes. *Biochim Biophys Acta* 1374:63–76, ISSN 0006-3002

Kaiser RD, London E (1998) Location of diphenylhexatriene (DPH) and its derivatives within membranes: comparison of different fluorescence quenching analyses of membrane depth. *Biochemistry* 37:8180–8190, ISSN 0006-2960

Kyrychenko A (2010a) A molecular dynamics model of rhodamine-labeled phospholipid incorporated into a lipid bilayer. *Chem Phys Lett* 485:95-99, ISSN 0009-2614

Kyrychenko A, Wu F, Thummel RP, Waluk J, Ladokhin AS (2010b) Partitioning and localization of environment-sensitive 2-(2'-pyridyl)- and 2-(2'-pyrimidyl)-indoles in lipid membranes: a joint refinement using fluorescence measurements and molecular dynamics simulations. *J Phys Chem B* 114:13574-13584, ISSN 1520-6106

Kyrychenko A, Sevriukov IY, Syzova ZA, Ladokhin AS, Doroshenko AO (2011) Partitioning of 2,6-Bis(1*H*-Benzimidazol-2-yl)pyridine fluorophore into a phospholipid bilayer: Complementary use of fluorescence quenching studies and molecular dynamics simulations. *Biophys Chem* 154:8-17, ISSN 0301-4622

Lakowicz, JR (2006) Principles of Fluorescence Spectroscopy, 3rd Ed. Springer, ISBN 978-0-387-31278-1, New York

Lentz BR (1989) Membrane "fluidity" as detected by diphenylhexatriene probes. *Chem Phys Lipids* 50:171–190, ISSN 0009-3084

Lentz BR (1993) Use of fluorescence probes to monitor molecular order and motions within liposome bilayers. *Chem Phys Lipids* 64:99–116, ISSN 0009-3084

López Cascales JJ, Huertas ML, García de la Torre J (1997) Molecular dynamics simulation of a dye molecule in the interior of a bilayer: 1, 6-diphenyl-1, 3, 5-hexatriene in dipalmitoylphosphatidylcholine. *Biophys Chem* 69:1–8, ISSN 0301-4622

Loura LMS, Prates Ramalho JP (2007) Location and dynamics of acyl chain NBD-labeled phosphatidylcholine (NBD-PC) in DPPC bilayers. A molecular dynamics and time-resolved fluorescence anisotropy study. *Biochim Biophys Acta* 1768:467–478, ISSN 0006-3002

Loura LMS, Fedorov A, Prieto M (2001) Exclusion of a cholesterol analog from the cholesterol-rich phase in model membranes. *Biochim Biophys Acta* 1511:236–243, ISSN 0006-3002

Loura LMS, Fernandes F, Fernandes AC, Prates Ramalho JP (2008) Effects of fluorescent probe NBD-PC on the structure, dynamics and phase transition of DPPC. A molecular dynamics and differential scanning calorimetry study. *Biochim Biophys Acta* 1778:491–501, ISSN 0006-3002

Loura LMS, Palace Carvalho AJ, Prates Ramalho JP (2010a) Direct calculation of Förster orientation factor of membrane probes by molecular simulation. *J Mol Struct (THEOCHEM)* 946:107-112, ISSN 0166-1280

Loura LMS, Prieto M, Fernandes F (2010b) Quantification of protein-lipid selectivity using FRET. *Eur Biophys J* 39:565-578, ISSN 0175-7571

Loura LMS, Fernandes F, Prieto M (2010c) Membrane microheterogeneity: Förster resonance energy transfer characterization of lateral membrane domains. *Eur Biophys J* 39:589-607, ISSN 0175-7571

Maier O, Oberle V, Hoekstra D (2002) Fluorescent lipid probes: some properties and applications (a review). *Chem Phys Lipids* 116:3–18, ISSN 0009-3084

Marrink SJ, Risselada HJ, Yefimov S, Tieleman DP, de Vries AH (2007) The MARTINI forcefield: coarse grained model for biomolecular simulations. *J Phys Chem B* 111:7812, ISSN 1520-6106

Mitchell DC, Litman BJ (1998) Molecular order and dynamics in bilayers consisting of highly polyunsaturated phospholipids. *Biophys J* 74:879–891, ISSN 0006-3495

Mukherjee S, Raghuraman H, Dasgupta S, Chattopadhyay A (2004) Organization and dynamics of *N*-(7-nitrobenz-2-oxa-1, 3-diazol-4-yl)-labeled lipids: a fluorescence approach. *Chem Phys Lipids* 127:91–101, ISSN 0009-3084

Repáková J, Čapková P, Holopainen JM, Vattulainen I (2004) Distribution, orientation, and dynamics of DPH probes in DPPC bilayer. *J Phys Chem B* 108:13438–13448, ISSN 1520-6106

Repáková J, Holopainen JM, Morrow MR, McDonald MC, Čapková P, Vattulainen I (2005) Influence of DPH on the structure and dynamics of a DPPC bilayer. *Biophys J* 88:3398–3410, ISSN 0006-3495

Repáková J, Holopainen JM, Karttunen M, Vattulainen I (2006) Influence of pyrene-labeling on fluid lipid membranes. *J Phys Chem B* 110:15403–15410, ISSN 1520-6106

Royer CA, Scarlata SF (2008) Fluorescence approaches to quantifying biomolecular interactions. *Methods Enzymol* 450:79–106, ISSN 0076-6879

Scheidt HA, Müller P, Herrmann A, Huster D (2003) The potential of fluorescent and spin-labeled steroid analogs to mimic natural cholesterol. *J Biol Chem* 278:45563-45569, ISSN 0021-9258

Shaw JE, Epand RF, Epand RM, Li Z, Bittman R, Yip CM (2006) Correlated fluorescence-atomic force microscopy of membrane domains: structure of fluorescence probes determines lipid localization. *Biophys J* 90:2170–2178, ISSN 0006-3495

Simons K, Ikonen E (1997) Functional rafts in cell membranes. *Nature* 387:569–572, ISSN 0028-0836

Skaug MJ, Longo ML, Faller R (2009) Computational studies of Texas Red-1,2-dihexadecanoyl-*sn*-glycero-3-phosphoethanolamine - model building and applications. *J Phys Chem B* 113:8758-8766, ISSN 1520-6106

Skaug MJ, Longo ML, Faller R (2011) The impact of Texas Red on lipid bilayer properties. J *Phys Chem B* 115:8500–8505, ISSN 1520-6106

Somerharju P (2002) Pyrene-labeled lipids as tools in membrane biophysics and cell biology. *Chem Phys Lipids* 116:57–74, ISSN 0009-3084

Song NC, Livanec, PW, Klauda, JB, Kuczera K, Dunn RC, Im W (2011) Orientation of fluorescent lipid analogue BODIPY-PC to probe lipid membrane properties: insights from molecular dynamics simulations. *J Phys Chem B* 115:6157–6165, ISSN 1520-6106

Straume M, Litman BJ (1987) Equilibrium and dynamic structure of large, unilamellar, unsaturated acyl chain phosphatidylcholine vesicles. Higher order analysis of 1, 6-

diphenyl-1, 3, 5-hexatriene and 1-[4-(trimethylammonio)phenyl]- 6-phenyl-1, 3, 5-hexatriene anisotropy decay. *Biochemistry* 26:5113–5120 Erratum in: *Biochemistry* 26:8030, ISSN 0006-2960

Stryer L (1978) Fluorescence energy transfer as a spectroscopic ruler. *Annu Rev Biochem* 47:829-846, ISSN 0066-4154

van der Meer BW, Coker G, Simon Chen S (1994) Resonance energy transfer, theory and data. VCH Publishers, ISBN-10: 0471185892, New York

Wolf DE (1988) Probing the lateral organization and dynamics of membranes. In: Loew LM (ed) Spectroscopic membrane probes, vol I. CRC, Boca Raton, pp 193–220, ISBN 0849345359

Worcester DL, Franks NP (1976) Structural analysis of hydrated egg lecithin and cholesterol bilayers. II. Neutrol diffraction. *J Mol Biol* 100:359-378, ISSN 0022-2836

Zhang Y, Li X, Becker KA, Gulbins E (2009) Ceramide-enriched membrane domains - structure and function. *Biochim Biophys Acta* 1788:178–183, ISSN 0006-3002

6

Thermoluminescence in Chloroplast Thylakoid

Amarendra Narayan Misra[1,2], Meena Misra[1,2] and Ranjeet Singh[1,2]
[1]*Post-Graduate Department of Biosciences & Biotechnology, Fakir Mohan University, Balasore*
[2]*Centre for Life Sciences, School of Natural Sciences, Central University of Jharkhand, Ratu-Lohardaga Road, Brambe, Ranchi, India*

1. Introduction

1.1 Historical perspective

Luminescence occurs in almost all the materials absorbing photon energy and is a phenomenon of light emitting process. There are various types of luminescence, e.g. fluorescence, phosphorescence, delayed luminescence, chemiluminescence and thermoluminescence. In these cases, light is emitted when a photo- or chomo-excited molecules is deexcited to its ground state. During this deexcitation process, radiationless internal conversion and heat dissipation occurs, which reduces the quantum yield of light emission. Luminescence can be also thermally induced and enhanced by heating the sample in the dark. This process is called thermoluminescence (TL) and describes the emission of light at characteristic temperatures from samples containing chemiluminescent active species, radical pair states or electron hole pairs (Ducruet, 2003; Misra et al., 2001). Many minerals heated at very high temperature emit luminescence and so TL has been used initially in geology, archeological dating and radiation dosimetry. The theory of charge recombination in these processes was first worked out for such minerals (Randall & Wilkins, 1945). Thermally induced photon emission by a pre-irradiated chloroplast or thylakoid or by leaf samples in darkness is known as thermoluminescence (TL) (Misra et al., 2001; Misra & Ramaswamy, 2001). This is characteristic of solid states (semi-conductors) under thermally activated recombination of electrons and positive holes that are generated by particle radiation or electromagnetic field at room or low temperature prior to their heating in dark (Chen & McKeever, 1997). TL signals were first detected in dried chloroplasts samples (Arnold & Sherwood, 1957; Tollin & Calvin 1957). Photosynthetic systems in dried chloroplasts are supposed to be severely damaged. TL emission was also recorded in intact leaves and algal cells (Arnold & Sherwood, 1957). Arnold (1966) proposed a model of recombination of free holes in PS I and of free electrons from PS II as the sources of thermally induced luminescence from algae (Chlorella) cells in darkness. However, Arnold & Azzi (1968) refuted the role of free holes from PS I. Based on further evidence on the generation of charges in irradiated chloroplast, in the new model for TL charge recombination the positive and negative charge traps were proposed to reside within PS II (Arnold & Azzi, 1968). Further, biophysical studies and availability of photosynthetic

mutants, paved the way to the charaterisation and conformation of the origin of TL peaks between the temperature range of -40°C to +50°C is unequivocally from the charge recombinations in PSII. This finding has been further corroborated by subsequent experimentation by several workers using bundle sheath chloroplasts of C-4 plants that apparently lack PSII and, therefore, show very weak TL. The inhibition of PSI activity by $HgCl_2$ does not affect the glow peak yield of isolated chloroplast (Sane et al., 1977; Horvath et al., 1978). Several other studies using herbicides and inhibitors that interact with PSI electron flow supports this conclusion.

Photosynthetic TL could be defined as an emission of light at characteristic temperatures from pre-illuminated photosynthetic samples (leaves, isolated chloroplasts or algae) during warming in the dark starting from low temperature (Sane, 2004). A set of different bands in TL emission curves appear as a result of recombination of different charge pairs. Even small changes in the redox properties of radical pairs affect the intensity and the peak position of TL bands. This complexity of information of TL emission curves can be used for selective monitoring of the effects of various biotic and abiotic stress factors. Thermoluminescence emission from freshly detached unfrozen leaves is defined as secondary or "afterglow" (AL) emission with T_m at 45°C and proves to be a sensitive test of energetic imbalance in the chloroplasts during various stress conditions (Ducruet, 2003). High-temperature thermoluminescence (HT1, HT2 and HT3 bands with T_m above 60°C) appears as a result of accumulation of lipid peroxides and can be used as a simple and efficient tool to monitor oxidative stress in leaves.

Randall & Wilkins (1945) considered that the charge recombination of fixed +/- charge pairs obeys a first order kinetics. Vass et al. (1981) postulate to photosynthetic TL studies. The probability of recombination *L(T)* for eachTL band at every measured temperature can be calculated, using the Arrhenius equation (Ducruet, 2003):

$$L(T)=N^{R}PT\Delta t\exp\left(-E_A/k_BT\right)$$

Where:

N = number of charge pairs able to recombine at temperature T.
R = order of reaction (R=1, as charge pairs are not exchangeable between PSII centres).
P = Pre-exponential factor related to the Arrhenius frequency factor s as P=*K(T)* x s, *K(T)* being an unknown factor; Δt sampling duration (~1 s); EA is the activation energy, and *kB* is the Boltzmann constant.

However, charge recombination in PSII varies from that of the minerals. So, DeVault et al. (1983) and DeVault & Govindjee (1990) proposed a theoretical calculation of photosynthetic TL (cf. Tyysjarvi & Vass, 2003).

Further, developments in the TL techniques and biophysical probing revealed that the charge arise as a reversal of the primary photochemical processes in PS II (Misra et al., 2001a, b; Sane, 2004). Therefore they are also in some relation with characteristics of fluorescence induction and emission (Ducruet, 1999; Setikova et al.,1999). There are reviews on thermoluminescence use in herbicide research (Horvath, 1986) and general reviews on TL in chloroplasts or photosynthetic organisms (Sane & Rutherford, 1986;, Inoue, 1996; Vass & Govindjee, 1996). In the present chapter, we focus mainly on the use of TL in studies of

primary photochemical processes in chloroplast thylakoid membranes particularly in PSII. The use of TL technique in the studies of thylakoid development, and the impact of environmental stresses are discussed.

TL measurements need excitation of the sample and the cooling of the sample at low temperature (liquid nitrogen), which is then followed by heating in the darkness and simultaneous recording the luminescence emitted during heating. There are several types of TL apparatus assembled and built so far (Tatake et al., 1971; Manche, 1979; Zeinalov & Maslenkova, 1996; Gilbert et al., 2003; Ducruet, 2004). For the measurement of steady-state TL, a sample such as a section of leaf, chloroplast, or algal material is placed on the sample holder and is illuminated by white light or light of a particular wavelength through a monochromator. A heater coil placed under the cupperplanchet (sample holder) slowly and linearly heats up the sample. A peltier cooling and heating system is used recently. The ultra weak TL emission is amplified several fold and is measured with a red sensitive photomultiplier. The emission(maxima same as prompt fluorescence at about 730 nm in leaves) recorded against temperature gives rise to the TL glow curve or a TL band as shown in Fig. 1. The shape of the glow curve depends on the excitation temperature, time period of excitation, heating and cooling rate, and intensity and wavelength of excitation light. The sample heating varies from 0.5 to 18°C/sec. A single flash illumination or continuous light illumination at low temperature gives rise to one TL band where as continuous illumination during sample cooling gives rise to multiple components as shown in Fig. 1. Luminescence emission from a leaf disc is sufficiently strong to be recorded with an analogue photomultiplier tube (PMT) positioned very close (about 1.5 cm above) to the sample by a light-proof holder that can slide laterally to an illumination position where a light guide comes in front of the sample whilst the PMT is protected from strong actinic light (Ducruet et al., 1998). Alternatively, luminescence can be conveyed to the detector by a light guide, which prevents heating of the PMT. In the conventional TL apparatus, the sample is frozen by liquid nitrogen in order to ensure that no recombination occurs before TL recording. A complete study on the effect of freezing on TL emission has been reported by Homann (1999), who reported few artifacts during freezing. So before the start of experiments, a comparison between TL emission in frozen and unfrozen samples be done, to ascertain the quality of TL signals.

2. Charge recombinations

In a leaf, algae, cyanobacteria, intact chloroplasts, isolated thylakoids, a brief (5 ms) flash induces one charge separation per PSII centre as shown in Fig. 1. This separated charges recombine to stabilize to S_2Q_B pair, and is able to emit luminescence with a exponential decay phase with $t_{1/2}$~40 s at 20 °C, or the B band with a maximum temperature T_m between 30°C and 40°C. When a sequences of 1 to 10 flashes are triggered before TL recording, the B band intensity oscillates with a period of 4 with maxima at two and six flashes, corresponding to the maximum S_2+S_3, the only two states able to yield luminescence upon recombination with Q_A^- or Q_B^-. The S_1 state is unable to recombine.

Following a light period that creates an equipartition of S_0, S_1, S_2, and S_3, the states S_0 and S_1 remain stable during a dark adaptation whilst S_2 and S_3 are converted to S_1, resulting in a 1/4 S_0 3/4 S_1 distribution in dark-adapted material. In leaves, approximately 40% of Q_B is reduced (Rutherford et al., 1984a), so that the Q_B^-/Q_B ratio weakly oscillates with a period of

2 according to flash number. In isolated thylakoids at low pH (<6.5) the B band, induced by two flashes, splits into two bands B_1 ($S_3Q_B^-$) and B_2 ($S_2Q_B^-$), because S_3 is more destabilized by protonation than S_2 (Joliot & Joliot, 1980; Rutherfordet al., 1984b; Demeter & Sallai, 1986; Miranda & Ducruet, 1995b). Upon treatment by a PSII-inhibiting herbicide (diuron, atrazine) which blocks the Q_A to Q_B electron transfer, the electron is stored as Q_A^-, a less stabilized state (i.e. the activation barrier is smaller) than Q_B^- and produces a Q-band peaking at a lower temperature (around 5 °C at neutral pH) than the B band upon recombination with S_2/S_3. This band is associated with a C-band at about 55 °C due to $D^+Q_A^-$ (Johnson et al., 1994), D^+ being the oxidized form of Tyrosine D on the inactive branch of PSII. The functional electron donor to the PSII P_{680} centre is Tyrosine Z: $Z+P_{680*}$ $Tyr_Z^+ + P_{680}$-.

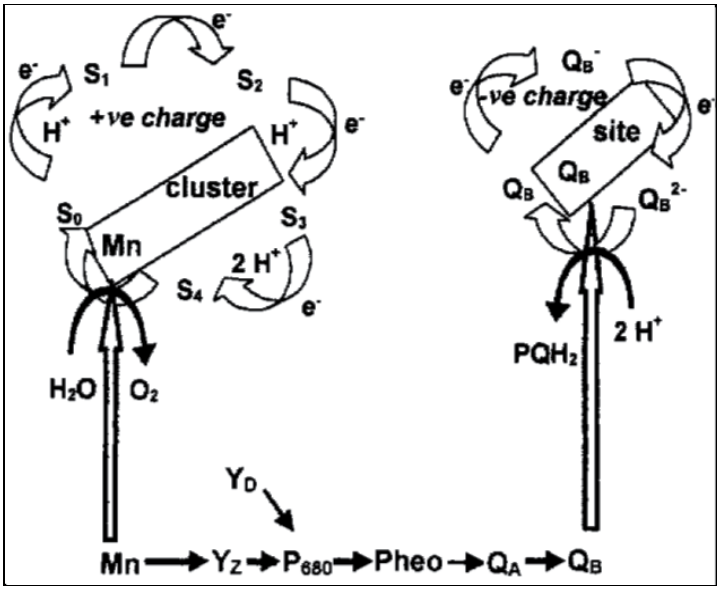

Fig. 1. Schematic view of the +ve and -ve charge formation in PS II. (Adapted from Misra et al., 2001a,b).

A fast rereduction of Z^+ by S states occurs, except when the oxygen-evolving manganese complex is damaged, which leads to the emergence of A band $Z^+Q_B^-$ at about -15 °C. Other TL bands exist at lower temperatures which are not fully explained and will not be considered here since they have been of little interest in plant biology. Twenty years ago, thermoluminescence brought a conformation of the charge stabilization model of PSII. It remains a valuable technique that gives a global view complementing more analytical tools and it is particularly well adapted to the study of PSII mutants. Furthermore, like chlorophyll fluorescence, TL is relevant to various levels of integration, from subchloroplast particles to algal cells or leaves (Farineau, 1993; Homann, 1999). However, applications to leaf photosynthesis have been relatively few until now, due to instrumental constraints and to a lack of understanding of in vivo signals. Several reviews already exist on photosynthesis TL (Sane & Rutherford, 1986; Vass & Inoue, 1992; Misra et al., 2001; Tyysjarvi & Vass, 2003). The present chapter will be focused on TL emission by leaves and will address the instrumental, theoretical and practical issues of measuring TL in leaf discs. Taking advantage of new and recently available components, simple instruments designed for leaf studies can now be built.

The properties of TL bands already characterized in thylakoids or subchloroplast particles are modified *in vivo* by the cellular environment, particularly when leaves are kept unfrozen during the cooling step. Different types of stresses also modify the shape and intensity of the existing bands or enhance minor bands. Furthermore, a TL `afterglow' band observable only in intact systems (intact chloroplasts, algae and leaf fragments) reflects the flow of electrons from reducing compounds present in the stroma to the plastoquinone pool and the quinonic acceptors of PSII. This back-transfer follows one of the pathways involved in the cyclic/chlororespiratory electron flow and appears to be a sensitive indicator of photosynthetic metabolism. Although PSII is totally destroyed at about 60 °C, huge chlorophyll TL bands can be observed at higher temperatures.

They correspond to a heat-enhanced chemiluminescence from molecular species generated by radical forms of oxygen, such as lipid peroxides, which accumulate in stress situations. Despite the fact that the mechanisms of high-temperature TL emission (HTL) is completely different from photosynthetic TL, recorded through a single temperature scan from 0 °C to 160 °C on the same leaf disc. Both the photosynthesis TL bands and the oxidative stress HTL bands proves to be of practical interest.

3. TL glow peaks: Nomenclatures and classifications

There are several classifications of TL glow bands. However, more acceptable are 'Roman number system – I, II, III, IV etc' (Table 1) or 'Alphabetic form - A, B_1, B_2, C, Z, Z_v or M_o' (Fig. 2, Misra et al., 2001) (Table 1). TL glow peaks that are well characterized are- A, AG AT, B, C, M_o, Q,Z and Z_v bands (Table 1). The TL band Z and Zv arise at -169˚C and at -80˚C to -30˚C (Inoue, 1996). These two bands are assigned to charge recombination between charged pigment molecules. The Chl^+Chl^- charge recombination give rise to Z-band and $P680^+ Q_A^-$ charged recombination gives rise to Z_v- band of the TL spectra. However alteration in the PS II RC is mainly studied through the changes in the TL bands A, AG, AT, B, C, M_o, or Q. So a detailed characteristic of the charge pairs and the factors responsible for such glow peaks are explained.

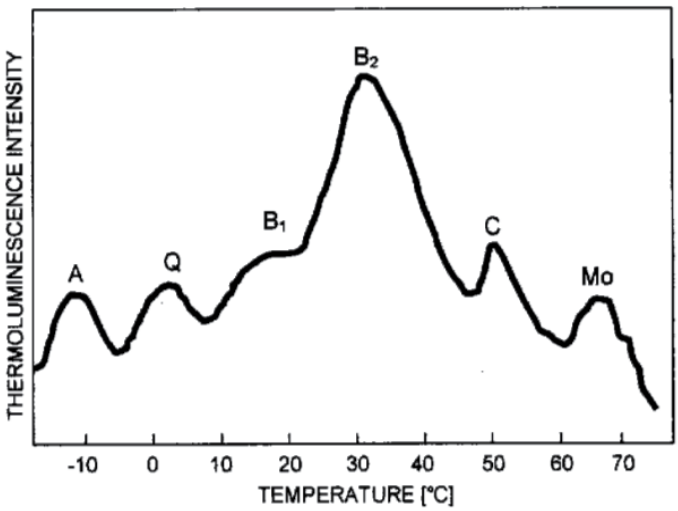

Fig. 2. Theoreticel picture of thermoluminescence (TL) glow peaks of photosynthetic materials.

3.1 A-band (II band)

A TL glow peak at -10˚C originates by photo-exiting photosynthetic samples by two flashes at room temperature, then cooling of samples to 77K, and further continuous irradiation of the sample (Laufer et al., 1978; Inoue, 1981; Tatake et al.,1981; Demeter et al., 1985). This band is designated as A-band. The charge recombination of $S_3Q_A^-$ is responsible for the origin of the A-band (Koike et al., 1986).

3.2 AG- band

An after glow (AG) or delayed luminescence rise is induced by far-red radiation (Bertsch & Azzi, 1965). This emission was reported by only in intact systems such as intact chloroplasts (Hideg et al., 1991), leaves (Bjorn, 1971), or protoplasts (Nakamoto et al., 1988), and could not be detected in isolated thylakoids or PS II RC complexes. This AG glow peak at 45˚C could be resolved by slow heating of leaf samples (Miranda & Ducruet, 1995a,b; Ducruet et al., 1997). The AG-band is suppressed by the PS II electron transport inhibitor diuron (Miranda & Ducruet, 1995a,b) and by the PS I cyclic electron transport inhibitor antimycin or uncouplers (Bjorn, 1971). This suggests that in addition to PS II, also the cyclic electron transport and/or the trans-thylakoid proton gradient are involved in the generation of AG glow peaks in leaves. Sundblad et al. (1988) assigned the AG glow peak primarily to the back reaction of $S_2/S_3Q_B^-$ charge recombination. The occurrence of AG peaks was also assigned to the presence of high concentrations of ATP and/or NADPH in the plant cells (Inoue et al., 1976).

3.3 A_T-band

The Tris-washed PS II particles show a TL glow peak similar to A-band (Inoue et al., 1977; Rozsa & Demeter, 1982). Tris washing depletes functional Mn cluster from PS II particles. So the generation of S-states is impaired. Unlike the A-band, this band at -10˚C arises due to charge recombination of $His^+Q_A^-$ (One & Inoue, 1991; Kramer et al., 1994). This positive charge is assigned to His195 residue and His190 residue of the D1 polypeptide (Kramer et al., 1994). This was confirmed by the impaired A_T-band in *Chlamydomonas reinhardtii* mutants substituted for the above His residues (Kramer et al., 1994).

3.4 B-band (III (B1), IV (B2))

This is the best-characterised TL glow peak in photosynthetic materials. The B-band arises usually at around 30-35˚C. It is correlated to the water-oxidising complex of PS II (Inoue, 1976; Rozsa & Demeter, 1982). Charge recombination between $S_2Q_B^-$ (band III or B_1 band) and $S_3B_Q^-$ (band IV or B_2 band), together generate the B-band (Rutherford et al., 1982). In dark-adapted chloroplasts, the distribution of S_0 and S_1 are 25% and 75%, respectively. Thus, the maxima obtained after the second flash indicate the participation of the S_3 state in the generation of peak IV (B band). Based on several studies it has been concluded that peak III (B_1 band) originates from $S_3Q_B^-$ and peak IV (B_2 band) originates from the recombination of $S_2Q_B^-$.

The peak V (C band) is not related to the photosynthetic electron chain (Table 1). Peak V (C band) was first observed in DCMU treated chloroplasts and in etiolated leaves (Vass et al. 1981). Since in etiolated leaves the oxygen evolving system is inactive, it has been suggested

that peak V is not related to the water splitting enzyme. However, several studies have shown that this peak also undergoes a period four oscillation and it has been proposed that this band may be originating from the charge recombination of the $S_0Q_A^-$ and $S_1Q_A^-$ redox couple (Demeter & Govindjee, 1989; Sane et al., 1983).

Peak	Approximate Temperature (^oC)	Origin	Mean Lifetime (t, sec)	Remarks
Illuminated samples				
Z	-160	Chl^+Chl^-		0.2
Z1	-70	$P680^+Q_A^-$	1.3	
II (A)	-10	$S_3Q_A^-$	-	Mn oxygen-evolving complex
Q	+5^{o}C	$S_2Q_A^-$	-	Secondary Qb, quinone acceptor (induced by herbicides)
III (B1)	+20	$S_3Q_B^-$	-	After one flash
IV (B2)	+30	$S_2Q_B^-$	29	After three flashes
V (C)	+50	$Y_D^+ Q_A^-$	1062	
AG	+45	S_2/S_3Q_B	1.3	
Oxidative bands(do not depend on preillumination)				
HTL1 (=Mo band*)	65 to85 °C	Aldehydes+H2O		A pseudo-HTL2 occurs in wet samples
HTL2	120 to140 °C	Lipid peroxides		dry samples
HTL3	> 160°C	Induce by warming		Oxidative band increases during TL warming

Notes: Peaks Z1, II (A), IV (B_2), and V (C) oscillate with flash number and the maxima differs between S_3 for peak II, S_2/S_3 for peak IV (B), and S_1 for peak V (C). Some peaks oscillate when diuron was added after excitation, for example, peaks II and V (C). *Misra et al. (2001)

Table 1. Nomenclature of TL Glow Peaks in Plants

3.5 High temperature (HTL) bands

Strong TL bands are observed even in dark adapted samples above physiological temperatures >50/60 °C. These bands are ascribed to chemiluminescence bands or HTL, and are few oxidative bands unrelated to PS II. Such TL bands in algae or leaves were reported by Venediktov et al., (1989), Vavilin et al., (1991) and Merzlyaket al., (1992). A HTL band around 60-75°C was also reported by Hideg & Vass (1993), Stallaert et al., (1995) and Marder et al., (1998). This band is reported to be due to the accumulation of lipidperoxides (Vavilin & Ducruet, 1998). When the samples were kept in water while heating to prevent desiccation a band at 130 °C was observed and this was proposed to be due to the hydrolysis of lipid peroxides (Ducruet & Vavilin, 1999) or an indicator of oxidative stress (Havaux & Niyogi, 1999). Similar HTL bands around 60-75°C is reported by other authors also (Skotnica et al., 1999; Havaux & Niyogi, 1999; Ducruet & Vavilin, 1999).

4. Thylakoid organization and changes in TL glow peak characteristics

In a healthy leaf, the B band at about 35 °C is prominent, although other bands the Q-band, AG or C-bands can also be detected. Oscillations were also seen in the case of TL bands, especially peaks III B_1), IV (B_2) and V(C) (Bhagawat & Bhattacharjee, 2005). The oscillation of peak IV (B band) of the TL band is the best-characterized band showing maxima at 2, 6, 10, etc., flashes with a periodicity of four (Misra et al., 1998). Manganese oxidation states S_2/S_3 were found to be the most luminescent states. The different TL peaks attributed to $S_2Q_A^-$ and $S_2Q_B^-$ reflects different activation energies for the recombination reaction to take place in each of these states. This energy difference may, in part, reflect a different midpoint potential between the Q_A/Q_A^- and Q_B/Q_B^- redox couple.

Increase of the Q-band (T_m ~5 °C), and the associated C-band (~55 °C), reflects a damage to Q_B of PSII e.g. during photoinhibition (Misra et al., 1996; 1998; Janda et al., 1992). The A band (~ +15 °C) is prominent in thylakoid samples or leaf with damaged oxygen evolving complex. However, frozen samples show Q and A bands, which are reported to be artefacts (Homann, 1999).

5. Stress induced changes in TL glow peaks

TL is a useful tool for the study of photosynthetic electron transfer both at the acceptor and the donor sides of PS II (Misra et al., 2001a, b; Misra & Ramaswamy, 2001) as well from the water–oxidase complex to PSI (secondary quinone acceptor) (Bhagawat & Bhattacharjee, 2005).

The effects of various abiotic and biotic stress factors that influence PSII activity, such as UV, high light, high temperature, drought, viral infection, hormonal effect, have also been studied. Major TL bands are missing in etiolated leaves. Intermittent illumination to greening leaves which does not develop Mn clusture properly do not show the TL bands (Inoue et al., 1976; Sane et al., 1977). Misra et al. (1998b) reported a gradual increase in the Q and B band from base to apex of that wheat leaves greening under continuous illumination, which confirms a developmental gradient across the wheat leaf lamina and a gradual development and organization of the photosynthetic PSII complexes. Leaf aging under continuous light or under continuous darkness resulted in a decrease in Q and B bands (Joshi et al., 1993). Biswal et al. (2001) showed through an elegant TL experiment a block in the electron flow from Q_A to Q_B during leaf aging and also showed a decrease in the quinone pools in PS II.

Salt stress affects differentially the Q and B band (Biswal et al. 2002; Sahu et al. 1998; Misra et al. 1998c). Relatively the B band is more affected than the Q band. These are dose and time dependant. Zurita et al. (2005) showed that not only the B band is affected, but there is a back flow of electrons in the salt stressed photosynthetic system.

Mineral supplementation of N, P, K or their mixtures induce a shift in the A band from nearly -13°C to 8°C, suggesting the accumulation of S_4 states in the mineral supplemented leaf (Soltnev et al., 1998). Heavy metals such as Cu^{2+}, Ni^{2+}, Co^{2+} and Zn^{2+} affects B band only (Mohanty et al., 1989). Inert gases (N_2, He, Ar, Xe) and anoxic environment reduces the B and C band intensities in leaves (Soltnev et al., 1999). Halogens like I^- quenches the TL peaks probably by donating electrons to the S-states (Solntsev et al., 1995). Drought stress shifts the

B band to a lower temperature, which is explained by the redox changes in the thylakoid membranes changing the redox pool in the chloroplast (Ducruet & Vavilin, 1999; Janda et al., 1999).

Leaves irradiated with 725 nm illumination showed B- and C- bands, but A- band was missing (Mirand & Ducruet, 1995a). Probably this is due to photoabsorption by P_{700} pigment in PSI and not by PSII. Increasing the duration of the illumination decreased the peak temperature of B-band, probably due to a progressive lumen acidification.

Photoinhibitory treatment which usually result in the decreased quantum efficiency of PSII and degradation of D1 polypeptide, do not affect the S-states but affects B-band with least effect on C-band (Misra et al., 1997; 1998a). Isolated thylakoids showed a parallel decrease in Q- and B-band (Vass et al., 1988) suggesting both Q_A and Q_B is affected by photoinhibition. Ohad et al. (1990) reported a band shift of B-band to lower temperature, suggesting lumen acidification and redox changes in PSII. Misra et al. (1997, 1998a) reported Q- and B-band intensity decreased with high temperature in pothos and spinach leaves. Janda et al. (1999) reported membrane leakiness and grana destacking might be the reason for the changes in AG bands both at high temperature and freezing.

Viral infection of the plant shifts the B-band to a higher temperature with a decrease in its intensity (Rahoutei et al., 1999). There appears a new peak at 70°C, which is suggested to be due to membrane lipid peroxidation due to hypersensitive reactions in the leaf cells (Stallaert et al., 1995).

6. Conclusion and future perspective

The phenomenon of thermoluminescence in photosynthetic materials has been used routinely in characterizing the redox reactions of PSII in thylakoid membrane both in isolated systems and intact leaves. TL methods are also used as a non-invasive method for the detection of genetic lessions or genetic modifications in the plants (Lurie & Bertsch, 1974; Ichikawa et al., 1975; Debus et al., 1988; Minagawa et al., 1999). Also, the screening of photosynthetic mutants from these genetically modified organism, led to the confirmation of the origin of TL bands. This simple instrument can be fabricated in a laboratory with minimum infrastructure facility. The charge pair interactions giving rise to TL bands of characteristic peaks is used routinely for the stress characterization both donor side and acceptor side of PS II in photosynthetic materials. The oscillation pattern of TL can denote the ''S'' state transition and can be used for a titre of the Mn clusture of oxygen evolving complex.

TL characteristics may help in identifying new site(s) of action of herbicides and other chaotropic agents. However, TL studies are only confined to PS II and the method has such limitations or confines. The other limitations are the shift in the peak temperature of TL bands due to differences in the instrumentation, illumination temperature, and several other parameters that are obscure. The phenomenon of HTL is now a days used as an useful tool for understanding oxidative changes in photosynthetic systems. Also this system is now used in 'sensors' for developing 'biosensors' (Zhang et al., 2007). However, before this proposition comes true, the instrumentation needs more precission and miniaturization.

7. Acknowledgements

This work was supported by funds from UGC-MRP No.36-302/2008(SR) and DST- INT/ BULGARIA/ B70/06 to ANM. MM acknowledges the award of DST-WoS and UGC PDF for Women.

8. References

Bendall, D.S. & Manasse, R.S. (1995). Cyclic photophosphorylation and electron transport, *Biochimica et Biophysica Acta,* 1229, 23-38

Bennoun, P. (1982). Evidence for a respiratory chain in the chloroplast, *Proc Natl Acad Sci USA,* 79, 4352-4356

Bertsch, W.F. & Azzi, J.R. (1965). A relative maximum in the decay of long-term delayed light emission from the photosynthetic apparatus, *Biochimica et Biophysica Acta,* 94, 1526

Bhagwat, A.S. & Bhattacharjee, S.K. (2005).Thermoluminescence as a tool in the study of photosynthesis, *Taylor & Francis Group*, LLC

Biswal, A.K.; Dilnawaz, F.; David, K.A.V.; Ramaswamy, N. K. & Misra, A.N. (2001). Increase in the intensity of thermoluminescence Q-band during leaf ageing is due to a block in the electron transfer from Q_A to Q_B, *Luminescence*, 16, 309-313

Biswal, A.K.; Dilnawaz, F.; Ramaswamy, N.K.; David, K.A.V. & Misra, A.N. (2002). Thermoluminescence characteristics of sodium chloride salt stressed Indian mustard seedlings, *Luminescence*, 17, 135-140

Bjorn, L.O. (1971). Far-red induced, long-live after glow from photosynthetic cells. Size of after glow unit and paths of energy accumulation and dissipation, *Photochemistry and Photobiology*, 13, 5-20

Briantais, J.M.; Ducruet, J.M.; Hogdes, M. & Krause, H. (1992). Effects of high light at chilling temperature on photosystem II in spinach leaves, *Photosynthesis Research,* 31, 1-10

Cser, K.; Deak, Z.; Telfer, A.; Barber, J. & Vass, I. (2008). Energetics of Photosystem II charge recombination in *Acaryochloris marina* studied by thermoluminescence and flash-induced chlorophyll fluorescence measurements, *Photosynthesis Research,* 98, 131–140

Demeter, S. & Govindjee (1989). Thermoluminescence in plants, *Physiological Plantarum*, 75, 121–130

Demeter, S. & Sallai, A. (1986). Effect of pH on thethermoluminescence of spinach chloroplasts in the presence and absence of photosystem II inhibitors, *Biochimica et Biophysica Acta,* 851, 267-275

Demeter, S. & Vass, I. (1984). Charge accumulation and recombination in photosystem II studied by thermoluminescence. I. Participationof the primary acceptor Q and secondary acceptor B in the generation of thermoluminescence in chloroplasts, *Biochimicaet Biophysica Acta*, 764, 24-32

DeVault, D.; Govindjee & Arnold W. (1983). Energetics of photosynthesis glow peaks. *Proceedings of the National Academy of Sciences, USA,* 80, 983-987

DeVault, D & Govindjee (1990). Photosynthetic glow peaks and their relationship with the free energy changes, *Photosynthesis Research*, 24, 175-181

Dilnawaz, F.; Vass, I. & Misra, A.N. (2001). Thermoluminescence glow peaks of chloroplasts along the axis of wheat leaf lamina, *Photosynthsis*, PS2001. CSIRO Publ., Melbourne, Australia S2-001

Ducruet, J.M. & Vavilin, D. (1999). Chlorophyll high-temperature thermoluminescence emission as an indicator of oxidative stress. Perturbating effects of oxygen and leaf water content, *Free Radical Research,* 31S, 187-192

Ducruet, J.M. & Vass, I. (2009). Thermoluminescence: experimental. *Photosynthesis Research,* 101, 195–204

Ducruet, J.M. & Miranda, T. (1992). Graphical and numerical analysis of thermoluminescence and fluorescence F_0 emission in photosynthetic material, *Photosynthesis Research*, 33, 15–27

Ducruet, J.M. (2003). Chlorophyll thermoluminescence of leaf discs: simple instruments and progress in signal interpretation open the way to new ecophysiological indicators. *Journal of Experimental Botany,* 54, 2419–2430

Ducruet, J.M.; Peeva, V. & Havaux, M. (2007). Chlorophyll thermofluorescence and thermoluminescence as complementary tools for the study of temperature stress in plants. *Photosynthesis Research,* 93, 159–171

Ducruet, J.M.; Roman, M.; Ortega, J.M. & Janda, T. (2005). Role of the oxidized secondary acceptor Q_B of Photosystem II in the delayed 'after glow' chlorophyll luminescence, *Photosynthesis Research,* 84, 161–166

Ducruet, J.M.; Toulouse, A. & Roman, M. (1998). Thermoluminescence of plant leaves: instrumental and experimental aspects. In: Garab G (ed) *Photosynthesis: mechanisms and effects*, vol V. Kluwer Academic Publishers, Dordrecht, pp 4353–4356

Farineau, J. (1993). Compared thermoluminescence characteristics of pea thylakoids studied in vitro and in situ (leaves). The effect of photoinhibitory treatments, *Photosynthesis Research,* 36, 25-34

Fedoulov, Y.P. (1998). System analysis of frost resistance in winter wheat and its use in breeding, *Euphytica*, 100, 101-108

Finazzi, G.; Rappaport, F.; Furia, A.; Fleischmann, M.; Rochaix, J.D.; Zito, F. & Forti G. (2002). Involvement of state transitions in the switch between linear and cyclic electron flow in *Chlamydomonas reinhardtii*, *EMBO Reports,* 31, 280-285

Garab, G.; Lajko, F.; Mustardy, L. & Marton L. (1989). Respiratory control over photosynthetic electron transport in chloroplasts of higher-plant cells: evidence for chloro-respiration, *Planta*, 179, 349-358

Gilbert, M.; Skotnica, J.; Weingart, I. & Wilhelm, C. (2004a). Effects of UV irradiation on barley and tomato leaves: thermoluminescence as a method to screen the impact of UV radiation on crop plants, *Functional Plant Biololgy*, 31, 825–845

Gilbert, M.; Wagner, H.; Weingart, I.; Skotnica, J.; Nieber, K.; Tauer, G.; Bergmann, F.; Fischer, H. & Wilhelm, C. (2004b). A new type of thermoluminometer: a highly sensitive tool in applied photosynthesis research and plant stress physiology. *Journal of Plant Physiology,* 161, 641–651

Glemin, A.; Miranda, T.; Ducruet, J.M. (1992). Temperature behavior of photosystem II in chilling-resistant and chilling-susceptible plant species, studied by fluorescence and luminescence methods. In: Murata N, ed. *Research in photosynthesis*, Vol. IV. Utrecht:Kluwer, 85-188

Havaux, M. & Niyogi K.K. (1999). The violaxanthin cycle protects plants from photo-oxidative damage by more than one mechanism. *Proceedings of the National Academy of Sciences*, *USA,* 96, 8762-8767

Havaux, M. (1996). Short-term responses of photosystem I to heat stress. *Photosynthesis Research*, 47, 85-97

Heber, U.; Neimanis, S.; Dietz, K.J. & Viil, J. (1986). Assimilation power as a driving force in photosynthesis, *Biochimica et Biophysica Acta*, 852, 144-155

Heldt, H.W.; Werdan, K.; Milovancev, M. & Geller G. (1973). Alkalization of the chloroplast stroma caused by light dependent proton flux into the thylakoid space, *Biochimica et Biophysica Acta*, 314, 224-241

Hideg, E. & Demeter S. (1985). Binary oscillation of delayed luminescence: evidence of the participation of Q_B in the charge recombination, *Zeitschriftfu Èr Naturforschung*, 40c, 827-831

Hideg, E.; Kobayashi, M. & Inaba H. (1991). The far-red induced slow component of delayed light from chloroplasts is emitted from Photosystem II. Evidence from emission spectroscopy. *Photosynthesis Research,* 29, 107-112

Hideg, E. & Vass I. (1993). The 75°C thermoluminescence band of green tissues: chemiluminescence from membrane-chlorophyll interaction, *Photochemistry and Photobiology*, 58, 280-283

Homann, P.H. (1999). Reliability of photosystem II thermoluminescence measurements after sample freezing: few artifacts with Photosystem II membranes but gross distortions with certain leaves, *Photosynthesis Research*, 62, 219-229.

Horvath, G.; Droppa, M.; Mustardy, L.A. & Faludi-Daniel, A. (1978). Functional characteristics of intact chloroplasts isolated from mesophyll and bundle sheath cells of maize, *Plant* 141, 239–251

Janda, T.; Szalai, G.; Giauffret, C.; Paldi, E.; Ducruet, J.M. (1999). The thermoluminescence 'After glow' band as a sensitive indicator of abiotic stresses in plants, *Zeitschriftfu Èr Naturforschung*, 54c, 629-633

Janda, T.; Szalai, G. & Paldi, E. (2000). Thermoluminescence investigation of low temperature stress in maize, *Photosynthetica,* 38, 635-639

Janda, T.; Wiessner, W.; Paldi, E.; Mende, D. & Demeter, S. (1992). Thermoluminescence investigation of photoinhibition in the green alga *Chlamydomonas stellata* and in *Pisum sativum L.* leaves, *Zeitschriftfu Èr Naturforschung* 47c, 585-590

Johnson, G.N.; Boussac, A. & Rutherford, A.W. (1994). The origin of 40-50°C thermoluminescence bands in Photosystem II, *Biochimica et Biophysica Acta,* 1184, 85-92

Joliot, P. & Joliot, A. (1980). Dependence of delayed luminescence upon adenosine triphosphatase activity in *Chlorella*, *Plant Physiology*, 65, 691-696

Jursinic, P.A. (1986). Delayed fluorescence: current concepts and status. In: Govindjee, Amesz, J. and Fork, D.C., eds. *Light emission by plants and bacteria*. Orlando: Academic Press, 291-328

Krieger, A.; Bolte, S.; Dietz, K.J. & Ducruet, J.M. (1998). Thermoluminescence studies on the facultative crassulean-acid metabolism plant *Mesembryanthemum crystallinum L*, *Planta,* 205, 587-594

Lavergne, J. & Junge, W. (1993). Proton release during the redox cycle of the water oxidase, *Photosynthesis Research*, 38, 279-296

Lavorel, J. (1975). Luminescence. In Govindjee, ed. *Bioenergetics of photosynthesis*, New York: Academic Press, 223-317

Malkin, S.; Bilger, W. & Schreiber U. (1994). The relationship between millisecond luminescence and fluorescence in tobacco leaves during the induction period, *Photosynthesis Reserach* 39, 57-66

Manche, E.P. (1979). Thermoluminescence. In: Ewing, G.W. (ed.). *Topics in Chemical Instrumentation, Journal of Chemical Education,* 56A, 273

Manuel, N.; Cornic, G.; Aubert, S.; Cholet Bligny, P. & Heber, U. (1999). Protection against photoinhibition in the alpine plant *Geummontanum*, *Oecologia*, 119, 149-158

Marder, J,B.; Droppa, M.; Caspi, V.; Raskin, V.I. & Horvath, G. (1998). Light-independent thermoluminescence from greening barley leaves: evidence for involvement of oxygen radicals and free chlorophylls. *Physiologia Plantarum,* 104, 713-719

Maslenkova, L. (2010).Thermoluminescence from photosynthesizing systems as a method for detection of early plant stress symptoms. Effect of desiccation on thermoluminescence emission parameters in mesophytic and poikilohydric plants, *General and Applied Plant Physiology,* 36, 87–99

Mellvig, S. & Tillberg, J.S. (1986). Transient peaks in the delayed luminescence from *Scenedesmus obtusiusculus* induced by phosphorous starvation and carbon dioxide deficiency. *Physiologia Plantarum,* 28, 180-188

Merzlyak, M.N.; Pavlov, V.K. & Zhigalova, T.V. (1992). Effect of desiccation on chlorophyll high temperature chemiluminescence in *Acer platanoides L.* and *Aesculushippo castanum L.* leaves, *Journal of Plant Physiology,* 139, 629-631

Miranda, T. & Ducruet J.M. (1995a). Characterization of the chlorophyll thermoluminescence after glow in dark-adapted or far-red-illuminated plant leaves, *Plant Physiology and Biochemistry*, 33, 689-699

Miranda, T. & Ducruet, J.M. (1995b). Effects of dark- and light induced proton gradients in thylakoids on the Q and B thermoluminescence bands, *Photosynthesis Research,* 43, 251-262

Misra, A.N. & Ramaswamy, N.K. (2001). Thermoluminescence of green plants (Review, New Trends in Photosciences). *Indian Photobiology Society News Lett*, 40, 45-50

Misra, A.N.; Dilnawaz, F.;Misra, M. & Biswal, A.K. (2001b). Thermoluminescence in chloroplasts. *In* Biophysical processes in living systems.Chapter 17. (PadhaSaradhiB,ed.), Oxford/IBH, New Delhi/ Science Publ., Enfield (NH), USA, Plymouth, UK. pp.303-311.

Misra, A.N.; Dilnawaz, F.; Misra, M. & Biswal, A.K. (2001a). Thermoluminescence in chloroplasts as an indicator of alterations in photosystem II reaction center by biotic and abiotic stress. *Photosynthetica,* 39, 1-9

Misra, A.N.; Ramaswamy, N.K. & Desai, T.S. (1997). Thermoluminescence studies on photoinhibition of pothos leaf discs at chilling, room and high temperature. *Journal of Photochemistry and Photobiology*, 38, 164-168

Misra, A.N.; Ramaswamy, N.K. & Desai, T.S. (1998a). Thermoluminescence properties and changes in D1 polypeptide of spinach chloroplasts during photoinhibition of spinach leaf discs at chilling, room and high temperatures. *In Photosynthesis : Mechanism and Effects.*Vol. III (Garab G, ed.), Kluwer Acad. Publ., The Netherlands pp.2213-2216

Misra, A.N.; Sahu, S.M.; Dilnawaz, F.; Mahapatra, P.; Misra, M.; Ramaswamy, N.K. & Desai, T.S. (1998b). Photosynthetic pigment-protein content, electron transport activity and thermoluminescence properties of chloroplasts along the developmental

gradient in greening wheat (*Triticum aestivum* L.) leaves. *In Photosynthesis : Mechanism and Effects*. Vol. IV (Garab G, ed.), Kluwer Acad. Publ., The Netherlands pp.3179-3182

Misra, A.N.; Sahu, S.M.; Misra, M.; Ramaswamy, N.K. & Desai, T.S. (1998c). Sodium chloride salt stress induced changes in thylakoid pigment-protein complexes, PS II activity and TL glow peaks of chloroplasts from mung bean (*Vigna radiata* L.) and Indian mustard (*Brassica juncea* Coss.) seedlings. Z. Naturforsch. Part: C, 54, 640-644

Nakamoto, I.; Sundblad, L.G.; Garderstro, È. P. & Sundbom E. (1988). Far-red stimulated long-lived luminescence from barley protoplasts, *Plant Science*, 55, 1-7

Palmqvist, K.; Sundblad, L.G.; Samuelsson, G. & Sundbom, E. (1986). A correlation between changes in luminescence decay kinetics and the appearance of a CO_2-accumulating mechanism in *Scenedes musobliquus*, *Photosynthesis Research*, 10, 113-123.

Pieralice, M.; Sergio, L.; Di Venere, D. & Venediktov, P. (2011). A brief note on thermoluminescence analysis of photosystem II and lipid peroxidation during the shelf life of ready-to-use rocket (*Diplotaxis tenuifolia* L.), *European Food Research Technology,* 232, 919–923

Rahoutei, J.; Baron, M.; Garcia-Luque, I.; Droppa, M.; Nemenyi, A. & Horvath, G. (1999). Effect of tobamo virus infection on thermoluminescence characteristics of chloroplasts from infected plants, *Zeitschriftfu Èr Naturforschung*, 54c, 634-639

Randall, J.T. & Wilkins, M.H.F. (1945). Phosphorescence and electron traps, *Proceedings of the Royal Society (London) Series A,* 184, 366-408

Ravenel, R.; Peltier, G. & Havaux, M. (1994). The cyclic electron pathways around photosystem I in *Chlamydomonas reinhardtii* as determined in vivo by photo-acoustic measurements of energy storage, *Planta,* 193, 251-259

Roman, M & Ducruet, J.M. (2000). Evidence from leaf thermoluminescence for a decrease of the [NADPH+ATP] energetic potential in cold-sensitive *Pisum sativum L.* varieties upon hardening at 5°C, *Journal of Plant Physiology*, 157, 177-181

Roman, M. (2002). Whole leaf thermoluminescence emission in *Pisum sativum* L: influence of leaflet position, *Photosynthetica* 40, 153-156

Rose, S.; Minagawa, J.; Seufferheld, M.; Padden, S.; Svensson, B.; Kolling, D R. J.; Crofts, A R. & Govindjee (2008). D1-arginine257 mutants (R257E, K, and Q) of *Chlamydomonas reinhardtii* have a lowered Q_B redox potential: analysis of thermoluminescence and fluorescence measurements, *Photosynthesis Research,* 98, 449–468

Rutherford, A.W.; Crofts, A.R. & Inoue, Y. (1982).Thermoluminescence as a probe of photosystem II photochemistry. The origin of the flash-induced glow peaks, *Biochimica et Biophysica Acta,* 682, 457-465

Rutherford, A.W. & Inoue, Y. (1984). Oscillations of delayed luminescence from PSII: recombination of $S_2Q_B^-$ and $S_3Q_B^+$, *FEBS Letters*, 165, 163-170

Rutherford, A.W.; Renger, G.; Koike, H. & Inoue, Y. (1984b). Thermoluminescence as a probe of photosystem II. The redox and protonation states of the secondary acceptor quinone and O_2-evolving enzyme, *Biochimica et Biophysica Acta*, 767, 548-556

Rutherford, A.W.; Govindjee; Inoue, Y. (1984a). Charge accumulation and photochemistry in leaves studied by thermoluminescence and delayed light emission, *Proceedings of the National Academy of Sciences, USA,* 81, 1107-1111

Sahu, S. M.; Dilnawaz, F.; Meera, I.; Misra, M.; Ramaswamy, N.K.; Desai, T.S. & Misra, A.N. (1999). Photosynthetic efficiency of mung bean (*Vigna radiata* L. Wilczek) and

Indian mustard (*Brassica juncea* Coss.) during seedling establishment under NaCl salinity, *InPlant Physiology for Sustainable Agriculture.*(Srivastava G C, Singh K and Pal M, eds.), Pointer Publ., Jaipur, India pp. 388-391.

Sane, P. & Rutherford, A.W. (1986). Thermoluminescence from photosynthetic membranes. In: Govindjee, Amesz J, Fork DC (Eds.).*Light emission by plants and bacteria*. Orlando: Academic Press, 291-329

Sane, P.V.; Desai, T.S. & Tatake, V.G. (1983). Characterization of glow peaks of chloroplast membranes. I. Relationship with ''S'' states, *Indian Journal Experimental Biology*, 21, 396–405

Sane, P.V. (2004). Thermoluminescence. A technique for probing photosystem II. In: *Methods in molecular biology. Photosynthesis research protocols*, ed. R. Carpentier, 229–248, Totowa, NJ: Humana Press. Inc.

Sane, P.V.; Desai, T.S. & Tatake, V.G. (1977). On the origin of glow peaks in *Euglena* cells, spinach chloroplasts and subchloroplast fragments enriched in system I and II, *Photochemistry and Photobiology,* 26, 33–39

Sane, P.V.; Ivanov, A.; Hurry, V.; Huner, N. & Oquist, G. (2003). Changes in the redox potential of primary and secondary electron-accepting quinones in photosystem II confer increased resistance to photoinhibition in Low-temperature-acclimated *Arabidopsis*, *Plant Physiology,* 132, 2144–2151

Scheller, H.V. (1996). In vitro cyclic electron transport in barley thylakoids follows two independent pathways. *Plant Physiology,* 110, 187-194

Schmidt, W. & Senger, H. (1987). Long-term delayed luminescence in *Scenedesmus obliquus, Biochimica et Biophysica Acta,* 891, 15-27

Schreiber, U. & Berry, J.A. (1977). Heat-induced changes in chlorophyll fluorescence in intact leaves correlated with damage to the photosynthetic apparatus, *Planta,* 136, 233-238

Schumann, A.; Bauer, A.; Hermes, M.; Gilbert, M.; Hengstler, J.G. & Wilhelm, G. (2009). A rapid and easy to handle thermoluminescence based technique for evaluation of carbon tetrachloride-induced oxidative stress on rat hepatocytes, *Arch. Toxicology,* 83, 709–720.

Skotnica, J.; Fiala, J.; Ilik, P. & Dvorak, L. (1999). Thermally induced chemiluminescence of barley leaves, *Photochemistry Photobiology,* 69, 211-217

Stallaert, V.M.; Ducruet, J.M.; Tavernier, E. & Blein, J.P. (1995). Lipid peroxidation in tobacco leaves treated with the elicitor cryptogein: evaluation by high-temperature thermoluminescence emission and chlorophyll fluorescence, *Biochimica et Biophysica Acta,* 1229, 290-295

Sundblad, L.G.; Palmqvist, K. & Samuelsson, G. (1986). Luminescence decay kinetics in relation to the relaxation of the trans-thylakoid ΔpH from high and low CO_2 adapted cells of *Scenedesmus obliquus*. *FEBS Letters,* 209, 28-32

Sundblad, L.G.; Schroder, W.P. & Akerlung, H.E. (1988). S-state distribution and redox state of Q_A in barley in relation to luminescence decay kinetics. *Biochimica et Biophysica Acta*, 973, 47-52

Sundby, C.; Melis, A.; MaÈenpaÈaÈ, P. & Andersson, B. (1986).Temperature-dependent changes in the antenna size of photosystem II. Reversible conversion of photosystem IIa to photosystem IIb, *Biochimica et Biophysica Acta,* 851, 475-483

Tatake, V.G.; Desai, T.S. & Bhattacharjee, S.K. (1971). A variable temperature cryostat for thermoluminescence studies, *Journal of Physics E: Scientific Instruments,* 4, 755–762

Thomas, P.G.; Quinn, P.J. & Williams, W.P. (1986). The origin of photosystem-I-mediated electron transport stimulation in heat stressed chloroplasts, *Planta,* 167, 133-139

Tyystjarvi, E. & Vass, I. (2004). Light emission as a probe of charge separation and recombination in the photosynthetic apparatus: relation of prompt fluorescence to delayed light emission and thermoluminescence. In: Papageorgiou GC, Govindjee (eds) *Chlorophyll a fluorescence: a signature of photosynthesis. Advances in Photosynthesis and Respiration.* Vol. 19, Springer, Dordrecht, pp 363–388

Vass, I.; Horvath, G.; Herczeg, T. & Demeter, S. (1981). Photosynthetic energy conservation investigated by thermoluminescence activation energies and half-lives of thermoluminescence bands of chloroplasts determined by mathematical resolution of glow curve. *Biochimica et Biophysica Acta,* 634, 140-152

Vass, I.; Horvath, G.; Herczeg, T. & Demeter, S. (1981). Photosynthetic energy conservation investigated by thermoluminescence. Activation energy and half life of thermoluminescence bands of chloroplasts determined by mathematical resolution of glow curves, *Biochim Biophys Acta*, 634, 140–152

Vass, I. & Inoue, Y. (1992). Thermoluminescence in the study of photosystem II. In: Barber J, ed. *The photosystems: structure,function and molecular biology*, Amsterdam: Elsevier, 259-294

Vass, I. (2005). The history of photosynthetic thermoluminescence. In: Govindjee, Beatty JT, Gest H, Allen JF (eds) *Discoveries in photosynthesis. Advances in Photosynthesis and Respiration*. Vol. 20, Springer, Dordrecht, pp 665–680.

Vavilin, D.V. & Ducruet, J.M. (1998). The origin of 120-130°C thermoluminescence bands in chlorophyll-containing material, *Photochemistry and Photobiology,* 68, 191-198

Vavilin, D.V.; Matorin, D.N.; Kafarov, R.S.; Bautina, A.L. & Venediktov, P.S. (1991). High-temperature thermoluminescence of chlorophyll in lipid peroxidation, *Biologicheskie Membrany*, 8, 89-98

Vavilin, D.V. & Vermaas, W.F. (2000). Mutations in the CD-loop region of the D2 protein in *Synechocystis* sp. PCC 6803 modify charge recombination pathways in photosystem II *in vivo*, *Biochem*istry, 39, 14831–14838

Venediktov, P.S.; Matorin, D.N. & Kafarov, R.S. (1989). Chemiluminescence of chlorophyll upon lipid photoperoxidation in thylakoid membranes. *Biofizika (Moscow)*, 34, 241-245

Weiss, E. (1984). Short term acclimation of spinach to high temperatures, *Plant Physiology*, 74, 402-407

Zeinalov, Y. & Maslenkova, L. (1996). A computerized equipment for thermoluminescence investigations, *Bulgarain Journal of Plant Physiology,* 22, 88–94

Zhang, L.; Xing, D. & Wang, J. (2007). A non-invasive and real-time monitoring of the regulation of photosynthetic metabolism biosensor based on measurement of delayed fluorescence in vivo, *Sensors,* 7, 52-66

Zurita, J. L.;Roncel, M.; Aguilar, M. & Ortega, J.M. (2005). A thermoluminescence study of Photosystem II back electron transfer reactions in rice leaves – effects of salt stress, *Photosynthesis Research,* 84, 131–137

7

Chlorophyll Fluorescence in Plant Biology

Amarendra Narayan Misra[1,2], Meena Misra[1,2] and Ranjeet Singh[1,2]
[1]*Post-Graduate Department of Biosciences & Biotechnology, Fakir Mohan University, Balasore,*
[2]*Centre for Life Sciences, School of Natural Sciences, Central University of Jharkhand, Ratu-Lohardaga Road, Brambe, Ranchi, India*

1. Introduction

1.1 Chlorophyll fluorescence: Basics

Several molecules absorb light energy which they emit after a time difference (lifetime) as radiation energy. Molecules remain at a low energy level or the ground electronic singlet state (S_o) or the lowest vibrational level at room temperature (Noomnarm and Clegg, 2009). On absorption of a photon, the molecule is excited from S_o to the first electronic excited singlet state S_1 within < 10-15 s^{-1} (Figure 1). These molecules can also be transferred to higher energy levels (S_2 to S_n) also. These excited state molecules can relax to the S_1 electronic state via vibrational relaxation within 10-12 s^{-1}. The molecule will ultimately relax to the S_o state through photon emission, which is called fluorescence emission. Also here, the energy of the emitted photon must equal the changes in the energy levels.

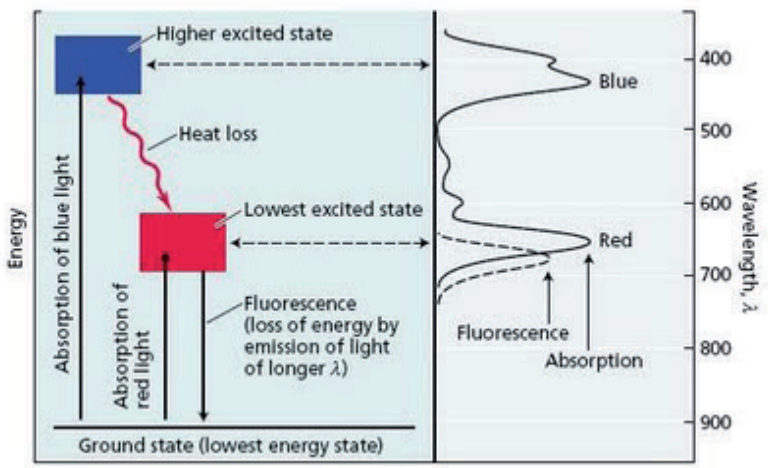

Fig. 1. The basic principles of excitation and deexcitation phenomena and the differences between excitation (absorption) spectra and emission (fluorescence) spectra of light absorbing pigment molecules (Chlorophyll) in green plants.

The molecular excitation follows the principle: $\Delta E = hv$, with ΔE, energy difference between ground and excited state; *h*, Planck quantum; and *v*, frequency of radiation (Rabinowitch & Govindjee, 1969; Kumke & Löhmannsröben, 2009).

Light energy is absorbed by chlorophyll, carotenoids and other pigment molecules present in the photosynthetic antenna molecules present in the thylakoid membranes of green plants (Strasser et al., 2000, 2004; Govindjee, 2004; Maxwell and Johnson, 2000; Falkowski & Raven, 2007). Absorption of a photon raises a chlorophyll *a* molecule to its lowest singlet excited state, for which three internal decay pathways exist: fluorescence, in which the molecule returns to the ground state with the emission of radiation; internal conversion, in which the energy of the molecule is converted into vibrational energy; and intersystem crossing, in which the singlet state is converted to the triplet state (Figure 2). If certain other molecules are present along with the chlorophyll, external decay pathway(s) may also become available in addition to the internal decay pathways. Such external pathways facilitate the transfer of energy to a molecule with a similar energy gap or the transfer of an electron to or from another molecule, such as in excitation energy transfer in light-harvesting antennae and charge separation in photochemical reaction centers, respectively. All of these downward processes competitively contribute to the decay of the chlorophyll excited state. Accordingly, an increase in the rate of one of these processes would increase its share of the decay process and lower the fluorescence yield (φf). The quantum yield of chlorophyll fluorescence from the photosynthetic apparatus is therefore 0.6-3%, while chlorophyll *a* in an organic solvent exhibits a high fluorescence yield of approximately 30% (Latimer et al., 1956; Trissl et al., 1993). Oxygenic photosynthesis is endowed with the unique property of a fluorescence emission. Light energy that is absorbed by chlorophyll in a photosynthetic systems can undergo three fates: a) it can be used to drive photosynthesis (photochemistry), b) it can be dissipated as heat or c) it can be re-emitted as red fluorescence (Figure 2). These three processes occur in competition. Since the sum of rate constants is constant, any increase in the efficiency of one process will result in a decrease in the yield of the other two. Therefore, determining the yield of chlorophyll fluorescence will give information about changes in the efficiency of photochemistry and heat dissipation (Figure 2).

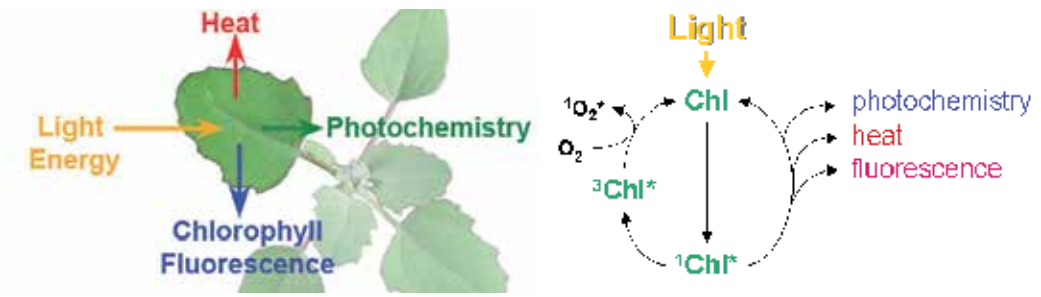

Fig. 2. The origin of chlorophyll fluorescence: basic aspects.

The oxygenic photosynthesis involves two light reactions operating simultaneously at photosystem (PS) II and PSI reaction centers (Figure 3). The light energy absorbed by the light harvesting antenna (LHC) pigments distribute the energy to the two photosystems, used to oxidize water to oxygen, reduce NADP+, and produce ATP (Rabinowitch & Govindjee, 1969; Blankenship, 2002; Falkowski & Raven, 2007). Most of the chlorophyll a

fluorescence, at room temperature, originates in the antenna complexes of PSII and originate as fluorescence emission at 685nm (F685) (Govindjee, 2004). The absorption of photons by antenna molecules is a very fast process and occurs within femtoseconds, leading to the formation of excited chlorophylls (Chl*). The main function of the antenna (LHC) is to transfer excitation energy to the photosynthetic reaction centers leading to photochemistry. But a part of the absorbed light energy is dissipated as heat and is emitted as fluorescence (Figure 3). Primary charge separation occurs in PSI and PSII reaction centers involving P700 and P680, respectively. Photochemistry takes place within picoseconds, and further reactions proceed independent of the presence of light (Stirbet & Govindjee, 2011). The characteristic of fluorescence emission is determined by the absorbing pigment molecules, the excitation energy transfer, and the orientation of the fluorescing pigments in the photosynthetic membrane. Besides these characteristics, fluorescence is also affected by the redox state of the donors and acceptors of photosystems, and thylakoid stacking etc. (Strasser et al. 2005). Although fluorescence measurements are indicators of indirect effects, still fluorescence is widely used as a luminescence signature for wide array of photosynthetic events and alterations in the photosynthetic systems. There are different types of fluorescence measurements used in plant biology and photosynthesis, which are described below. Depending on the type of study and the suitability of the photosynthetic system, different fluorescence techniques are used. The analysis of these fluorescence curves or images and its analysis gives an insight to the photosynthetic energy transducing or pigment protein orientation in the photosynthetic systems.

2. Types of chlorophyll fluorescence

Chlorophyll *a* fluorescence is a highly versatile tool, not only for researchers studying photosynthesis, but also for those working in broader fields related to biophysics, biochemistry and physiology of green plants. Chlorophyll fluorescence analysis is sensitive, non-invasive, and relatively simple. With the advent of different instrumental techniques and time resolved spectroscopy, fluorometry developed into various types with timescale of signal capturing. The fluorescence measurements, that are conventionally used, are

i. Room temperature fluorescence (Rabinowitch & Govindjee, 1969) ,
ii. Low temperature fluorescence (77K fluorescence) (Rabinowitch & Govindjee, 1969),
iii. Fluorescence temperature curve, (Ilik et al., 2003),
iv. Variable Chl a fluorescence, differing in the manner by which the photochemistry is saturated (e.g., shutterless and LED-based instruments) for direct fluorometry:
    a. fast Chl fluorescence or plant efficiency analyser (PEA) (Strasser & Govindjee, 1991; 1992),
    b. pulse amplitude modulation, PAM, fluorometry (Schreiber et al., 1986; Schreiber, 2004),
    c. the pump and probe (P & P) fluorometry (Mauzeralla, 1972; Falkowski et al., 1986),
    d. the fast repetition rate (FRR) fluorometry (Kolber et al. 1998),
    e. the pump during probe (PDP) fluorometry (Olson et al., 1996), and several others that are functionally similar, such as
    f. the fluorescence induction and relaxation (FIRe) technique (Gorbunov & Falkowski, 2005),
    g. the background irradiance gradient single turnover (BIG-STf) fluorometry (Johnson, 2004), and
    h. advanced laser fluorometry (ALF) (Chekalyuk & Hafez, 2008).

However, the working principle and the phenomenon for analysis are similar for these instruments. In the present chapter we describe the commonly used room temperature fluorescence, low temperature or 77 K fluorescence, fast Chl fluoresce and PAM fluorescence. The other methods are useful but are not discussed due to their specialized use in various fields. However, the techniques and principles described here are routinely used in plant biology at present.

2.1 Room temperature fluorescence

Under a physiological state of active chloroplasts in green plants at room temperature, chlorophyll fluorescence emission is a net result of heat dissipation, stimulation of dark reduction of plastoquinone, and increased cyclic electron flow to light, also increases the leakage of electrons from the thylakoid, there may be a deactivation of Rubisco (ribulose 1,5 bi-phosphatecarboxylase- oxygenase), and the generation of reactive oxygen species such as the superoxide anion (O_2^-) and H_2O_2. The chlorophyll fluorescence emission spectra is taken as a measure of the amount of chlorophyll content in the green plants (Buschmann, 2007). There are two maxima for Chl fluorescence at room temperature, (i) in the red region at 685 nm emitted by PS II and (ii) in the far-red region at 720-740 nm emitted by PS I. At higher chlorophyll concentrations, chlorophyll fluorescence is mainly detected in the range of 720-740 nm. But the re-absorption of the emitted red fluorescence by the chlorophyll in PS II results in a strong fluorescence emission band at 685 nm (Figure 4). The technique and the instrumentation are simple. The fluorescence emission is measured at right angle (90°) or 45° to the excitation beam of blue or red wavelength band of visible light. However, when cooled to liquid nitrogen temperature (77K) the fluorescence emission at 685nm, 695nm and 735nm can be resolved separately and can be analysed (see the section 77K fluorescence).

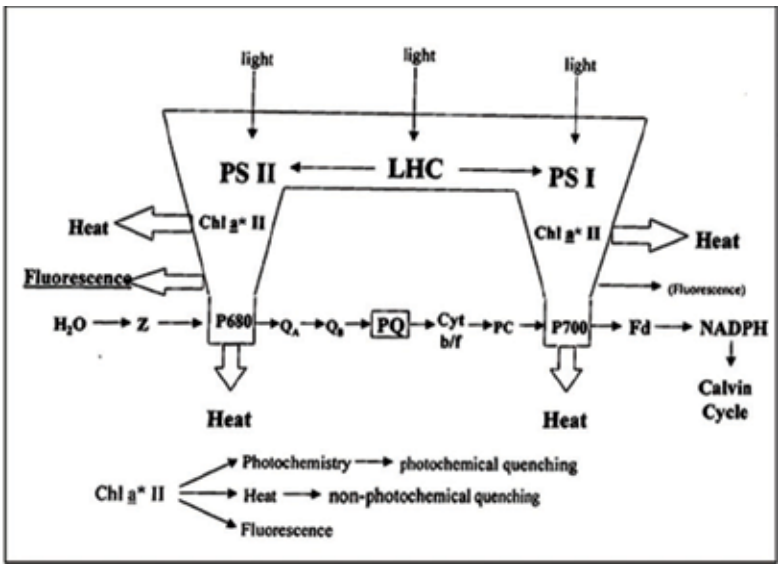

Fig. 3. Schematic illustration of primary conversion in photosynthesis which governs *in vivo* chlorophyll fluorescence yield. Variable fluorescence originates almost exclusively from PSII. Maximal fluorescence yield is lowered by photochemical charge separation and dissipation.

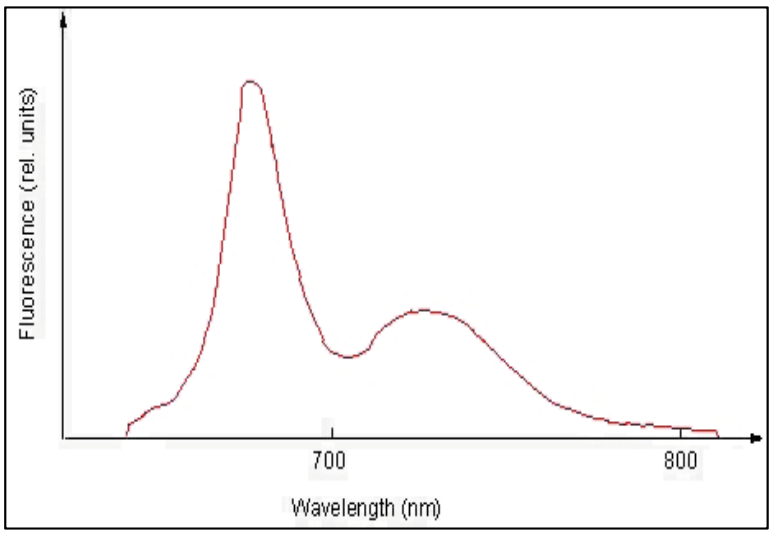

Fig. 4. A typical room temperature fluorescence emission by green to leaf.

2.2 77K fluorescence

The fluorescence at liquid-nitrogen temperature from algal cells and isolated thylakoid membranes to show a distinct spectral bands at approximately 685, 695, and 735 nm (Murata et al., 1966; Boardman et al., 1966; Govindjee et al., 1967). The two bands at approximately 685 and 695 nm corresponded to fluorescence emitted from Chl in PSII, while the band at 735 (usually a broad band between 715–740 nm) correspond to the fluorescence from the Chl in PSI (Figure 5). This study led to the discovery of state transitions, which is a regulatory mechanism for balancing the distribution of light energy between PSI and PS II. When algal cells were illuminated with light wavelength (567nm) exciting the pigment molecules in PS II named as 'light II,' and then frozen to liquid-nitrogen temperature (77K), the fluorescence at 685 nm and 695 nm was repressed and the emission at 715 nm was enhanced (Murata et al., 1966).

To the contrary, illumination with 'light I' at 405 nm plus 435 nm, which was absorbed by PSI, enhanced the emission at 685 nm from PSII (Murata et al., 1966). A regulatory mechanism existed in the algal cells that balanced the distribution of light energy to PSI and PSII depending on the energy of excitation or the quality of light. With an elegant and simultaneous measurement of changes in the oxygen-evolving activity and the fluorescence yield of *Chlorella pyrenoidosa* under 'light I' and 'light II,' Bonaventura and Myers (1969) proposed the concept of - state transitions. This concept is routinely used for decades as 'state 1', referring to photosynthetic organisms exposed to light that is preferentially absorbed by PSI (light I) and 'state 2' to describe photosynthetic organisms exposed to light that is preferentially absorbed by PSII (light II) (Murata, 1970). This phenomena is extended to the energized state of thylakoid membranes. In the presence of ATP, the membranes seemed to establish state 2 and vice-versa. Subsequently, divalent and trivalent ion dependent distribution of light energy between the two photosystems in isolated thylakoid membranes were reported (Murata, 2009).

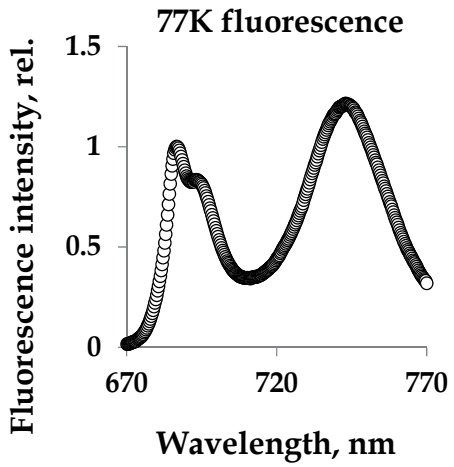

Fig. 5. 77K fluorescence spectrum of a healthy green leaf.

It is now known that under state II light illumination, LHCII becomes phosphorylated by thylakoid membrane localized protein kinase(s), which is regulated by the redox state of the plastoquinone pool (Misra & Biswal, 2000; Zer et al., 2003). The phosphorylated fraction of LHCII then dissociates from PSII and binds to PSI. Reversal of light to state I results in inactivation of the kinase(s), and the LHCII antennae becomes dephosphorylated by constitutively active phosphatases. The (dephosphorylated) LHCII complexes migrate to stacked regions of the grana and re-associate with PSII, restoring its original capacity to absorb light (Allen, 1992; Aro & Ohad, 2003; Mullineaux & Emlyn-Jones, 2005; Rochaix, 2007). This leads to structural changes in the thylakoid membrane itself (Anderson, 1999; Garab & Mustardy, 1999; Dekker & Boekema, 2005). Taking into account of recent developments in several microscopic techniques to study the morphological changes that occur in thylakoid membranes of higher plant chloroplasts during state transitions, Chuartzman et al. (2008) reported that the rearrangements in membrane architecture occurs during the state transition, and involves both granal and stroma lamellar domains. However, due to experimental set-up, repeatability of the experiments and pigment concentration that affects the shape and characteristic of 77K fluorescence, this technique is used to a limited extent and is not as routine as the fast chlorophyll fluorescence or PAM fluorometry as described in the following sections. 77K finds its applications only for conformation of certain temporal and structural orientation of the pigment protein complexes in the thylakoid membranes and energy tunneling within the two photosystems.

2.3 Fast chlorophyll fluorescence

Illumination of dark adapted photosynthetic materials emit, Chl a fluorescence with a characteristic induction or transient which was discovered by Hans Kautsky and is named after him as the Kautsky curve (Kautsky & Hirsh, 1931). Chl a fluorescence induction curve measured under continuous light has a fast (less than a second) exponential phase, and a slow decay phase (few minutes duration). Kautsky curve of a healthy green leaf is shown in Figure 6. The expansion of the fast rise phase gives rise to the exponential 'OJIP' curve (Figure 6). The analysis of the OJIP curve taking the theoretical assumptions and probabilities derives different photosynthetic parameters for the dark adapted state of the

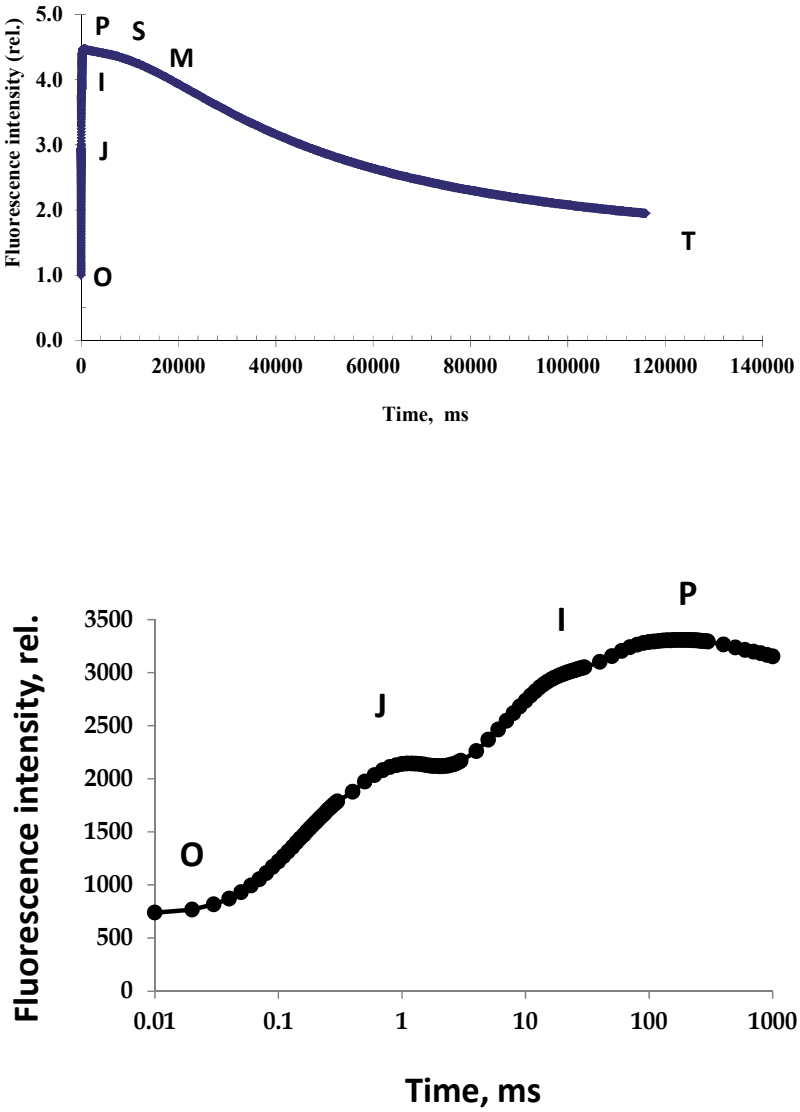

Fig. 6. Kautsky curve of a healthy green leaf and the expansion of the fast rise phase to the exponential 'OJIP' curve. The analysis of the OJIP curve gives rise to different parameters for the dark adapted state of the photosynthetic systems (details in text and also refer Strasser et al., 2004; Stirbet & Govindjee, 2011).

photosynthetic systems (Strasser et al., 2000, 2004; Stirbet & Govindjee, 2011). The slow phase **is** known as 'SMT' and is assigned to a various factors like energy transduction, ATP synthesis, CO_2 fixation, State transition, non-photochemical Chl a fluorescence quenching etc. (Stirbet & Govindjee, 2011). The nomenclature for 'OJIP' is O for origin or F_0 level measured at 20-50μs after illumination, J and I are intermediate states measured after 2ms

and 30 ms, and P is the peak or F_M (maximal fluorescence). In contrast to the angiosperms, the foraminifers, zooxanthellae and lichens, show an additional G peak and H (=P) peak (Tsimilli-Michael et al., 1998; Ilik et al., 2006). The origin G peak is assigned to an early activation of the ferredoxin-NADP+-reductase, FNR, (Ilik et al., 2006). In heat-stressed samples, another peak arises between F_0 and F_J at 300 μs which is designated as K peak (Guisse et al., 1995; Srivastava et al., 1997; Strasser, 1997; Misra et al., 2001b, 2007).

The OJIP curve from F_0 to F_M (=F_P) is correlated with the primary photochemical reactions of PS II (Duysens & Sweers, 1963) and the fluorescence yield is controlled by a PSII acceptor quencher (called ''Q'' = Q_A) (van Gorkom, 1986). Thus, the OJIP transient can be used for the titration of the photochemical quantum yield of PSII photochemistry, and the electron transport properties. As such the OJIP fluorescence curve analysis is routinely used to monitor the effect of various photosynthetic inhibitors, climatic stress, and photosynthetic mutations altering the structure, architecture and function of the photosynthetic apparatus (Misra et al., 2001a, b, 2007; Strasser et al., 2004).

The photosynthetic samples kept in darkness, have the electron acceptor side of PSII in the oxidized state, as there is no electron flow in the photosynthetic electron transport chain and water oxidation by PS II. So the PSII reaction centers remain open, and the fluorescence intensity is minimum, i.e. equal to F_o (='O' level in OJIP curve). On illumination with a strong intensity of light that can theoretically excite all the pigment molecules in the pigment protein bed of the thylakoid membrane, a fast electron transport process takes place and is recorded by a O-J transition or rise within 2 ms. This is followed by slow phases J–I and I–P rise, which are known as thermo sensitive or thermal phases. The F_M level (=P) or F_{max} is attained within 1s, representing a closed PS II centres or complete reduction of all the primary electron acceptor in PS II, the Q_A molecules and saturating the electron flow on the acceptor side of PS II (Schansker et al., 2005). This chapter explains the OJIP curve analysis under saturating light intensities and its use in photosynthetic studies.

The fluorescence induction curve, from photosynthetic samples kept in darkness, are used empirically and commonly using F_0 or F_M values. The difference between F_M and F_0, known as the variable fluorescence, F_V, and the ratio F_V/F_M in a healthy plant ranging from 0.78–0.84 (Bjorkman & Demmig 1987) is used extensively as the maximum quantum yield of primary PSII photochemistry (Butler & Kitajima, 1975; Palliton, 1976). Considering the connectivity parameter or the excitation energy migration among PSIIs (Butler, 1978) and using the relative variable fluorescence at time t, $V_t = (F_t - F_0)/(F_M - F_0)$, the fraction of closed PSII centers (B_t) can be calculated as

$$B_t = [Q_A^-]/ [Q_A^-]_{total}, \text{ since } V_t = B_t/[1 + C (1 - B_t)],$$

where C is probability of connectivity among the PSIIs. When C = 0, or there is no connectivity, $V_t = B_t$. This'separate package model of PSII units' is the fundamental postulate of the JIP test (Strasser et al., 2000; 2004; Tsimilli-Michael & Strasser, 2008). In a recent chapter, Stirbet & Govindjee (2011) revised the JIP-test including the connectivity parameters, as described above, and given a revision of calculations for fluxes and PSII performances as shown in Table 1.

Information selected from the fast OJIP fluorescence induction (data necessary for the calculation of the so-called JIP parameters)	
$F_o = F_{50\mu s}$ or $F_{20\mu s}$	Initial fluorescence after the onset of actinic illumination
F_J F_{2ms}	Fluorescence value at 2 ms (J-level)
F_I F_{30ms}	Fluorescence value at 30 ms (I-level)
F_P(F_M)	Fluorescence maxima under saturating illumination
t_{Fmax}	Time to reach F_M
Area	Area under F_o and F_M
$V_v = F_t - F_o$	Variable Chl fluorescence
$F_V = F_M - F_o$	Maximum variable Chl fluorescence
$V_t = (F_t - F_o)/(F_M - F_o)$	Relative variable Chl fluorescence
$M_o = (dV/dt)_o = 4\ ms^{-1}\ .\ (F_{300\mu s} - F_o)/(F_V)$	Value of the initial slope of curve under V_t
$S_m = Area/F_V$	Normalized area (proportional to the number of reduction and oxidation of one QA-molecules or the number of electron carriers per electron transport chain)
Energy fluxes (Stirbet & Govindjee, 2011)	
$J^{ABS} = J^{TR} + J^{DI}$	
J^{TR}	Rate of photon absorption by total PSII antenna = *absorbed photon flux*
J_o^{TR}	Rate of exciton trapping (Q_A reduction) by all PSII RCs = *trapped exciton flux*
J_o^{DI}	Maximum (initial) trapped exciton flux
J_o^{ET2}	Rate of energy dissipation in all the PSIIs = *dissipated energy flux*
J_o^{RE1}	Electron transport flux from Q_A to Q_B
	Electron transport flux until PSI acceptors (at F_I level)
Quantum yields and efficiencies	
φ_{Po} $J_o^{TR} / J^{ABS} = 1 - F_o/F_M$	Maximum quantum yield of primary PSII photochemistry
φ_{Pt} $J^{TR}/J^{ABS} = 1 - F_t/F_M = \varphi_{Po} \cdot (1 - V_t)$	Quantum yield of primary PSII photochemistry
φ_{ET_o} $J_o^{ET2}/J^{ABS} = 1 - F_J - F_M = \varphi_{Po} \cdot (1-V_J)$	Quantum yield of the electron transport from Q_A to Q_B
φ_{RE1o} $J_o^{RE1}/J^{ABS} = 1 - F_I/F_M \varphi_{Po} \cdot (1-V_I)$	Quantum yield of the electron transport upto the PSI electron acceptors
φ_{ET2o} $J_o^{ET2}/J_o^{TR} = 1 - V_J$	Efficiency of trapped electron transfer from Q_A to Q_B
φ_{ET1o} $J_o^{RE1}/J_o^{TR} = 1 - V_I$	Efficiency of electron transfer from PSII to PSI acceptors
φ_{RE1o} $J_o^{RE1}/J_o^{ET2} = (1 - V_I)/ (1-V_j)$	Efficiency of electron transfer from Q_B to PSI acceptors
Specific energy fluxes (per active PSII RC)	
$J^{ABS}/RC = (M_o/V_J) \cdot (1/\varphi_{Po})$	
$\gamma_{RC2} = Chl_{RC}/Chl_{tot}$	
$RC/J^{ABS} = \varphi_{Po} \cdot V_J/M_o = \gamma_{RC2}/(1 - \gamma_{RC2})$	Absorbed photon flux per PSII RC (apparent antenna size of active PSII)
$J_o^{TR}/RC = M_o/V_J$	Probability that a PSII Chl functions as RC
$J_o^{ET2}/RC = (M_o/V_J) \cdot (1 - V_J)$	Number of Q_A reducing RCs per PSII antenna Chl
$J_o^{RE1}/RC = (M_o/V_J) \cdot (1 - V_I)$	Maximum trapped exciton flux per PSII
	Electron transport from Q_A to Q_B per PSII RC
Phenomenological energy fluxes (per CS_o)	Electron transport to PSI acceptors per PSII RC
$J^{ABS}/CS_o = F_o$ or $J^{ABS}/CS_M = F_M$	
$RC/CS = (RC/J^{ABS}) \cdot (J^{ABS}/CS)$	
$J_o^{TR}/CS = (J_o^{TR} / J^{ABS}) \cdot (J^{ABS}/ CS)$	Absorbed photon flux per cross section (apparent PSII antenna size)
$J_o^{ET2}/CS = (J_o^{ET2}/J^{ABS}) \cdot (J^{ABS}/ CS)$	The number of active PSII RCs per cross section
$J_o^{RE1}/CS = (J_o^{RE1}/J^{ABS}) \cdot (J^{ABS}/ CS)$	Maximum trapped exciton flux per cross section
	Electron transport from Q_A to Q_B per cross section
De-excitation rate constants of PSII antenna	Electron transport flux until PSI acceptors per cross section
$k_N = k_F - J^{ABS}/F_M$	
$k_P = k_F - J^{ABS} - F_V/(F_o - F_M) = k_N - F_V/F_o$	Non-photochemical de-excitation rate constant; k_F = rate constant of fluorescence emission
Performance index	Photochemical de-excitation rate constant
$PI_{ABS} = [\gamma_{RC2}/(1 - \gamma_{RC2})].[\varphi_{Po}/(1-\varphi_{Po})].[\varphi_{ET2o}/(1-\varphi_{ET2o})]$	
$PI_{ABS}^{tota} = PI_{ABS} \cdot [\varphi_{RE1o}/(1-\varphi_{RE1o})]$	Performance index for energy conservation from photons absorbed

Table 1. Equations and definitions of JIP parameters by Strasser et al. (2004; 2010) and modified by Stirbet & Govindjee (2011)

2.4 PAM fluorescence

The widely used chlorophyll fluorescence technique is the so-called quenching analysis of modulated fluorescence by the saturation pulse method. In this type of measurement system instead of using a continuous light, a high intensity light mimicking the 'sun light intensity' is switched on and off (pulse) at high frequency and the detector is tuned to measure the fluorescence emission only, thereby providing a more efficient and more powerful system to measure fluorescence emission in presence of background measuring light (Bradbury & Baker, 1981; Quick & Horton, 1984; Schreiber et al., 1986; Schreiber, 2004). A leaf is dark adapted for at least 10-15 min prior to the measurement. The ground fluorescence (F_o) in darkness is measured by a weak modulating light beam (ML). Then the application of a saturating pulse (SP) (about 8000 μmol m^{-2} s^{-1} for 0.6 - 1 s), raises the fluorescence to a maximum value, F_m. This measurement allows the determination of the maximum quantum efficiency of photosystem II (PSII) primary photochemistry, given as $\underline{F_v/F_m}$, as described for the fast chlorophyll fluorescence measurements described in earlier section. This parameter is often called as 'intrinsic quantum yield' (Kitajima & Butler, 1975). Initially after this first light pulse the actinic light (AL) is switched on (photosynthetic samples are illuminated) and SP is turned on repeatedly. This induced F_m' (fluorescence maxima at light adapted state). The F_m' increases initially with few pulses and then starts declining (quenching) after few minutes. The intial phase of rise in fluorescence in light adapted state is called 'photochemical quenching' which is ascribed to the photochemical phenomena in generating reductants and subsequent reduction of carbon dioxide pool in the leaves (van Kooten & Snell, 1990; Edwards & Baker, 1993) subsequent pulses of saturating light interrupted with dark period gradually reduces the intensity of fluorescence emission otherwise known as 'non-photochemical fluorescence quenching' or NPQ (Walter & Horton, 1991; Johnson et al., 1993; Oxbrough & Baker, 1997, Niyogi et al., 1997). A typical PAM fluorescence measurement is shown in Figure 7. The calculation of quenching parameters

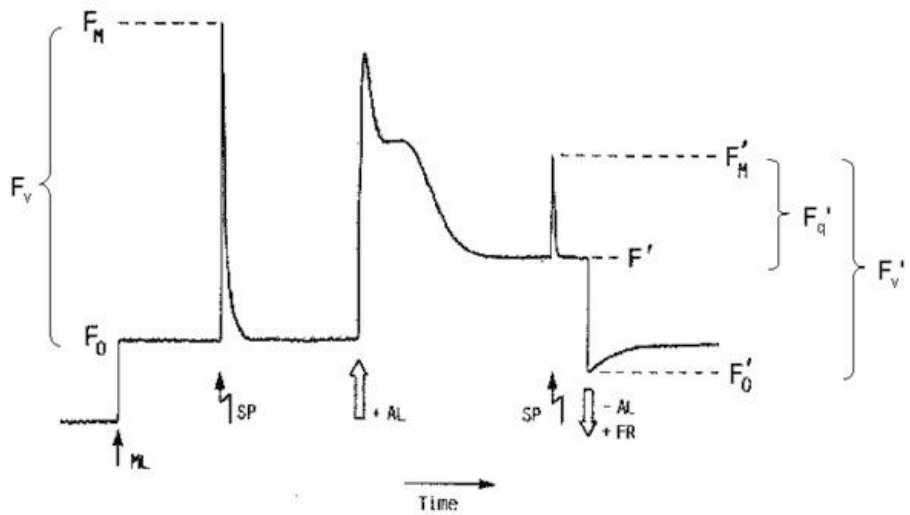

Fig. 7. A typical PAM fluorescence signal of a leaf disc. The fluorescence in dark adapted leaves are denoted by F and in the light adapted state F′ are recorded and different quenching parameters are measured (see Text).

needs either a shift from NPQ to photochemical quenching or vice versa. It is not practicable to shift completely away from NPQ to a complete photochemical quenching situation, so the alternative of complete shift from photochemical quenching to a NPQ stage is suggested by many workers (Bradbury & Baker, 1981; Quick & Horton, 1984). The terminology suggested by van Kooten & Snell (1990) and then modified by Maxwell & Johnson (2000) and Baker (2008) is used widely.

The sample is first dark adapted. The test is started and F_o, or minimal fluorescence, is measured without actinic light. Then a saturation pulse (SP) completely closes all the primary electron acceptors (Q_A) in PSII by completely reducing PSII. So maximal fluorescence, F_m, is the result. After the saturation pulse, an actinic light is turned on and the fluorescent signal declines slowly with the onset of CO_2 fixation until it reaches steady state. Photochemical quenching a measure of open PSII centers, photo-protective non-photochemical quenching and other heat dissipation mechanisms occur. Saturation pulses during steady state photosynthesis provide F_m', maximal fluorescence in light adapted state, after NPQ has reached equilibrium with photochemistry. qP, or qL, now represents the fraction of PSII receptors that remain open or oxidized. F′ (or F_s) represents fluorescence related to current steady state photochemical levels. Then the actinic light is turned off, and simultaneously far red (FR) illumination is turned on to allow the transfer of electrons quickly to reduce PSI, and allow the re-oxidation of PSII. F_o' represents this value with un-relaxed non-photochemical quenching. The rising values of the saturation pulses after the actinic light has been turned off represent the relaxation of NPQ over time. A portion of NPQ, qE (or Y(NPQ), represents photo-protection mechanisms of thylakoid lumen ΔpH and the xanthophyll cycle. The remainder of NPQ represents qT, and qI, (or Y(NO). qT is quenching due to state 1 and state 2 transitions and is negligible in higher plants. qI represent photo-inhibition and photo-damage (adapted from Fracheboud & Leipner 2003; http://www.ab.ipw.agrl.ethz.ch/ ~yfracheb/ flex.htm).

2.4.1 Photochemical quenching

As shown in the fast Chl fluorescence measurement, the maximum quantum efficiency of PSII photochemistry is calculated as:

$$F_v/F_m = (F_m\text{-}F_o) \,/\, F_m$$

A decrease in F_m and/or an increase in F_o results in a decrease in F_v/F_m. The F_o increase is provoked by dissociation of LHCII from the PSII core complex and is reported to be due to the free pigments (Misra & Terashima, 2003; Misra et al., 2001a,b, 1998, 2007).

In natural conditions, sun light far exceeds the quantum requirements for photochemistry in photosynthesis, commonly referred as 'photoinhibition' (Misra, 1993; Misra et al. 1997; 2001; 2007). Under these conditions, the PSII RC undergoes photoinduced damages of the D1 protein. The first turn-over of this polypeptide copes up with the photoinhibitory situations. However, under severe stress, the capacity for repair of damaged PSII RC becomes suboptimal and an irreversible inhibition of PSII can be detected *in vivo* as a decrease in the chlorophyll fluorescence ratio F_v/F_m. So F_v/F_m is often used as a useful parameter to estimate the extent of photoinhibition of photosynthesis. However, when NPQ induces a decrease in F_v/F_m, this quantification can be erroneous. However, under photoinhibitory conditions, NPQ is lowered due to low F_m signal (Misra et al., 2006, 2011). Since

photoinhibition will reduce the excitation pressure on the reducing site of PSI, these leaves are often characterised by higher values of F_q'/F_v' (Misra et al. 2003, 2006, 2011).

The application of a SP in the presence of AL allows the determination of the maximum fluorescence in the light-adapted state (F_m') or of the PSII 'open centres'. But F_m' shows a decrease compared to that of F_m value, indicating the presence of NPQ. Genty et al. (1989) proposed the 'photochemical quenching' which later became popularly known as 'Genty parameter' and is calculated as:

$$F_q'/F_m' = (F_m'-F') \; / \; F_m'$$

Theoretically 'Genty parameter' is proportional to the quantum efficiency of PSII photochemistry in the light adapted state (PSII quantum efficiency = Φ_{PSII}), which is affected by the level of electron acceptors, e.g. $NADP^+$, available at the acceptor side of PSI (Oxborough & Baker, 1997). However, F_q'/F_m' is greatly affected by the light intensity. So precaution has to be done during measurements under natural conditions where changes in the incident sun light intensity is frequented. This terminology is also used in the literature as Φ_{PSII}, $\Delta F/F_m'$, $(F_m'-F_t)/F_m'$ and $(F_m'-F_s)/F_m'$ (where $\Delta F = F_q'$, and F_t and F_s is equal to F'). Both, the changes in the electron flux on the reducing side of PSII and the down-regulation of PSII affects F_q'/F_m', as this is the product of $\underline{F_q'/F_v'}$ (PSII quantum efficiency factor = coefficient of photochemical quenching (qP) and $\underline{F_v'/F_m'}$ (maximum quantum efficiency of PSII). $\underline{F_v'/F_m'}$ is affected by antenna quenching. F_q'/F_v' or qP is an approximation of the redox state of the primary electron acceptor Q_A in the light adapted state.

qP is a measure of the fraction of open PSII reaction centers and is defined as the coefficients of photochemical fluorescence quenching (van Kooten & Snel, 1990). In cases where qN is greater than 0.4 this may not be a good assumption. Under such a condition, the calculation of qN and qP values are affected. So another parameter – Fod is introduced to minimize the effect of qN on the calculation of qP (van Kooten & Snel, 1990). Kramer et al. (2004) used qL as photochemical quenching parameter. It is a measure of the fraction of open PSII reaction centers. 1- qP, reflects the proportion of closed centers or the "excitation pressure" on PS II (Maxwell et al.,1994; Misra et al., 2006, 2011).

2.4.2 The rate of linear electron transport in PSII (ETR)

The electron transport rate in PSII (ETR) can be calculated as proposed by Fryer et al. (1998):

$$ETR = F_q'/F_m' \cdot PFD \cdot a_L \cdot (PSII/PSI)$$

Where:
PFD is the photosynthetic photon flux density in µmol quanta m^{-2} s^{-1}, measured with a quantometer;
a_L the leaf absorbance, measured with an integrating sphere; and
PSII/PSI = proportion of light absorption by PSII and PSI (assumed value).

The maximum ETR is the sum total of all electron sinks in a chloroplast such as carbon fixation, photorespiration, nitrate assimilation, Mehler reaction. A perturbation or change in any of these parameters affects ETR.

2.4.3 Non-photochemical quenching (NPQ)

Non-photochemical quenching of chlorophyll fluorescence is an indicative of the level of non-radiative energy dissipation in the LHC II of PSII, which is ascribed to prevent over-reduction of the electron transfer chain and, therefore, provides protection from photodamage. The parameter NPQ is derived from the Stern-Volmer equation and can be used to follow changes in apparent quencher concentration (Bilger & Bjorkman, 1990). *NPQ* is related to the rate constant for excitation quenching by regulated thermal dissipation (k'_N). Non photochemical quenching is measured in plants by several methods depending on the NPQ limitations. NPQ – the non-photochemical quenching is a measure of heat dissipation and is the sum total for the photo-protective mechanisms, state transition quenching, and photo-inhibition (Krause and Weis, 1991; Muller et al., 2001; Finazzi et al., 2006).

$$NPQ = qE + qT + qI.$$

NPQ is calculated as: $NPQ = (F_m/F_m') - 1$

NPQ can occur even at low light intensity. Stress conditions such as high light intensity or photoinhibition, low internal CO_2 concentration due to drought or chilling (low temperature) accelerate NPQ. So NPQ serves as an index of stress. At moderate light intensity, the NPQ steady state value is temperature dependent. However, NPQ saturates after a specific temperature limiting the capacity of quencher, which is altered by acclimation. Low temperature decreases the rate of NPQ development irrespective of the light intensity. Bilger and Björkman (1991) demonstrated that the development of NPQ upon exposure of leaves to excess light is, at least partially, determined by the rate of zeaxanthin formation (Misra et al., 2006, 2011). In higher plants, NPQ is divided into two different components (i) rapidly relaxing ΔpH- or energy-dependent NPQ, known as q_E and (ii) a slower photoinhibitory NPQ, known as q_I. qE is ΔpH dependent and depends on the xanthophyll cycle dependent photo-protective mechanisms in the leaf, qT value is negligible in higher plants and so increasing value of q_I indicates enhanced stress in higher plants (Muller et al. 2001).

This is independent of F_o estimation or the quantification of 'closed' PSII RCs and reflects heat-dissipation of 'excess excitation energy' in the antenna system.

qN is similar to NPQ but requires Fod (dark adapted state after a far-red illumination) or F_o' (light adapted state) for estimation. qN is defined as the coefficient of non-photochemical fluorescence quenching. The assumptions for using qN is that it affects primarily the 'variable fluorescence' (F_v) and not the F_o and qN is not greater than 0.4. By using the Far-Red source after actinic illumination, the PSII acceptors re-oxidized and PSI is reduced. A new Fod value is measured and used for corrections to the quenching coefficients (van Kooten & Snel, 1990). NPQ is relatively insensitive to the part of non-photochemical quenching associated with qN values lower than 0.6 This range of qN is affected by ΔPH of the thylakoid lumen which is an important aspect of photosynthetic regulation. (Bilger & Björkman, 1990). Kramer et al. (2004) introduced new quenching parameters such as Y(NPQ) that represents heat dissipation related to all photo-protective mechanisms and Y(NO) represents all other components that are not photo-protective.

2.4.4 Calculations for quenching parameters

$qP = (F_m' - F) / (F_m' - F_o')$
$NPQ = (F_m - F_m') / (F_m')$
$NPQ = qE + qT + qI$
$qE = F_m'$ after rapid relaxation is complete with the actinic light turned off usually one to ten minutes - F_m' during steady state fluorescence with actinic light on/F_m' at steady state.
$qT = F_m'$ after rapid relaxation is complete usually with the actinic light turned off usually one hour - F_m' at qE /F_m' at steady state.
$qI = F_m - F_m'$ at qT/ F_m' at steady state.
$qN = F_m - F_m' / F_m - F_o$
$qL = qP(F_o'/F')$
$Y(NO) = 1/NPQ + 1 + qL((F_m/F_o)-1)$
$Y(NPQ) = 1 - Y - Y(NO)$
$1 = qL + Y(NPQ) + Y(NO)$

3. Applications of chlorophyll fluorescence measurements in plant biology

The primary use of fluorescence has been the estimation of chlorophyll concentration and pigment-protein interaction studies, stability of thylakoid membranes etc. However, the relationship between chlorophyll and in vivo fluorescence varies with a wide range of time and space. These processes included species changes, nutrient concentrations, incident radiation, etc (Falkowski & Raven, 2007). The use of sun-stimulated fluorescence to estimate primary productivity is suggested.

Not only that the fluorimetric techniques are used for aquatic plant productivity, but also these chlorophyll fluorescence measurements, have a wide range application in the field of forestry, crop or plant productivity estimates and in stress adaptation studies (for reviews see Sayed, 2003; Baker & Rosenquivst, 2004; Rohacek et al., 2008; Strasser et al., 2004; Tsimilli-Michael et al., 1998; Tsimilli-Michael & Strasser,2008; Srivastava et al., 1995, 1997).

An extensive study is done on the application of fluorimetry especially PAM and fast Chl fluorimetry on the stress adaptation studies in plants. The most widely studied stress is 'photoinhibition' as this process is related to the fundamental principle of fluorescence energy quenching. The role of the xanthophyll cycle in non-photochemical quenching is the most interesting out come of these photoinhibitory studies using fluorescence parameters (Demmig-Adams, et al., 1996; Frank et al., 1994; Horton et al., 1994; Misra et al, 2003; 2006; 2011).

Recently, chlorophyll fluorescence is used as one of the sensitive parameters for biosensors using thylakoid membranes or algal cells as the transducers (Apostolova et al., 2011; Dobrikova et al. 2009; Giardi & Pace, 2005; Koblizek et al., 1998; Misra et al., 2003, 2006, 2011; Raskov et al., 2011; Vladkova et al, 2009, 2011). Besides this fast Chl fluorescence can be used as a sensitive device for detection of ion/ salt sensitivity and other environmental stress factors (Misra et al., 2001a,b, 2007).

A consorted effort on the improvement of the instrumentation, miniaturization and quickness of the data acquisition will help in further information flux in this field which still has a wide scope and utility.

4. Acknowledgements

This work was supported by funds from UGC-MRP No.36-302/2008(SR) and DST- INT/ BULGARIA/ B70/06 to ANM. MM acknowledges the award of DST-WoS and UGC PDF for Women.

5. References

Allen, J.F. (1992). How does protein phosphorylation regulate photosynthesis? *Trends Biochem Sci,* 17, 12–17

Anderson, J.M. (1999). Insights into the consequences of grana stacking of thylakoid membranes in vascular plants: A personal perspective, *Aust J Plant Physiol,* 26, 625–639

Apostolova, E.; Dobrikova, A.G.; Rashkov, G.D.; Dankov, K.G.; Vladkova, R.S. & Misra, A.N. (2011). Prolonged sensitivity of immobilized thylakoid membranes in cross linked matrix to atrazine, *Sensors and Actuators B,* 156, 140–146

Aro, E.M. & Ohad, I. (2003). Redox regulation of thylakoid protein phosphorylation, *Antioxid Redox Signal*, 5, 55–67

Baker, N.R. (2008). Chlorophyll fluorescence: a probe of photosynthesis in vivo, *Annu Rev Plant Biol,* 59, 659–668

Boardman, N.K.; Thorne, S.W. & Anderson, J.M. (1966). Fluorescence properties of particles obtained by digitonin fragmentation of spinach chloroplasts, *Proc Natl Acad Sci, USA*, 56, 586–593

Baker, N.R. & Rosenqvist, E. (2004). Applications of chlorophyll fluorescence can improve crop production strategies: an examination of future possibilities, *Journal of Experimental Botany*, 55, 1607–1621

Bilger, W. & Bjorkman, O. (1990). Role of the xanthophyll cycle in photoprotection elucidated by measurements of light-induced absorbance changes, fluorescence and photosynthesis in leaves of *Hedera canariensis*. *Photosynth Res,* 25, 173-185

Bjorkman, O. & Demmig, B. (1987). Photon yield of O_2 evolution and chlorophyll fluorescence characteristics at 77 K among vascular plants of diverse origins, *Planta,* 170, 489-504

Blankenship, R.E. (2002). Molecular Mechanisms of Photosynthesis, *Blackwell Science,* Oxford, UK, 321pp

Bonaventura, C. & Myers, J. (1969). Fluorescence and oxygen evolution from *Chlorella pyrenoidosa*. *Biochim Biophys Acta,* 189, 366-383

Bradbury, M. & Baker, N. R. (1981). Analysis of the slow phases of the in vivo chlorophyll fluorescence induction curve. Changes in the redox state of photosystem II electron acceptors and fluorescence emission from photosystems I and II, *Biochim Biophys Acta,* 635, 542-551

Buschmann, C. (2007). Variability and application of the chlorophyll fluorescence emission ratio red/far-red of leaves, *Photosynthesis Research*, 92, 261-271

Butler, W. L. & Kitajima, M. (1975). Fluorescence quenching in photosystem II of chloroplasts, *Biochim Biophys Acta,* 376, 116-125

Butler, W.L. (1978). Energy distribution in the photochemical apparatus of photosynthesis, *Ann Rev Plant Physiol,* 29, 345-378

Chekalyuk, A. & Hafez, M. (2008). Advanced laser fluorometry of natural aquatic environments, *Limnol Oceanogr Methods,* 6, 591 – 609

Chuartzman, S. G.; Nevo, R.; Shimoni, E.; Charuvi, D.; Kiss, V.; Ohad, I.; Brumfeld, V. & Reicha, Z. (2008). Thylakoid membrane remodeling during state transitions in *Arabidopsis, Plant Cell,* 20, 1029 – 1039

Dekker, J.P. & Boekema, E.J. (2005). Supramolecular organization of thylakoid membrane proteins in green plants, *Biochim Biophys Acta,* 1706, 12 – 39

Demmig-Adams, B.; Gilmore, A.M. & Adams III, W.W. (1996). In vivo functions of carotenoids in higher plants, *FASEB J,* 10, 403-412

Dobrikova, A.; Vladkova, R.; Rashkov, G.; Busheva, M.; Taneva, S. G.; Misra, A.N. & Apostolova, E. (2009). Assessment of sensitivity of photosynthetic oxygen evolution and chlorophyll florescent parameters to copper for use in biosensors, *Compt Rend Acad Bulgar des Sci,* 62(6), 723-728

Duysens, L.M.N. & Sweers, H.E. (1963). Mechanism of the two photochemical reactions in algae as studied by means of fluorescence, in: Japanese Society of Plant Physiologists (Ed.), *Studies on Microalgae and Photosynthetic Bacteria*, University of Tokyo Press, Tokyo, pp 353 – 372

Edwards, G.E. & Baker, N.R. (1993). Can CO_2 assimilation in maize leaves be predicted accurately from chlorophyll fluorescence analysis? *Photosynthesis Researach*, 37, 89 – 102

Falkowski, P.G. & Raven, J.A. (2007). *Aquatic Photosynthesis*, 2nd ed., Princeton University Press, Princeton, NJ, 484pp

Falkowski, P.G.; Wyman, K.; Ley, A.C. & Mauzerall, D. (1986). Relationship of steady state photosynthesis to fluorescence in eucaryotic algae, *Biochim Biophys Acta,* 849, 183 – 192

Finazzi, G.; Johnson, G.N.; Dall'Osto, L.; Zito, F.; Bonente, G.; Bassi, R. & Wollman, F.A. (2006). Nonphotochemical quenching of chlorophyll fluorescence in *Chlamydomonas reinhardtii*, *Biochemistry,* 45, 1490-1498

Fracheboud, Y. & Leipner, J. (2003). The application of chlorophyll fluorescence to study light, temperature, and drought stress. In: *Practical Applications of Chlorophyll Fluorescence in Plant Biology* (eds. J.R. DeEll & P.M.A. Toivonen), Kluwer Academic Publishers, Dordrecht, pp 125-150

Frank, H.A.; Cua, A.; Chynwat, V.; Young, A.; Gosztola, D. & Wasielewski, M.R. (1994). Photophysics of the carotenoids associated with the xanthophyll cycle in photosynthesis, *Photosyn Res,* 41, 389-395

Fryer, M.J.; Andrews, J.R.; Oxborough, K.; Blowers, D.A. & Baker, N.R. (1998). Relationship between CO_2 assimilation, photosynthetic electron transport, and active O_2 metabolism in leaves of maize in the field during periods of low temperature, *Plant Physiol,* 116, 571-580

Garab, G., & Mustardy, L. (1999). Role of LHCII-containing macrodomains in the structure, function and dynamics of grana, *Aust J Plant Physiol,* 26, 649 – 658

Gorbunov, M.Y. & Falkowski, P.G. (2004). Fluorescence induction and relaxation (FIRe) technique and instrumentation for monitoring photosynthetic processes and primary production in aquatic ecosystems, in: A. van der Est, D. Bruce (Eds.), *Photosynthesis: Fundamental Aspects to Global Perspectives, Proc*, 13th International Congress of Photosynthesis, Montreal, August 29 – September 3, 2004, Allen Press, Springer, 2005, pp 1029-1031

Genty, B.; Briantais, J.M. & Baker, N.R. (1989). The relationship between the quantum yield of photosynthetic electron transport and quenching of chlorophyll fluorescence, *Biochim Biophys Acta* 990, 87-92

Giardi, M.T. & Pace, E. (2005). Photosynthetic proteins for technological applications, *Trends Biotech,* 23, 257-263

Gorbunov, M.Y. & Falkowski, P.G. (2005). Fluorescence induction and relaxation (FIRe) technique and instrumentation for monitoring photosynthetic processes and primary production in aquatic ecosystems, in: A. van der Est, D. Bruce (Eds.), *Photosynthesis: Fundamental Aspects to Global Perspectives, Proc*, 13th International Congress of Photosynthesis, Montreal, August 29 – September 3, 2004, Allen Press, Springer, pp 1029-1031

Govindjee (2004). Chlorophyll a fluorescence: a bit of basics and history, in: G.C.Papageorgiou, Govindjee (Eds.), Chlorophyll a Fluorescence: A Signature of Photosynthesis, *Advances in Photosynthesis and Respiration*, vol. 19, Springer, Dordrecht, The Netherlands, pp 1 – 41

Govindjee, Papageorgiou, G. & Rabinowitch, E. (1967). Chlorophyll fluorescence and photosynthesis. In *Fluorescence Instrumentation and Practice.* Edited by G. G. Guilbaut. Marcel Dekker Inc., N. Y., p.511-564

Guisse, B.; Srivastava, A. & Strasser, R.J. (1995). The polyphasic rise of the chlorophyll a fluorescence (OKJIP) in heat stressed leaves, *Arch Sci Geneve,* 48, 147 – 160

Horton, P.; Ruban, A.V. & Walters, R.G. (1994). Regulation of light harvesting in green plants, *Plant Physiol*, 106, 415-420

http://www.ab.ipw.agrl.ethz.ch/~yfracheb/flex.htm

Ilik, P.; Kouril, R.; Kruk, J.; Mysliwa-Kurdziel, B.; Popelkova, H.; Strzałka, K. & Naus, J. (2003). Origin of Chlorophyll Fluorescence in Plants at 55 – 75oC, *Photochemistry and Photobiology,* 77, 68 – 76

Ilik, P.; Schansker, G.; Kotabova, E.; Vaczi, P.; Strasser, R.J. & Bartak, M. (2006). A dip in the chlorophyll fluorescence induction at 0.2 – 2 s in Trebouxia-possesing lichens reflects a fast reoxidation of photosystem I. A comparison with higher plants, *Biochim Biophys Acta,* 1757, 12 – 20

Johnson, G.N.; Yong, A.J.; Scholes, J.D. & Horton, P. (1993). The dissipation of excess excitation energy in British plant species, *Plant Cell Env,* 16, 673-679

Johnson, Z. (2004). Description and application of the background irradiance gradient single turnover fluorometer (BIG STf), *Marine Ecol Prog Ser,* 283, 73 – 80

Kautsky, H. & Hirsch, A. (1931). Neue Versuche zur Kohlensaure assimilation, *Naturwissenschaften*, 19, 964

Kitajima, M. & Butler, W.L. (1975). Quenching of chlorophyll fluorescence and primary photochemistry in chloroplasts by dibromo-thymoquinone, *Biochim Biophys Acta,* 376, 105-115

Koblizek, M.; Masojidek, J.; Komenda, J.; Kusera, T.; Pilloton, R.; Mattoo, A.K. & Giardi, M.T. (1998). A sensitive photosystem II based biosensor for detection of a class of herbicides, *Biotech Bioenerg,* 60, 664-669

Kolber, Z.S.; Prašil, O. & Falkowski, P.G. (1998). Measurements of variable chlorophyll fluorescence using fast repetition rate techniques: defining methodology and experimental protocols, *Biochim Biophys Acta,* 1367, 88 – 106

Kramer, D.M.; Johnson, G.; Kiirats, O. & Edwards, G. E. (2004). New fluorescence parameters for the determination of Q_A redox state and excitation energy fluxes, *Photosynth Res,* 79, 209-218

Krause, G. H. & Weis, E. (1991). Chlorophyll fluorescence and photosynthesis: The basics, *Annu Rev Plant Physiol Plant Mol Biol,* 42, 313-349

Kumke, M. & Lohmannsroben, H.G. (2009). Fluorescence - Introduction. In: *Optical monitoring of fresh and processed agricultural crops*, Zude, M. (Ed.). Boca Raton: CRS Press, Taylor & Francis Group, 253-271

Latimer, P.; Bannister, T.T. & Rabinowitch, E. (1956). Quantum yields of fluorescence of plant pigments *Science,* 124, 585-586

Mauzerall, D. (1972). Light-induced changes in *Chlorella*, and the primary photoreaction for the production of oxygen, *Proc Natl Acad Sci, USA,* 69, 1358 – 1362

Maxwell, D. P.; Falk, S.; Trick, C. G. & Huner, N. (1994). Growth at low temperature mimics high-light acclimation in *Chlorella vulgaris*, *Plant Physiol,* 105, 535-543

Maxwell, K. & Johnson, G.N. (2000). Chlorophyll fluorescence-a practical guide, *J Exp Bot,* 51, 659 – 668

Misra, A.N. (1993). Molecular mechanism of turn-over of 32 kDa-herbicide binding protein of photosyntem II reaction center. In *Advances in Plant Biotechnology & Biochemistry* (Lodha, M.L.; Mehta, S.L.; Ramagopal, S. & Srivastava, G.P., eds.), IARI, New Delhi pp 73-78

Misra, A.N. ; Ramaswamy, N.K. & Desai, T.S. (1997). Thermoluminescence studies on photoinhibition of *pothos* leaf discs at chilling, room and high temperature, *J Photochem Photobiol B (Biol),* 38, 164-168

Misra, A.N.; Sahu, S.M.; Misra, M.; Ramaswamy, N.K. & Desai, T.S. (1998). Sodium chloride salt stress induced changes in thylakoid pigment-protein complexes, PS II activity and TL glow peaks of chloroplasts from mung bean (*Vigna radiata* L.) and Indian mustard (*Brassica juncea* Coss.) seedlings, *Z Naturforsch,* Part: C, 54, 640-644

Misra, A.N. & Biswal, A.K. (2000). Thylakoid membrane protein kinase activity as a signal transduction pathway in chloroplasts, *Photosynthetica*, 38, 323-332

Misra, A.N. & Terashima, I. (2003). Changes in photosystem activities during adapatation of *Vicia faba* seedlings to low, moderate and high temperatures, *Plant Cell Physiol*, Abstract, Annual Symp. JSPP, Nara, 2003

Misra, A.N.; Latowski, D. & Strzalka, K. (2003). De-epoxidation state of lutein and violaxanthin in the seedlings of salt sensitive and salt tolerant plants grown under NaCl salt stress, *Plant Biology, 2003*, Honolulu, Hawaii

Misra, A.N.; Latowski, D. & Strzalka, K. (2006). The xanthophylls cycle activity in kidney bean and cabbage leaves under salinity stress, *Russian J Plant Physiol*, 53, 102-109

Misra, A.N.; Latowski, D. & Strzalka, K. (2011). Violaxanthin de-epoxidation in aging cabbage (*Brassica oleracea* L.) leaves play as a sensor for photosynthetic excitation pressure, *J Life-Sciences*, 5, 182-191

Misra, A.N.; Srivastava, A. & Strasser, R.J. (2001a). Utilisation of fast Chlorophyll *a* fluorescence technique in assessing the salt/ion sensitivity of mung bean and brassica seedlings, *J Plant Physiol*, 158, 1173-1181

Misra, A.N.; Srivastava, A. & Strasser, R.J. (2001b). Fast chlorophyll a fluorescence kinetic analysis for the assessment of temperature and light effects: A dynamic model for stress recovery phenomena, *Photosynthsis, PS2001*. CSIRO Publ., Melbourne, Australia S3-007

Misra, A.N.; Srivastava, A, & Strasser, R.J. (2007). Elastic and plastic responses of *Vicia faba* leaves to high temperature and high light stress, *Gordon Conference on "Temperature stress in plants"* , Ventura, USA 25-30 Jan. 2007

Muller, P.; Li, X.P. & Niyogi, K.K. (2001). Non-photochemical quenching. A response to excess light energy, *Plant Physiol*, 125, 1558 – 1566

Mullineaux, C.W. & Emlyn-Jones, D. (2005). State transitions: An example of acclimation to low-light stress, *J Exp Bot,* 56, 389 – 393

Murata, N. (2009). The discovery of state transitions in photosynthesis 40 years ago, *Photosynth Res* 99, 155 – 160

Murata, N. (1970). Control of excitation transfer in photosynthesis. IV. Kinetics of chlorophyll a fluorescence in *Porphyra yezoensis*, *Biochim Biophys Acta,* 205, 379 – 389

Murata, N., Nishimura, M. & Takamiya, A. (1966). Fluorescence of chlorophyll in photosynthetic systems. III. Emission and action spectra of fluorescence; three emission bands of chlorophyll a and the energy transfer between two pigment systems, *Biochim Biophys Acta,* 126, 234 – 243

Niyogi, K.K.; Bjorkman, O. & Grossman, A.R. (1997). *Chlamydomonas* xanthophyll cycle mutants identified by video imaging of chlorophyll fluorescence quenching, *Plant Cell,* 9, 1369-1380

Noomnarm, U. & Clegg, R. (2009). Fluorescence lifetimes: fundamentals and interpretations, *Photosynthesis Research*, 101,181-194

Olson, R.J.; Chekalyuk, A.M. & Sosik, H.M. (1996). Phytoplankton photosynthetic characteristics from fluorescence induction assays of individual cells, *Limnol Oceanogr,* 41, 1253 – 1263

Oxborough, K. & Baker, N.R. (1997). Resolving chlorophyll *a* fluorescence images of photosynthetic efficiency into photochemical and non-photochemical components: calculation of qP and F_v'/F_m' without measuring F_o', *Photosynth Res,* 54, 135-142

Paillotin, G. (1976). Movement of excitations in the photosynthetic domains of photosystem II, *J Theor Biol,* 58, 237 – 252

Quick, W.P. & Horton, P. (1984). Studies on the induction of chlorophyll fuorescence in barley protoplasts. II. Resolution of fluorescence quenching by redox state and the trans-thylakoid pH gradient, *Philos Trans R Soc Lond B Biol Sci,* 220, 371-382

Rabinowitch, E. & Govindjee (1969). *Photosynthesis*, John Wiley and Sons Inc., NY, 273pp.

Rashkov, G.D.; Dobrikova, A.G.G.; Pouneva, I.D.; Misra, A.N. & Apostolova, E. (2011). Sensitivity of *Chlorella vulgaris* to herbicides. Possibility of using it as a biological receptor in Biosensors, *Sensors & Actuators: B.* (accepted).

Rochaix, J.D. (2007). Role of thylakoid protein kinases in photosynthetic acclimation, *FEBS Lett*, 581, 2768 – 2775

Rohacek, K., Soukupova, J. & Bartak, M. (2008). Chlorophyll fluorescence: A wonderful tool to study plant physiology and plant stress. *Plant Cell Compartments* – Selected Topics, Editor: Benoit Schoefs. Chapter 3. pp. 41-104. Research Signpost, Trivandrum, India. ISBN: 978-81-308-0104-9

Sayed, O.H. (2003). Chlorophyll fluorescence as a tool in cereal crop research, *Photosynthetica,* 41, 321-330

Schansker, G., Toth, S.Z. & Strasser, R.J. (2005). Methylviologen and dibromothymoquinone treatments of pea leaves reveal the role of photosystem I in the Chl a fluorescence rise OJIP, *Biochim Biophys Acta,* 1706, 250 – 261

Schreiber, U. (2004). Pulse-amplitude-modulation (PAM) fluorometry and saturation pulse method: an overview, in: G.C. Papageorgiou, Govindjee (Eds.), Chlorophyll a Fluorescence: A Signature of Photosynthesis, *Advances in Photosynthesis and Respiration*, vol. 19, Springer, Dordrecht, The Netherlands, pp 279 – 319

Schreiber, U.; Schliwa, U. & Bilger, W. (1986). Continuous recording of photochemical and non-photochemical chlorophyll fluorescence quenching with a new type of modulation fluorometer, *Photosynth Res,* 10, 51-62

Srivastava, A.; Greppin, H. & Strasser, R.J. (1995), Acclimation of land plants to diurnal changes in temperature and light, in: P. Mathis (Ed.), *Photosynthesis: From Light to Biosphere*, vol. 4, Kluwer Academic Publishers, The Netherlands, pp. 909 – 912

Srivastava, A.; Guisse, B.; Greppin, H. & Strasser, R.J. (1997). Regulation of antenna structure and electron transport in PSII of *Pisum sativum* under elevated temperature probed by the fast polyphasic chlorophyll a fluorescence transient OKJIP, *Biochim Biophys Acta,* 1320, 95 – 106

Stirbet, A. & Govindjee (2011). On the relation between the Kautsky effect (chlorophyll a fluorescence induction) and Photosystem II: Basics and applications of the OJIP fluorescence transient, *J Photochem Photobiol B Biol,* doi:10.1016/j.jphotobiol.2010.12.010

Strasser, B.J. (1997). Donor side capacity of photosystem II probed by chlorophyll a fluorescence transients, *Photosynth Res,* 52, 147 – 155

Strasser, R.J. & Govindjee (1991). The F_o and the OJIP fluorescence rise in higher plants and algae, in: J.H. Argyroudi-Akoyunoglou (Ed.), *Regulation of Chloroplast Biogenesis*, Plenum Press, New York, pp. 423 – 426

Strasser, R.J. & Govindjee (1992). On the OJIP fluorescence transients in leaves and D1 mutants of *Chlamydomonas reinhardtii*, in: N. Murata (Ed.), *Research in Photosynthesis*, vol. II, Kluwer Academic Publishers, Dordrecht, The Netherlands, pp. 39 – 42

Strasser, R.J.; Srivastava, A. & Tsimilli-Michael, M. (2000). The fluorescence transient as a tool to characterize and screen photosynthetic samples, in: M. Yunus, U. Pathre, P. Mohanty (Eds.), *Probing Photosynthesis: Mechanism, Regulation and Adaptation*, Taylor and Francis, London, UK, pp. 443 – 480

Strasser, R.J.; Tsimilli-Michael, M. & Srivastava, A. (2004). Analysis of the chlorophyll fluorescence transient, in: G.C. Papageorgiou, Govindjee (Eds.), Chlorophyll Fluorescence: A Signature of Photosynthesis, *Advances in Photosynthesis and Respiration*, vol. 19, Springer, Dordrecht, The Netherlands, pp. 321 – 362

Trissl, H.W.; Gao, Y. & Wulf, K. (1993). Theoretical fluorescence induction curves derived from coupled differential equations describing the primary photochemistry of photosystem II by an exciton-radical pair equilibrium, *Biophys J*, 64, 974-988

Tsimilli-Michael, M. & Strasser, R.J. (2008). In vivo assessment of plants' vitality: applications in detecting and evaluating the impact of mycorrhization on host plants, in: A. Varma (Ed.), Mycorrhiza: State of the Art, *Genetics and Molecular Biology, Eco-Function, Biotechnology, Eco-Physiology, Structure and Systematics*, 3rd ed., Springer, Dordrecht, The Netherlands, pp. 679 – 703

Tsimilli-Michael, M.; Pecheux, M. & Strasser, R.J. (1998). Vitality and stress adaptation of the symbionts of coral reef and temperate foraminifers probed in hospite by the fluorescence kinetics OJIP, *Archs Sci Geneve*, 51, 205 – 240

van Gorkom, H.J. (1986). Fluorescence measurements in the study of photosystem II electron transport, in: Govindjee, J. Amesz, D.C. Fork (Eds.), *Light Emission by Plants and Bacteria*, Academic Press, Ontario, pp. 267 – 289

van Kooten, O. & Snel, J. F. H. (1990). The use of chlorophyll fluorescence nomenclature in plant stress physiology. *Photosynth Res*, 25, 147-150

Vladkova, R.; Dobrikova, A.G.; Singh, R.; Misra, A.N. & Apostolova, E. (2011). Photoelectron transport ability of chloroplast thylakoid membranes treated with NO donor SNP: Changes in flash oxygen evolution and chlorophyll fluorescence, *Nitric Oxide: Biology and Chemistry*, 24, 84-90

Vladkova, R.; Ivanova, P.I.; Krastera, V.; Misra, A.N. & Apostolova, E. (2009). Assessment of chlorophyll florescent and photosynthetic oxygen evolution parameters in pea thylakoid membranes for use in biosensors against Q_B binding herbicide- atrazine, *Compt Rend Acad Bulgar des Sci*, 62(3), 355-360

Walters, R.G. & Horton, P. (1991). Resolution of non-photochemical chlorophyll fluorescence quenching in barley leaves, *Photosynth Res*, 27, 121 – 133

Zer, H.; Vink, M.; Shochat, S.; Herrmann, R. G.; Andersson, B. & Ohad, I. (2003). Light affects the accessibility of the thylakoid light harvesting complex II (LHCII) phosphorylation site to the membrane protein kinase(s), *Biochemistry,* 42, 728-738

8

Electromagnetic Radiation and Life: Bioelementological Point of View

A.Kh. Tambiev[1] and A.V. Skalny[2]
[1]*Moscow State University,*
[2]*Institute of Bioelementology, Orenburg State University,*
Russia

1. Introduction

Life on Earth has formed and evolved under exposure to electromagnetic radiation (EMR) of the Sun, which is the most potent natural source of electromagnetic waves. Besides the Sun, electromagnetic oscillations form during lightning strikes. Also, there is geomagnetic background of our planet. Artificial electromagnetic radiation is produced by different electrical equipment, electric motors, radars, transmitters, computers, mobile phones and other devices. It is impossible to imagine modern civilization without television, radio, telemetry, radars and navigation systems. Along with the traditional technical use of almost the whole scale of electromagnetic waves, there expands their practical application in various fields: medicine, biology, agriculture and biotechnology. The Sun radiates its energy almost over the whole scale of electromagnetic waves, including radio, ultra high frequency and optical ranges as well as the range of ionizing radiation. Basically, all the energy of Sun's EMR lies within the wavelength range from 1500 Å to 5 mm, and the share of our planet is an enormous amount of energy equal to 2×10^{17} watts per second. There was emerged a new science electromagnetobiology, which deals with a part of the general problem of biological effects of mild and ultramild physical and chemical factors. It is believed that the action of such factors lies below the threshold for activation of protective biological mechanisms and therefore is capable of cumulating at the subcellular level. Man-made electromagnetic pollution is increasing very rapidly: during the last 45 years, as estimated, electromagnetic pollution has grown 45-50 thousand times. Currently the world is published several thousand articles on electromagnetobiology per year. Standards on electromagnetic safety for man are developed by a number of different national and international organizations. Thus, the biological effects of ultramild agents, particularly EMR, are a fundamental scientific problem with distinct application-oriented character. Apparently, there is no other external factor, which would have such a powerful influence on living objects as electromagnetic waves do. In the biosphere permanently occur periodic electromagnetic processes with frequencies distributed throughout the whole electromagnetic spectrum. It is natural to assume that any part of this spectrum has played a certain role in the evolution of living organisms, affecting their vital processes. For example, a trace effect of low frequency natural electromagnetic fields on living organisms could be fixed in the form of biorhythmic oscillations. Though electromagnetic waves existed on Earth ever, the mankind "has guessed" about the existence of this form of matter only in the

second half of the 19th century (D. Maxwell, H. Hertz). Men were first used artificial electromagnetic waves for their purposes only in the late 19th century (A. Popov, G. Marconi). It has long been observed that changes in the static magnetic field are not indifferent to living organisms; these changes always accompany the development of life on Earth. Some believe that, for instance, inversions of poles of the Earth magnetic dipole could cause biological effects of global scale, in particular, cause appearance and disappearance of biological species and life as a whole. According to conception of bioelements and bioelementology as a new integrative approach in life sciences, proposed by A.V.Skalny (2003-2011) the existing of biosystems depends on combination of internal factors (presence of bioelements as blocks of life) and external conditions including electromagnetic fields. Biosphere is an assembly of bioelements and living organisms existing under permanent regulatory influence of physico-chemical factors of terrestrial and cosmic origin. Electromagnetic waves can be powerful agent for production of so called secondary bioelements from primary ones, according to our (Skalny, 2009, 2011a) concept of bioelements. Thus, we suppose that electromagnetic technologies can be an effective instrument of enlargement of biomass with increased "food density", enriched by essential nutrients, for Humankind (Skalny, 2011c). It is also known that some ions participate in magnetoreception. Thus, calcium ions have been shown to be involved in many biological processes: synaptic transmission, excretion of various compounds to the environment, flagellar motility, enzymatic activation, muscular contraction, reproduction, growth and development. Since some proteins, which bind calcium, can bind magnesium too, the cites of binding for the calcium and magnesium may be identical, so that ions of magnesium and calcium may be considered as potential targets of magnetic fields. Around the same way of involving in the processes of life is probable for potassium, sodium, rubidium and lithium. Electromagnetic waves of millimeter scale exist in the spectrum of the Sun, but do not reach the Earth's surface, because absorbed by water vapor. Consequently, this range could not be an environmental factor that participated in evolution running in the biosphere. It was artificially obtained recently in 1965-1966, when Russian scientists under the guidance of academician N.D. Devyatkov and professor M.B. Golant developed generators that produce this kind of waves. From that time these waves started to be applied in medicine and then in biology. There were used mostly the waves of low, non-thermal intensity, when the upper limit of the incident power density was ca. 10 mW/cm2. Thus, as for the quantity of absorbed energy, this range can be attributed to mild or even ultramild influence. Millimeter waves have several important features: strong absorption by molecules of water, a resonant effect, the ability to produce convective mixing of the irradiated liquid. At the same time, the biological effect of millimeter waves is usually cumulative. We have first (Tambiev et al., 1997) identified a significant biological effect of these waves on the photosynthetic organisms: cyanobacteria and microalgae. It was shown in many studies that water retains the information about the history of physical influences on it, which significantly affects the flow of processes in the aquatic environment and creates opportunities for developing new channels of control of chemical, biochemical and biological processes. The experiments showed that millimeter waves can influence on the chemical (mineral) content of cells of the photosynthetic organisms – cyanobacteria and microalgae, which are widespread objects of photobiotehnology. We have managed to significantly increase the synthesis of so-called secondary bioelements by microalgae Spirulina platensis and Spirulina maxima. Under the

influence of millimeter wave radiation there is observed increased accumulation of a number of trace elements from the environment: selenium, chromium, zinc, copper, lithium, etc., with dramatic change in elemental composition of the algal cells (Tambiev et al., 2000-2011). Our studies indicate the applicability of electromagnetic millimeter waves for the efficient biosynthesis of secondary bioelements and the necessary building blocks for life maintenance, and finally for increasing the mass and diversity of living matter on the planet, which has an undoubted theoretical and practical importance.

2. Electromagnetic radiation of millimeter range (EHF-radiation) of low intensity and its effect on phototrophic microorganisms

Life on Earth has been formed under the influence and in environments of solar electromagnetic radiation, which is the most powerful external factor affecting the existence of living organisms. The biosphere is constantly full of electromagnetic processes with various wavelengths. It is possible that any part of this spectrum anyhow influences the evolution and vital processes, causing either extinction or adaptation of living species. For example, natural rhythms of electrical oscillations in living organisms may form as a result effected by natural low-frequency electromagnetic fields.

Sun, as we know, is a giant thermonuclear boiler with a temperature of 5780 K at the surface and up to 16 million K in the center. Its spectrum contains lines of more than 70 chemical elements, and it radiates its energy over almost the entire scale of electromagnetic waves.

Every second Sun spends for radiation more than 4 million tons of its mass, which totally amounts about 2×10^{21} million tons. The share of our planet is 2×10^{17} W of electromagnetic energy per second. Electromagnetic oscillations also emerge in discharges of lightning, including little-known ball lightning. Despite the fact that electromagnetic waves existed on our planet ever, scientists began to closely study this form of matter just in the second half of the XIX century (J. Maxwell in 1865; H. Hertz in 1888). All life processes, as it became evident later, are accompanied by generation of electromagnetic waves.

Artificial electromagnetic waves were first used by man for technical purposes in 1895-1896 (A. Popov, G. Marconi). This application has developed to such an extent that now it is impossible to imagine modern civilization without television, computers, radios, power lines, radar and navigation systems, radiophones, electric motors, diagnostic and magnetotherapeutic medical equipment etc.

In medicine, electromagnetic waves are used currently in a broad range from ultra-low frequency to x-rays and gamma radiation: as therapeutic and diagnostic means, for heating tissues, in medical lasers etc. In addition, electromagnetic waves are used in such areas as industrial techniques, agriculture, biotechnology and, in particular, in photobiotehnology, which we will discuss below.

In recent decades, a discipline “electromagnetobiology” is formed as a part of the research on biological effects of weak and ultra-weak physical and chemical factors. It may be suggested that influence of these factors is below the threshold of protective biological mechanisms and is therefore capable of accumulating at subcellular level. At the same time, electromagnetic pollution is accumulating in the environment, and its increase over the last two decades was estimated in some works tens of thousands times as much. This makes the

problem a very urgent. Various organizations develop standards for Electromagnetic Safety, investigate connection between low-frequency (mostly) electromagnetic fields and the risk of cardiovascular, oncologic, immune and other diseases, study the problems arising from wide use of mobile phones, etc. Currently, several thousand articles on electromagnetobiology is published in the world annually (Bingi, 2002).

Radio-wave range				Microwave range (MW)				Optical range			Ionizing radiation	
>1000m	100…1000 m	110…100 m	1…10 m	10…100 cm	1…10 cm	1…10 mm	0.1…1 mm	100…0.76 μm	0.76…0.4 μm	400…10 nm	10…0.01 nm	0.01…0.0001 nm
Myriametric waves	Long waves	Medium wave	Short waves	Decimeter waves	Centimeter waves	Millimeter waves	Submillimeter waves	Infrared radiation (IR)	Visible light	Ultraviolet radiation (UV)	X-radiation	Gamma radiation
This range has long been widely used in various devices for wireless communication (radio, television, etc.). It is traditionally called "radio-wave range". Some parts of it are used in medical devices.				Technical use of microwaves began to develop rapidly in the second half of XX century after invention of radar, radio relay links, satellite communication systems, control systems, mobile phones etc. Microwave electronic devices made it possible to create medical equipment for diagnostics and treatment of many diseases.				These types of radiation are of considerable interest for medical application, especially after the invention of IR, visible and UV lasers, xenon radiators and improved mercury lamps.			Ionizing radiation is the very first type of electromagnetic waves, which have been applied in medicine at the end of XIX century to diagnose and treat cancer.	

Table 1. The scale of electromagnetic waves

In 1965-1966 a team led by academician N.D.Devyatkov has developed generators for medical and biological use on the basis of wide-range backward wave tubes. This made it possible to get an artificial radiation of the millimeter range (wavelength 1-10 mm), called EHF radiation (denoted “extremely high frequency”), and gave the opportunity to explore the effect of millimeter waves of low (non-thermal) intensity on various microorganisms and experimental animals. The interest in such work was supported by the fact that in nature there are no strong sources of these waves since this range is much absorbed by water molecules, which have a large dipole moment. For example, a water layer 1 mm thick degrades the millimeter waves with $\lambda = 8$ mm by 100 times, and with $\lambda = 2$ mm by 10,000

times. Thus these waves present in the spectrum of solar radiation, did not reach the surface of Earth, because they were stopped by water vapor in the atmosphere. And therefore they could not be a factor of evolution.

The biological action of this kind of electromagnetic waves was to be studied with allowance for their peculiarities. In almost all experiments on the effect of millimeter waves on unicellular and multicellular organisms there was used the upper limit of low intensity, not exceeding 10 mW/cm2. Larger intensity produced undesirable thermal effects in biological objects and eliminated the possibility to find previously unknown effects, such as informational ones.

An important point was also the fact that quantum of energy in the EHF range has a magnitude less than the energy of thermal motion of atoms and molecules at room temperature. In the literature this is called "kT problem" because it is unclear how these rays can change the speed of biochemical reactions, i.e. to cause a resonance-like biological effect. If to imagine the position of EHF quantum on energy scale, then it will be located below the energy of hydrogen bonds, the oscillation energy of atoms and molecules, the energy of activation and ionization, but above the energy of rotational motions of atoms and molecules and the energy of magnetic ordering. Hence at room temperature the EHF quanta can affect mainly only the kinetic energy of rotation of polar molecules (Tambiev et al., 2003). In terms of physics this phenomenon is yet have no explanation but only a hypothesis. And this is a very important, just maybe the most important problem of magnetobiology, discussed in literature (Bingi, 2002).

The next important effect of millimeter waves is convective mixing of the irradiated fluid. This is a consequence of high field gradients and high temperature in the irradiated thin surface layer, which can further extend to the entire irradiated volume. The convection can enhance transport of ions, water and various substances through biomembranes.

Effects caused by irradiation of objects with millimeter waves, as a rule, are frequency-dependent. The effective frequencies are called "resonance" or active, and the reasons for their action are not always explainable, – most likely, there are subtle mechanisms of their influence on some parts of cell metabolism. The biological effect can be seen only at these resonant frequencies and disappears when you shift them by 100-200 MHz. Thus, in experiments with microorganisms, diagrams of dependence of the biological effect on the incident power density of electromagnetic waves have extended regions (plateau), where the effect was not manifested until fit to resonant values of power. At the resonant values the effect became observed, but after passing off these values the plateau could extend again until the next resonance values approach. Biological effects caused by the action of millimeter waves, in many cases, have a cumulative nature, which apparently suggests that the manifestation of them involves not only fast, but also relatively slow biochemical processes.

It is important to note that a very small amount of energy absorbed by objects during its irradiation with low-intensity millimeter waves (EHF irradiation) allow us to categorize this physical factor as a weak or even ultra-weak influence, which in recent years attracted much attention (Tambiev et al., 2003).

Since the beginning of practical use of the millimeter waves, the most impressive achievements have been obtained in medicine. More than thirty-five years' experience of

EHF radiation use in clinical practice has shown its high therapeutic efficacy in treatment of various diseases by devices with active wavelengths of 4.9, 5.6, 7.1 mm. The incident power density of the radiation is typically a few tenths of milliwatt or several milliwatts per square centimeter. EHF therapy is well combined with other treatments, as well as frequently used as monotherapy; it increases body functional reserves, improves immune status.

In the mid-1980s we were first published works, which described the effect of EHF radiation on photosynthetic organizms – representatives of a vast world, vital for the existence of the biosphere. As the objects, we chose cyanobacteria of Spirulina genus, which are common targets in photobiotechnology.

Now photobiotechnology is an intensively developing field of science and industry. It uses productive facilities of phototrophic organisms, especially prokaryotic cyanobacteria (blue-green algae), eukaryotic microalgae (green, yellow-green, red, brown etc.), and higher plants. Industrial cultivation of microalgae and cyanobacteria has several advantages, which include the ease of growing in controlled conditions, rapid proliferation and the possibility of quick obtaining of large biomass, whose composition exceeds many natural sources of organic compounds. Particularly, the biomass of cyanobacteria and microalgae contains all essential amino acids, several essential vitamins and other nutrients. In addition, at mass cultivation it is possible to obtain biomass with different chemical composition, thereby conducting controlled biosynthesis.

In cultivators of open type (sunlit) the average productivity of dry biomass of cyanobacteria per day can reach 50-60 g/m2, which is equal to 45-70 tons/ha per year. I.e. the total yield of the relatively low-cost biomass is 10 times as much as the yield of wheat and 15 times as much as the yield of soybeans. The biomass can be used in animal and poultry farming, pisciculture, sericulture, horticulture, crop production, food and feed production, for creating a protein-vitamin supplements and drugs, food dyes, enzymes, vitamins, in cosmetics, in metal-working, microbiological and chemical industries, for obtaining additional energy resources as through bioconversion into methane, alcohols or other products. Besides, direct synthesis of hydrocarbons by algae is a process connected to purification of waste water and protecting the environment.

World production of the dry biomass of cyanobacteria and microalgae for food and feed purposes reaches more than ten thousand tons per year. Only Japanese production of macrophytic algae grown in aquaculture exceeds 1.5 million tons per year.

We studied the possibility to stimulate growth and biomass productivity using millimeter waves on cyanobacteria Spirulina platensis, Spirulina maxima (prokaryotes), and a Black Sea green flagellate Platymonas viridis (eukaryote). These organisms can serve as a non-traditional source of protein, may be the first link in the mariculture food chain. They tolerate wide variations in temperature, light and salinity, and is resistant to chemical pollution. S. platensis and S. maxima, as the most suitable subjects for large-scale production of edible micro-algae, are cultivated in the United States, Japan, Germany, Israel, Mexico, Brazil, India, Taiwan, Italy, China, Thailand and other countries.

As it can be seen from Table 2, protein amounts up to 70% of the cyanobacterial cells (dry weight). Its composition is close to that of egg white and fairly balanced for all essential amino acids. Besides the listed components, the composition includes vitamins B1, B2, B3,

B6, B12, E, folic acid, biotin and pantothenic acid. Beta-carotene in spirulina is 20-25 times as much as in carrots. Among the lipids there prevail unsaturated fatty acids and rare gamma-linolenic acid, necessary for humans. Spirulina is relatively rich in potassium, magnesium, iron, phosphorus, calcium. It also contains many essential trace elements such as zinc, manganese, copper, and these minerals are contained in chelate form, friendly for human body. Unlike most of the algae, cell's wall of spirulina is composed of complex carbohydrates, rather than cellulose. Due to this, spirulina is easily digested, and its assimilability equals to 85–95%. Biological value of spirulina puts it on par with such products as meat and soy protein, and is significantly higher than that of such foods as legume and cereal flour.

Humidity, %	4.0-6.0
Ash, %	6.4-9.0
Protein, %	60.0-71.0
Carbohydrates, %	13.0-16.0
Triglycerides, %	6.0-7.0
Ribonucleic acid, %	2.2-3.5
Deoxyribonucleic acid, %	0.65-1.0
Chlorophyll a, %	0.61-0.76
β-carotene	0.15-0.19
Palmitic acid, %	1.65
Linoleic acid, %	1.09
Linolenic acid, %	0.8-2.0

Table 2. Overall chemical composition of S.platensis biomass.

Spirulina (S. platensis, S. maxima) is usually cultivated either in artificial reservoirs with stirring, or in photobioreactors of open or closed type. Biomass of S. maxima is directly extracted and dried from Lake Texcoco (Mexico). In Central Africa, spirulina S. platensis for hundreds of years was collected in the Lake Chad and surrounding area, where it was used by local population for food. Pacific spirulina S. pasiphyca, a strain obtained and cultivated by the company Cianotech in Hawaii, have the highest content of carotenoids in comparison with other species and strains. Growth conditions for the genus Spirulina is very simple: you need carbon dioxide, water, inorganic salts and light. Also an important advantage is the need for highly alkaline environment.

Experiments to study the potential stimulation of growth and yield of biomass using millimeter waves (EHF radiation) were carried out by us on the cultures of S. platensis and P. viridis.

Table 3 shows that the largest statistically significant stimulation of biomass production on the 30th day of growth was observed for S. platensis after a single irradiation for 15 and 30 min, and for P. viridis after a single irradiation for 30 and 60 min. In both cases the wavelength was 8.34 mm, incident power density was 2.2 mW/cm^2.

Exposure time, min.	Age of culture, days				Stimulation of growth on the 30th day	
	I		II			
	A	B	A	B	A	B
10 days						
15	0.15	0.5	0.30•	0.16•		
30	0.20	0.05	0.23	0.18•		
60	0.13	0.05	0.13	0.15		
120	0.12	0.12	0.10	0.16		
360	0.07	0.20	0.043	0.16		
20 days						
15	0.75	0.31	1.40•	0.60•		
30	0.71	0.31	1.07	0.17*		
60	0.67	0.31	1.05	0.54*		
120	1.52	0.27	1.03	0.28*		
360	0.32	0.40	0.26	0.40		
30 days						
15	2.40	0.40	5.20*	0.91•	217	228
30	2.12	0.40	4.16•	0.92*	196	230
60	1.96	0.40	2.08	1.15•	106	288
120	3.24	0.44	2.92	0.49	90	111
360	1.56	0.57	1.44	0.52•	92	91

Note: differences are significant at * - $p < 0.05$; • - $p < 0.01$.

Table 3. Effect of EHF radiation on the biomass production in non-irradiated (I) and irradiated (II) cultures of photosynthetic organisms: S.platensis (A) and P.viridis (B), g/l

Since organisms excreted exometabolites into cultural medium, we proposed a method for measuring reactivity of the medium (RM). It involves the ratio of oxidative (OA) and antioxidant (AOA) activity of the medium. The RM parameters of the cultural medium are closely related to physiological state of the producers in all phases of growth and development. This was shown previously for many species of cyanobacteria, micro- and macrophytic algae, fungi, bacteria, actinomycetes and other objects (Tambiev, 1984).

Figure 1 shows that in irradiated cultures of the cyanobacteria and microalgae OA of the native exometabolites increased and correlated with an increase in biomass. The data obtained earlier on unicellular and macrophytic algae indicated that their normal metabolism is most often accompanied by release of much oxidizing compounds into the medium, thus manifesting OA. On the contrary, metabolic disorders reduce the release of oxidants and induce leak of antioxidants into the medium (which in normal conditions are kept inside the cell and present in the medium just in small amounts), thus manifesting AOA. Therefore, the ratio of oxidants and antioxidants in the medium allow us to monitor

physiological status of the cyanobacterial and algal cultures. Figure 1 demonstrates that a single exposure of the cultures by low-intensity millimeter waves in optimal time, which is accompanied by the highest yield of biomass, has the greatest value of OA.

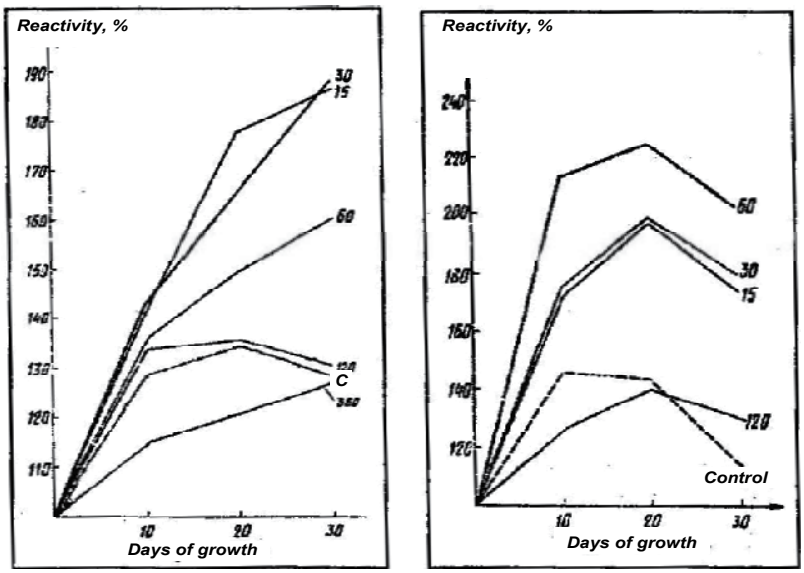

Fig. 1. Effect of EHF radiation on reactivity of cultural medium for S. platensis (left) and P. viridis (right)

Above we have mentioned that millimeter waves possess a resonance effect. We have identified a number of active wavelengths, which caused much more accumulation of S. platensis biomass in comparison with control when irradiated in a liquid medium.

Table 4 shows that at different incident power density and irradiation time equal to 30 min the resonant wavelengths were 7.1, 7.89, and 6.66 mm. During irradiation of S. platensis in the same conditions but at the constant incident power density equal to 1.3 mW/cm2, the greatest effect was observed at the wavelengths 7.1 and 6.25 mm. For culture P. viridis the active wavelengths were 8.34 and 8.30 mm with an increase in biomass of 241 and 218% as compared to control, respectively. At the same time, irradiation at wavelengths 8.25 and 8.20 mm resulted in inhibition of growth. It should be noted that, as before, the changes in RM were correlated with the accumulation of biomass.

In experiments on the same irradiated cultures at wavelength 8.34 mm and incident power density 2.2 mW/cm2, we observed an intensification of photosynthetic process, accompanied by an increase of oxygen and growth of biomass. At the same time, there was increased amount of chlorophyll in cells of the irradiated cultures as compared to control, and the ratio of dark respiration to photosynthesis shifted toward more favorable process for the cells – to photosynthesis.

It was also shown that millimeter waves affect the absorptive-excretory transport of sodium ions, recorded in the medium. This was observed in irradiated cultures earlier than changes in photosynthesis, pigment composition of the cells or growth of biomass.

Experimental conditions	10 days	20 days	30 days		
	Biomass	Biomass	Biomass	pH	RM (% to the control)
Control	0.16	0.49	0.62	9.75	97
8.34 mm, 2.6 mW/cm2	0.21	0.68	0.87	9.84	71
7.1 mm, 1.54 mW/cm2	0.25	0.88	1.35	9.91	158
7.89 mm, 2.38 mW/cm2	0.28	0.95	1.3	9.91	141
7.4 mm, 3.0 mW/cm2	0.25	0.85	1.1	9.93	127
6.66 mm, 3.1 mW/cm2	0.25	0.90	1.4	9.95	180
6.25 mm, 1.64 mW/cm2	0.20	0.77	0.92	9.90	84
6.06 mm, 3.0 mW/cm2	0.17	0.80	1.0	9.83	101

Table 4. Effect of EHF radiation of different frequencies on the increase of S. platensis biomass (liquid medium)

Table 5 shows that after the exposure the excretion of organic compounds (carbohydrate, riboflavin) by S. platensis into the cultural medium was increased, which also manifested the resonance effect; and the biomass of irradiated cultures exceeded that of non-irradiated by 1.6–1.8.

Experimental conditions	Biomass, g/l	Carbohydrates, mg/g dry biomass	Riboflavin, μg/g dry biomass
Control	0.488	266.3	20.5
Irradiation:			
λ = 7,89 mm	0.720	291.0	25.6
λ = 6,66 mm	0.736	315.0	30.7
P = 0.8 mW/cm2			
Control	0.420	619.0	29.7
Irradiation:			
λ = 7,89 mm	0.700	960.0	35.7
λ = 6,66 mm	0.660	827.2	26.5
P = 2.2 mW/cm2			

Table 5. Effect of EHF radiation on excretion of organic compounds by S. platensis (age 40 days)

Some published works studied the influence of millimeter waves of low intensity on non-photosynthetic organisms. Here is a summary (Table 6) from our review (Tambiev et al., 2002), which also includes our works conducted on phototrophic organisms and published before the review.

Active wavelengths (mm)	Organisms	Effects of exposure
Prokaryotes		
Bacteria		
6,0–6,7; 7,1; 5,6; 5,95–7,2	*Escherichia coli*	Stimulation of growth; increasing resistance to dehydration
6,0–6,7; 8,0; 5,95–7,2	*Staphylococcus aureus, Staphylococcus sp.*	Weakening of pigmentation, reduction of colony size
5,95–7,2	*Bacillus mucilaginosus*	Activation of biosynthetic processes
5,95–7,2; 6,2	*Bacillus firmus*	Increase of enzymatic activity and biomass accumulation
8,0	*Salmonella typhimurium*	Activation of free radical reactions
4,04	*Rhodobacter sphaeroides*	Increased yield of triplet states of reaction centers; increase in lifetime of the triplet
4,04	*Halobacterium halobium*	Acceleration of proton transport
6,96; 4,16; 7,1; 4,46	*Photobacterium leiognathi*	Bioluminescence quenching or activation
Actinomycetes		
5,95–7,2	*Streptomyces spheroides*	Increased biosynthesis of enzymes
5,6; 4,6	*Streptomyces xanthochromogenes*	Increase of colony growth rate
5,95–7,2	*Nocardia sp.*	Increased biosynthesis of enzymes
Cyanobacteria		
6,06; 6,25; 6,66; 7,1; 7,89; 8,34; 4,6; 5,6	*Spirulina platensis, Spirulina maxima*	Stimulation of growth; intensification of photosynthesis
8,34	*Anacystis nidulans, Anabaena variabilis, Plectonema boryanum, Fremyella diplosiphon*	Stimulation of growth
Eukaryotes		
Mold fungi		
5,95 – 7,2	*Aspergillus oryzae*	Increase in biomass accumulation and biosynthesis of enzymes
5,95 – 7,2	*Aspergillus awamory*	Weakening of pigmentation; decreased formation of conidia
Yeast-like fungi		
5,95 – 7,2	*Endomyces fibuliger*	Stimulation of yeast cells formation, increased activity of glucoamylase and alpha amylase

Mycophilous fungi		
5,95 – 7,2	*Dacthilyum dendraides*	Increase in protease activity
Yeast		
8,5; 7,17 – 7,21; 5,95 – 7,2	*Saccharomyces cerevisiae*	Stimulation of growth and biosynthetic activity
5,95 – 7,2; 6,035	*Saccharomyces carlsbergensis (pastorianus)*	Accelerating development; temporary discreteness
Algae		
7,1; 5,6	*Scenedesmus quadricauda*	Reducing toxicity of the medium
6,06; 7,1; 8,34	*Platymonas viridis*	Stimulation of growth, intensification of photosynthesis

Table 6. Effects of EHF radiation on different taxonomic groups of microorganisms

There is a certain similarity in effects of single exposure by millimeter waves on photosynthetic and non-photosynthetic organisms. The former were already mentioned above; the latter include bacteria, actinomycetes, fungi, yeast-like fungi, mycophilous fungi, and yeast. Both groups of objects demonstrated intensification of growth and biomass yield, more expressed, as a rule, in photosynthesizing objects. Also, there were observed (1) changes of cell membrane permeability; (2) dependence of the effect on the incident power density; (3) the resonance effect at certain wavelengths; (4) growth inhibition or no effect when removing from the resonant wavelengths; (5) changes in synthesis of biologically active compounds; (6) individual taxonomic sensitivity to resonant wavelengths; (7) absence of mutagenic effect of the irradiation; (8) prolongation (in some cases) of the stimulatory effect on subsequent passages of the cultures.

The identified differences are: (1) non-photosynthetic microorganisms, especially yeast, in some cases needed repeated exposure to obtain distinct stimulatory effect, while photosynthetic organisms were irradiated only once; (2) in non-photosynthetic microorganisms, especially yeast and fungi, morphological changes in cells were observed, which never happened in photosynthetic organisms; (3) the range of resonant wavelengths in the photosynthetic organisms was shifted toward 10 mm; (4) in some cases there was a bactericidal effect of millimeter waves on the non-photosynthetic microorganisms.

Besides the above-mentioned physiological characteristics, we have first studied the effect of nonthermal low-intensity EHF radiation on mineral composition of cyanobacterial cells and on the possibility of the accumulation of certain trace elements in them.

Trace elements are chemical elements contained in human or animal body in very small quantities, 10^{-3}–10^{-12} % by weight, and this low concentration range in living cells and tissues is virtually the only defining attribute of them. Life, as we know, has been originated in the ocean with its extreme diverse but simultaneously definite chemical composition.

The biological evolution (Skalny, 2011b) has led to a sharp increase in mass and diversity of the living substance on the planet, including formation of new chemical compounds and molecules, the novel (secondary) bioelements (in cells).

There appeared the biosphere as an open thermodynamic system in which some secondary bioelements can disappear and others can appear, while the set of primary bioelements – progenitors of life – is likely to remain mainly stable (Skalny, 2011a; Skalny, Skalnaya, 2011).

Simple bioelements produced four fundamental components of cellular life, which, according to J.D.Marth (2008), divided into 68 molecular building blocks ("building blocks of life"). I.e., the simplest bioelements formed more complicated, macromolecular bioelements (Skalny, 2011a; Skalny, Skalnaya, 2011).

Following this logic, we proposed to subdivide bioelements into simple (atoms, ions and water as the universal solvent), and complicated ones, consisting of the above-mentioned 68 molecules (8 of them are nucleosides, which compose DNA and RNA, 20 are natural amino acids necessary for protein synthesis, at least 32 glycans, 8 types of lipids (Marth, 2008)).

The simplest (H, C, O, N, P, S, vital chemical elements, evolutionarily selected by cells from the environment to supply biological functions) (a) and derivative (the 68 molecules, water, oxygen etc.) (b) bioelements we propose to call primary bioelements: respectively, simple (a) and complicated (b). Primary bioelements are, in essence, pre-biological elements or "prebiotic" (Ferris 1999). Other bioelements are likely secondary, because for their formation the primary bioelements were "selected" by cells from the extracellular environment in the process of evolution for performing specific regulatory functions. It is very important for understanding the biological role of chemical elements, which is determined not so much by a chemical element as such, as by its chemical species in the body. I.e., the talk about a specific role of a chemical element in living organism has no biological meaning. The biological meaning is in its chemical variety (Skalny, 2009, 2011a; Skalny, Skalnaya, 2011).

Among the most important properties of the primary single-celled organisms were chemoreception and selective permeability, which helped them adapting to changes in the environmental concentration of various elements, and thus not to die but to adjust to new conditions.

Primary bioelements once produced the first protocell – LUCA (Hoenigsberg, 2003) or probiont (Galimov, 2004) – a hypothetical primary organism which originated all the modern diversity of life on Earth. This organism contained, inter alia, the macromolecules (pro-proteins and pro-DNA) and acquired the ability to reproduce itself (Galimov, 2004).

Primary bioelements existed long before the emergence of life. They had the highest resistance to external conditions due to its simplicity (Skalny, 2009, 2011a; Skalny, Skalnaya, 2011). Bioelements are components and legacy of the "primordial soup", from separate ions to H2O, CO2, O2, glucose and other sugars, amino acids and "proto-RNA". Electric discharges, electromagnetic fields, ultraviolet and visible light, gases – these are the conditions (environment) in which bioelements can unite and "turn in the living" (Skalny, 2009, 2011a; Skalny, Skalnaya, 2011).

Some of the bioelements became components of active centres in enzymes, dramatically accelerating the evolution of life due to formation of metabolic pathways. In the course of evolution, the developed elemental composition common to cells of different species of living organisms has become their most important feature.

Thus, bioelements can be subdivided into primary, i.e. those which could exist before the origin of life, and secondary, i.e. those which have formed as production of living

organisms. This division is necessary for us to better understand the nature and role of bioelements. For example, the fact that life is a self-sustaining process that can produce "raw material" for new living structures. This agrees with the theory of natural self-organization of pre-biological processes by M.Eigen (1971) and ideas of I.Prigogine (1980) about self-organization in open systems (Skalny, 2009, 2011a; Skalny, Skalnaya, 2011).

Based on the ideas of V.P.Kaznacheyev (Kaznacheev, Spirin, 1991), we can assume bioelements the internal condition (medium) for the existence of biological systems, while electromagnetic components – the external condition (environment). Biosphere is an assembly of bioelements and living organisms existing under permanent regulatory influence of physico-chemical factors of terrestrial and cosmic origin.

Trace elements are important part of bioelements. They are not incidental ingredients of tissues, cells and fluids of living things, but components of a naturally developed very ancient and complex physiological system involved in regulating vital functions of the organisms at all stages of their life (Skalny, Rudakov, 2004; Skalny, 2011a). The definition of trace elements is based on three fundamental principles (Avtsyn et al., 1991): selective absorption of them; their selective concentration in certain organisms, organs, tissues or organelles of some cells; selective elimination. Interaction of these mechanisms is just what maintains the trace element homeostasis. In their biological effects and physico-chemical properties, trace elements can be quite dissimilar to one another and the same way different from macro elements, but their main feature remains the extremely small concentration in cells.

The biological role of chemical elements has come under intensive studying in the second half of the twentieth century. There was opened the essentiality of about 20 chemical elements to living organisms, deepened the knowledge of toxic and carcinogenic properties of a number of trace elements, created tens of thousands of drugs and dietary supplements containing trace elements, and food products fortified with them. But “the lack of multidisciplinary approach has been the Achilles heel of biological trace element research” (Iyengar, 1989).

According to the biological role for mammalians and humans, chemical elements are divided into vital (or essential: calcium, phosphorus, potassium, chlorine, sodium, zinc, manganese, molybdenum, iodine, selenium, sulfur, magnesium, iron, copper, cobalt), probably essential (fluorine, silicon, titanium, vanadium, chromium, nickel, arsenic, bromine, strontium, cadmium) and elements with little-known or unknown role (lithium, boron, aluminum, germanium, zirconium, tin, cesium, mercury, bismuth, thorium , beryllium, scandium, gallium, rubidium, silver, antimony, barium, lead, radium, uranium) (Skalny, Rudakov, 2004; Skalny, 2011a). New facts, accumulating from year to year, provide prerequisites for moving certain trace elements from the third group into the second, and from the second into the first. Although this process is not fast, it happens permanently. Among 92 naturally occurring chemical elements 81 are found in human body.

According to the current definition, bioelementology is a science studying formation of bioelements, their metabolism, physiological and pathochemical mechanisms of their participation in the regulation of vital functions at either cellular or population and biosphere levels of organization of the living matter (Skalny, Rudakov, 2004).

“Bioelement” is the main term of bioelementology. In literature we found term “bioelement”. Different authors are using it mainly as a synonym to “chemical element”

which “plays some biological role” or “exists in the living body”. Why we named elements “chemical” but not “physical”? Only following tradition, because chemistry as science formed much earlier than nuclear physics and physics of elementary particles. The elements have chemical and even more physical properties, but it is nonsense to separate special “biological elements”. Active use of the term "bioelement" by A.V.Skalny and his followers in recent years in scientific articles (Skalny, Rudakov, 2005; Skalny, 2009), books (Skalny, Rudakov, 2004; Oberleas et al., 2008; Skalny et al., 2009), in textbooks (Borisova et al., 2008; Toxicological Chemistry, 2010) and in reports at international scientific meetings showed that part of scientists, especially chemists, feel a certain rejection of it because of association with the term "chemical element." Nevertheless, it is difficult to find another term which would be more apt and apparently satisfying most scientists. In fact, “element” is a multivocal word. We comfortably use expressions “electrical element”, “heating element”, or “data element”. So, “bioelement” can be a similar case.

Atoms, atomic nuclei, elementary particles and fields that bind them, which have independent significance at the physicochemical stage of evolution, after being included in biological molecules lose this self-importance and play their role in the ensemble, called bioelement, where everything is interdependent, more complicated and at the same time more vulnerable to external influence. Since the general conditions of biological evolution (the composition of biosphere), are continuously changing, a set of bioelements in a living organism can also change. This distinguishes them from chemical elements as objects of physicochemical stage, which remain identical to themselves along the course of evolution. So, bioelement is the elemental functioning unit of living matter, which is a biologically active complex of chemical elements as atoms, ions and nanoparticles with organic compounds of exogenous (primary) or biogenous (secondary) origin under the influence of electromagnetic fields (Skalny, Skalnaya, 2011).

Bioelements can continuously form from ionic compounds when they enter the cell. Inside the cell, biopolymers and their complexes create a complicated, coordinated and regulated system for transformation of substances. Cell is the main place of natural birth of secondary bioelements and their destruction (Skalny, Skalnaya, 2011).

We were interested in the possibility of production (biosynthesis) of secondary bioelements through increased accumulation of various trace elements, primarily essential, in cells of cyanobacteria, and in the influence of physical and chemical factors on this process. The physical factor was the exposure to millimeter waves of low nonthermal intensity; the chemical factor was the fortification of cultural medium with gradually increasing concentrations of selected trace elements.

First we have studied the ability of cyanobacteria S. platensis, S. maxima and Nostoc commune to accumulate elevated concentrations of As, Mo, Se, Zn. We added salts of these elements into the cultural medium during the logarithmic phase on the 7th day of cultures’ growth. It is known that for most mineral components there is more or less wide plateau of concentrations not affecting growth of microorganisms. At the same time, a number of elements, e.g. Se, Cu, Zn, are characterized by very narrow boundary between the concentrations which are necessary for growth and which are toxic. For different groups of microorganisms the inhibitory effect of high concentrations of elements is also different.

The results of the experiments studying toxicity of four trace elements on S. platensis are shown in Fig.2.

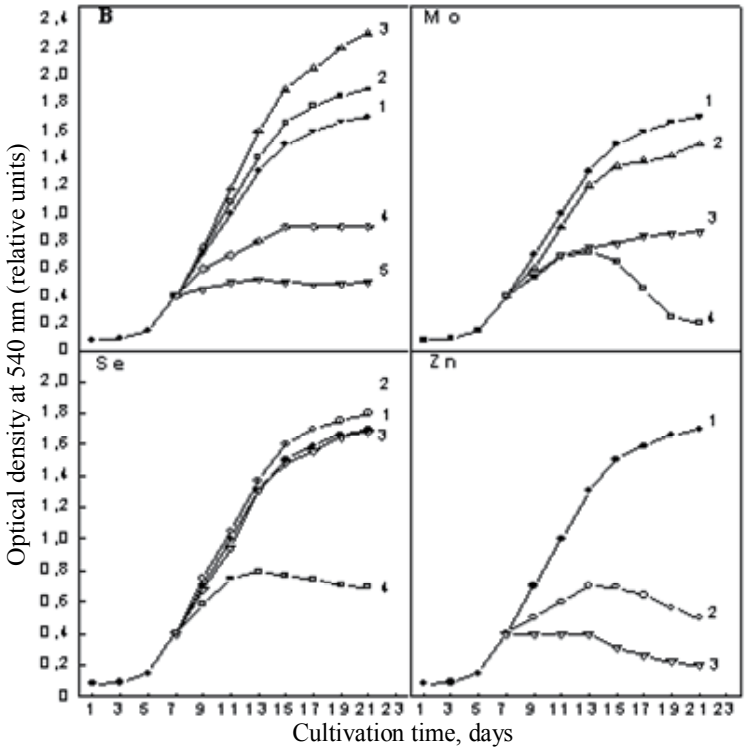

Concentration of the salts in the medium (mmol/l): 1 = control (Zarrouk medium);
B – 2 = 50, 3 = 100, 4 = 200, 5 = 250; Mo – 2 = 40, 3 = 60, 4 = 80;
Se – 2 = 0.06, 3 = 0.03, 4 = 0.6; Zn – 2 = 0.03, 3 = 0.06

Fig. 2. Effect of B, Mo, Se, Zn, introduced into the cultural medium in high concentrations, on the growth of S. platensis

Figure 2 shows a significant difference between the elements, which by the degree of toxicity for the cultures of S. platensis and N. comunne can be arranged in series: Zn> Se> Mo> B. Resistance of cyanobacteria to elevated content of boron and molybdenum in the medium is apparently due to the ability of these elements to complexation. As for selenium, its introduction into the medium of S. platensis in concentrations above 0.6 mmol/l caused a color change to tile-red, which was due to adaptation of the cyanobacteria to high concentrations of selenium in the medium. As it is known from the literature, the excessive amounts of selenium accumulated by the cells are transferred from organic to inorganic form. And as for zinc, even its introduction into the medium in concentration 0.03 mmol/l significantly inhibited growth of the culture, shortened the logarithmic growth phase, and made the maximum density of the cells' suspension in stationary phase of growth not to exceed half of the control value. It is known that zinc ions, showing toxicity when introduced in concentration 0.06 mmol/l in our experiments, affect the entire complex of light and dark reactions of photosynthesis in inhibiting manner.

We proposed the concept of optimum concentration of a trace element, introduced into the cultural medium: this is the concentration that causes maximum possible accumulation of the trace element in the cells without leading to pronounced decrease in the yield of

biomass. When determining the optimal concentrations, we used the criterion equal to the product of intracellular trace element content by the yield of biomass at the given concentration of the trace element in the medium. The maximum value of the criterion corresponds to the optimal concentration of the element in the medium. The optimal concentrations are specific to certain trace elements and to the objects under study. In some cases, apparently, it is more sensible to say about a range of optimal concentrations (Tambiev et al., 2003).

S. platensis		*N. commune*	
Optimal concentrations (mmol/l)	Content in cells (μg/g)	Optimal concentrations (mmol/l)	Content in cells and sheath (μg/g)
B			
150.0	907.2 ± 56.8	1.5	14448.9 ± 423.4
Mo			
20.0	5912.0 ± 295.5	0.25	11206.1 ± 560.7
Se			
0.3	450.0 ± 30.5	0.25	6288.6 ± 310.1
Zn			
0.03	455.5 ± 28.1	0.03	1500.9 ± 75.1

Table 7. The inclusion of B, Mo, Se, Zn in cells of S. platensis, N. commune after their introduction into the medium in optimal concentrations

Table 7 shows that optimal concentrations are higher for less toxic B, Mo, and considerably lower for Se, Zn, which are more toxic for the cyanobacteria. The objects differ in optimal concentrations and intracellular accumulation of the trace elements due to their individual sensitivity and to the fact that, unlike S. platensis, N. commune has a thick mucous sheath, which can also accumulate certain trace elements in considerable amounts.

The first time we were able to establish the effect of individual trace elements, introduced into the cultural medium in high concentrations, on the total mineral composition of cyanobacterial cells. The data are presented in Table 8.

Elements, added to the medium	Species	The observed changes	
		Macro elements	Trace elements
B	*S. platensis*	-	Zn
	N. commune	-	Ca
Mo	*S. platensis*	-	Fe, Mn, Zn
	N. commune	-	Fe, Mn, Zn
Se	*S. platensis*	Ca, Mg	Fe, Zn
Zn	*S. platensis*	Na, K*, Mg, Ca	Fe, Mn, Cu
	N. commune	Na, Mg, Ca	Mn, B

* Note: For intracellular K it was a decrease, for all other elements – an increase.

Table 8. Change in mineral composition of cyanobacteria after adding optimal concentrations of the trace elements into the cultural medium

Table 8 shows that the most significant changes in mineral composition of the cyanobacterial cells happened after introduction of zinc, which is most toxic for cyanobacteria among the investigated trace elements. The least changes were observed after introduction of boron, which is least toxic. Molybdenum and selenium were placed at intermediate positions. These data seem to us very important. We can make the assumption that toxicity of certain trace elements in comparison with others is largely determined by larger or smaller shifts in the overall mineral composition of cells.

We have managed to obtain the greatest possible accumulation of some essential trace elements by cell cultures of S. platensis and S. maxima. This could considerably increase the value and applicability of spirulina biomass in human health care nutrition. The work has begun from registering a patent (Tambiev et al., 1997) for a method of obtaining selenium-containing preparation of spirulina biomass enriched with selenium in organic form with pronounced antioxidant properties. The content of selenium in the cells was determined by atomic-adsorption and fluorometric methods, the total elemental composition of the cell – by developed complex of ICP-AES methods (Sedykh et al., 2005; Skalny et al., 2009).

The possibility to obtain spirulina biomass enriched with selenium in organic form, which has increased bioavailability, has promptly caused the appearance of works extending this direction. In some works a spirulina preparation enriched with bioavailable selenium in combination with reduced glutathione was administered to rats, allowing normalization of intestinal permeability, impaired after systemic anaphylaxis. In other studies it was shown that effective regulation of homeostasis was possible by addition of selenium-rich spirulina to rats' feed. Also there were reports about successful use of selenium-enriched spirulina and yeast as a dietary supplement for patients with non-specific ulcerative colitis and for patients with coronary heart disease (Mazo et al., 2001; Notova et al., 2006).

The optimal concentration of selenium in the cultural medium for S. platensis was taken as 0.3 mmol/l (Table 7), since with it there was no sharp decline in biomass growth, and the cells actively captured selenium. It was revealed that the best way to introduce selenium is to add it into the medium at the logarithmic growth phase of cyanobacteria (5-10 days). There was found clear correlation between selenium content in the cells and in the cultural medium.

There were also shown notable changes in concentrations of certain elements in the cells of S. platensis after the introduction of selenium into the medium (Table 8). When comparing cultures of S. platensis and S. maxima, it was shown that in the presence of sodium selenite in the medium S. maxima accumulates 1.7 as much selenium as S. platensis.

We have separated the biomass of S. platensis, enriched with selenium, molybdenum and zinc, into the following fractions: (1) the sediment, which includes cell wall fragments obtained after ultrasonic cell disruption, amphiphilic proteins and polysaccharides; (2) the chloroform fraction, which includes hydrophobic proteins and lipids; and (3) the water-methanol fraction containing low molecular compounds, hydrophilic cytoplasmic proteins and monosaccharides. The balance of cellular fractions was accurate enough: in total for selenium 95.5%, for molybdenum 91.2% and for zinc 97.4%.

A significant portion of molybdenum, accumulated by cells of S. platensis and N. commune, was found in the chloroform fraction and less than 30% of it contained in the sediment. Over

70% of selenium accumulated by both cultures was found in the sediment and less than 20% – in the chloroform fraction. Similar to selenium, much of the accumulated zinc was also found in the sediment, and about 30% was in the chloroform fraction.

Subsequently we determined optimal concentrations of copper when adding copper sulfate, nitrate and acetate to the medium of S. platensis and S. maxima. Copper sulfate was appeared to be the most toxic: it strongly inhibited growth of S. platensis at the concentration 1.25 mg/l. Copper from nitrate began to markedly incorporates into cells (80 μg/g dry biomass) at the concentration 0.125 mg/l. Acetate at the concentration 0.5 mg/l gave the greatest incorporation of copper into the cells (323 μg/g dry biomass vs. 11.35 μg/g in the control).

Toxicity of copper nitrate and copper acetate did not differ significantly from each other. Nevertheless, in case of copper nitrate (0.5 mg/l), we observed a lengthening of trichomes in S.platensis by 50%, while in case of copper acetate (0.5 mg/l) – by 100% as compared to control.

We have examined the influence of EHF radiation on the accumulation of certain trace elements by cyanobacterial cells and on overall mineral composition of the cells. We introduced zinc sulfate in concentration 0.06 mmol/l into cultural medium of S. platensis at the logarithmic growth phase. Without irradiation its accumulation in the cells was somewhat more than 1000 μg/g dry biomass, while at 0.09 and 0.12 mmol/l growth of the culture was virtually stopped due to high toxicity of zinc (Table 9, upper part).

Experimental conditions	Zn content in the cells and suspension density	Zn concentration in the cultural medium (mol/l)			
		0.03	0.06	0.09	0.12
Zn adding	Zn, μg/g	455±22.7	1015±50.5	-	-
	D_{540}	*0.5±0.01*	*0.20±0.01*	-	-
EHF irradiation + Zn adding	Zn, μg/g	450.2±32.0	1102.2±50.9	5417.0±570.5	11269.8±810.2
	D_{540}	*1.25±0.02*	*0.88±0.02*	*0.63±0.01*	*0.54±0.02*

Note: age of culture = 21 days; Zn content in the control (Zarrouk medium) = 63.8 ± 10.7 μg/g; D = 1.7 ± 0.1; yield of biomass = 1.01 ± 0.04 g/l dry weight.

Table 9. The inclusion of Zn in S. platensis cells (μg/g) after adding different concentrations of ZnSO4 into the cultural medium and after previous exposure to EHF irradiation

Single EHF irradiation (wavelength 7.1 mm, incident power density 1.5 mW/cm2) of S. platensis before introduction of zinc sulfate into the medium significantly reduced its toxicity. At zinc concentrations in the medium 0.09 and 0.12 mmol/l, which previously stopped the growth, now the biomass on the 21st day reached 50% and 40%, respectively, with significant accumulation of zinc in the cells (Table 9, lower part).

Experiments have shown that EHF radiation also affected mineral composition of S. platensis and N. commune cells.

Figure 3 demonstrates that in the cells of S. platensis the amount of sodium, potassium and magnesium increased. For a number of other studied elements there was observed only a tendency to increase that may be due to low incident power density in the experiment. We have previously stated that EHF radiation causes a stimulating effect on growth and yield of biomass of cyanobacteria. As it can be seen, after irradiation of N. commune there was observed an increase in the amount of not only intracellular sodium and potassium, but also boron, which can bind to the polysaccharide sheath of the cells.

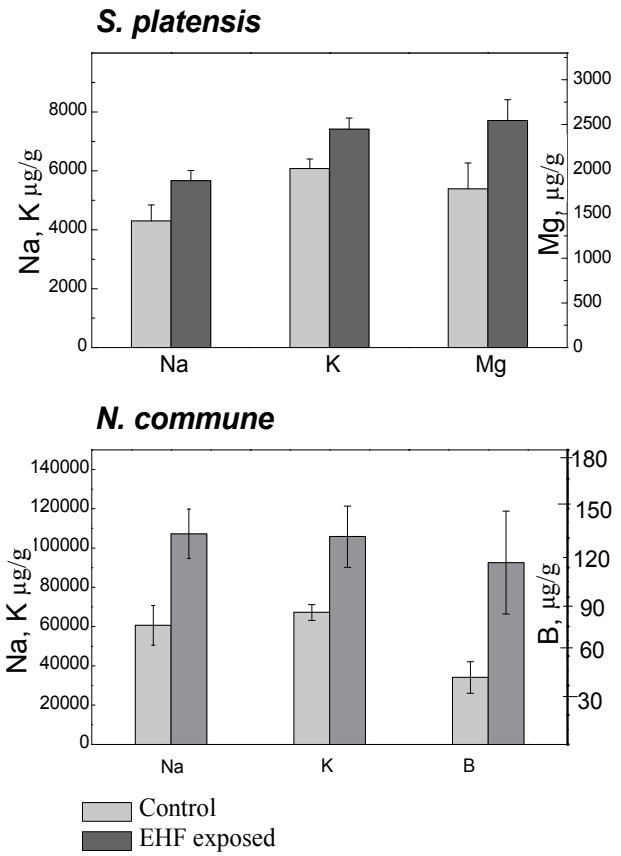

Fig. 3. Effect of EHF radiation on mineral composition of S. platensis, N. commune cells

The cyanobacterium N. commune is a food species, widely spread from the Far North, e.g. Taimyr wetlands and Yakutia, up to the South – Mongolia, Java, India etc. Nutritional properties of this genus are known from the VI century AD. Currently species of this genus, including N. commune, are used for food besides the mentioned places also in China, Japan and the Philippines. China in the 1990s planned to organize mass cultivation of this species.

We have studied chemical composition of N. commune biomass, including the total content of components, amino acids, vitamins, fatty acids, inter alia essential ones, and the content of 13 macro and trace elements.

Parameter	Content	Determination method
The overall composition (% of dry biomass)		
Humidity	93.9	Gravimetric method
Dry matter	6.1	Gravimetric method
Free amino acids	0.167	Amino acid analyzer
Protein	23.5	Lowry assay
Carbohydrates	36.5	Phenol-sulfuric method
Lipids	2.2	Folch method
Vitamins (μg/g)		
β-Carotene	350.5	Gas-liquid chromatography (HPLC Jasco, Japan)
Thiamin (vitamin B1)	2.8	Fluorescence spectrofluorimetry (Perkin Elmer MPF-43A, UK)
Riboflavin (vitamin B2)	5.3	Fluorescence spectrofluorimetry (Perkin Elmer MPF-43A, UK)
Nicotinamide (vitamin B3)	38.4	Spectrophotometry
Pantothenic acid (vitamin B5)	5.27	Method with β-naphthoquinone-4-sulfonate (Folin reagent)
Pyridoxine (vitamin B6)	1.5	Gas-liquid chromatography (HPLC Jasco, Japan)
Inositol (vitamin B8)	2772.7	Method with rhodizonic acid
Folic acid (vitamin B9)	0.0066	Spectrophotometry
Cobalamin (vitamin B12)	15.4	Spectrophotometry
Biotin (Vitamin H)	2.69	Microbiological method with lactic-acid bacteria
Tocopherol (vitamin E)	3.0	Fluorescence spectrophotometry
Naphthoquinones (vitamin K)	25.5	Thin layer chromatography
Macro and trace elements (μg/g)		
Calcium	1687.0	Atomic-emission spectrometry with inductively coupled plasma (ICP-AES)
Phosphorus	3719.0	
Magnesium	2727.0	
Iron	704.7	
Zinc	43.38	
Copper	3.379	
Manganese	55.11	
Chrome	3.303	
Sodium	12890.0	
Potassium	11120.0	

Pigments (μg/mg)		
Phycocyanin	9.8	Spectrophotometry
Chlorophyll	18.4	
Carotenoids	8.28	
Fatty acids (μg/mg)		
Linoleic *	2.29	Gas chromatography with mass spectrometric detector
γ-Linolenic *	0.32	
Oleic	1.03	
Palmitic	0.86	
Amino acids		
Alanine, arginine, aspartic acid, glutamic acid, cystine, glycine, histidine, isoleucine, leucine*, lysine*, methionine*, phenylalanine*, praline*, serine, threonine, tryptophan*, tyrosine*, valine*		Amino acid analyzer

* - Essential fatty acids and essential amino acids

Table 10. Chemical and mineral composition of N. commune biomass

Also, we studied accumulation of important essential trace elements, namely boron, molybdenum, selenium, zinc, by N. commune cells, and determined the optimal concentrations for them (Table 7). It was also shown that introduction of these trace elements into the cultural medium in optimal and higher concentrations causes shifts in mineral composition of the N. commune cells (Table 8).

Currently there is an interest in studying the biological properties of vanadium compounds, which potentially can be used in treatment of diabetes and cancer, as confirmed by clinical studies. It was noted that the effects of insulin on carbohydrate and lipid exchange can be simulated by vanadium compounds. Therefore vanadium compounds having high hypoglycemic activity and low toxicity are actively investigated.

We studied effects of VOSO4 (vanadyl sulfate) and NaVO3 (sodium vanadate), possessing high biological activity and insulin-like action. The compounds were introduced into cultural medium of S. platensis and S. maxima in elevated concentrations, on growth and yield of biomass. We determined dynamics of vanadium accumulation by both cultures and the optimal concentration for obtaining valuable biomass enriched with vanadium in organic form.

We have shown that S. platensis and S. maxima accumulates vanadium in form of either vanadyl cation (+4) or vanadate anion (+5) more effectively when the cultural medium is enriched with vanadate. Thus, when vanadium concentration in the medium was 2.0 g/l (vanadate), its accumulation in S. platensis cells was 3050 ± 280 μg/g, while if the medium was enriched to the same concentration by vanadyl, than the accumulation in the cells was 1550 ± 165 μg/g. An increase of vanadium concentration in the medium over 2.0 g/l led to a sharp slowdown of the vanadium accumulation by cells. These data are shown in Fig. 4, 5.

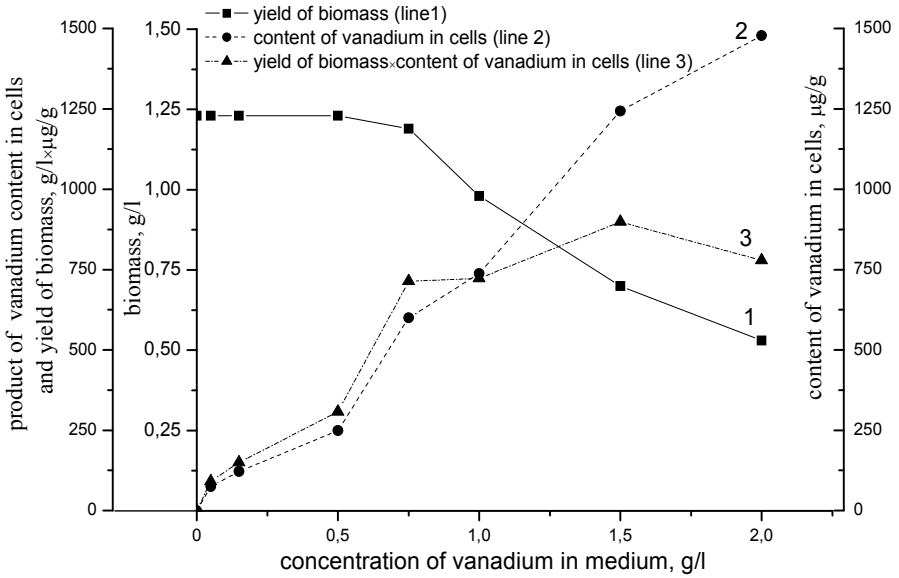

Fig. 4. Content of vanadium in S. platensis cells and yield of biomass depending on concentration of vanadium in the form of vanadyl cation in cultural medium and the value of optimal concentration

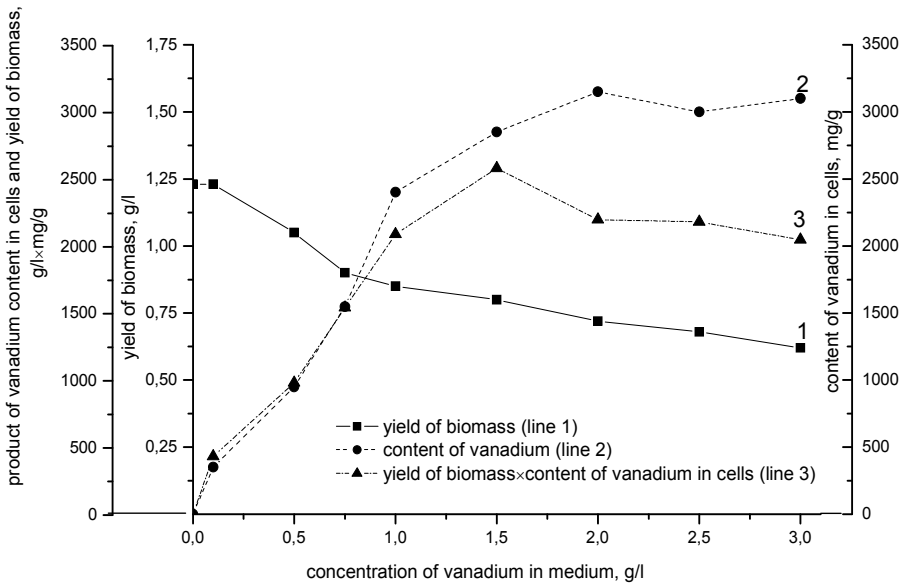

Fig. 5. Content of vanadium in S. platensis cells and yield of biomass depending on concentration of vanadium in the form of vanadate anion in cultural medium and the value of optimal concentration

The optimal concentration of vanadium introduced into the medium in the form of vanadyl was taken as 1.5 g/l, and intracellular accumulation was 1550 ± 75 μg/g (S.platensis) and

1245 ±105 μg/g (S.maxima). The optimal concentrations of vanadium introduced into the medium in the form of vanadate were somewhat different, being for S. platensis 1.5 g/l with intracellular accumulation 3180 ± 185 μg/g, and for S. maxima 1.0 g/l with intracellular accumulation 2650 ± 206 μg/g. It was shown that S. maxima is more resistant to high concentrations of vanadium and stores it in the cells in higher amounts compared with S. platensis (Vasilieva et al., 2011).

The introduction of these forms of vanadium into the growth medium of both cultures caused similar changes in mineral composition of the cells. This apparently indicates that both forms affect the same aspects of metabolism of the cyanobacteria. After adding 2 g/l vanadyl sulfate into the medium, there was observed a decrease in calcium concentration, an increase in concentrations of iron, magnesium, manganese, and a significant increase in boron, chromium and zinc.

At present, there is a significant amount of data suggesting that lithium may be an essential element for humans. Low level of lithium in drinking water leads to an increase in mental illness and suicide, increased crime and drug addiction. Lithium salts are used in medicine for prevention and treatment of mental illness; they promote cell regeneration after injury resulted from the disease. Today, lithium is used, in addition, in dermatology and in treatment of cancer. Some data indicate that organic compounds of lithium are more effective and less toxic than inorganic ones.

We have studied the ability of S. platensis and S. maxima to accumulate lithium in organic form, the dynamics of this process, and the effect of elevated lithium concentrations on mineral composition of cells. The element was introduced as LiCl into the cultural medium of both cultures in the middle of the exponential growth phase.

Relatively small concentration of lithium in the medium caused an increase in biomass of both cultures by 15-17% as compared with the control. A further increase in concentration cancelled the stimulating effect; the first signs of growth inhibition in S. maxima were observed at lithium concentration in the medium 0.75 g/l, in S. platensis – at 0.5 g/l.

Figures 6 and 7 shows that further increase of lithium concentration in the medium to 2.0 g/l resulted in biomass reduction by 41-44% for S. platensis and by 33-36% for S. maxima. The data demonstrates a somewhat greater stability of S. maxima culture to high concentrations of this element. However under the same cultivation conditions cells of both cultures accumulated similar amounts of lithium. The optimal concentration of lithium in cultural medium we took as 1.5 g/l. At this concentration there were no visible morphological changes in cells, while intracellular lithium content in S. platensis and S. maxima became 853 ± 103 and 805 ± 78 μg/g, respectively.

As it can be also seen from the Figures 6-7, the upper limit of the optimal concentrations of lithium was 2.0 g/l. At this concentration there was observed somewhat reduction in biomass, but there was high lithium content in the cells: 1470 ± 189 (S. platensis) and 1508 ± 137 (S. maxima) μg/g. However, by the 17th-18th day of growth in the cultural medium dense clumps of interwoven trichomes began to form, cell morphology altered, trichomes varied in size, multiple fractures and inflations appeared on them, trichomes sticked together in structureless mass, spherical or filamentous forms.

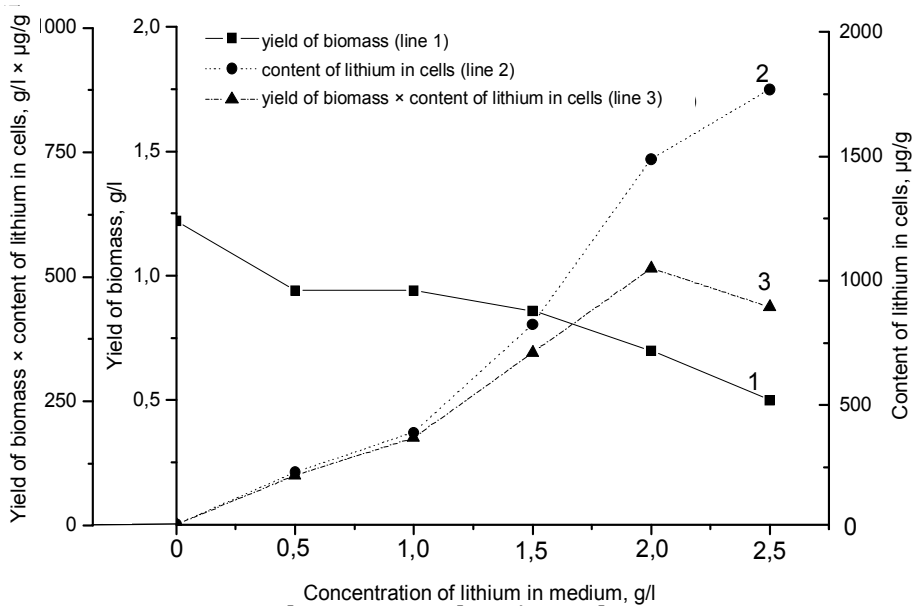

Fig. 6. Content of lithium in S. platensis cells and yield of biomass depending on lithium concentration in cultural medium and the value of optimal concentration

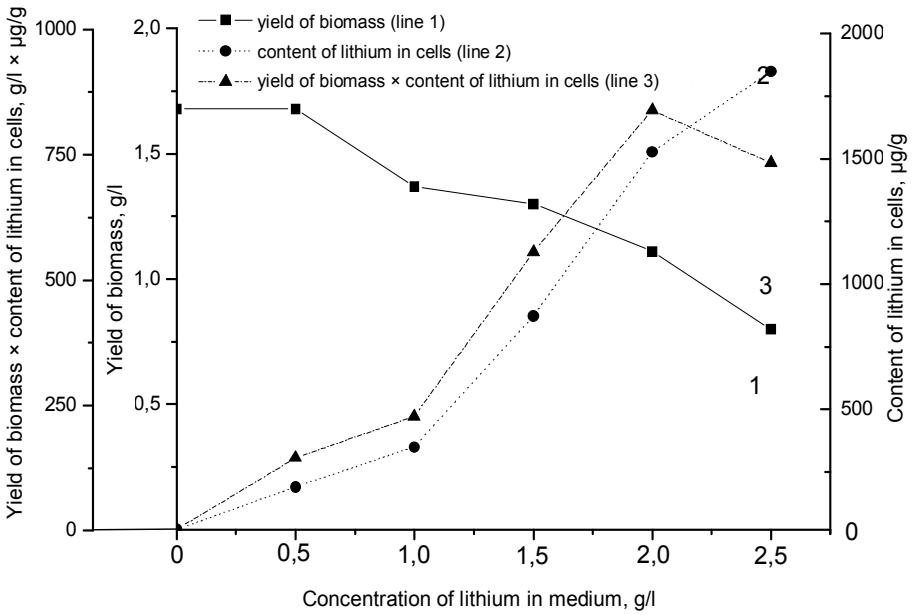

Fig. 7. Content of lithium in S. maxima cells and yield of biomass depending on lithium concentration in cultural medium and the value of optimal concentration

We have studied the effect of elevated lithium concentrations in the medium on mineral composition of cells in both cultures, as it was shown previously for other trace elements. Thus, in S. platensis the intracellular content of potassium had decreased by 30%

(comparing to control) when lithium concentration in the medium was 1.0 g/l and by 60% when it was 2.0 g/l. In cells of S. maxima at the same concentrations of lithium in the medium the potassium in cells decreased by 20 and 40%, respectively. In cells of S. platensis, starting with the lithium concentration in the medium 0.5 g/l, the sodium content, on the contrary, had increased by 50%. In cells of S. maxima this increase in sodium had not yet been observed, but at the lithium concentration in the medium equal to 2.0 g/l the sodium content in cells had grown 3 times in S.platensis, and 2.5 times in S.maxima as compared with the control.

At the same concentration of lithium in the medium (2.0 g/l), in the cells of both cultures manganese content grew 80% and iron content – 50%. The content of magnesium, calcium, zinc, copper, chromium did not change with the introduction of elevated lithium concentrations in the medium of both cultures.

This material demonstrates that electromagnetic radiation of millimeter range (EHF) at low non-thermal intensity, which can be characterized as extremely weak and possibly even superweak physical influence, can affect various aspects of metabolism of phototrophic cyanobacteria and microalgae, stimulate growth and yield of biomass of the cultures etc. It can also influence the accumulation of some essential trace elements in cells of cyanobacteria. It is shown that EHF radiation can reduce the toxicity of trace elements introduced into the medium. And, for the first time, it is established that the entering of elevated concentrations of certain trace elements into cultural medium causes shifts in general mineral profile of the cyanobacterial cells.

The development of bioelementology may lead to appearance of modified cells or technologies for creation of new cells which can be used for medical purposes. Without going into details, we only note that this tale may sooner become a reality with the correct formulation of tasks, based on the correct understanding of the hierarchy of "pre-living" processes and of the life itself, on the formation of new methodological approaches on its basis, on the proper division of essential substances in necessary and sufficient, primary and secondary, with a better understanding of the boundary between "pre-living" and "living", between the set of bioelements and life.

3. References

Avtsyn A.P., Zhavoronkov A.A., Rish M.A., Strochkova L.S. (1991) *Human microelementoses: etiology, classification, organopathology*. Moscow: Meditsina. 355 p. [in Russian]

Bingi V.N. (2002) *Magnetobiology: experiments and models*. Moscow: Milta. 592 p. [in Russian]

Borisova, E.Ya., Ivanov G.P., Kaletina N.I., Mischihin V.A., Simonov E.A., Skalnaya M.G., Skalny A.V., Smirnov A.V., Chukarin A.V. (2008) *Toxicological Chemistry. Metabolism and analysis of toxicants: a training manual*. Ed. by N.I.Kaletina. Moscow: GEOTAR-Media. 1016 p. [in Russian]

Eigen M. (1971) Selforganization of matter and the evolution of biological macromolecules. *Naturwissenschaften*. Vol.58. No.10. pp. 465-523.

Ferris J.P. (1999) Prebiotic synthesis on minerals: bridging the prebiotic and RNA worlds. *Biol Bull*. Vol.196. pp. 311-314.

Galimov E.M. (2004) Phenomenon of life: Between Equilibrium and non-linearity. *Origin Life Evol Biosph*. Vol.34. pp. 599–613.

Hoenigsberg H. (2003) Evolution without speciation but with selection: LUCA, the Last Universal Common Ancestor in Gilbert's RNA world. *Genet Mol Res*. Vol.2. No.4. pp. 366-375.

Iyengar V. (1989) *Elemental analysis of biological systems*. Vol.1. Boca Raton: CRC Press.

Kaznacheev V.P., Spirin E.A. (1991) *Cosmoplanetary phenomenon of the human: problems of a comprehensive study*. Novosibirsk: Nauka. [in Russian]

Marth J.D. (2008) A unified vision of the building blocks of life. *Nat Cell Biol*. Vol.10. No.9. pp. 1015-1016.

Mazo V.K., Gmoshinski I.V., Parfenov A.I., Ekisenina N.I., Safonova S.A., Shahovskaya A.K., Popova Yu.P., Nizov A.A. (jr) (2001) Selenium status in some groups of patients suffering from gastrointestinal diseases. *Trace Elements in Medicine (Moscow)*. Vol.2. No.1. pp. 28-31. [in Russian]

Notova S.V., Baranova O.V., Barysheva E.S., Nigmatullina J.F., Frolova O.O., Gubajdullina S.G. (2006) Modern conditions and ways of correcting the nutritional status in various age and industrial groups in the population of Orenburg region. *Proc Int Kongress Hannover 2006.* Hannover. pp. 50-52.

Oberleas D., Harland B., Skalny A. (2008) *The biological role of macro and trace elements in humans and animals*. St.Petersburg: Nauka. 544 p. [in Russian]

Prigogine I. (1980) *From Being To Becoming*. New York: W.H.Freeman & Co Ltd.

Sedykh E.M., Lyabusheva O.A., AH Tambiev A.Kh., Bannykh L.N. (2005) Determination of the elemental composition of cyanobacteria cells and individual cell fractions by atomic emission and atomic absorption spectrometry. *Journal of Analytical Chemistry*. Vol.60. No.1. pp. 35-40. [in Russian]

Skalny A.V. (2009) Development of the concept of bioelements and the prospects of bioelementology. *Trace Elements in Medicine (Moscow)*. Vol.10. No.3-4. pp. 1-6. [in Russian]

Skalny A.V. (2011a) Bioelementology as an interdisciplinary integrative approach in life science: terminology, classification, perspectives. *J Trace Elem Med Biol*. Vol.25S. pp.S3-S10.

Skalny A. (2011b) Bioelementology as integrative approach in trace element research *Abstr of 14th International Symposium on Trace Elements in Man and Animals.* Enshi, Hubei, China. pp. 229.

Skalny A.V. (2011c) Bioelementology *Biotechnology: current state and prospects. Proc. 6th Int. Congr*. Part.1. Moscow: D.Mendeleyev University of Chemical Technology of Russia. pp. 302-303. [in Russian]

Skalny A.V., Lakarova E.V., Kuznetsov V.V., Skalnaya M.G. (2009) *Analytical methods in bioelementology*. St. Petersburg: Nauka. 264 p. [in Russian]

Skalny A.V., Rudakov I.A. (2004) *Bioelements in medicine*. Moscow: Onix 21 vek: Mir. 272 p. [in Russian]

Skalny A.V., Rudakov I.A. (2005) Bioelementology – a new term or a new research direction? *Vestnik OSU*. Vol.2. pp. 4-8 [in Russian]

Skalny A.V., Skalnaya M.G. (2011) Metal ions as bioelements. *Metal ions in Biology and Medicine*. John Libbey Eurotext, Paris. Vol. 11. pp. 53.

Tambiev A.Kh. (1984) *Reactivity of plant exometabolites*. Moscow: Moscow State University. 72 p. [in Russian]

Tambiev A.Kh., Kirikova N.N., Betsky O.V., Gulyaev Yu.V. (2003) *Millimeter wave and photosynthetic organisms*. Moscow: Radiotekhnika. 175 p. [in Russian]

Tambiev A.Kh., Kirikova N.N., Lukyanov A.A. (2002) The use of active frequencies of electromagnetic radiation of millimeter and centimeter range in microbiology. *Naukoemkie Tekhnologii*. Vol.3. No.1. pp.34-53. [in Russian]

Tambiev A.Kh., Kirikova N.N., Lyabusheva O.A., Sedykh E.M., Bannykh L.N., Rumsh L.D. (2003) Effect of adding zinc to the medium and effect of EHF radiation on change in macro and trace element composition of cells of the cyanobacterium Spirulina platensis. *Biomeditsinskie tekhnologii i elektronika*. No.10. pp. 43-49. [in Russian]

Tambiev A.Kh., Kirikova N.N., Mazo V.K., Skalny A.V. (1997) *A method of obtaining selenium-containing preparation of spirulina biomass*: Patent RF 2096037 from 17.04.1996.

Toxicological Chemistry. Analytical toxicology: textbook. (2010) Ed. by R.Habriev, N.Kaletina. Moscow: GEOTAR-Media. 752 p. [in Russian]

Vasilieva S.G., Tambiev A.Kh., Sedykh I.M., Lukyanov A.A., Bannikh L.N. (2011) The enrichment of biomass of cyanobacteria with vanadium using the cation and anion forms of its compounds. *J Trace Elem Med Biol*. Vol.25. pp. 109-112.

Edited by A.N. Misra

Biophysics is a vast cross-disciplinary subject encompassing the fields of biology, physics and computational biology etc in microbes, plants, animals and human being. Wide array of subjects from molecular, physiological and structural are covered in this book. Most of these chapters are oriented toward new techniques or the application of techniques in the novel fields. The contributions from scientists and experts from different continents and countries focuss on major aspects of biophysics. The book covers a wide range of topics reflecting the complexity of the biological systems. Although the field of biophysics is ever emerging and innovative, the recent topics covered in this book are contemporary and application-oriented in the field of biology, agriculture, and medicine. This book contains mainly reviews of photobiology, molecular motors, medical biophysics such as micotools and hoemodynamic theory.

ISBN 978-953-51-5253-8

Photo by Rost-9D / iStock

IntechOpen